



**EFFECTS OF THE GRAPHENE ON THE
MECHANICAL PROPERTIES OF FIBRE
REINFORCED POLYMER**

- A NUMERICAL AND EXPERIMENTAL STUDY.

Marzena Pawlik

Doctor of Philosophy 2018

Supervisors:

Dr Yiling Lu

Professor Angela Dean

Table of Contents

| | |
|--|-------|
| List of Figures | VII |
| List of Tables | XI |
| List of abbreviations | XIII |
| List of symbols..... | XVI |
| Author’s declaration..... | XX |
| Abstract..... | XXI |
| Acknowledgement | XXIII |
| 1 Introduction | 1 |
| 1.1 Background | 1 |
| 1.2 Mechanical properties of fibre reinforced polymers (FRPs) modified with graphene | 3 |
| 1.3 Research scope and objectives | 4 |
| 1.4 Structure of this thesis | 5 |
| 2 Literature Review | 7 |
| 2.1 Introduction to fibre-reinforced polymers..... | 7 |
| 2.1.1 Role of fibre reinforcement in FRPs..... | 7 |
| 2.1.2 Interphase and interface in FRPs | 10 |
| 2.1.3 Manufacturing of FRPs..... | 11 |
| 2.2 Material modelling of unidirectional FRPs..... | 13 |
| 2.2.1 Mechanics of FRPs | 13 |
| 2.2.2 Unidirectional lamina..... | 15 |
| 2.2.3 Laminate | 19 |
| 2.3 Nanofillers in fibre-reinforced polymers..... | 23 |
| 2.3.1 Introduction..... | 23 |
| 2.3.2 Graphene and CNTs – definition, classification and properties. | 24 |
| 2.3.3 Method of production of FRPs reinforced with nanofillers..... | 29 |
| 2.4 Multiscale analysis – Finite Element Methods | 37 |
| 2.4.1 Nanocomposite modelling | 37 |
| 2.4.2 Micromodelling modelling of FRPs with interphase..... | 39 |
| 2.4.3 Fuzzy fibre reinforced polymer | 41 |
| 2.4.4 FRPs reinforced with graphene..... | 42 |
| 2.5 Inverse analysis | 43 |
| 2.5.1 Introduction..... | 43 |
| 2.5.2 Objective function..... | 44 |

| | | |
|-------|---|-----|
| 2.5.3 | Inverse analysis of FRPs | 45 |
| 2.5.4 | Challenges in inverse problems | 46 |
| 2.6 | Literature review summary | 47 |
| 3 | Methodology..... | 49 |
| 3.1 | Introduction | 49 |
| 3.2 | Multiscale analysis framework..... | 50 |
| 3.2.1 | Nanoscale - Mori Tanaka method..... | 52 |
| 3.2.2 | Microscale – RVE methods | 56 |
| 3.2.3 | Macroscale simulation | 61 |
| 3.3 | Experimental work | 63 |
| 3.3.1 | Materials | 64 |
| 3.3.2 | Spraying nanofillers on the prepreg..... | 65 |
| 3.3.3 | Spraying nanofillers solution on carbon fibre fabric – wet lay-up process | 72 |
| 3.3.4 | Sample inspection | 75 |
| 3.4 | Inverse analysis | 80 |
| 3.4.1 | ANSYS DesignXplorer..... | 80 |
| 3.4.2 | Inverse analysis methodology to determine interphase properties | 81 |
| 3.5 | Summary | 85 |
| 4 | Influence of Graphene nanoplatelets reinforced interphase on the CFRPs elastic constants..... | 87 |
| 4.1 | Introduction | 87 |
| 4.2 | Properties of GNPs reinforced interphase..... | 88 |
| 4.2.1 | Properties of the GNPs and Matrix..... | 88 |
| 4.2.2 | Results..... | 90 |
| 4.3 | Elastic constants of the lamina with the GNPs reinforced interphase..... | 94 |
| 4.3.1 | RVE modelling | 94 |
| 4.3.2 | Longitudinal and transverse elastic moduli. | 96 |
| 4.3.3 | Longitudinal and transverse shear moduli | 97 |
| 4.3.4 | Poisson’s ratio..... | 98 |
| 4.4 | Macroscale model | 99 |
| 4.4.1 | Prediction of CFRP laminate properties | 99 |
| 4.4.2 | Results..... | 101 |
| 4.5 | Discussion | 101 |
| 4.6 | Summary | 104 |
| 5 | Fuzzy Fibre Reinforced Polymer – numerical modelling | 106 |
| 5.1 | Introduction to fuzzy fibre reinforced polymer (FFRP)..... | 106 |

| | | |
|-------|--|-----|
| 5.2 | CNTs reinforced interphase properties – Mori Tanaka method..... | 107 |
| 5.2.1 | RVE models | 111 |
| 5.2.2 | Material properties of each phase | 111 |
| 5.3 | Results | 112 |
| 5.3.1 | Longitudinal modulus of CFRP and FFRP | 113 |
| 5.3.2 | Transverse modulus of CFRP and FFRP | 113 |
| 5.3.3 | In-Plane Shear modulus of CFRP and FFRP..... | 114 |
| 5.3.4 | Out-of-Plane Shear Modulus of CFRP and FFRP | 114 |
| 5.4 | Discussion | 116 |
| 5.5 | Summary | 118 |
| 6 | Effects of spraying nanofillers on mechanical properties of Fibre Reinforced Polymers - experimental results. | 119 |
| 6.1 | Introduction | 119 |
| 6.2 | Experimental results on the carbon fibre prepreg sprayed with nanofillers..... | 120 |
| 6.2.1 | Flexural properties | 120 |
| 6.2.2 | Interlaminar properties | 122 |
| 6.2.3 | Fracture toughness | 127 |
| 6.3 | Experimental results on the carbon fibre fabric sprayed with nanofillers..... | 142 |
| 6.3.1 | Flexural properties | 142 |
| 6.3.2 | Interlaminar properties..... | 143 |
| 6.3.3 | Discussion | 146 |
| 6.4 | Summary | 148 |
| 7 | Prediction of interphase properties via inverse analysis and optimisation..... | 149 |
| 7.1 | Introduction | 149 |
| 7.2 | Validation of optimisation..... | 150 |
| 7.2.1 | Forward simulations..... | 150 |
| 7.2.2 | Testing optimisation algorithms at the microscale | 152 |
| 7.3 | Indirect prediction of the interphase properties..... | 154 |
| 7.3.1 | Optimisation at the macroscale | 154 |
| 7.3.2 | Optimisation at the microscale..... | 160 |
| 7.3.3 | Discussion | 171 |
| 7.4 | Summary | 173 |
| 8 | Conclusions | 174 |
| 8.1 | Summary of findings and contribution to knowledge..... | 174 |
| 8.2 | Limitations and future work..... | 176 |
| 8.3 | Publications from this work | 177 |

| | |
|---|-----|
| References..... | 179 |
| APPENDIX A: Multiscale model..... | 193 |
| APPENDIX B: Experimental results..... | 205 |
| APPENDIX C: Fuzzy fibre reinforced polymer..... | 213 |
| APPENDIX D: Optimisation..... | 224 |

List of Figures

| | |
|---|----|
| Figure 1-1 Materials composition of Boeing 787 aircraft (Boeing 787, 2018) | 1 |
| Figure 2-1 Comparison between thermosets and thermoplastics resin..... | 9 |
| Figure 2-2 Schematic representation of FRP with the concept of the interphase. | 11 |
| Figure 2-3 Example of unidirectional and cross-plyed laminates | 13 |
| Figure 2-4 Modelling of unidirectional fibre reinforced polymers at micro and microscale. 15 | |
| Figure 2-5 Schematic representation of two types of microstructures with the same fibre volume fraction, where (a) is a periodic microstructure and (b) is a random microstructure. Square, hexagonal and cylindrical unit cells are shown in the periodic microstructure..... | 19 |
| Figure 2-6 Angled lamina annotated with local coordinate system..... | 20 |
| Figure 2-7 Location of each ply of laminate with respect to the mid-plane. | 21 |
| Figure 2-8 Resultant moments and forces which are acting on laminate. | 22 |
| Figure 2-9 Schematic diagrams of (a) hexagonal graphene structure (b) carbonaceous nanofillers (Geim, 2009)..... | 25 |
| Figure 2-10 Schematic representation of (a) armchair nanotube, (b) a zig-zag nanotube, (c) a chiral nanotube. Reproduced with permission from Terrones 2001..... | 28 |
| Figure 2-11 Schematic representation of (a) Electrophoretic deposition of graphene on fibre process (b) Dip coating fibre in graphene solution..... | 32 |
| Figure 2-12 Chemical grafting (reproduced with permission from Chen et al., 2014) | 35 |
| Figure 2-13 Nanocomposite modelling methods..... | 37 |
| Figure 2-14 Bilinear traction-separation law of the cohesive element (reproduced with permission from Yang et al., 2012). | 41 |
| Figure 2-15 Direct problem versus inverse problem | 45 |
| Figure 3-1 Flowchart of a multiscale approach | 51 |
| Figure 3-2 Local coordinates system of single graphene nanoplatelet. | 52 |
| Figure 3-3 Quarter of cross-section view of carbon fibre with (a) randomly orientated GNPs and (b) aligned GNPs within the reinforced interphase. Global coordinate system (1-2-3) is used as shown. | 54 |
| Figure 3-4 Schematic drawings of (a) CFRP lamina and (b) its three-phase representative volume element with the reinforced interphase. The 1-2-3 coordinate system is added to define the material property..... | 57 |
| Figure 3-5 Implementation of the material properties of the three-phase RVE model - an excerpt of an exemplary APDL input file..... | 59 |
| Figure 3-6 Mesh independent study for 3 phase RVE model. | 59 |
| Figure 3-7 Orthotropic elastic properties assigned to the lamina (note that x-direction is aligned with fibre direction). Image used courtesy of ANSYS, Inc. | 62 |
| Figure 3-8 Example of layered section command ANSYS created for 12 layers unidirectional specimen, with fibres orientated in 90° direction. Image used courtesy of ANSYS, Inc..... | 63 |
| Figure 3-9 FEA model of the three-point bending test of a laminate specimen. Boundary conditions assigned in ANSYS workbench. | 63 |
| Figure 3-10 Comparison of two solution mixtures of methanol and CNTs at a concentration of 0.25 wt% with two different surfactants (a) CTAB (b) PVP immediately after mixing. ... | 65 |
| Figure 3-11 Laminate preparation for a 28 layer sample by hand lay-up process (14 th layer of DCB panel with PTFE film inserted) (a) and de-bulking process for a certain number of layer (b) | 67 |
| Figure 3-12 Schematic illustration of the spraying process (reproduced with permission from Zhang et al., 2015) | 68 |

| | |
|--|----|
| Figure 3-13 Schematic representation of (a) top view of unidirectional laminate manufactured for 3PB and SBT (part I sprayed with nanofillers, and part II control CFRP) (b) Cross-section view of laminate sprayed with nanofillers (part I) | 69 |
| Figure 3-14 Schematic representation of (a) top view laminate manufactured for DCB test (part I a –pure CFRP, part II b – 0.00035 wt% of CNTs, part III c- 0.00065 wt% of GNPs, part IV d - 0.00044 wt%) (b) Cross-section view of laminate sprayed with nanofillers. | 70 |
| Figure 3-15 Schematic representation of the vacuum bagging process..... | 70 |
| Figure 3-16 Curing cycle of the MTC801 unidirectional laminate. | 71 |
| Figure 3-17 Illustration of the cutting process using COMPCUT 200..... | 72 |
| Figure 3-18 Wet lay-up process: (a) epoxy degassing using vacuum chamber at 1 bar for 20 minutes, (b) Impregnating unidirectional carbon fibre fabric with epoxy resin..... | 73 |
| Figure 3-19 (a) Spraying process of GNPs/epoxy/ethanol solution using an airbrush, (b) Evaporating the solvent under 60° for 2 hours, (c) Curing sprayed laminate under vacuum..... | 75 |
| Figure 3-20 (a) Preparation of the polished specimen for the microscope study, (b) Images extract using optical microscope and data processing (c) Cutting microscope samples. | 76 |
| Figure 3-21 Cross-sectional view of the unidirectional laminate CFRP with sprayed CNTs and GNPs. | 77 |
| Figure 3-22 Optical micrographs of unidirectional laminate (manufactured by prepreg hand lay-up method) (a) cross-section view of the sample in the direction parallel to fibres (b) carbon fibre distribution- examples of packaging arrays: hexagonal and square (c) and (d) side view of the specimen in direction perpendicular to fibres. | 78 |
| Figure 3-23 Optical microscope images of unidirectional laminate (manufacture by wet lay-up) (a) cross sample view of the specimen in the direction parallel to the fibre (b) carbon fibre distribution- examples of packaging arrays: hexagonal and square (c) side view of the side of the specimen in direction perpendicular to fibres, (d) side view of the side of the specimen in direction perpendicular to fibres..... | 79 |
| Figure 3-24 Schematic of the macroscale optimisation process performed in ANSYS Design Xplorer. Image used courtesy of ANSYS, Inc..... | 82 |
| Figure 3-25 Framework of Adoptive Multi-Objective Optimisation Algorithm (ANSYS, 2018). Image used courtesy of ANSYS, Inc..... | 83 |
| Figure 3-26 Initial input parameters defined in ANSYS APDL..... | 83 |
| Figure 3-27 Parameterisation of interphase properties in the RVE modelling – excerpt of APDL script. | 84 |
| Figure 3-28 Structure of the microscale optimisation process performed in ANSYS Design Xplorer. Image used courtesy of ANSYS, Inc..... | 85 |
| Figure 4-1 The cross-section views of the carbon fibre coated with GNPs following 1-2-3 global coordinate system (a) randomly orientated (b) aligned..... | 90 |
| Figure 4-2 Elastic Modulus of the reinforced interphase with randomly orientated GNPs as a function of the volume fraction of GNPs in the interphase. | 91 |
| Figure 4-3 Poisson’s ratio of the reinforced interphase with randomly orientated GNPs as a function of the volume fraction of GNPs in the interphase. | 91 |
| Figure 4-4 In-plane elastic modulus of the reinforced interphase with aligned GNPs as a function of the volume fraction of GNPs in the interphase. | 92 |
| Figure 4-5 In-plane shear modulus of the reinforced interphase with aligned GNPs as a function of the volume fraction of GNPs in the interphase. | 93 |
| Figure 4-6 Out-of-plane elastic modulus of the reinforced interphase with aligned GNPs as a function of the volume fraction of GNPs in the interphase. | 93 |

| | |
|--|-----|
| Figure 4-7 Out-of-plane shear modulus of the reinforced interphase with aligned GNPs as a function of the volume fraction of GNPs in the interphase. | 94 |
| Figure 4-8 VEORIENT command applied to the transversely isotropic interphase. Image used courtesy of ANSYS, Inc. | 95 |
| Figure 4-9 Effects of the volume fraction of GNPs in the reinforced interphase on the longitudinal elastic modulus of the unidirectional lamina. | 96 |
| Figure 4-10 Effects of the volume fraction of GNPs in the reinforced interphase on the transverse elastic modulus of the unidirectional lamina. | 97 |
| Figure 4-11 Effects of the volume fraction of GNPs in the reinforced interphase on the longitudinal shear modulus of the unidirectional lamina. | 98 |
| Figure 4-12 Effects of the volume fraction of GNPs in the reinforced interphase on the transverse shear modulus of the unidirectional lamina. | 98 |
| Figure 4-13 Effects of the volume fraction of GNPs in the reinforced interphase on longitudinal Poisson's ratio of the unidirectional lamina. | 99 |
| Figure 4-14 Boundary conditions for a meshed model of 0° sample without interphase. Image used courtesy of ANSYS, Inc. | 100 |
| Figure 5-1 Schematic of a fuzzy fibre consisting of fibre which is coated with radially aligned CNTs (Kundalwal et al., 2011). | 107 |
| Figure 5-2 Schematic illustrations of (a) Cross-section view of the fuzzy fibre, (b) Perspective view of the fuzzy fibre, (c) Hexagonal RVE model of FFRP RVE model. | 110 |
| Figure 5-3 Longitudinal modulus of carbon fibre reinforced polymer versus carbon fibre volume fraction - the influence on the presence of CNTs interphase. | 113 |
| Figure 5-4 Transverse modulus of carbon fibre reinforced polymer versus carbon fibre volume fraction - the influence on the presence of CNTs interphase. | 114 |
| Figure 5-5 In-plane shear modulus of carbon fibre reinforced polymer versus carbon fibre volume fraction - the influence on the presence of CNTs interphase. | 115 |
| Figure 5-6 In-plane shear modulus of carbon fibre reinforced polymer versus carbon fibre volume fraction - the influence on the presence of CNTs interphase. | 115 |
| Figure 6-1 Three-point bending test rig according to BS EN ISO 14125 (span length 80mm). | 120 |
| Figure 6-2 Load-deflection curve for UD 90° carbon fibre long beam in the three-point bending test. The laminate sample was prepared from prepreg plies sprayed with nanofillers. | 121 |
| Figure 6-3 Typical failure modes in SBT acceptable single and multiple pure shear failure modes (a,b), unacceptable failure mode: tension (c) and compression (d) (schematic drawing created based on BS EN ISO 14130, 1998). | 123 |
| Figure 6-4 Short beam test experimental set-up (Loading roller diameter =10mm, support diameter=4mm). | 123 |
| Figure 6-5 Force-deflection results of short beam test (black colour represents pure CFRP, red colour represents CFRP sprayed with nanofillers solution). | 124 |
| Figure 6-6 Glass transition temperature of MTC801 laminate measured by DMA. | 125 |
| Figure 6-7 Samples inspection after SBT. Digital images of tested samples (a) optical micrographs of the tested sample (b) region near the load cell compression force and (c) delamination observed on the side view of the sample. | 125 |
| Figure 6-8 Double cantilever beam test (DCB) (a) Experimental set-up (b) Sample preparation (c) Crack propagation recording. | 127 |
| Figure 6-9 Load displacement trace for DCB test – initial loading. Dashed line represents sample 3 (pure CFRP), which has been used for exemplar post-processing. | 129 |

| | |
|---|-----|
| Figure 6-10 Frames from the video recorded during the initial loading of sample 3 (a) crack length at the time of 145 seconds is 74mm (b) rapid unstable crack propagation to 80 mm a second later. | 129 |
| Figure 6-11 PTFE insert film inspection of the sample after the completion of the DCB test. | 130 |
| Figure 6-12 Example of the load-displacement trace for DCB test – reloading of sample 3. | 130 |
| Figure 6-13 Modified Beam Theory – determination of the correction factor for specimen 3. | 132 |
| Figure 6-14 Compliance Calibration method – determination of n component for specimen 3. | 132 |
| Figure 6-15 Modified Compliance Calibration Method – determination of A1 component for sample 3. | 133 |
| Figure 6-16 Strain energy release rate versus delamination length. Comparison of Modified Beam Theory, Compliance Calibration and Modified Compliance Calibration Methods. ... | 134 |
| Figure 6-17 Methods for Introducing Opening load to DCB specimen (large displacement correction) (ASTM D 5528-01, 2009) | 135 |
| Figure 6-18 Average mode I strain energy release versus crack length (panel IIIC -0.00065 wt% of GNPs, panel IVD 0.00044 wt%) | 136 |
| Figure 6-19 Mode I strain energy release versus crack propagation – comparison of average curve of all four group of samples. | 137 |
| Figure 6-20 Schematic drawing of the tested sample. Yellow area indicates the location where SEM samples were cut– distance from the end of inserted PTFE film (not in scale). | 138 |
| Figure 6-21 SEM images of fracture surface area (a) pure CFRP, (b) 0.00035 wt% of CNTs CFRP (yellow arrows indicate the crack propagation direction)..... | 139 |
| Figure 6-22 SEM images of 0.00065wt% GNPs sprayed CFRP (a) carbon fibre coated with GNPs (b) GNPs (c) fibre bridging and (d) resin cusps on the carbon fibre. | 139 |
| Figure 6-23 The relationship between force and deflection obtained from short beam test. Influence on the span to thickness (s/t) ratio on the material behaviour. | 144 |
| Figure 6-24 (a) Image of tested SBT specimen (thickness to span ratio=7) (b) delamination observed in a cross section of the specimen (magnification 50) | 144 |
| Figure 6-25 The relationship between force and deflection for CFRPs (red colour represents the sample with GNPs, black is pure CFRP) | 145 |
| Figure 7-1 Influence of the optimisation algorithm on the behaviour of input parameters. Young’s modulus of interphase versus a number of iterations..... | 154 |
| Figure 7-2 Macroscale simulation optimisation..... | 155 |
| Figure 7-3 Bar chart represents the influence of the input lamina elastic constant on the deflection of 0° unidirectional laminate in three-point bending test simulations. | 157 |
| Figure 7-4 Bar chart represents the influence of the input lamina elastic constant on the 90° deflection in three-point bending test simulations. | 158 |
| Figure 7-5 Parameterisation of the two-phase RVE model in APDL script. | 161 |
| Figure 7-6 Parameterisation of the three-phase RVE model in APDL script..... | 164 |
| Figure 7-7 Parameters sensitivity study for epoxy-coated CFRP. | 166 |
| Figure 7-8 Parameterisation of the three-phase RVE model in APDL script..... | 168 |

List of Tables

| | |
|---|-----|
| Table 2-1 Mechanical properties of selected types of fibres..... | 8 |
| Table 2-2 Mechanical properties of selected matrices | 10 |
| Table 2-3 Experimental results on the influence of nanofillers matrix modification on mechanical properties of FRPs | 31 |
| Table 2-4 Influence of nanofillers on mechanical properties of FRP applied by dip coating or EPD methods | 34 |
| Table 2-5 Summary of selected experimental data using grafting technique and its influence on mechanical properties of FRP..... | 36 |
| Table 3-1 Comparison between different solvents and surfactants and their effects on the dispersion with nanofillers 48 hours after the mixing process. | 66 |
| Table 4-1 Exemplar graphene properties taken from the literature | 89 |
| Table 4-2 Properties of graphene nanoplatelet in the local coordinate system (1'-2'-3') | 89 |
| Table 4-3 Properties of carbon fibre and matrix in the global coordinate system (1-2-3)..... | 95 |
| Table 4-4 Properties of the single lamina with and without graphene reinforced interphase. | 100 |
| Table 4-5 Comparison between the flexural modulus predicted by present multiscale modelling and experimental data. | 101 |
| Table 5-1 Mechanical properties of SWCNT and epoxy resin. | 108 |
| Table 5-2 Comparison between the properties of the CNTs reinforced interphase predicted by self-consistent method and present Mori-Tanaka approach. | 110 |
| Table 5-3 Transversely isotropic material properties of carbon fibre T650. | 112 |
| Table 6-1 Comparison of 0° and 90° flexural properties of the unidirectional carbon fibre reinforced laminate (pure CFRP and CFRP reinforced with CNTs and GNPs)..... | 122 |
| Table 6-2 Dimensions and specifications of specimens prepared for fracture toughness test. | 128 |
| Table 6-3 DCB post-processing results example for pure CFRP. | 135 |
| Table 6-4 Comparison of average mode I strain release energy for various wt % of nanofillers. | 138 |
| Table 6-5 Comparison of 0° and 90° flexural properties of the unidirectional carbon fibre reinforced laminate (pure CFRP and CFRP reinforced with 0.5 wt% of GNPs). | 142 |
| Table 6-6 Specimen dimensions prepared for short beam test..... | 143 |
| Table 6-7 Apparent interlaminar shear strength results and standard deviations for pure CFRP and CFRP reinforced with GNPs. | 145 |
| Table 7-1 Properties of carbon fibre (T300) epoxy resin (914C) and interphase. | 151 |
| Table 7-2 Comparison of T300/914C properties predicted by the present model with available published data. | 152 |
| Table 7-3 Objective and constraints selected in the validation case – ANSYS optimisation process..... | 152 |
| Table 7-4 Interphase properties predicted by ANSYS goal-driven optimisation. | 153 |
| Table 7-5 Samples dimensions and specification used in macroscale simulations..... | 155 |
| Table 7-6 Upper and lower bounds of the parameters sensitivity study – optimisation at macroscale level..... | 156 |
| Table 7-7 Initial guess parameters predicted by RVE models. | 158 |
| Table 7-8 Comparison of input and optimised lamina properties for non-coated CFRP..... | 159 |
| Table 7-9 Comparison of input and optimised lamina properties for epoxy-coated CFRP.. | 160 |
| Table 7-10 Comparison of input and optimised lamina properties for GNPs-coated CFRP. | 160 |

| | |
|---|-------------------------------------|
| Table 7-11 Upper and lower bounds of the carbon fibre input parameters..... | 162 |
| Table 7-12 Results of the optimisation study on the carbon fibre properties – non-coated CFRP (two-phase RVE model)..... | 163 |
| Table 7-13 Absolute percentage error results. Difference between calculated lamina properties from new carbon fibre parameters at microscale and lamina properties obtained from the macroscale optimisation study | 163 |
| Table 7-14 Objectives of this optimisation study and upper and lower bounds of interphase properties in epoxy-coated CFRP. | 165 |
| Table 7-15 Results of the optimisation study on the carbon fibre properties – epoxy-coated CFRP..... | 167 |
| Table 7-16 Absolute percentage error results. Difference between calculated lamina properties and experimental lamina properties obtained from the macroscale optimisation study..... | 167 |
| Table 7-17 Objectives of this optimisation study and upper and lower bounds of interphase properties – GNPs coated CFRP..... | 169 |
| Table 7-18 Results of the optimisation study on the carbon fibre properties – GNPs-coated CFRP..... | Error! Bookmark not defined. |
| Table 7-19 Absolute percentage error results for GNPs coated CFR. Difference between calculated lamina properties and experimental lamina properties obtained from the macroscale optimisation study (sought target). | 170 |

List of abbreviations

| | |
|---------|---|
| 3PBT | Three-point bending test |
| 4PBT | Four-point bending test |
| AFM | Atomistic force microscopy |
| a-SWCNT | Amine functionalized single-wall carbon nanotubes |
| BMI | Bismaleinide resin |
| CC | Compliance calibration. |
| CCA | Composite cylinder assemblage |
| CES | Cambridge Engineering Selector |
| CF | Carbon fibre |
| CFRP | Carbon fibre reinforced polymer |
| CLT | Classical Lamination Theory |
| CNTs | Carbon Nanotubes. |
| CPT | Cured ply thickness |
| CST | Compression shear test |
| CT | Compression test |
| CTAB | Cetyltrimethylammonium bromide |
| CuO | Copper oxide nanoparticles |
| CVD | Chemical vapour deposition |
| DBSA | Dodecylbenzensulfonic acid |
| DC | Dip coating |
| DCB | Double Cantilever Beam |
| DIC | Digital image correlation |
| DVB | Divinylbenzene |
| EPD | Electrophoretic deposition |
| FEA | Finite element analysis |
| FEM | Finite elements methods |
| FESEM | Field emission scanning microscopy |
| FFRP | Fuzzy fibre reinforced polymer |
| FGO | Functionalized graphene oxide |
| FLG | Few layered graphene |
| FRP | Fibre reinforced polymer |

| | |
|--------|--|
| FT | Fatigue test |
| GF | Glass fibre |
| GNPs | Graphene nanoplatelets |
| GO | Graphene oxide |
| gsm | Grams per square metre. |
| IFSS | Interfacial shear strength |
| ILSS | Interlaminar shear strength |
| ISO | International Organisation for Standardization |
| LAMMPS | Large Scale Atomic/Molecular Massively Parallel Simulation |
| MBT | Modified Beam theory. |
| MCC | Modified compliance calibration. |
| MD | Molecular Dynamics |
| MD | Multidirectional. |
| MM | Matrix modification |
| MT | Mori Tanaka |
| NF | Natural fibre |
| PANI | Polyaniline |
| PEEK | Poly-ether-ether-ketone |
| PTFE | Polytetrafluoroethylene |
| PVP | Polyvinylpyrrolidone |
| RGO | Reduced graphene oxide |
| ROM | Rule of mixture |
| RTM | Resin transfer moulding |
| RVE | Representative Volume element |
| SBT | Short beam test |
| SEM | Scanning electron microscopy |
| SFTT | Single fibre tensile test |
| sGO | Silinaized graphene oxide |
| STM | Scanning tunnelling microscopy |
| TEM | Transmission electron microscopy |
| TRGO | Thermally reduced graphene oxide |
| TT | Tensile test |
| UD | Unidirectional. |

| | |
|-------|---|
| VARTM | Vacuum assisted resin transfer moulding |
| VIS | Point at which delamination is visually observed on the side of the sample. |
| VOC | Volatile organic compound. |
| XPS | X-ray photoelectron spectra |

List of symbols

| | |
|-------------------|---|
| ε_j | Strain |
| σ_i | Stress |
| τ_{ij} | Shear stress |
| C_{ij} | Stiffness matrix |
| E_1 | Lamina Longitudinal Young's Modulus |
| E_1 | Longitudinal modulus of CFRP lamina |
| $E_{1'}^{CNT}$ | CNT longitudinal modulus |
| $E_{1'}^I$ | In-plane elastic modulus of the aligned GNPs reinforced interphase |
| $E_{1'}^R$ | In-plane modulus of graphene nanoplatelet |
| E_1^f | Carbon fibre longitudinal modulus |
| E_2 | Transverse modulus of CFRP lamina |
| E_2, E_2 | Lamina Transverse Young's Moduli |
| $E_{2'}^{CNT}$ | CNT transverse modulus |
| E_2^f | Carbon fibre transverse modulus |
| $E_{3'}^I$ | Out-of-plane elastic modulus of the of the aligned GNPs reinforced interphase |
| $E_{3'}^R$ | Out-of-plane modulus of graphene nanoplatelet |
| E^I | Elastic modulus of the randomly orientated GNPs reinforced interphase |
| E_f | Flexural modulus |
| E^m | Elastic modulus of matrix |
| F_{max} | Critical force in 3-point bend test. |
| $G_{1'3'}^I$ | Out-of-plane shear modulus of the aligned GNPs reinforced interphase |
| $G_{1'3'}^R$ | Out-of-plane shear modulus of graphene nanoplatelet |
| G_{12} | Longitudinal shear modulus of CFRP lamina |
| $G_{12}, G_{13},$ | Lamina In-plane shear moduli |
| $G_{12'}^{CNT}$ | CNT longitudinal shear modulus |
| G_{12}^f | Carbon fibre longitudinal shear modulus |
| G_{23} | Lamina Out-of-plane shear modulus |
| G_{23} | Transverse shear modulus of CFRP lamina |
| G_{IC} | Critical strain energy release rate. |

| | |
|------------------|--|
| S_{ij} | Compliance matrix |
| V_f | Volume fraction of fibre in the FRPs |
| V_m | Volume fraction of matrix in the GNPs reinforced interphase |
| V_r | Volume fraction of GNPs in the reinforced interphase |
| a_0 | Initial delamination length. |
| c_m | Volume fraction of matrix in the CNTs reinforced interphase |
| c_r | Volume fraction of CNTs in the reinforced interphase |
| k_m | Matrix plane-strain bulk modulus |
| k_r | GNP or CNT plane-strain bulk modulus under lateral dilatation in the (1',2') plane |
| l_m | Matrix cross modulus |
| l_r | GNP or CNT cross modulus |
| m_m | Matrix shear modulus |
| m_r | GNP or CNT shear modulus in the (1',2') plane |
| n_m | Matrix modulus for longitudinal uniaxial straining |
| n_r | GNP or CNT modulus under uniaxial tension in 3' direction |
| p_m | Matrix shear modulus |
| p_r | GNP or CNT shear modulus in the (1',3') or (2',3') plane |
| $v_{1'2'}^r$ | In-plane Poisson's ratio of graphene nanoplatelet |
| $v_{1'2'}^l$ | In-plane Poisson's ratio of the aligned GNPs reinforced interphase |
| $v_{1'3'}^l$ | Out-of-plane Poisson's ratio of the of the aligned GNPs reinforced interphase |
| $v_{1'3'}^r$ | Out-of-plane Poisson's ratio of graphene nanoplatelet |
| v_{12} | Longitudinal Poisson's ratio of CFRP lamina |
| v_{12}, v_{13} | Lamina Major Poisson's ratio |
| $v_{12'}^{CNT}$ | CNT longitudinal Poisson's ratio |
| v_{12}^f | Carbon fibre longitudinal Poisson's ratio |
| v_{23} | Lamina Minor Poisson's ratio |
| $v_{23'}^{CNT}$ | CNT transverse Poisson's ratio |
| v_{23}^f | Carbon fibre transverse Poisson's ratio |
| v^l | Poisson's ratio of the randomly orientated GNPs reinforced interphase |
| v^m | Poisson's ratio of matrix |

| | |
|------------------|---|
| $\bar{\epsilon}$ | Volume average strains |
| κ^I | Effective bulk modulus of randomly orientated GNPs reinforced interphase |
| κ^m | Bulk modulus of matrix |
| μ^I | Effective shear (or rigidity) modulus of randomly orientated GNPs reinforced interphase |
| μ^m | Shear (or rigidity) modulus of matrix |
| $\bar{\sigma}$ | Volume average stresses |
| a | Delamination length. |
| A_I | Slope of a/h vs $C^{1/3}$ graph used in MCC method. |
| b | Width of specimen. |
| C | Compliance (displacement/force) |
| h | Thickness of the macroscale specimen |
| k | Plane-strain bulk modulus for lateral dilatation without longitudinal extension |
| K_{IC} | Critical Stress intensity factor. |
| L | Half of span length. |
| l | Cross modulus |
| m | Rigidity modulus for shearing in any transverse direction |
| n | Slope of $\log C$ vs $\log a$ graph used in CC method. |
| n | Modulus for longitudinal uniaxial strain |
| P | Applied load in DCB test |
| p | Rigidity modulus for shearing in longitudinal direction |
| t | Time. |
| V | Volume of the Representative Volume Element |
| δ | Load point deflection. |
| Δ | Effective delamination extension to correct for the rotation of the DCB arms at delamination front. |
| C | Stiffness matrix |
| F | Force applied to the middle of sample in three-point bending test |
| L | Span length in three-point bending test |
| b | Width of the macroscale specimen |
| s | Deflection of the sample in three-point bending test |

- α Dimensionless parameter of Mori-Tanaka method for randomly orientated GNPs
- β Dimensionless parameter of Mori-Tanaka method for randomly orientated GNPs
- δ Dimensionless parameter of Mori-Tanaka method for randomly orientated GNPs
- η Dimensionless parameter of Mori-Tanaka method for randomly orientated GNPs

Author's declaration

At no time during the registration for the degree of Doctor of Philosophy has the author been registered for any other University Award.

Work submitted for this research degree at the University of Derby is the authors' work and has not formed part of any other University degrees.

None conflict of interest declared.

Author's signature

.....

Abstract

Mechanical properties of carbon fibre reinforced polymer (CFRP) are greatly affected by interphase between fibre and matrix. Coating fibre with nanofillers, i.e. graphene nanoplatelets (GNPs) or carbon nanotubes (CNTs) has suggested improving the interphase properties. Although the interphase is of small thickness, it plays an important role. Quantitative characterisation of the interphase region using experimental technique such as nanoindentation, dynamic mechanical mapping remains challenging. More recently, computational modelling has become an alternative way to study the effects of interphase on CFRP properties. Simulation work of CFRP reinforced with nanofillers mainly focuses on CNTs grown on the fibre surface called fuzzy fibre reinforced polymers. Modelling work on the effects of GNPs on CFRP properties is rather limited. This project aims to study numerically and experimentally the effects of the nano-reinforced interphase on mechanical properties of CFRP.

A multiscale model was developed to study the effects of the GNPs reinforced interphase on the elastic properties of CFRP laminate. The effective material properties of the reinforced interphase were determined by considering transversely isotropic features of GNPs and various orientation. The presence of GNPs in the interphase enhances the elastic properties of CFRP lamina, and the enhancement depends on its volume fraction. The incorporation of randomly orientated GNPs in the interphase increased longitudinal and transverse lamina moduli by 5 and 12 % respectively. While aligned GNPs in the interphase yielded less improvement. The present multiscale modelling was able to reproduce experimental measurements for GNPs reinforced CFRP laminates well. The multiscale model was also proven successful in predicting fuzzy fibre reinforced polymer. Moreover, the interphase properties were inversely quantified by combining with the multiscale model with some standard material testing. A two-step optimisation process was proposed, which involved the microscale and macroscale modelling. Based on the experimental data on flexural modulus, the lamina properties were derived at macroscale modelling, which were later used to determine the interphase properties from the optimisation at the microscale. The GNPs reinforced interphase modulus was 129.1 GPa which is significantly higher than epoxy coated carbon fibre of 60.51 GPa.

In the experiment, a simple spraying technique was proposed to introduce GNPs and CNTs into the CFRP. Carbon fibre prepreg was sprayed with a nanofillers-ethanol solution

using an airbrush. The extremely low volume fraction of nanofillers introduced between prepreg plies caused a noticeable improvement in mechanical properties, i.e. 7% increase in strain energy release. For the first time, the GNPs-ethanol-epoxy solution was sprayed directly on the carbon fibre fabric. Resultant nano-reinforced interphase created on fibre surface showed moderate improvement in samples flexural properties.

In conclusion, a multiscale modelling framework was developed and tested. The GNPs reinforced interphase improved the mechanical properties of CFRP. This enhancement depended on the orientation and volume fraction of GNPs in the interphase. Spraying was a cost-effective method to introduce nanofillers in CFRP and showed huge potential for the scale-up manufacturing process. In a combination of multiscale framework and optimisation process, the nanofillers reinforced interphase was for the first time determined. This framework could be used to optimise the development process of new fibre-reinforced composites.

Acknowledgement

Firstly, I would like to express my sincere gratitude to my director of the study Dr Yiling Lu for his patience, valuable advice and the continuous support throughout my research study. His guidance helped me in developing a range of academic skills, such as teaching, presentation skills, academic writing and many more. I could not have imagined having a better supervisor for my PhD study.

Besides my advisor, I would like to thank Prof Angela Dean, Professor Huirong Le, and Dr Tahir Sharif for their constructive comments and encouragement. I also would like to thank all lecturers in the discipline of mechanical engineering who helped me during undergraduate study. Massive thanks go to my dear colleague, Dr Maozhou Meng, for his valuable help, advice on manufacturing composites, SEM study and exciting discussions, which motivated me to widen my research from various perspectives. I am sincerely grateful to Mrs Sue Shelton and Mr Michael Keefe for the help provided with mechanical testing.

I would like to sincerely acknowledge the financial support provided by College of Engineering and Technology, the University of Derby for my PhD study through a Graduate Teaching Assistant Scholarship. I would like to thank for the support provided by SHD Company, Sleaford, the UK, in particular, Mr Jack Holyoak for his guidance on manufacturing composite materials.

Great appreciation attributes to my colleagues for the precious help and companionship during the past three years. In particular, I am grateful to Miss Claire McKee who has accompanied and encouraged me through the whole academic journey in the UK. Many thanks to Mr Daniel Odiyi for his help during the laboratory experiments.

I am deeply grateful to my family here and in Poland: my parents, my brothers and to my grandparents for supporting me spiritually throughout my life. Without their love and support, I would not be able to be where I am now. Last but not least, many thanks to my fiancé, Patryk Jalkiewicz, for his patience, understanding and support in the preparation of this thesis.

1 Introduction

1.1 Background

Use of fibre reinforced polymers (FRPs) had begun in the 1930s and was later dramatically increased when the method of mass production glass strands was discovered (Milewski and Rosato, 1981). FRPs have now become an indispensable alternative to metal materials in many industries due to their exceptional properties. For example, Boeing 787, one of the newest passenger aircraft, is composed of more than 50% (by weight) of carbon fibre reinforced laminate (CFRP) (**Figure 1-1**). Advanced composite materials allow a lighter and simpler structure, which significantly reduces fuel consumptions (Boeing 787, 2018). FRPs also feature with superior environmental resistance and fatigue life, which can minimise the scheduled maintenance. Because of all advantages and a wide range of potential applications, FRPs have drawn intense interest from both industry and research community. Researchers are constantly endeavouring to improve the mechanical and thermal properties of these composites further. One of the promising techniques is to introduce a small amount of nanoscale inclusion to reinforce FRPs, which will enhance not only their matrix-dominated properties such as interlaminar shear strength, flexural modulus, mode I fracture toughness, but also their multi-functionality.

Figure 1-1 is unavailable due to copyright restrictions.

Figure 1-1 *Materials composition of Boeing 787 aircraft* (Boeing 787, 2018)

In the FRPs, nanofillers such as carbon nanotubes (CNTs) or graphene can be introduced in various ways. These methods of introduction will have direct effects on the location of nanofillers existing in FRPs. In the industrial scale, the most popular one is mixing nanofillers with the resin. Cambridge Nanosystems Company has reported that adding 0.3 wt% graphene in the matrix improved tensile strength, toughness and elongation to failure by 60%, 100% and 45% respectively. As a result, it was estimated that use of this graphene-enhanced CFRP could potentially save 3700 kg of Boeing 787 plane (Cambridge Nanosystems, 2017). More and more companies, such as Haydale Composite Solutions (Composite World, 2016) or SHD Composites (SHD composites, 2017), started to launch graphene-reinforced ‘prepreg’ – material consisting of fibre impregnated with the polymeric resin mixed with graphene. These new CFRP expect to increase the material properties like fracture toughness or impact resistance due to the reinforcement of graphene and improve performance in applications such as automotive and sports goods such as bike frames, fishing rod and racing boats. Mixing graphene with the resin is not the only way. Graphene can also be integrated into fibres directly by coating; forming a distinct layer. In combination with the development of new experimental approaches, computer simulation can act as a cost-effective alternative to develop and optimise the process.

Since its discovery, graphene has been coined as ‘magical’ material and is expected to play an essential role in a wide range of FRPs related application. A few challenges are anticipated to overcome from the numerical and experimental point of view:

- i. Lack of existing numerical material models on finite element software to model graphene reinforced FRPs
- ii. Lack of new methods for the large-scale production of graphene-based products
- iii. The capability of modified composites is still below the expectations in comparison to excellent graphene properties. Which parameters influence the improvement?
- iv. Limited knowledge on designing and simulating graphene coating on the fibre surface
- v. Need of the simple yet effective technique to introduce the graphene in the fibre/matrix interphase

Although some research has been carried out on the numerical modelling of FRPs reinforced with graphene, no studies have been found which numerically analyse the effect of

the graphene orientation and volume fraction on the mechanical properties of the composite. Therefore, this research work primarily focuses on the numerical and analytical modelling of FRPs reinforced with nanofillers. In addition to forward simulations, the inverse process is developed to determine the interphase properties indirectly. The experimental part of this project aims to introduce nanofillers in FRPs with the aid of spraying technique and test its influence on the mechanical properties.

1.2 Mechanical properties of fibre reinforced polymers (FRPs) modified with graphene

To successfully use FRPs reinforced with nanofillers; engineers must be able to predict their mechanical behaviour under certain loadings and conditions. Mechanical properties of any material are usually extracted from traditional tests. Manufacturers or standard handbooks supply only some of these material data. However, due to FRP anisotropy and non-homogeneity experimental identification of the mechanical properties become a complicated engineering problem requiring a wide range of tests (Bruno and Poggialini, 2005). In a case of the thin unidirectional laminate, determination of the basic four elastic constants of material needs at least three separate tests such as tension, compression and shear tests (Bledzki *et al.*, 1999). However, to explore more complex properties - other types of test are used, for instance, open-hole tension/compression, compression after impact, interlaminar fracture toughness or short beam test. The number of necessary tests depends on the application of a certain type of composites. One of the most demanding industry is aerospace, where composites testing is complex over the range of temperatures and in a variety of environmental conditions. In terms of required equipment, a range of testing machines and grips are needed. Consequently, traditional mechanical testing of composites based on static loading is slow and expensive.

On the other hand, Finite Element Analysis (FEA) is a computer simulation method that allows designing and analysing complex material models. With suitable input parameters and model definition, FEA can reflect truly the behaviour of materials. However, the analysis of the FRPs is already challenging as involve a combination of fibre, matrix, interphase and lamina never mind the addition of another scale nano-reinforcement. Some of these properties are extremely difficult to measure. For example, for carbon fibre (CF) itself is described by five transversely isotropic parameters; however, the majority of the fibre are properties not usually provided by material suppliers. Same applies to interphase between fibre and matrix or graphene properties. Therefore, a mixed experimental-numerical technique called in other

words inverse analysis has become very useful in indirect identification of complex parameters. The principle of this method is to update the elastic constants iteratively in FEA of the test specimens in a way that the computed results match the measured results. Thus, a specimen of the same dimensions as in the experiment is designed and simulated to predict the mechanical response to the loading. Using this technique can assist experimental measurements, and determined the complicated mechanical properties of FRPs and reducing the number of experimental tests.

1.3 Research scope and objectives

Some experimental work had investigated the effects of nanofillers on mechanical properties of FRPs, i.e. fracture toughness, interlaminar shear strength, and flexural properties. Numerical modelling is a cost-effective tool to gain insight into this reinforcement by nanofillers, but very few works had been reported in this direction (Sabuncuoglu, Gorbatiikh and Lomov, 2018). The present work aims to provide a better understanding of the enhancement of graphene nanoplatelets (GNPs) or CNTs on mechanical properties of FRPs. The main focus is to develop the multiscale modelling framework to study the effects of the GNPs reinforced interphase on FRPs. The objectives are as follows:

- To predict the GNPs reinforced interphase properties at nanoscale, and investigate the effects of GNPs orientation and volume fraction
- To develop an representative volume element (RVE) model at a microscale to predict the unidirectional lamina elastic constants based on the properties of each constituents'
- To develop macroscale modelling to predict the mechanical response of CFRP laminate subjected to external loading
- To test the multiscale framework to either GNPs or CNTs reinforced CFRP
- To develop the spraying technique to apply nanofillers on the prepreg surface, and investigate their influence on mechanical properties
- To develop a novel spraying technique to introduce GNPs directly to the carbon fibre fabric forming nano-reinforced interphase
- To develop a two-step optimisation process which involves bridging micro and macroscale

- To quantify the interphase properties for GNPs and epoxy coated CFRP from measured experimental data

1.4 Structure of this thesis

This thesis is organised into eight chapters. After the introduction in **Chapter 1**, the following chapters are included.

Chapter 2 provides a detailed literature review on: an introduction to FRPs, manufacturing FRPs reinforced with nanofillers, effects of the nanoscale reinforcement on mechanical properties of FRPs, numerical and analytical studies of FRPs reinforced with nanofillers and inverse problem. At the end of this chapter, the research gap and contribution to knowledge are presented.

Chapter 3 presents research methods, which are divided, into numerical and experimental sections. The numerical section provides an insight into the multiscale analysis and optimisation study. Whereas, the experimental section presents the preparation of the specimen, spraying procedure and assessment of manufacturing defects.

Chapter 4 numerically studies FRPs with the graphene nanoplatelets coated on the fibre surface using multiscale analysis. The effects of the graphene nanoplatelets volume fraction and orientation on the interphase properties is presented at the nanoscale. Then, lamina properties are simulated using three-phase representative volume element containing fibre, nano-reinforced interphase and matrix. Finally, the macroscale model is simulated in three-point bending and compared with available experimental data.

Chapter 5 provides a numerical investigation of the ‘fuzzy fibre’ reinforced polymer at nano and microscale. This model contains carbon nanotubes that are radially grown on the fibre surface. The unique three-phase RVE model, where the material properties of the CNTs reinforced layer are dictated by the orientation of the nanofillers is simulated. The obtained results are compared with theoretical composite cylinder method.

Chapter 6 reports mechanical tests on the CFRP sprayed with GNPs and CNTs to examine flexural, interlaminar and fracture toughness properties. The effectiveness of two types of spraying techniques are discussed, and experimental results are compared to the available literature. Recommendations on how to improve to the spraying and manufacturing process are listed here.

Chapter 7 presents the optimisation results, where GNPs reinforced interphase properties are indirectly predicted based on the combination of experimental and numerical results. Firstly, the effectiveness of various optimisation algorithms is tested using ANSYS DesignXplorer based on the available RVE models. Then, sensitivity analysis is presented which indicates which input parameters influence the most output results. Finally, attempts to indirectly prediction the GNPs reinforced interphase are discussed.

Chapter 8 concludes the main findings of this project. Recommendations and future research directions are summarised here.

2 Literature Review

2.1 Introduction to fibre-reinforced polymers

Composite is composed of at least two constituent and nearly relates to all solid materials. The principle of the composite is to combine distinct materials in such a way that the properties of the whole mixture are superior to constituent parts. One of the popular types of composite materials is a fibre-reinforced polymer (FRP). It forms a combination of a matrix that surrounds and holds in place fibres. This type of material is widely used in the aerospace industry, marine, structural, electrical and civil engineering. FRPs have outstanding design properties like stiffness-to-weight and strength-to-weight ratio; thus, become a lightweight alternative to steel and other metals. The demand from industries for better properties of FRPs never stops.

2.1.1 Role of fibre reinforcement in FRPs

FRPs differ from other composite materials as fibres influence significantly on their overall properties. With appropriate selection and placement of fibres, composite properties can be optimised to meet the requirements of specific applications. Continuous fibres are characterised by high length-to-diameter ratio, high strength and stiffness properties while having a low density when compared to common material such as metals. The most commonly used fibre reinforcements are glass (GF), carbon (CF), aramid and natural fibre. Their primary role in polymer matrix composite is to bring desired structural performance. **Table 2-1** summarises the properties of various commercially available fibres. Fibres tend to have high tensile strength but much lower transverse strength.

To overcome the limitation of weak transverse properties of fibres, manufacturers make fabric from the continues fibres, which are bonded with the matrix. Weaving is the most conventional manner to produce a two-dimensional weaving sheet that can be stacked up to make FRPs. Plain weave is the most common textile wave and forms a simple criss-cross pattern. Such fabric has difficulty in making fibres oriented with angles other than 0° and 90° to each other respectively. The unidirectional lamina with an arrangement of parallel, continuous fibre is the most convenient starting point to facilitate the understanding and design of new FRPs. It is convenient to conduct engineering analysis for such a pattern, which forms the basis for the analysis for different types of FRPs.

Laminate contains multiple laminas stack together at diverse orientations (**Figure 2-3**), where lamina is one thin plate of fibres embedded in the matrix. Each lamina has its preferred high-strength directions. The properties of these structural composites depend not only on the properties of the constituent material but also on the geometrical design of each lamina. Laminates are classified into 4 classes: unidirectional, cross-ply, angle-ply and multidirectional. When all laminae are orientated in the same direction, the laminate is considered as unidirectional.

The matrix in the composite is a general term used to designate the polymer, which binds the fibre reinforcement. The role of the matrix is to give the composite component its shape, protect the fibres from an environment and transfer the applied load to the fibres. The selection of matrix affects the final properties of the composite material, for example, interlaminar shear strength and in-plane shear properties (Kaw, 2006).

Table 2-1 Mechanical properties of selected types of fibres [*a* (Kaw, 2006) *b* (Torrays, 2018) *c* (Hexcel, 2016) *d* (Dupont, 2017) *e* (Speciality Materials INC., 2018)]

| Type of Fibre | Diameter (µm) | Density (g/cc) | Young's Modulus (GPa) | Ultimate Tensile Strength (MPa) |
|--|---------------|----------------|-----------------------|---------------------------------|
| E-Glass ^a | 16 | 2.54 | 72 | 3447 |
| S-Glass ^a | 9 | 2.5 | 86 | 4585 |
| Carbon Torray (T300) ^b | 7 | 1.76 | 230 | 3530 |
| Carbon Torray (T800) ^b | 5 | 1.80 | 294 | 5880 |
| Carbon Hexcel (AS4) ^c | 7.1 | 1.79 | 231 | 4412 |
| Aramid DuPont ^d (Kevlar* 149) | 12 | 1.47 | 179 | 3450 |
| Boron ^e | 102 | 2.61 | 400 | 3600 |

In FRPs, there are two main types of polymeric matrices (**Figure 2-1**): thermosets and thermoplastics:

- a. Thermosets matrix is usually liquid resin at the room temperature and contains polymers that cross-link together during the curing process. Curing process forms an insoluble and infusible material with irreversible chemical bonds. Typical examples of thermoset consist of epoxies, polyesters, and phenolic.

- b. On the other hand, thermoplastics matrices are usually solid at the room temperature and melt to the desired shape when the heat is applied. No chemical bond takes. They will soften when heated and harden when cooled - the process becomes entirely reversible. Some of the examples of thermoplastics include polyethene, polystyrene, poly-ether-ether-ketone (PEEK).

Epoxy-based resins are the most popular and represent more than two-thirds of the polymer matrices in aerospace applications (Kaw, 2006). Epoxy resin has low molecular weight and low viscosity, which allows good wetting of fibres, low volatility, and low shrink rates during cure. Epoxy-based FRPs offer excellent mechanical and physical properties with high thermal and chemical resistance. However, its cost is usually higher than the other polymeric matrices. Comparison of commercially available various types of matrices and their properties is provided in **Table 2-2**.

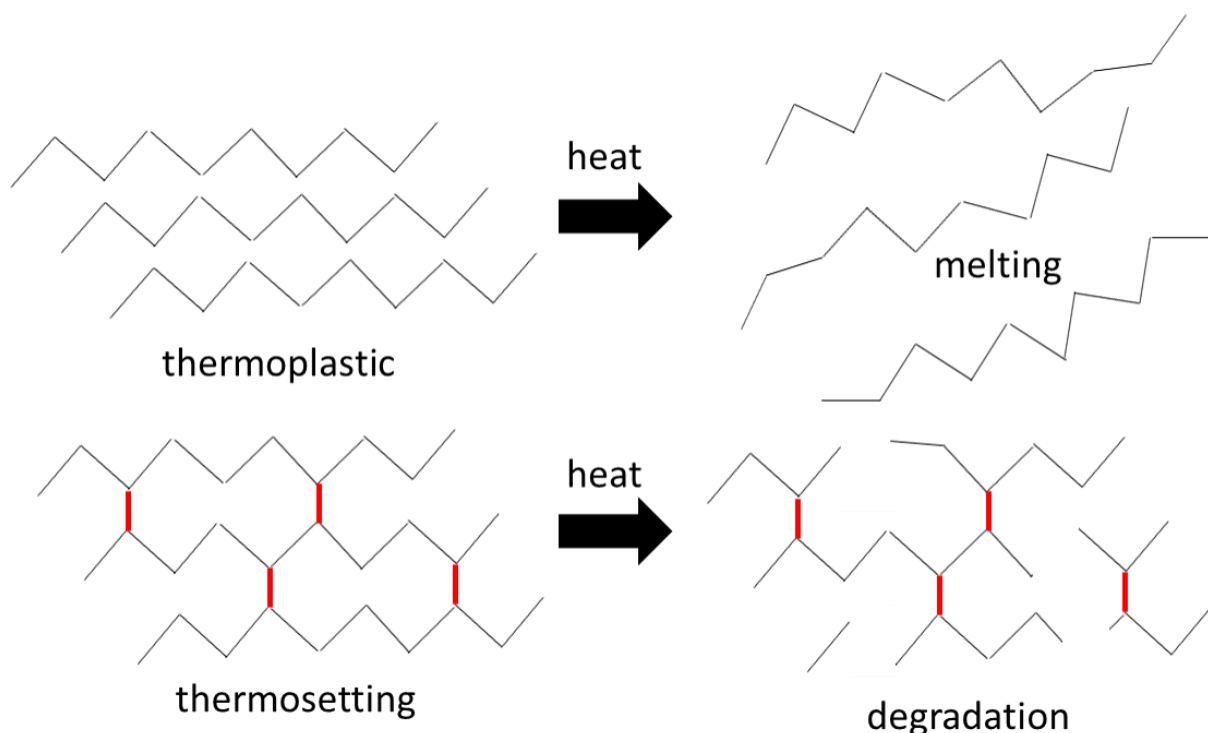


Figure 2-1 Comparison between thermosets and thermoplastics resin.

Table 2-2 Mechanical properties of selected matrices [^a (Cytec Engineered Materials, 2012) ^b (Hetron, 2015) ^c (Derakane, 2008) ^d (Vicat, 2014)]

| Matrix type | Density (g/cm^3) | Young's Modulus (GPa) | Tensile strength (MPa) | Flexural Modulus (GPa) | Flexural Strength (MPa) | Tg (°C) |
|--|-------------------------|-----------------------------|------------------------------|------------------------------|-------------------------------|------------|
| Epoxy (Cycom® 977-2) ^a | 1.31 | 3.52 | 81.4 | 3.45 | 197.7 | 212 |
| Polyester (Hetron™ 92) ^b | 1.33 | 3.65 | 55 | 3.79 | 86 | 188 |
| Vinyl ester (DERAKANE) ^c | 1.12 | 3.3 | 81 | 3.1 | 124 | 102 |
| PEEK (VICTREX®) ^d | 1.30 | 4.1 | 100 | 3.9 | 170 | 143 -250 |

2.1.2 Interphase and interface in FRPs

The interphase or interface in the development of composite materials becomes more important to all kind of applications of FRPs. The interface in fibre reinforced composites is a surface formed by a common boundary of reinforcing fibre and matrix that is in contact with and maintains the bonding in between for the load transfer (Kim and Mai, 1998). This 2D surface has different physical and/or mechanical properties from that of fibre and matrix. Whereas, the interphase (**Figure 2-2**) is a three-dimensional zone of finite interlayer which includes the geometrical surface of the fibre-matrix contact. The main role of the interphase is to effectively transfer the load from matrix to fibre which helps to reduce stress concentration (Sabuncuoglu, Gorbatikh and Lomov, 2018).

The nature of the interphase depends on the types of adhesion between fibre and matrix. Different bonding mechanisms for example adsorption and wetting, electrostatic attraction, chemical bonding, reaction bonding or mechanical interlocking are possible. It is more likely that at the interphase the combination of these mechanisms takes place to produce the final bond. The interphase's chemical, physical and mechanical properties can vary continuously between the fibre and matrix material. These properties are difficult to obtain due to the very low thickness of the interphase layer. Recently some experimental technique has been proposed to characterise fibre-matrix interphase. Liu *et al.* (2015) provided a comprehensive review of the interfacial characterisation methods. For example, atomistic force microscopy (AFM) may be used to characterise the thickness and modulus of the interphase. X-ray photoelectron

spectra (XPS) is suitable to characterise the distribution of surface coating and the diffusion between resin and sizing fibres.

Influence of the interphase on mechanical properties can also be indirectly tested using micro or macro-composites. The micro-composite test allows to successfully compare fibres with different surface treatments and determine the failure mechanism related to the interphase, i.e. single fibre compression test, the fibre fragmentation test, the fibre push out/pull out tests. On the other hand, a number of macroscale testing techniques have been devised to assess interlaminar properties such as interlaminar shear strength (ILSS), in-plane shear strength and transverse tensile strength.

The interphase is a critical factor in composite performance; therefore, its design has engaged both academia and industry. Interphase properties can be tailored by considering different parameters, such as improving structural (mechanical) and non-structural (sensing, actuation, barrier, self-healing) properties (Karger-Kocsis *et al.*, 2017). Considering the dominant failure mode in FRP as debonding between fibre and matrix, improving the interphase bonding strength and ability to detect its failure or even its healing is much needed.

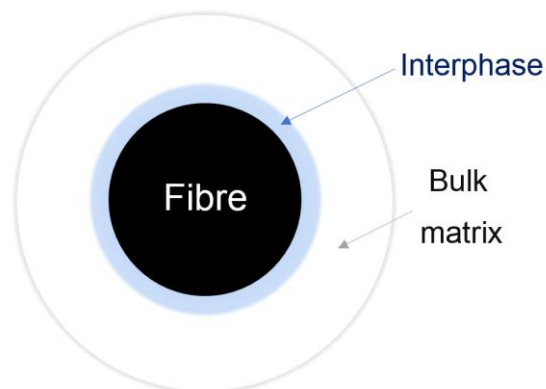


Figure 2-2 Schematic representation of FRP with the concept of the interphase.

2.1.3 Manufacturing of FRPs

Different fabrication processes have been used to design and build FRPs. The most commonly methods are:

- i. Wet lay-up of FRPs is often used in the production of large components. It is also suitable for the small-scale such as a research laboratory. During the fabrication,

reinforcement fabric is manually placed in the mould. A resin is applied through a roller, which is commonly used for consolidation following by curing the polymer at the required temperature. During the lay-up, the quality of the finished product is heavily influenced by the experience and skills of the laminator.

- ii. Prepreg lay-up follows a similar procedure to wet lay-up process. Prepreg is a material where the fibres impregnated with resin are partially cured. As a result, the prepreg is laid-up on the mould without any extra resin. Stacked up layers create a laminate which is cured under the combination of pressure and heat. This method offers many advantages, i.e. part uniformity, repeatability, less curing time. The main disadvantages of prepreg lay-up are cost, and limited shelf life as prepreg requires to be stored in freezers.
- iii. Resin transfer moulding (RTM) is an alternative technique and uses a closed mould with inlets to introduce resin and outlets to allow air to escape. Dry fibres are placed in the mould, the mould is closed, and low viscosity resin is pumped into the mould using injection ports. When all fibres are wet, resin supply is closed, and part is cured. The benefits of RTM include less expensive process producing dimensionally accurate complex parts with good surface details.
- iv. Vacuum-assisted resin transfer moulding (VARTM) is a process similar to RTM and typically uses an open-top mould. The vacuum bag is attached to the top the mould tool and applies vacuum to assist the continuous flow of infused resin from one side of the mould to the other. The vacuum removes trapped air, and this process can provide parts with near zero void content.
- v. Pultrusion is a continuous manufacturing process used to produce constant cross-section shapes of various length. Fibres are continuously impregnated and pulled through a heated die, where they are shaped and cured. The process is simple and low cost and offers flexibility in profiles design and various material combinations.

2.2 Material modelling of unidirectional FRPs

2.2.1 Mechanics of FRPs

Mechanical properties are measured from the loading response of material samples, which later become constants used in the constitutive model. Hooke's Law is most commonly used to describe the behaviour of isotropic, orthotropic, and anisotropic materials (Nye, 1985). A stress-strain relation can be expressed in the tensor form of either equation 2-1 or equation 2-2. Correspondingly, C_{ij} is the stiffness matrix, S_{ij} is the compliance matrix, and σ_i, ε_j are components of engineering stress and strain respectively.

$$\sigma_i = C_{ij} \varepsilon_j \quad 2-1$$

$$\varepsilon_j = S_{ij} \sigma_i \quad 2-2$$

The simplest constitutive model for the material is macroscopically homogeneous and isotropic. Composites are complex in their constitutive models due to their anisotropy and non-homogeneity (Bolton and Higgins, 2015). This project focuses on the one type of FRPs called laminate. Laminate contains multiple laminas stack together at diverse orientations (**Figure 2-3**), where lamina is one thin plate of fibres embedded in the matrix.

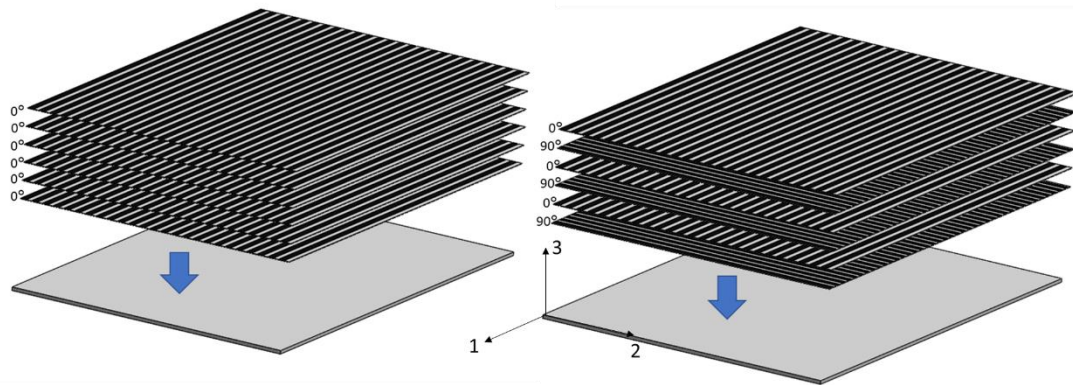


Figure 2-3 Example of unidirectional and cross-ply laminates

Considering FRPs, compliance matrix can be reduced due to material symmetry. The generalised 3-D Hooke's Law for an orthotropic material is given by equation 2-3; therefore, 9 elastic constants are necessary to describe the behaviour of the individual lamina.

$$\begin{bmatrix} \varepsilon_1 \\ \varepsilon_2 \\ \varepsilon_3 \\ \gamma_{23} \\ \gamma_{31} \\ \gamma_{12} \end{bmatrix} = \begin{bmatrix} \frac{1}{E_1} & -\frac{\nu_{21}}{E_2} & -\frac{\nu_{31}}{E_3} & 0 & 0 & 0 \\ -\frac{\nu_{12}}{E_1} & \frac{1}{E_2} & -\frac{\nu_{32}}{E_3} & 0 & 0 & 0 \\ -\frac{\nu_{13}}{E_1} & -\frac{\nu_{23}}{E_2} & \frac{1}{E_3} & 0 & 0 & 0 \\ 0 & 0 & \frac{1}{G_{23}} & 0 & 0 & 0 \\ 0 & 0 & 0 & \frac{1}{G_{31}} & 0 & 0 \\ 0 & 0 & 0 & 0 & \frac{1}{G_{12}} & 0 \end{bmatrix} \begin{bmatrix} \sigma_1 \\ \sigma_2 \\ \sigma_3 \\ \tau_{23} \\ \tau_{31} \\ \tau_{12} \end{bmatrix} \quad 2-3$$

Taking into account direction 1 as fibre axial, and plane 2-3 as a plane of isotropy, then Hooke's law can be further reduced to 5 independent parameters resulting from the relationship given in **2-4**. This material is called transversely isotropic.

$$E_2 = E_3, \nu_{12} = \nu_{13}, G_{12} = G_{13} \text{ and } G_{23} = \frac{E_2}{2(1+\nu_{23})} \quad 2-4$$

Accordingly, five elastic constants describe the behaviour of unidirectional lamina:

E_1 = Longitudinal Young's Modulus,

E_2 = Transverse Young's Modulus,

ν_{12} = Major Poisson's ratio,

ν_{23} = Minor Poisson's ratio,

G_{12} = In-plane shear modulus,

G_{23} = Out-of-plane shear modulus.

Figure 2-4 presents different methods of estimating the properties of the FRPs. To predict the properties of unidirectional composite several analytical and computational theories have been reviewed. The following subchapters present the modelling of FRPs at two different scales: lamina and laminate level and intend to review standard methods of two-phase (fibre and matrix) models.

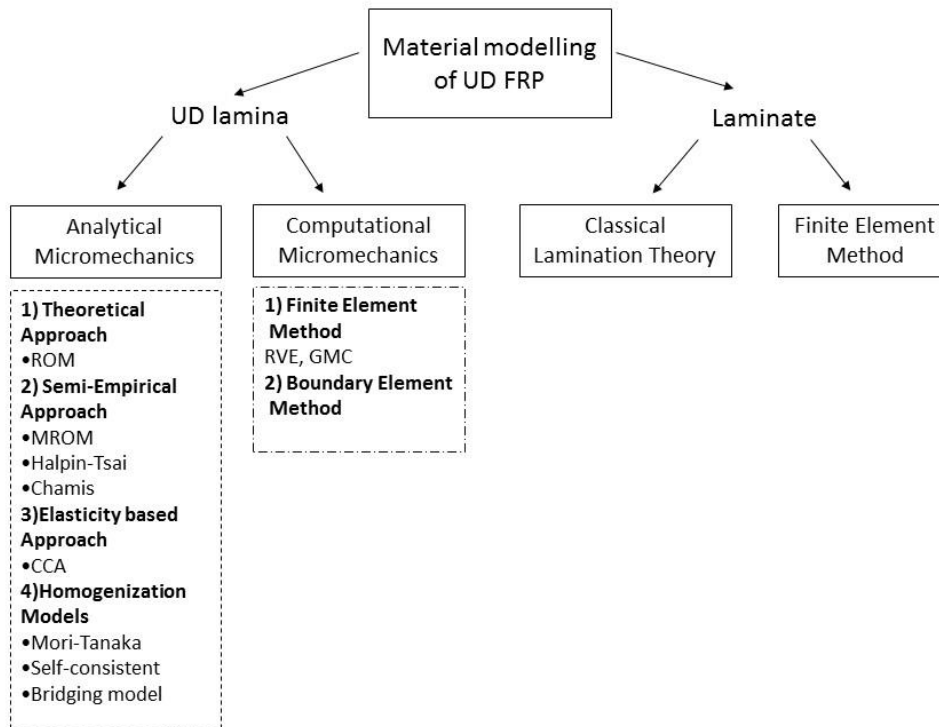


Figure 2-4 Modelling of unidirectional fibre reinforced polymers at micro and microscale.

2.2.2 Unidirectional lamina

There are two approaches to predict the unidirectional lamina properties: analytical and computational methods. Analytical micromechanics methods aim to predict lamina properties based on available constituents' properties and volume fraction. Whereas, computational micromechanics model a small volume of the material called representative volume element (RVE), which under certain analysis can represent the behaviour of the whole material. Both of these methods assume that constituents obey Hooke's law. Fibres are circular in the cross-section of uniform diameter and parallel. Perfect bonding conditions exist between fibre and matrix. There are no voids and fibre and matrix are the only two phases.

2.2.2.1 Analytical micromechanics

I. Rules of mixtures (ROM) - Voigt upper bound and Reuss lower bound

A general rule of mixtures is a formulation to predict the properties of the composite made with unidirectional fibres. It provides a theoretical upper and lower bounds on composite properties assuming that fibres and matrix are subjected to a uniform strain in the fibre direction (Voigt)

and uniform stress (Reuss) in the transverse fibre direction. When loading is applied in the direction parallel to fibres, the upper bound of the elastic modulus is found as:

$$E_1 = fE^f + (1 - f)E^m \quad 2-5$$

Where:

$f = \frac{V^f}{V^f + V^m}$ is the volume fraction of the fibres

E^f is the material properties of the fibres

E^m is the material property of matrix

E_1 is the composite longitudinal elastic modulus

E_2 is the composite transverse elastic modulus

The lower bound of elastic modulus, corresponding to the transverse direction follows the equation:

$$\frac{1}{E_2} = \left(\frac{f}{E^f} + \frac{1-f}{E^m} \right) \quad 2-6$$

II. Semi-empirical models

Although the longitudinal properties predicted by ROM match well the experimental data, transverse properties such as E_2 or G_{12} quite the reverse. Therefore, semi-empirical models have been introduced to correct the ROM with the correcting factors obtained from experiments. Three important models including the modified rules of mixtures, the Halpin-Tsai model and Chamis model are briefly described in this subchapter. Formulations below are given for transverse longitudinal modulus only.

Modified rules of mixtures:

$$\frac{1}{E_2} = \frac{\eta^f E^f}{E_{22}^f} + \frac{\eta^m V^m}{E^m} \quad 2-7$$

Where factors η^f and η^m are calculated as:

$$\eta^f = \frac{E_{11}^f V^f + [(1 - \nu_{12}^f \nu_{21}^f) E^m + \nu^m \nu_{21}^f E_1^f] V^m}{E_{11}^f V^f + E^m V^m} \quad 2-8$$

$$\eta^m = \frac{[(1 - \nu^m)^2] E_1^f - (1 - \nu^m + \nu_{12}^f) E^m V^f + E^m V^m}{E_{11}^f V^f + E^m V^m} \quad 2-9$$

Halpin-Tsai Model:

$$E_2 = E^m \left(\frac{1 + \zeta \eta V^f}{\eta V^f} \right) \quad 2-10$$

$$\eta = \left(\frac{\frac{E^f}{E^m} - 1}{\frac{E^f}{E^m} + \zeta} \right) \quad 2-11$$

Where ζ is called reinforcing factor and depends on: fibre geometry, packing geometry, loading conditions (usually $\zeta = 1$ or 2).

Chamis Model

$$E_2 = \frac{E^m}{1 - \sqrt{V^f} (1 - E^m/E_{22}^f)} \quad 2-12$$

III. Elasticity approach models

A composite cylinder assemblage (CCA) model proposed by Hashin and Rosen can also evaluate the elastic properties of unidirectional composites. This model assumes that fibres are circular in cross-section, arranged in periodic distribution and made of repeating elements called representative volume element (RVE). The RVE is theoretically the smallest volume representing the whole material. In the CCA model, the RVE consists of the composite cylinder, where the inner cylinder represents the fibre, and outer annulus is the matrix. The analysis of one composite cylinder is sufficient to determine all transversely isotropic material properties.

IV. Homogenization models (inclusion based models)

The Mori-Tanaka (MT) method approximates the interaction between the phases by assuming that each inclusion is embedded in an infinite matrix subjected to the average matrix strain or stress. The Benveniste (1987) formulation of Mori-Tanaka is given as:

$$C_{MT} = C_m + [V_f \langle (C_f - C_m) A_{Eshelby} \rangle [V_m I + V_f \langle A_{Eshelby} \rangle]^{-1} \quad 2-13$$

Where C_m and C_f are the stiffness matrices of the matrix phase and the reinforcement (fibre) phase respectively. $A_{Eshelby}$ is the strain concentration tensor of the dilute solution and depends i.e. on the shape of the inclusion. More details on the formulation of the MT method and remaining homogenization models like self-consistent or bridging models can be found in (Kaw, 2006).

V. Comparison of available analytical models

Younes *et al.* (2012) provided a comprehensive review of analytical methods and experimental data on FRP at various fibre volume fraction. It was observed that all methods are in good agreement with experimental data for longitudinal modulus E_1 and longitudinal Poisson's ratio ν_{12} . For transverse properties, (E_2, G_{12}) , rules of mixtures always underestimated them moderately. Semi-empirical models, especially Halpin-Tsai and Chamis model predicted well transverse properties of composites. The accuracy of models, which belongs to the elasticity approach or inclusion-based approach, depends greatly on the type (isotropic or transversely isotropic) and volume fraction of fibres but tends to overestimate the transverse properties.

2.2.2.2 Computational models

Computational micromechanics analyses the composite properties at the microscale level using a representative volume element (RVE) (Barbero, 2014). The RVE model of FRPs usually consists of two phases: fibres and matrix. A random fibre distribution generally characterises FRPs, but application of a periodic microstructure can simplify the modelling process. Thus, the RVE models can be represented by either randomly (Kari *et al.*, 2008; Wang *et al.*, 2011; Y Liu *et al.*, 2012) or periodically (Rucevskis S., 2002; Wang, Crouch and Mogilevskaya, 2006; Kumar, Chandra and Singh, 2010; Maligno, Warrior and Long, 2010; Xu *et al.*, 2012) distributed fibres. The latter can be divided into three types including cylindrical, square and hexagonal fibres arrays (**Figure 2-5a**). Randomly orientated RVE models can be generated by image processing or numerical generation techniques (Ghayoor, Hoa and Marsden, 2018). These models have been successfully applied to the determination of the FRPs properties, where the proposed RVE models consist of two phases such as the fibre and matrix (Sun and Vaidya, 1996). Trias *et al.* (2006) reported that periodic microstructure is sufficient to calculate the elastic properties of the lamina, whereas failure and damage analyses are more accurately studied by random fibre distribution. This was also supported by Ghayoor *et al.* (2018), who compared the stress distribution for various volume fraction and microstructures. Higher stresses were observed in the random microstructures and were located in the places where fibres are closer to each other. Therefore, an adequate representation of the microstructures in fibre reinforced composites is of critical importance for the analysis of the material properties, damage onset and propagation (Romanov *et al.*, 2013)

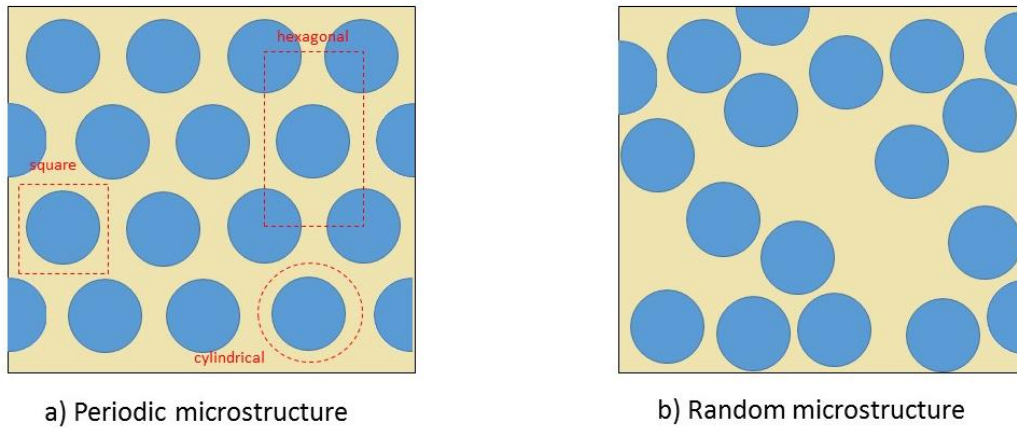


Figure 2-5 Schematic representation of two types of microstructures with the same fibre volume fraction, where **(a)** is a periodic microstructure and **(b)** is a random microstructure. Square, hexagonal and cylindrical unit cells are shown in the periodic microstructure.

2.2.3 Laminate

2.2.3.1 Classical lamination theory

Classical lamination theory (CLT) adopts simplified assumptions and develops an analytical relationship for a laminate plate under in-plane loads such as shear and axial forces, bending and twisting moments. The laminate is treated as a single layer with the perfect bonding between laminae and follows the Kirchhoff plate hypothesis. The most important theories and formulae are quoted below; further details are presented by (Kaw, 2006).

CLT approach has been divided into the following steps:

- i. Reduced stiffness matrix for a unidirectional lamina.

The process includes a review of the stress-strain behaviour of an individual lamina.

$$\begin{bmatrix} \sigma_1 \\ \sigma_2 \\ \tau_{12} \end{bmatrix} = \begin{bmatrix} Q_{11} & Q_{12} & 0 \\ Q_{12} & Q_{22} & 0 \\ 0 & 0 & Q_{66} \end{bmatrix} \begin{bmatrix} \varepsilon_1 \\ \varepsilon_2 \\ \gamma_{12} \end{bmatrix} \quad 2-14$$

Where Q_{ij} are reduced stiffness coefficients and are related to the engineering constants as follow:

$$Q_{11} = \frac{E_1}{1-\nu_{21}\nu_{12}}, Q_{12} = \frac{\nu_{12}E_2}{1-\nu_{21}\nu_{12}}, Q_{22} = \frac{E_2}{1-\nu_{21}\nu_{12}}, Q_{66} = G_{12}, \frac{\nu_{12}}{E_1} = \frac{\nu_{21}}{E_2}. \quad 2-15$$

ii. Transformed reduced stiffness matrix for an angle lamina.

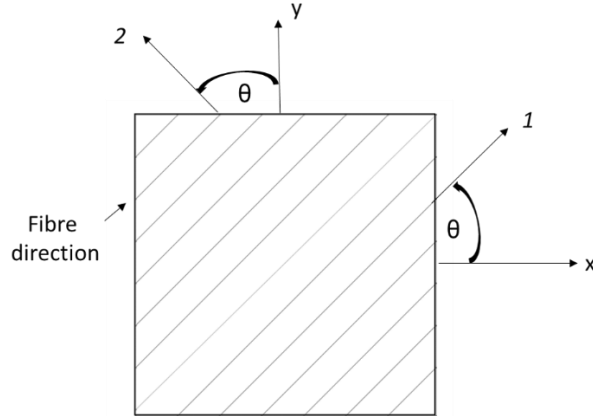


Figure 2-6 Angled lamina annotated with local coordinate system.

The above derives the relation for lamina where fibres are aligned with the major axis.

Figure 2-6 represents the relation between global axes denoted as x and y and local axes 1 and 2. A transformation similar to coordinate transformations is required :

$$\begin{bmatrix} \sigma_1 \\ \sigma_2 \\ \tau_{12} \end{bmatrix} = \begin{bmatrix} \bar{Q}_{11} & \bar{Q}_{12} & \bar{Q}_{16} \\ \bar{Q}_{12} & \bar{Q}_{22} & \bar{Q}_{26} \\ \bar{Q}_{16} & \bar{Q}_{26} & \bar{Q}_{66} \end{bmatrix} \begin{bmatrix} \varepsilon_1 \\ \varepsilon_2 \\ \gamma_{12} \end{bmatrix} \quad 2-16$$

where, \bar{Q}_{ij} are elements of transformed reduced stiffness matrix.

$$\bar{Q}_{11} = Q_{11}c^4 + Q_{22}s^4 + 2(Q_{12} + 2Q_{66})s^2c^2 \quad 2-17$$

$$\bar{Q}_{12} = (Q_{11} + Q_{22} - 4Q_{66})s^2c^2 + Q_{12}(c^4 + s^4)$$

$$\bar{Q}_{22} = Q_{11}s^4 + Q_{22}c^4 + 2(Q_{12} + 2Q_{66})s^2c^2$$

$$\bar{Q}_{16} = (Q_{11} - Q_{12} - 2Q_{66})c^3s - (Q_{22} - Q_{12} - 2Q_{66})s^3c$$

$$\bar{Q}_{26} = (Q_{11} - Q_{12} - 2Q_{66})s^3c - (Q_{22} - Q_{12} - 2Q_{66})c^3s$$

$$\bar{Q}_{66} = (Q_{11} + Q_{22} - 2Q_{12} - 2Q_{66})s^2c^2 + Q_{66}(s^4 + c^4)$$

$$c = \cos(\theta) \text{ and } s = \sin(\theta).$$

From the above equation, it can be seen that elements of the transformed, reduced stiffness matrix are functions of the four stiffness coefficients, Q_{11} , Q_{12} , Q_{22} , Q_{66} , and the angle of lamina fibres, θ .

iii. Stress and strain variations through the thickness of the laminate.

A_{ij}, B_{ij}, D_{ij} matrices have to be found using equations quoted below, where h is the vertical position of the ply from the mid-plane of the laminate, k is the number of plies (**Figure 2-7**) and \bar{Q}_{ij} is transformed reduced stiffness matrix.

$$\begin{aligned}
 A_{ij} &= \sum_{k=1}^N [\bar{Q}_{ij}]_k (h_k - h_{k-1}) \\
 B_{ij} &= \frac{1}{2} \sum_{k=1}^N [\bar{Q}_{ij}]_k (h_k^2 - h_{k-1}^2) \\
 D_{ij} &= \frac{1}{3} \sum_{k=1}^N [\bar{Q}_{ij}]_k (h_k^3 - h_{k-1}^3) \\
 ABD &= \begin{bmatrix} A & B \\ B & D \end{bmatrix}
 \end{aligned}
 \tag{2-18}$$

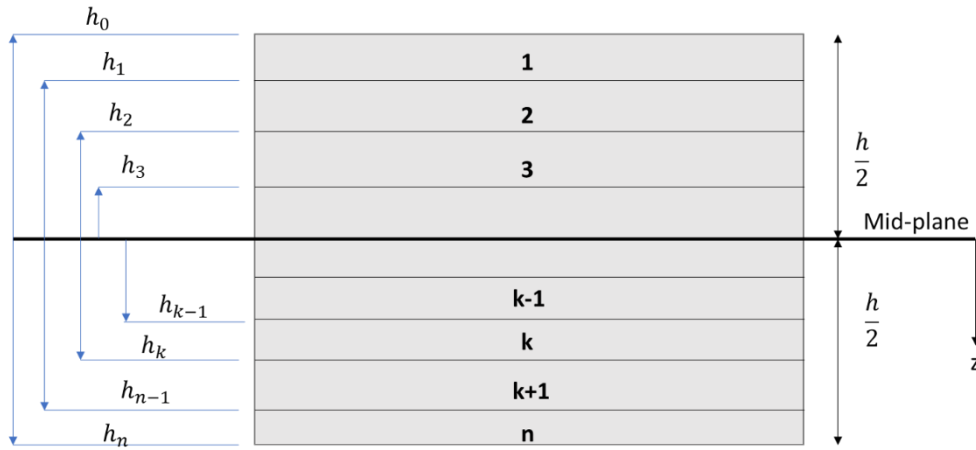


Figure 2-7 Location of each ply of laminate with respect to the mid-plane.

iv. Relationship of laminate forces and moments to the strains and curvatures.

Substituting the three-dimensional version of the composite compliance matrix into CLT equations, the relation can be written as equation 2-19, where N are resultant forces, M are resultant moments, and ε^0, κ are midplane strains and curvatures respectively (**Figure 2-8**).

$$\begin{bmatrix} N_x \\ N_y \\ N_{xy} \\ M_x \\ M_y \\ M_{xy} \end{bmatrix} = \begin{bmatrix} A_{11} & A_{12} & A_{16} & B_{11} & B_{12} & B_{16} \\ A_{12} & A_{22} & A_{26} & B_{12} & B_{22} & B_{26} \\ A_{16} & A_{26} & A_{66} & B_{16} & B_{26} & B_{66} \\ B_{11} & B_{12} & B_{16} & D_{11} & D_{12} & D_{16} \\ B_{12} & B_{22} & B_{26} & D_{12} & D_{22} & D_{26} \\ B_{16} & B_{26} & B_{66} & D_{16} & D_{26} & D_{66} \end{bmatrix} \begin{bmatrix} \varepsilon_x^0 \\ \varepsilon_y^0 \\ \gamma_{xy}^0 \\ \kappa_x \\ \kappa_y \\ \kappa_{xy} \end{bmatrix}
 \tag{2-19}$$

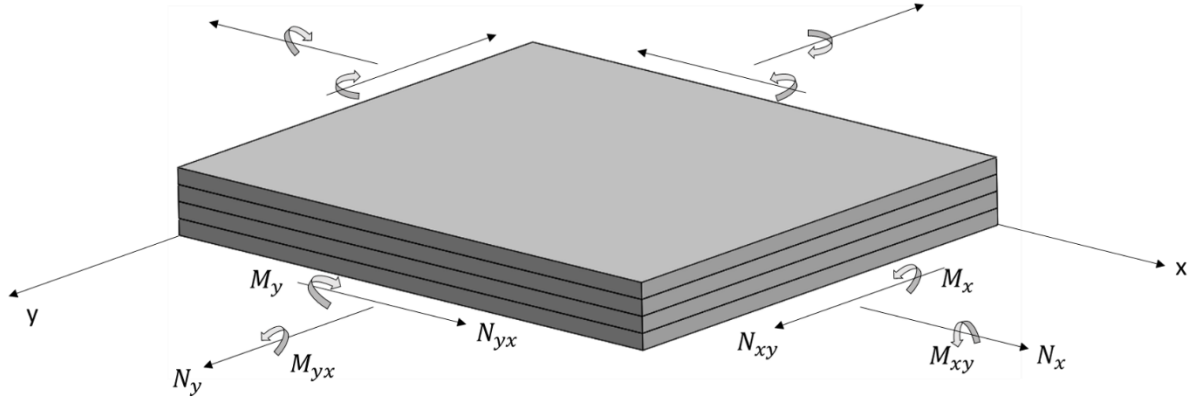


Figure 2-8 Resultant moments and forces which are acting on laminate.

- v. Stresses and strains at the top and bottom surface of each ply can be found using the following equations:

$$\begin{bmatrix} \varepsilon_x \\ \varepsilon_y \\ \gamma_{xy} \end{bmatrix} = \begin{bmatrix} \varepsilon_x^0 \\ \varepsilon_y^0 \\ \gamma_{xy}^0 \end{bmatrix} + z \begin{bmatrix} \kappa_x \\ \kappa_y \\ \kappa_{xy} \end{bmatrix} \quad 2-20$$

$$\begin{bmatrix} \sigma_x \\ \sigma_y \\ \tau_{xy} \end{bmatrix} = \begin{bmatrix} \bar{Q}_{11} & \bar{Q}_{12} & \bar{Q}_{16} \\ \bar{Q}_{12} & \bar{Q}_{22} & \bar{Q}_{26} \\ \bar{Q}_{16} & \bar{Q}_{26} & \bar{Q}_{66} \end{bmatrix} \begin{bmatrix} \varepsilon_x \\ \varepsilon_y \\ \gamma_{xy} \end{bmatrix} \quad 2-21$$

Other excellent references on laminate theory are Mechanics of Composite Materials (Christensen, 2005) and Mechanics of Composites Structures (Kollar and Springer, 2003).

2.2.3.2 Finite Element Methods

Finite element methods (FEM) is an extremely useful tool in the design process of composites. FEM can be used to understand the internal behaviour of each constituent within the composite, to characterise the composite mechanical properties and reduce the number of required physical testing. ANSYS (2018) is a popular software dedicated to the simulation of composites. In the macroscale, composites materials were studied under different loading such as uniaxial tensile test (Comellas *et al.*, 2015), biaxial tensile test (Lecompte *et al.*, 2007), three-point bending test (Meng *et al.*, 2015). For example, the model containing the number of lamina layers represents the laminate at the macroscale. Orthotropic material properties and orientation of fibre are then assigned to each layer. Properties of each lamina are estimated using micromechanical analysis. The software can readily determine the interaction between plies known as a cohesive zone. After the boundary conditions are assigned, results extracted from the analysis are stresses, strains and deformations calculated based on CLT.

2.3 Nanofillers in fibre-reinforced polymers

2.3.1 Introduction

The discovery of carbon nanofillers like fullerenes, nanotubes and graphene created great opportunities to improve the properties of existing materials and to produce new ones. Over past 25 years, extensive research for improvement of mechanical, electrical and thermal properties of polymer matrices have been done. Nanofillers are unique in their properties, i.e. stiffness and strength (Bhattacharya et al. 2003; Bhattacharya 2016; McNally and Potschke 2011) and attracted immense interest in their application to polymer matrices. Nanofillers can improve the composites in a wide range of properties not only mechanical such as strength, stiffness and fracture toughness but also multifunctional such as self-damage diagnostic, sensing capabilities (Pal and Kumar, 2016). These materials have already a wide range of applications such as topcoat of the aeroplanes, aircraft components such as interior panels or brake pads, fuel cells, and micro-electro-mechanical systems (Njuguna, Pielichowski and Fan, 2012).

The nanocomposite macroscopic response is mainly determined by two key factors: microstructure design (shape, size and volume fraction of nanofillers) and the interaction between matrices and fillers. However, effective introduction of nanofillers to polymer matrices presented some challenges. The main one is that the maximum concentration of nanofillers is limited to only a few percentages. Polymer matrices viscosity increases with the volume fraction of nanofillers making the uniform mixing difficult instead resulting in uneven distribution and nanofillers agglomerations. With the low volume fraction of nanofillers, enhancement in the mechanical properties of nanocomposites is significant in comparison with the pure polymer, but not good enough to compete with conventional FRPs like carbon fibre reinforced polymer.

More recently researchers designed multiscale composite by combining nanofillers and FRP in a new composite to enhance their high-performance (Zhao *et al.*, 2005; Sager *et al.*, 2009; Wood *et al.*, 2012; Zhang *et al.*, 2012; Jin, Young and Eichhorn, 2014; Knoll *et al.*, 2014; L. Chen *et al.*, 2014; Ashori, Rahmani and Bahrami, 2015; Deng *et al.*, 2015b; Qin *et al.*, 2015; R. L. Zhang *et al.*, 2016; Wang *et al.*, 2016; Mahmood *et al.*, 2018). These materials combine reinforcement at two scales: nano and micro and are often called multiscale, nano-engineered or hierarchical composites. This approach has capabilities in dealing with the limitations of FRPs such as poor transverse and out-of-plane properties.

Present work focuses on two specific type of carbonaceous nanofillers, particularly on graphene and carbon nanotubes. The subchapter describes the methods of introduction of nanofillers in the FRPs, which are divided into three categories: a) mixing with the matrix, b) coating on fibres surface or c) implementing between layers.

2.3.2 Graphene and CNTs – definition, classification and properties.

2.3.2.1 Graphene

Graphene material has acquired enormous attention in the field of material science since was firstly isolated at Manchester University in 2004 (Novoselov, 2004). This two-dimensional sheet has carbon atoms arranged in a honeycomb structure and is characterised by high chemical reactivity as each of atom can undergo chemical reactions from the sides (Atif and Inam 2016). Carbon atoms are joined with strong sp^2 covalent bonds (**Figure 2-9a**). Single graphene sheet of the thickness around 0.134 nm is also the basic building piece of other important allotropes. It can be wrapped to form 0D fullerenes, rolled to form 1D nanotubes or stacked to form 3D graphite (**Figure 2-9b**). One of the main challenges since the graphene was discovered is to find a method of production, which allows obtaining good quality material at the large scale. Several techniques have been used to synthesize graphene and can be classified into two categories: top-down and bottom-up (Dhand *et al.*, 2013).

Top-down methods produce graphene from graphite by chemical synthesis, mechanical or chemical exfoliation. Mono-layer of graphene was first produced and reported in 2004, where mechanical exfoliation namely ‘scotch-taped method’ was used to repeatedly slice down the graphene layer on the substrate (Novoselov, 2004). Mechanical cleaving process is the reverse of stacking, where an external force is required to separate layers of graphite. Exfoliated graphene is then usually characterised by optical microscopy, Raman spectroscopy and AFM to assess thickness, number of layer and mechanical properties.

Figure 2-9 is unavailable due to copyright restrictions.

Figure 2-9 *Schematic diagrams of (a) hexagonal graphene structure (b) carbonaceous nanofillers (Geim, 2009).*

Although this method produces very high-quality graphene with almost no defects, it is labour extensive and large amount of graphene are difficult to obtain. Chemical exfoliation is a two-step process where graphite is dispersed in the colloidal suspension, which reduces the interlayer van der Waals forces and increases the interlayer spacing. The second step involves exfoliating graphene by rapid heating or sonication. Due to its simplicity and cost-effectiveness, it is versatile to produce large scale-up graphene. The main challenges of this method are the selection of suitable solvents and process parameters. Like chemical exfoliation, chemical synthesis produces the graphene through the reduction of graphite oxide to graphene oxide. Graphite oxide is usually achieved by the so-called Hummer's Method (Hummers and Offeman, 1958), where functional oxygen groups are introduced on the surface of graphene sheets. Then, graphite oxide is dispersed in water and sonicated to obtain individual graphene oxide (GO) sheets in water. Production of GO has a vast potential in low cost-industrial scale production; however, some challenges such as defects of graphene due to the oxidation process, the environmentally friendly process need to be addressed.

The bottom-up methods consist of chemical vapour deposition (CVD), pyrolysis, epitaxial growth, and unzipping CNTs. For example, CVD is a process where the gaseous reactant is deposited onto a substrate and then heated to create a material film on the substrate surface. In the case of graphene metallic substrates such as nickel or copper are usually used. In contrast to CVD, the growth of graphene called "epitaxial growth" on SiC contains already

carbon in the substrate. Heating SiC substrate in an ultra-high vacuum causes Si to sublime, leaving a carbon-rich surface and generating wafer-scale graphene layers (Tetlow *et al.*, 2014). The bottom-up methods usually produce high-quality graphene in relatively small quantity yet at a high cost. Researchers are constantly seeking methods, which are applicable for mass-scale production of high-quality graphene. The comprehensive description of individual methods and their advantages can be found in Dasari *et al.* (2017).

According to Pumera (2010) graphene can be categorised based on the thickness and number of layers and it is usually named as:

- i. single-layer graphene sheet with lateral dimensions from tens nanometers,
- ii. double-layer graphene with lateral dimensions above tens nanometres,
- iii. few-layer graphene (fewer than 10 layers of graphene),
- iv. graphene nanoplatelets (10-100 graphene layers; ~3-30 nm thick).

Based on the chemical nature of nanosheets, graphene can be classified as:

- i. pristine graphene (“an ideal graphene nanosheet”, which possesses the maximum consistent of carbon structure, supreme electrical, mechanical and thermal properties)
- ii. graphene oxide (graphene nanosheets with oxygen atoms, well dispersible in the water and other solvents)
- iii. reduced graphene oxide (graphene oxide that has been reductively processed by chemical, thermal or other methods to reduce its oxygen content)
- iv. functionalized graphene oxide (chemically functionalized graphene oxide- to enhance the dispersion and prevent agglomeration (Kuila *et al.*, 2012)).

Graphene properties can be characterised by the following techniques: SEM, scanning tunnelling microscopy (STM), TEM, AFM, XPS, Raman spectroscopy (Papageorgiou, Kinloch and Young, 2017). SEM and STM are usually employed to observe surface morphology - wrinkles, folds, defects. TEM is suitable to investigate the atomic structure of the graphene, thus bond location, dislocation edges, layer stacking and other features. AFM is one of the most common techniques to characterise the thickness and number of the layers. Raman spectroscopy provides spectra by which the composition of molecules can be identified.

Graphene mechanical properties, measured by nanoindentation in the AFM, showed exceptional properties including Young’s modulus of 1TPa, the ultimate tensile strength of 130.0 GPa (Lee, Wei, Jeffrey W. Kysar, *et al.*, 2008). However, these properties depend on

many factors such as the purity of graphene sheets, thickness, and defects, i.e. wrinkles. For instance, Frank *et al.* (2007) using the same technique measured Young's modulus of single-layer graphene to be 0.5 GPa only. More recently, Nicholl (et al. 2015) measured the mechanical properties of graphene by the non-contact approach. Suspended graphene was electrostatically pressurised by applying a voltage between graphene and a gating cheap. The measured in-plane stiffness was below 300.0 GPa - much smaller than the expected value of 1.0 TPa. It was found that these properties are temperature and size dependent. Direct measurements of the properties of 2D graphene have been challenging. Therefore a wide range of available properties exists in the literature. Besides experimental investigation of graphene properties, attempts to study this material numerically and theoretically have been made. More details will be provided in section 2.4.

Outstanding properties of graphene make it an excellent candidate to improve composite properties. Recent research has shown a high interest in applying graphene oxide (Deng *et al.*, 2015) and graphene nanoplatelets (Kandare *et al.*, 2015) into FRPs. Most current studies investigate the effect of weight percentage of graphene on various mechanical tests, such as tensile (Deka *et al.*, 2016), compression (Mannov *et al.*, 2013), flexural (Kamar *et al.*, 2015), impact (Yang *et al.*, 2013) and fatigue (Shen *et al.*, 2013). Experimental results proved the theory that the addition of graphene nanofillers can enhance the mechanical properties of FRPs. For instance, Ashori et al. (2015) achieve a 22.4% increase in tensile strength and a 76% increase in flexural strength with the addition of 0.3 % graphene oxide into a matrix of CFRPs. Whereas, Chen et al. (2014) obtained 42% increase in interlaminar shear strength (ILSS) by grafting graphene oxide on the glass fibre. Graphene as 2-D sheet benefits from greater contact with the polymer than the tube-shaped CNTs, because the polymer chains are unable to enter the interior of nanotubes (Bhattacharya, 2016).

2.3.2.2 Carbon nanotubes

Carbon nanotubes (CNTs) discovered by Iijima (1991) are rolled cylinders of graphene sheets. CNTs are synthesised through various chemical processes such as arc-discharge evaporation method, chemical vapour deposition and thermal plasma method. These nanofillers have long been tried as the enhancer of composites because of their superior properties; the axial Young's modulus exceeds 1.0 TPa with tensile strength 37.0 GPa and yet low density (1.4 g/cm^3) (Popov, 2004). CNTs can be divided into two main categories based on the number of layers: single-walled (SWCNTs) and multi-walled (MWCNTs). SWCNTs

contains one layer of graphene and have diameter in the range of 0.4 nm to 5 nm. Whereas MWCNTs have a diameter from 1.4 nm to over 100 nm (Bhattacharya, Kamal and Gupta, 2003). Length of CNTs generally range from hundreds of nanometers to hundreds of microns. Depending upon the structure, CNTs can be represented as a) armchair, b) zigzag or c) chiral as shown in **Figure 2-10**.

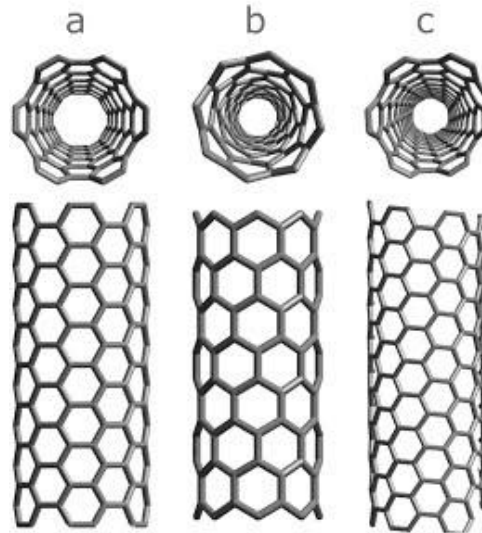


Figure 2-10 Schematic representation of (a) armchair nanotube, (b) a zig-zag nanotube, (c) a chiral nanotube. Reproduced with permission from Terrones 2001.

CNTs mechanical properties have been extensively studied both numerically and experimentally. In 1997, Wong *et al.* for the first time directly measured Young's modulus and strength of MWCNT as 1.28 TPa and 14 GPa respectively using the AFM. In the same year, Lu (1997) using MD simulations determined Young's modulus of SWCNT as around 970 GPa and reported this value is independent of CNT diameter and chirality. Whereas Salvetat *et al.* (1999) measured the properties of SWCNT using atomic force microscope (AFM) and reported Young's and shear moduli to be 1TPa and 1 GPa respectively. Generally, CNTs properties reported properties are around 1 TPa and depend on the type, diameter and method of production. More detailed information on mechanical properties of CNTs is provided in (Thostenson, Ren and Chou, 2001).

It has been proven that CNTs particularly improve the properties of FRPs which are dominated by the behaviour of the matrix and interphase (Karger-Kocsis *et al.*, 2017). This enhancement depends on the variety of factors like type of CNTs, their surface functionalization, the toughness of the base matrix. Apart from mechanical improvement,

CNTs gives opportunities to develop multifunctional composites with enhanced sensing capabilities (Zhang *et al.*, 2015).

2.3.3 Method of production of FRPs reinforced with nanofillers

2.3.3.1 Nanofillers in the matrix

The primary purpose of developing FRPs reinforced with nanofillers is to increase the bonding strength between fibre and matrix. One way to produce multiscale FRPs is to mix the nanofillers with the matrix directly, so-called matrix modification (MM). Many researchers modified the matrix with nanotubes (Wichmann *et al.*, 2006; Fan, Santare and Advani, 2008) graphene (Mannov *et al.*, 2013; Shen *et al.*, 2013; Ashori, Rahmani and Bahrami, 2015) or more than one type of nanofillers (Yang *et al.*, 2013; Wang *et al.*, 2015). This approach tends to create a homogeneous distribution of the nanofillers, which is usually achieved by an appropriate selection of material (solvent, nanofillers, low viscosity resin), processing technique (ultrasonic sonication, magnetic stirring, three roller mill) and parameters (mixing time, temperature) (Cho, Chen and Daniel, 2007; Deka *et al.*, 2016). Enhancement in FRPs properties was reported at a low volume fraction of nanofillers, but decrease observed at higher concentration due to agglomeration effects. The volume fraction of nanofillers is usually restricted to maximum 10 wt%. The multiscale FRPs can be prepared by Resin Transfer Moulding (RTM) (Fan, Santare and Advani, 2008; Deka *et al.*, 2016) or Wet lay-up (Ashori, Rahmani and Bahrami, 2015; Cheng *et al.*, 2016) techniques.

Table 2-3 summarises the influence of matrix modification on the range of mechanical properties. All results are provided in comparison with the control sample of the same material without nanofillers. The increase of shear, flexural, compressive, tensile, fatigue and fracture toughness properties was observed. For example, Ashori *et al.* (2015) reported 22% and 76% improvement in tensile and flexural strength respectively for CF epoxy material containing 0.3 wt% of GO. An interface adhesion enhancement after addition of GO was shown in SEM images of the tensile failure surfaces. Mannov *et al.* (2013) observed a 19 % improvement of residual compressive strength tested with compression after impact set-up, which was attributed to the incorporation of 0.3 wt % of GO in the composite. The synergistic effects of MWCNTs and GNPs on CF epoxy material were reported by Wang *et al.* (2015). Various ratios of MWCNTs and GNPs in the matrix were tested to find optimal value (reported as 1:9). A significant improvement of mechanical properties was observed, such as a 40 % increase in ILSS and 84.9 % increase in G_{IC} when 1 wt% of MWCNT and GNPs were added to the

composite. Besides traditional static tests, a 60% growth of fatigue life due to the addition of 0.25 wt% GNPs in the matrix was also reported by Shen *et al.* (2013).

Improvement in mechanical properties is generally reported in the literature due to the modification of the matrix with nanofillers. However, some paper noted no improvement (Wichmann *et al.*, 2006) or even a decrease of some mechanical properties (Kandare *et al.*, 2015). To achieve desirable improvement in mechanical properties, one needs to take extra care to nanofillers type, size, and weight fraction.

2.3.3.2 Coating fibres with nanofillers

Before the manufacturing process of FRPs, fibres are usually subjected to surface treatment (oxidised or non-oxidised). For example, sizing is designed to increase the wettability of fibres thus bonding strength by coating fibres with a mix of chemical (Strong, 2008). This kind of methods are effective, but they involve rigid chemicals which may decrease the strength of the fibres (Paper *et al.*, 2013). Moreover, most of this kind of treatment are complex in their structure and often expensive.

It has been demonstrated that introducing nanoparticles, nanowires, nanotubes, or nanosheets in the fibre/matrix interphase is a successful method to enhance composite high-performance (Zhao *et al.*, 2005; Sager *et al.*, 2009; Wood *et al.*, 2012). Graphene related materials can be applied to the fibre surface by dip coating (Zhang *et al.*, 2012; Knoll *et al.*, 2014; L. Chen *et al.*, 2014; Qin *et al.*, 2015), electrophoretic deposition (Deng *et al.*, 2015; Wang *et al.*, 2016; Mahmood *et al.*, 2018) or chemical grafting (Zhang *et al.*, 2016). Other nanofillers such as CNTs have also been applied in FRP by Chemical Vapour Deposition (CVD) (Sager *et al.*, 2009; Wood *et al.*, 2012) or spraying solvent onto the fibre surface (Davis *et al.*, 2011). Coated with CNTs carbon fibres are embedded in the matrix forming the fuzzy fibre reinforced polymer (FFRP). These methods will make the interphase layer distinctive from matrix and fibre in terms of mechanical properties (Dai and Mishnaevsky, 2014). The properties of the interphase are heavily affected by the method of production, which dictates the variation of dispersion, orientation and volume fraction of nanofillers within the interphase (Atif and Inam, 2016). For example, dip coating of fibres in nanofillers-epoxy solution tends to create a random orientation of nanofillers in the interphase, whereas electrophoretic deposition or chemical grafting will make graphene more aligned along the fibre surface.

Table 2-3 *Experimental results on the influence of nanofillers matrix modification on mechanical properties of FRP*

| Reference | Fibre | Matrix | Nanofiller | Method | Test | Results |
|--|-------|--------|---------------|------------------|-------------------------|---|
| (Deka <i>et al.</i> , 2016) | CF | PES | GO + CuO | CuO+ CFs, GO -MM | TT, In-plane ST | 61.2% ↑ in tensile strength , 89.9% ↑ in shear strength (WCF/CuO (120)/GO(1.2)/PES) |
| (Mannov <i>et al.</i> , 2013) | CF | Epoxy | TrGO | MM | CAI | 19% ↑ in residual compressive strength (TrGO 0.3 wt %) |
| (Kandare <i>et al.</i> , 2015) | CF | Epoxy | GNP, SNP, SNW | MM | TT, 4PBT | 14.7 % ↑ in flexural modulus ,2% ↓ in tensile modulus |
| (Ashori <i>et al.</i> , 2015) | CF | Epoxy | GO and FGO | MM | 3PBT, TT | 22.4 % ↑ in tensile strength, 76 % ↑ flexural strength (GO 0.3 wt %) |
| (Kostagiannakopoulou <i>et al.</i> , 2015) | CF | Epoxy | GO or GNPs | MM | DCB | 51% % ↑ in total G_{IC} (GNP 0.5 wt %) 49% ↑ in total G_{IC} (GO 0.5 wt %), |
| (Shen <i>et al.</i> , 2013) | CF | Epoxy | GNPs | MM | FT | 60% ↑ of number of cycles to failure (95% normalised cyclic stress, 0.25 wt% of GNP) |
| (Wichmann <i>et al.</i> , 2006) | GF | Epoxy | MWCNTs | MM | ILSS, DCB, ENF | 15.9 % ↑ in ILSS (MWCNT 0.3 wt%), no significant improvement in crack propagation is observed |
| (Cho, Chen and Daniel, 2007) | CF | Epoxy | GPs | MM | CT, In-plane shear test | 15.7% ↑ in compressive strength and 17.2% ↑ in in-plane shear modulus (GP 5 wt %) |
| (Fan, <i>et al.</i> , 2008) | GF | Epoxy | MWCNTs | MM | SBT | 18 % ↑ in ILSS (MWCNT 1wt %) |

TT-tensile test, ST-shear test, CAI-compression after impact, 3PBT- three-point bending test, 4PBT-four-point bending test, DCB-double cantilever beam, FT-fatigue test, ILSS-interlaminar shear strength, ENF-end notched flexural test, CT compression test, SBT-short beam test

i. Electrophoretic deposition

Electrophoretic deposition (EPD) is a colloidal processing method that enables to deposit a variety of materials on substrates to create thin films or coating. This method allows achieving a uniform and homogeneous coating of nano-fillers on the fibre surface. EPD is a cost-effective technique with potential to scaling up the process. It is also applicable to complex structures (Hung *et al.*, 2018). Schematic of typical EPD setup which consists of two electrodes connected to the power supply is presented in **Figure 2-11a**. Charged nanoparticles are dispersed in the liquid, deposited on the fibre of opposite charge through the application of a DC electric field. EPD process produces a rough surface on the fibre surface, which is beneficial to the interphase properties.

The quality of the coating depends on parameters such as applied voltage (1-300V), nanofillers concentration in the suspension (0.01- 5 mg/ml) and deposition time (few seconds to few hours) (Diba *et al.*, 2016). In the EPD process, GO dispersed in an aqueous solution is commonly used. Mahmood *et al.* (2016) observed a linear relationship between the applied voltage and coating deposition rate. A remarkable 219 % increase in interfacial shear strength was reported due to the deposition of GO solution (1mg/mL) at rate 10V/cm. The biggest challenge in the EPD process is to obtain the stable suspension of the charged particles. To overcome this problem, researchers often introduce the ultrasonicator or magnetic stirrer, which continuously mix the solution during the deposition process. Wang *et al.* (2016) reported a more uniform deposition of the GO on the glass fibre surface due to the ultrasonic treatment.

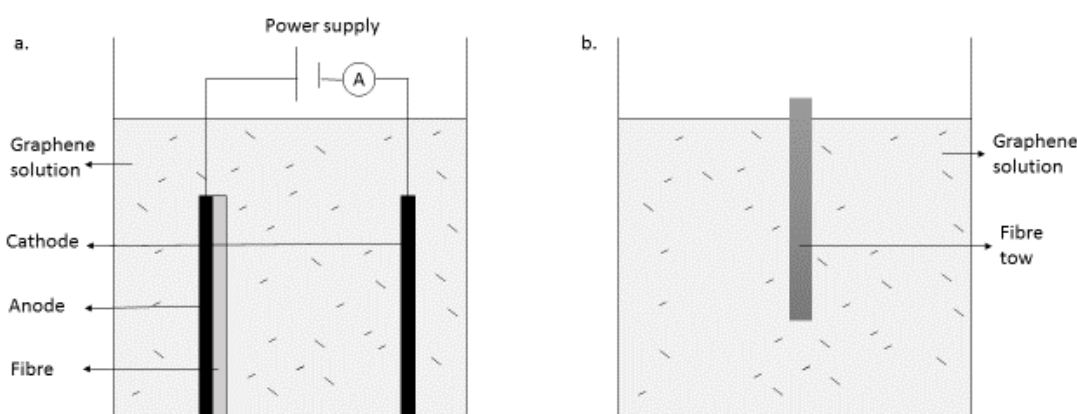


Figure 2-11 Schematic representation of **(a)** Electrophoretic deposition of graphene on fibre process **(b)** Dip coating fibre in graphene solution.

ii. Dip Coating

Dip coating (DC) is a simple method to produce fibres coated with nanofillers (**Figure 2-11 b**). The process involves impregnating fibres in nanofillers solution. Nanofillers can be dispersed in the solvent (deionised water, acetone) only (L. Chen *et al.*, 2014) or epoxy based solution (epoxy+ hardener+ solvent) (Zhang *et al.*, 2012; Qin *et al.*, 2015; W. Li, Yue, *et al.*, 2016). Well-dispersion of these nanofillers in the solution is usually achieved by mechanical stirring and ultra-sonication. After dip coating, fibres need to undergo a drying process, which is applied to remove the solvent completely. This method allows creating either nanofillers on the surface fibre or the nano-reinforced interphase layer. The primary challenge of this method is how to control a uniform and homogeneous distribution of the related nanofillers on the fibre surface.

The positive impact of the dip coating process on overall composite properties was supported experimentally. Qin *et al.* (2015) applied GNPs coating to carbon fibre and observed a very high density of deposited particles on the surface. The sample from the beginning and the end of the tow were investigated to check the quality of the coatings. No major difference regarding coating homogeneity was found. A 17% increase in flexural modulus in 90° fibre direction and 82 % of flexural strength were reported for unidirectional laminate. Also, Zhang *et al.* (2012) investigated the carbon fibre with a range of GO weight fraction in the coating (1-10 wt%). The thickness of the coating varied from 0.4 – 1.0 µm. The interlaminar shear strength increased by 12.7 % for GO at a concentration of 5%. Increasing the GO concentration to 7.5 and 10 wt%; however, slightly decreased the maximum obtain IFSS to 12.1 and 11.4 % respectively. These results suggested that increasing GO weight fraction above 10 % might result in deterioration of interfacial properties due to graphene agglomeration and stress concentration regions.

iii. Grafting

Grafting is the process which allows to 'anchor' or 'grow' nanofillers directly on the fibre surface by chemical reactions. This process is achieved by functionalizing nanofillers (-COOH, -OH, epoxy) and adding reactive groups to the fibre surface to enhance coupling reaction, for example, amidation. **Figure 2-12** presents the schematic of chemical grafting (Chen *et al.*, 2014). Due to this technique, nanofillers are covalently grafted on the fibre surface forming a new hierarchical structure with increased fibre surface roughness and interlaminar/interfacial properties accordingly (H. Lu *et al.*, 2014; R. L. Zhang *et al.*, 2016).

Table 2-4 Influence of nanofillers on mechanical properties of FRP applied by dip coating or EPD methods

| Reference | Fibre | Matrix | Nanofillers | Method | Test | Results |
|----------------------------|-------|--------|-------------------------------------|-----------------|--------------------------|--|
| (Deng et al. 2015) | CF | Epoxy | GO | EPD | SBT | 55% increase in ILSS |
| (Jiang et al., 2016) | CF | PU | GO | EPD Or MM | TT | 16.6 % increase in tensile strength, 7% increase in Young's modulus for 0.1wt% GO (MM), 16.9 % increase in tensile strength, 28% increase in Young's modulus (EPD) |
| (Mahmood et al., 2016) | GF | Epoxy | GO (1mg/mL) | EPD | SFFT | 219 % improvement of ISS of GF coated with GO (EPD rate 10V/cm) |
| (Wang et al., 2016) | CF | Epoxy | GO, RGO | EPD | SFFT IFSS | 26.5 increase in tensile strength and 69.9% in IFSS (RGO-CFs-U) |
| (W. Li, Yue, et al., 2016) | CF | BMI | GO (0.15 wt%) | DC | ILSS 3PB | 24.4 % increase in ILSS 28.7% increase in flexural strength, 27.9% increase in flexural modulus |
| (Zhang et al., 2012) | GO | Epoxy | GO | DC | SBT, TT | 70.6 % increase in IFSS (10 wt% of GO), 11.4% increase in ILSS (10 wt% of GO) 34.2 % increase in tensile strength (5 wt% of GO) |
| (L. Chen et al., 2014) | GF | Epoxy | SGO (0.5%) | DC | SBT | 60 % increase in ILSS |
| (Qin et al., 2015) | CF | Epoxy | GNPs | DC | 3PB 0°, 90° SBT | (90°) 82 % increase in flexural strength (0°) 7% increase in flexural strength 19 % increase in ILSS |
| (Knoll et al., 2014) | CF | Epoxy | MWCNT (0.3 wt%) FLG (0.3 wt%) | DC | FT | For load level 745 MPA fatigue life rises from 6.61×10^3 to 3.40×10^4 cycles for MWCNT and to 7.55×10^4 cycles for FLG |

IFSS- interfacial shear strength, SFFT- single fibre fragmentation test

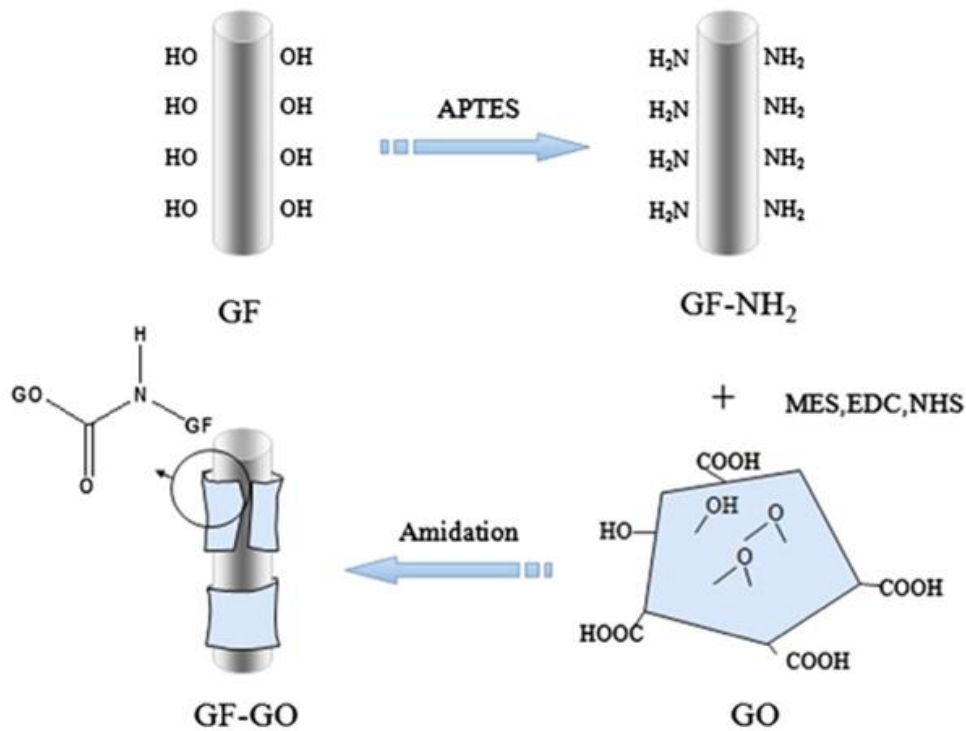


Figure 2-12 Chemical grafting process. Reproduced with permission from Chen *et al.*, 2014.

Another popular technique is growing nanotubes or nanofibers onto the fibre surface by Chemical Vapour Deposition (CVD). This process creates a “hairy” fibre surface, which is embedded into the matrix and often called “fuzzy fibre reinforced polymer” (FFRP). CVD is usually based on two steps: a) coating fibres with proper catalyst, and b) growth of the nanotubes in a reactor using hydrocarbon sources (Karger-Kocsis, Mahmood and Pegoretti, 2015). The main purpose of the fuzzy fibre composites is to increase the transverse properties. According to Kulkarni *et al.* (2010), the transverse elastic modulus of FFRP can usually be improved about three times with respect to the value of the pure matrix. This enhancement depends on the CNTs length, waviness and CNTs’ concentration on the fibre surface.

The main drawback of CVD is the possible reduction of the tensile strength of CF due to the penetration of the catalysts into the CF and damage caused by high temperature (Sager *et al.*, 2009). This process can be further improved by testing various temperature, temperature resistance coating on fibre or excluding toxic hydrocarbons or catalysts (Tehrani *et al.*, 2014).

Table 2-5 Summary of selected experimental data using grafting technique and its influence on mechanical properties of FRP.

| Reference | Fibre | Matrix | Nanofillers | Method | Testing | Results |
|---------------------------------|--------|--------|---------------|----------|-----------------------|--|
| (J. Chen <i>et al.</i> , 2014) | GF | Epoxy | GO(1.5 mg/mL) | Grafting | SBT | 41.4 % ↑ in ILSS |
| (H. Lu <i>et al.</i> , 2014) | CF mat | Epoxy | GO | Grafting | FESEM | Thickness of the GO coating 0 – 178.3 μm Random structure of GO |
| (S. Zhang <i>et al.</i> , 2016) | CF | Epoxy | GO | Grafting | SFTT, Micro-bond test | 8% ↑ in tensile strength 36.43 % ↑ in IFSS |
| (Sager <i>et al.</i> , 2009) | CF | Epoxy | MWCNT | CVD | SFFT SFTT | 71% ↑ in IFSS for randomly orientated MWCNT 11% ↑ in IFSS for aligned MWCNT. ≈30% ↓ decrease in tensile strength |
| (Wood <i>et al.</i> , 2012) | GF | Epoxy | MWCNT | CVD | Nano-indentation | 35% enhancement of peak modulus over neat matrix modulus for out of plane nanotubes direction. |

FESEM – Field emission scanning microscopy, SFTT – single fibre tensile test

2.3.3.3 Spraying nanofillers

This process involves spraying nanofillers solution using a spray gun. Nanofillers can be applied to the raw fibre fabric (Davis *et al.*, 2011) or directly on the prepreg surface (Zhang *et al.*, 2015). Nanofillers are usually mixed with organic solvents such as methanol or ethanol at required weight concentration. After spraying, the material needs drying up to remove the remaining solvent. A layer of the nanofillers coating will be created on the sprayed surface. The quality and density of the coating depend on many factors such as the nanofillers concentration, dispersion of nanofillers in the solution, the distance between the nozzle and material, the diameter of the nozzle. The spray gun operator skills also play a large role. The effectiveness of the spraying technique was proved by (Davis *et al.*, 2011; Zhang *et al.*, 2015), where improvement in tensile and fracture toughness properties was reported.

2.4 Multiscale analysis – Finite Element Methods

To predict the mechanical behaviour, design and expand the application of graphene-based composites, the development of the accurate theoretical method is important. Nanoscale composite modelling is a crucial step when attempting the analysis of the influence of nanofillers on FRPs properties. As mentioned in the experimental section, nanofillers can be introduced to FRPs for example to the matrix (mixing nanofillers with matrix) or to the interphase (coating process). Both of these cases can treat the reinforcing phase as the nanocomposite. The only difference is the volume fraction of the nanofillers, which is substantially higher in the interphase due to the high concentration of nanofillers in the thin layer. The behaviour of this material can be investigated at different scales beginning with atomistic scale through nanoscale, microscale, and finally macroscale.

2.4.1 Nanocomposite modelling

Nanocomposite modelling methods can be divided into two categories: computational chemistry and computational mechanics as shown in **Figure 2-13**. Computational chemistry represents the method of designing nanocomposite using quantum mechanics or nanomechanics modelling tools. The simulation performed at this level usually employ discrete molecular structures. On the other hand, computational mechanics includes micromechanics and structural mechanics and assumes the presence of continuous material structures.

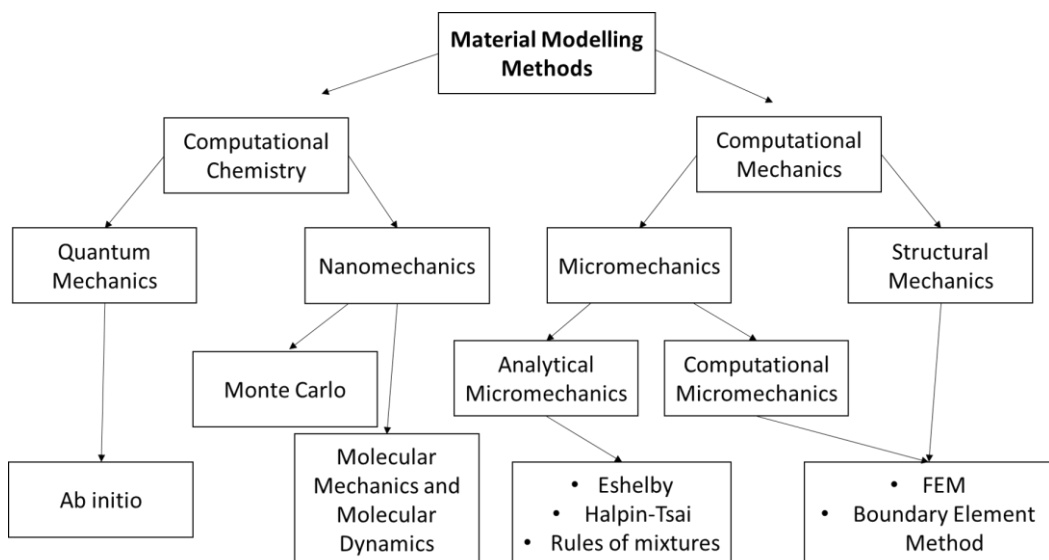


Figure 2-13 Nanocomposite modelling methods.

To study the mechanical properties of the epoxy matrix reinforced with randomly distributed graphene sheets, Cho *et al.* (2007) combined molecular mechanics and Mori-Tanaka approach. Firstly, the transversely isotropic elastic constants of graphene nanoplatelets were calculated based on their molecular force field. Then, moduli of the epoxy reinforced graphene nanoplatelets were derived with the Mori-Tanaka approach. Predicted results were in good agreement with the experimental data; it was found that nanocomposite moduli depend highly on the aspect ratio of graphene nanoplatelets. Montazeri and Rafii-Tabar (2011) combined MD, molecular structural mechanics and FEM to predict elastic constants of nanocomposite reinforced with graphene sheet and carbon nanotubes. Axial Young's modulus obtained for perfectly flat and bonded graphene sheet in the RVE model overestimated experimental ones. Therefore, effects on temperature, wrinkles and sliding between graphene layers on properties of the graphene reinforcement were considered. It was numerically found that the wavy structure of graphene sheet with sliding between layers decreases the axial Young's modulus in comparison to perfectly flat graphene sheets. Graphene sheet with wrinkles is believed to be a more realistic representation of real experiment. Unlike in Montazeri and Rafii-Tabar work, Shokrieh *et al.* (2014) combined MD with micromechanics approach assuming that the graphene nanofillers are randomly distributed in the nanocomposite. After mixing the graphene with resin, it is indeed more likely to obtain the random distribution. MD method was also utilised to find the transversely isotropic parameters of the RVE, which contained aligned graphene sheet and epoxy matrix. The results from randomly orientated graphene model were input to laminate theory and compare with experimental data for 1 wt% graphene reinforced nanocomposite.

On the other hand, Giannopoulos and Kallivokas (2014) studied the elastic properties of graphene monolayer embedded in matrix considering an interface region. This analysis was performed through multiscale finite element approach, where firstly the atomistic representation of graphene was used to extract graphene properties. Then, mechanical properties of graphene become an input to the analysis of representative volume element (RVE) at the nanoscale. In addition, micromechanics model for the prediction of the elastic properties of nanocomposites, based on the types, geometry, the orientation of the reinforcement, elastic properties of reinforcement and matrix such as Rules of mixtures, Halpin-Tsai, Nielsen, Mori-Tanaka, and Eshelby models were also reported.

2.4.2 Micromodelling modelling of FRPs with interphase

The behaviour of FRPs can be studied with a micromechanical model called Representative Volume Element (RVE). Traditionally, RVE contains fibre and matrix that can be arranged in the periodic or random arrangement as discussed in section 2.2.2. However, interaction between fibre and matrix called interphase have attracted a lot of interest in RVE modelling. The interphase can be treated as a separate thin layer between fibre and matrix perfectly bonded to them or as cohesive zone layer.

When the interphase is treated as a separate layer of defined thickness, consequently the RVE model contains three phases: fibre, interphase and matrix. The selection of bonding condition between the phases depends on the results to be achieved. Perfect bonding conditions are sufficient to simulate the RVE in elastic region and to predict elastic constants of the lamina. Whereas, the cohesive zone layer is usually used to describe the failure mechanism of the composite. The thickness of the interphase layer varies from a hundred of nm (Maligno, Warrior and Long, 2010; Yujia Liu *et al.*, 2012) to few μm (Chatzigeorgiou, Seidel and Lagoudas, 2012) and depends on the type composite. Interphase properties are extremely difficult to determine experimentally due to its small thickness. Numerically, interphase's properties can be represented by either homogeneous (Rucevskis S., 2002; Kumar, Chandra and Singh, 2010; Xu *et al.*, 2012) or inhomogeneous (Wacker, Bledzki and Chateb, 1998; Wang, Crouch and Mogilevskaya, 2006) material models. These material models are usually estimated based on some experimental measurements; however, efforts of estimating the interphase properties by molecular dynamics simulations (Johnston *et al.*, 2017; Subramanian *et al.*, 2018) and inverse methods (Matzenmiller and Gerlach, 2005) have been also reported.

Homogeneous models consider interphase as isotropic. Three-phase RVE models were often used to investigate the influence of the interphase properties and thickness on overall elastic properties of materials. Kari *et al.* (2008) observed that overall material properties of the unidirectional lamina were significantly affected by interphase, particularly in the transverse direction. Riano *et al.* (2018) also observed an increase in the composite elastic modulus, with the increment of Young's modulus of the interphase. This improvement also depends on the thickness of the interphase and is increasingly significant at higher fibre volume fraction. Xu *et al.* (2012) discussed the results of volume fraction and stiffness of the interphase on the engineering elastic constants of the composite. In most work, the interphase is

simplistically treated as isotropic with properties values, which are usually between those of fibre and matrix.

However, the simulations of the “soft interphase” with Young’s modulus lower than that of the matrix have also been performed (Maligno, Warrior and Long, 2010; Upadhyaya and Kumar, 2015; Riaño *et al.*, 2018). For instance, Riaño *et al.* (2018) studied the effect of the interphase region on the elastic behaviour of unidirectional glass fibre reinforced composites. This research group measured the elastic modulus of the interphase using AFM to be 1.7 ± 0.2 GPa that was 35% lower than that of matrix. For the “soft interphase” the results of FRP elastic constants are lower in comparison to the composite with the interphase properties the same or higher than matrix properties. On the other hand, (Maligno, Warrior and Long, 2010) observed that “soft interphase” in the presence of residual stresses (introduced during curing and cooling processes) delay the action of the transverse loading stress on the regions of the unit cells.

On the other hand, inhomogeneous interphase properties changes in the gradient manner (Sabiston *et al.*, 2016). Wang *et al.* (2006) modelled the interphase layer as a system of thin bands with different properties in the radial direction. Four variations of interphase Young’s modulus namely uniform “soft interphase”, uniform “stiff interphase”, linear and cubic were investigated. Forty homogenous layers represented and approximated each inhomogeneous interphase. It was concluded that the presence of radially graded interphase had significant effects on the stress fields. Stress jumps when crossing the boundary of the interphase zone where reduced. It was suggested that the overall properties of the composite could be tailored through the various pattern on the interphase for desired composite design (Al-Ostaz and Jasiuk, 1997; Wacker, Bledzki and Chateb, 1998).

The other method to introduce the interphase into the RVE model is a cohesive zone layer. This layer is usually introduced to simulate interfacial deboning or damage model between fibre and matrix (Yang *et al.*, 2012). Many cohesive laws were proposed in the literature, and they can be categorised as linear, bilinear or non-linear softening laws (Wang *et al.*, 2011). The example of bilinear damage cohesive law is provided in **Figure 2-14**. The initial linear response is followed by the initiation of damage, based on the maximum stress criterion, and the descending slope describes softening behaviour. This cohesive zone layer is described by following parameters fracture energy (G), interface elastic stiffness (K), normal

and shear interfacial strength (t_n, t_s), interface damage parameter (D), and normal and shear displacement (δ_n, δ_s).

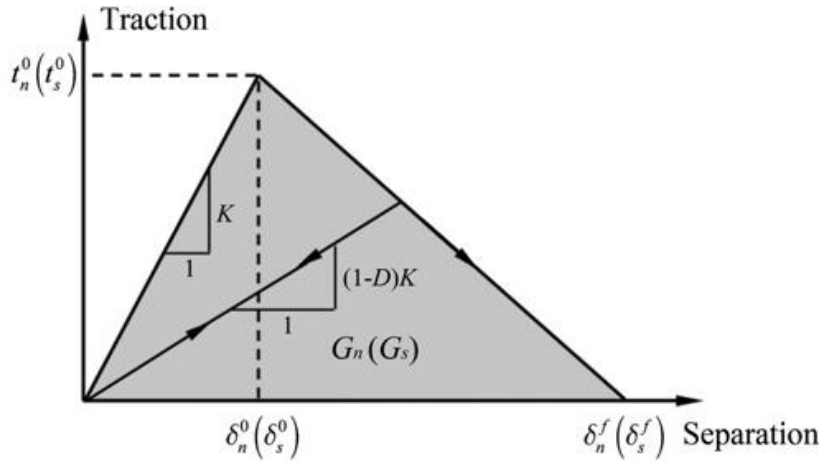


Figure 2-14 Bilinear traction-separation law of the cohesive element. Reproduced with permission from Yang et al., 2012.

Wang *et al.* (2011) studied the effects of interphase on the transverse tensile strength of unidirectional fibre reinforced composite, where the interphase was described as a cohesive zone layer. It was observed that with the smaller interphase thickness a relatively weaker stiffening effect of the composite was observed. The strength of the composite increased with increasing of interphase strength. Yang *et al.* (2012) investigated the damage initiation in fibre reinforced composite under transverse tension and compression loads. It was reported that tension initiation damage occurred at fibre-matrix interphase followed by matrix plastic deformation, while the compression failure is dominated by matrix plastic damage. Other research groups (Melro *et al.*, 2013; Yunyu Li, Guo, *et al.*, 2016) also supported these finding. Similar types of interfacial laws have also been applied in the Method of Cells or Generalized Methods of Cells (Johnston *et al.*, 2017).

2.4.3 Fuzzy fibre reinforced polymer

Promising experimental results have motivated researchers to study the effects of CNTs on the fuzzy fibre reinforced polymer (FFRP) properties by analytical and numerical approaches (Kulkarni *et al.*, 2010; Kundalwal and Ray, 2011, 2012; Rafiee and Ghorbanhosseini, 2017). Fuzzy fibre consists of circular cylindrical carbon fibre, with a CNTs growth on the fibre surface. In the numerical simulation, CNTs on the fibre surface are usually

considered as a separate layer of the nanocomposite. For example, Kulkarni *et al.* (2010) estimated mechanical properties of a nano-reinforced laminated composite with two different volume fractions of CNTs using two-step multiscale modelling method. Nanoscale, cylindrical RVE containing a single isotropic CNT and the interphase surrounded by the polymer matrix was simulated to predicted properties of the nano-reinforced layer. Then, three-phase RVE cylindrical model containing the carbon fibre and nano-reinforced matrix was simulated. Kundalwal and Ray (2011) developed a method to evaluate the elastic constants of continuous fuzzy fibre composites using mechanics of materials combined with the Mori-Tanaka approach. Chatzigeorgiou, Seidel and Lagoudas (2012) characterised fuzzy fibre reinforced composites considering various CNTs volume fractions and lengths. Ren *et al.* (2015) experimentally and computationally investigated the piezoresistivity of fuzzy fibre reinforced polymer by 3-D FEM multiscale model. Ray (2010) proposed a shear lag model to obtain the response of the CNTs coated piezoelectric fibre reinforced composites. More recently, Rafiee and Ghorbanhosseini (2017) applied a stochastic multiscale model to obtain mechanical properties of FFRP with randomly orientated CNTs on the fibre surface. Numerically predicted transverse modulus was 40% higher than the experimentally determined value.

2.4.4 FRPs reinforced with graphene

The simulations work of FRPs reinforced with graphene is rather limited. Few works with graphene either introduced in the matrix or on the fibre surface were reported. For example, Hadden *et al.* (2015) proposed multiscale approach consisting of molecular dynamics and two-step micromechanics simulations of GNPs/CF/epoxy hybrid composite. At the molecular level, nine orthotropic material properties for GNPs/epoxy were predicted considering a different number of graphene layers and crosslink density. Then, at the microscale level, the RVE containing pure epoxy and effective properties from MD simulation was simulated to obtain homogenised properties of GNPs/epoxy with desired GNPs volume fraction. Finally, the results from GNPs/epoxy simulation were input into a micromechanical model consisting of circular carbon fibre, and GNPs reinforced epoxy. The similar multiscale approach was also adopted by (Aluko, Gowtham and Odegard, 2017).

Another multiscale approach was presented by Mishnaevsky and Dai (2014) and analysed the fatigue resistance of fibre reinforced composite with the nanoclay or CNTs. In the model, nanofillers were distributed either in a matrix or at the fibre surface. Two scale nano and micro were performed. At the nanoscale, RVE model contained nano-reinforcement,

‘effective interphase layer’ and matrix. At the microscale, the RVE contained three phases: the matrix, fibres and interphase. The various types of reinforcement orientation (aligned and random) were investigated.

More recently, Sabuncuoglu *et al.* (2018) introduced two types of nano-reinforcement (CNT, GNPs) on the steel fibre surface to investigate their effects on stress concentration. The simulations were performed on microscale level only using hexagonal RVE. Nanofillers were introduced to the RVE by modelling a separate layer of defined thickness. The properties of the layer were predicted using the Mori-Tanaka approach, where volume fraction, dimensions, properties of nanofillers and matrix were considered.

The advantage of FEA is the ability to study complex and large shape. The reliability of the numerical results is highly dependent on the adequacy of the input data such as material parameters. Composite manufacturers usually provide the properties as a whole rather than specifying each layer separately, and for this reason, correct parameters identification become challenging.

2.5 Inverse analysis

2.5.1 Introduction

Multiscale modelling of FRPs can consider complex structures of the materials in realistic manners, such as various shape of fibres (Pathan, Tagarielli and Patsias, 2017), interfacial de-bonding (Kostagiannakopoulou *et al.*, 2015) fibre arrangement, and void distribution (Lim *et al.*, 2016). However, the main challenge is the accurate implementation of material properties, such as the fibre, matrix and the interphase, in the model. The elastic properties of many matrix materials, which usually behave isotropic, are easily obtained from standard tensile tests. However, in the case of fibre elastic properties, manufacturers provide only longitudinal properties. This property can be directly measured through a single fibre tensile test. On the other hand, transverse properties because of the small diameter of a single fibre are more difficult to measure, and the values of these properties often scatter. For the same fibre type AS4 the values for transverse modulus varies from 12.97 GPa to 17.2 GPa and for the longitudinal shear modulus from 12.28 GPa to 28 GPa (Soden, Hinton and Kaddour, 2004; Naya *et al.*, 2017). Challenges with the direct identification of complex material parameters motivated researchers to identify material properties in FRPs by inverse analysis called in other words mixed numerical-experimental technique. Interphase properties have

become particularly interesting in the inverse analysis as they are extremely difficult to identify (see sections 2.1.2 and 2.4.2).

2.5.2 Objective function

The output of a complex system can be predicted with known input parameters and a reliable constitutive model, which is referred to a direct or forward problem. The direct problem can be represented by the following mathematical form:

$$g(p) + \epsilon = z \quad 2-22$$

Where g is a function of a physical system, p is a vector of input parameters, z is a collected output vector, and ϵ is a total error vector of the problem (Szeliga, Gawad and Pietrzyk, 2004). Direct methods use conventional experimental techniques to determine constitutive parameters. In contrast, an inverse problem needs to estimate unknown parameters p with measured output data z from mechanical testing. The comparison between direct and inverse problem is shown in **Figure 2-15**. If there is no explicit relation from measured data to unknown parameters, it is exceptionally difficult to determine parameters from experimental data directly.

In the very first step of the inverse problem procedure, it is necessary to choose the experiment. Results can be obtained in the form of a force-displacement curve or by a mean of strain field. Strain field can be collected using various techniques such as well-known strain gauges (Kam, Chen and Yang, 2009) or optical full-field technique (Lecompte *et al.*, 2007). Following, the numerical study is performed by FEM, and the objective function is formed, that represents some norm of a difference between experimental and computed results (Buljak, 2012). Objective functions have various forms, but the least squares problem is one of the most common methods employed in the inverse analysis (Gavin, 2016). The best parameters set is determined with optimisation algorithms. The choice of the optimisation method is crucial and influence on the efficiency of the method. The three leading families of the optimisation algorithm are gradient-based methods, nature-inspired algorithms and artificial intelligence algorithms. However, taking into account the efficiency and CPU low cost, gradient-based method, are fully capable of successfully determining material parameter sets for mechanical constitutive models (Andrade-Campos, De-Carvalho and Valente, 2012).

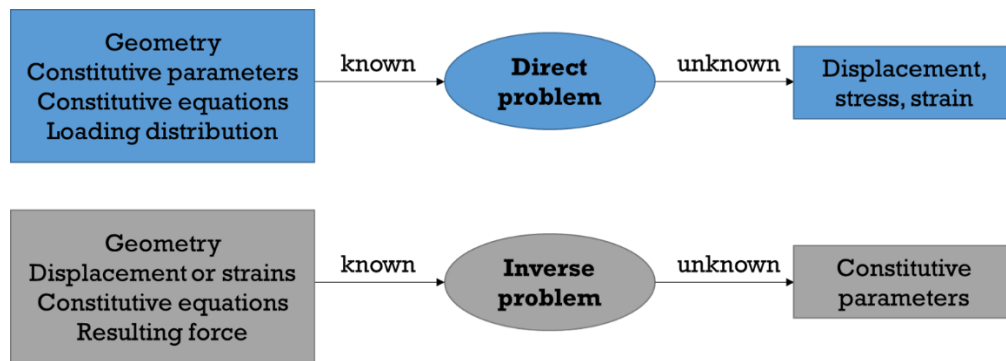


Figure 2-15 Direct problem versus inverse problem

2.5.3 Inverse analysis of FRPs

Inverse problem in FRPs can be solved at different scales, i.e. micro or macroscale. Geers *et al.* (1999) developed a gradient-enhanced damage model to identify unknown parameters of glass fibre reinforced polypropylene. Compact-tension notched specimen were subjected to a tensile load, and Digital Image Correlation (DIC) measured the displacement field. A Gauss-Newton algorithm was applied to minimise the objective function. Wang and Kam (2000) developed a non-destructive evaluation method for determination of material parameters. The number of square graphite/epoxy laminates were subjected to two types of loadings, namely, a centre point load or a uniformly distributed load. Minimisation between stress-strain curve obtained experimentally and predicted by FEM was achieved with the unconstrained global optimisation algorithm. Genovese *et al.* (2004) presented a hybrid numerical-experimental procedure for the in-plane mechanical characterisation of orthotropic materials. Speckle interferometry and FEM were combined together in order to minimise the difference between the displacement field obtained by three-point bending test and numerical simulations. The results of four elastic constants were in good accuracy with the error of less than 0.7 %. Lecompte *et al.* (2007) performed the biaxial tensile test on glass/epoxy cruciform specimen. Heterogeneous strain field was measured by DIC and calculated based on finite element method. The difference between the experimental and numerical data was formulated in a least-squares sense with a Gauss-Newton optimisation algorithm. Material constant determined by this method were in good agreement with the values obtained by traditional uniaxial tests. In 2009, Kam *et al.* developed an effective method for elastic constant identification of laminated graphite/epoxy angle beam subjected to three-point-bending. The strain measurements from the beam were used in a stochastic global optimisation method. More

recently, the method presented by Comellas et al. (2015) employed the mixing theory as a tool for modelling the behaviour of composites structures in FEM. It allows combining several constitutive models representing the individual behaviour of the component materials to obtain global behaviour of the composite. This method in combination with genetic algorithm allows extracting material data from the force-displacement curve obtained by a tensile test.

Identification of unknown material properties from the effective FRPs moduli requires a detailed knowledge of the microscopic structure of the composite. For example, to predict interphase properties in FRPs, the fibre and matrix properties, fibre volume fraction and dimensions have to be assumed. Additionally, some range of the interphase thickness needs to be estimated. Matzenmiller and Gerlach (2005) predicted the elastic properties of the glass fibre/epoxy interphase using generalised method of cells with the aid of a gradient-based solution algorithm. Square RVE model was used to simulate the mechanical behaviour, where all constituents were assumed isotropic. Experimental results of the transverse elastic modulus of the lamina with different carbon fibre volume were used for optimisation. Different thickness of the interphase, i.e. 0.3, 0.4, 0.7 μm was considered. Isotropic properties of the interphase were predicted; however, numerical results did not satisfy all cases. More recently, Lu *et al.* (2014) identified transverse properties of carbon fibre, stiffness and thickness of the interphase region by square RVE micromechanical model and Kriging metamodeling. Cohesive zone layer described the interphase region with normal and tangential stiffness. Inverse problem has successfully predicted all of the sought parameters.

2.5.4 Challenges in inverse problems

Although it is stable and unique to solve direct problem, its corresponding inverse problem is ill-posed and unique solution is not guaranteed. Several unknown parameters can be obtained simultaneously and solve the inverse problem. Uniqueness ensures a reliable solution and avoids false results. More information will help the likeliness of obtaining a unique solution; for instance, increase the set of experimental data or robustness of the optimisation methods. In the field of composite material, the success of inverse analysis will greatly depend on the correct identification of key parameters entering the governing equation.

2.6 Literature review summary

This chapter has presented a literature review on the FRPs composites reinforced with nanofillers and their influence on mechanical properties. Some conclusions, as well as the research gaps found in the literature, are the following:

- Substantial experimental research work has been dedicated to the techniques of introducing the nanofillers in FRPs. Nanofillers can be mixed with the matrix or coated on the fibre surface forming nano-reinforced interphase. Presence of the nanofillers in either matrix or nano-reinforced interphase has shown improvement in mechanical properties of the FRPs such as IFSS, ILSS, flexural modulus and strength, fracture toughness and many more.
- Nano-reinforced interphase in the FRPs can be created by dip coating, EPD or grafting. A comprehensive description of the advantages and disadvantages of each of these processes has been provided in this chapter. Despite the success of coating methods, there is still a room to develop a more controllable deposition process. The special attention should be paid to: finding environmental friendly solvent, reducing the amount of the solution needed, controlling the amount of deposited nanofillers, and the possibility to scale-up the process.
- Numerical and analytical modelling methods have focused on the fuzzy fibre reinforced polymer, where CNTs are radially grown on the fibre surface. Numerical work to study FRP reinforced with graphene is still limited. Previous numerical studies considered either graphene reinforced nanocomposites or fibre reinforced polymer model. This thesis has developed a multiscale approach (from nano to microscale) to combine three scale simulations. The effects of the graphene orientation and volume fraction in the interphase have been studied systematically for the first time.
- Interphase properties have a high impact on overall FRPs behaviour, but are difficult to determine experimentally. Inverse analyses have been widely used in the identification of composite material properties. Only a few studies employed inverse analysis to determine interphase properties. This was limited to the traditional FRPs. Properties of the interphase were often extracted from lamina properties. Here, the two-scale

optimisation method has been established to predict the properties of the graphene reinforced interphase from three-point bending test of laminated samples.

3 Methodology

3.1 Introduction

The previous chapter has reviewed manufacturing methods for fibre-reinforced polymers (FRPs). Nanofillers have shown a varying extent of enhancement to FRPs. To fully exploit their potential and accelerate the development cycle of new material, numerical modelling has an important role to play. Finite Element Analysis (FEA) has become a commonly used computer simulation technique, which allows design engineers to construct, verify, assess and optimise the product design at various stages of the development. FEA analysis can significantly reduce the time and cost for the design process. Application of this modelling technique to composite material is challenging because their material constitutive equations can be very complicated.

Numerical modelling work has been reported to study the behaviour of the FRP reinforced with nanofillers (Chatzigeorgiou, Seidel and Lagoudas, 2012; Hadden *et al.*, 2015). Fuzzy fibre model where carbon nanotubes (CNTs) are grown on the fibre surface was most commonly studied (Kulkarni *et al.*, 2010). Less work reported on developing models for the FRP with graphene nanoplatelets (GNPs) coated on the fibre surface. In this work, a multiscale modelling framework was developed to study the behaviour of the FRP with nanofillers coated on the fibre surface. GNPs coated on the fibre surface was referred to the GNPs reinforced interphase. The effects of the GNPs orientation in the interphase were examined, and their influence on the unidirectional CFRP lamina properties was studied. Numerical simulations conducted at the macroscale level were directly compared with experimental measurements, such as the three-point bending test.

In addition to numerical simulations, CFRP reinforced with GNPs was also manufactured and samples were subjected to different experimental tests. Generally, matrix modification is the most commonly used experimental technique to employ nanofillers. More recently, coating fibre with nanofillers has become an alternative way to reinforce FRPs. EPD and dip coating are popular processes (Qin *et al.*, 2015; Mahmood *et al.*, 2018). The main difficulty of this manufacturing techniques is limited control of the GNPs deposition. There is a great need for the development of another simple, effective and yet scalable manufacture method. In this project the spraying technique was employed to introduce GNPs into the composite: nanofillers were sprayed either on prepreg surface or carbon fibre fabric. All samples with/without

nanofillers were tested in different ways, such as three-point bending, short beam and double cantilever beam tests.

To characterise the interphase directly, the author performed an inverse analysis based on the experimental measurement data and developed multiscale modelling framework. ANSYS DesignXplorer was adopted to determine the properties of the nanofillers-reinforced interphase. The inverse analysis involved two scales separately. Experimental data of the three-point bending test from the literature were used as objective, and laminae's properties were firstly derived at the macroscale modelling. The follow-up inversed analysis at the microscale modelling yields a direct prediction of properties of the interphase. This is for the first time that nanofillers reinforced interphase properties were determined from experiment.

3.2 Multiscale analysis framework

The multiscale analysis framework presented in **Figure 3-1** was used to predict the properties of FRP reinforced with GNPs. Properties of the GNPs reinforced interphase were firstly calculated following the Mori-Tanaka method at the nanoscale. In this calculation, transversely isotropic GNPs together with isotropic epoxy resin was assumed. Various GNPs concentration and orientation were considered in the interphase layer. Once the GNPs reinforced interphase properties were determined, the 3D micromechanical RVE model was built and simulated using ANSYS APDL. The RVE model contained three phases: transversely isotropic carbon fibre, isotropic epoxy resin and GNPs reinforced interphase. Given the volume fraction of carbon fibre and the thickness of the interphase, this microscale simulation investigated the effects of different concentration and orientation of GNPs on the lamina elastic constants. Finally, these properties were input to the macroscale model to simulate the behaviour of the specimen in the three-point bending test. Samples of the same dimensions, laminate lay-up as the one experimentally tested was simulated using ANSYS Workbench. Calculated flexural modulus was compared with experimental data.

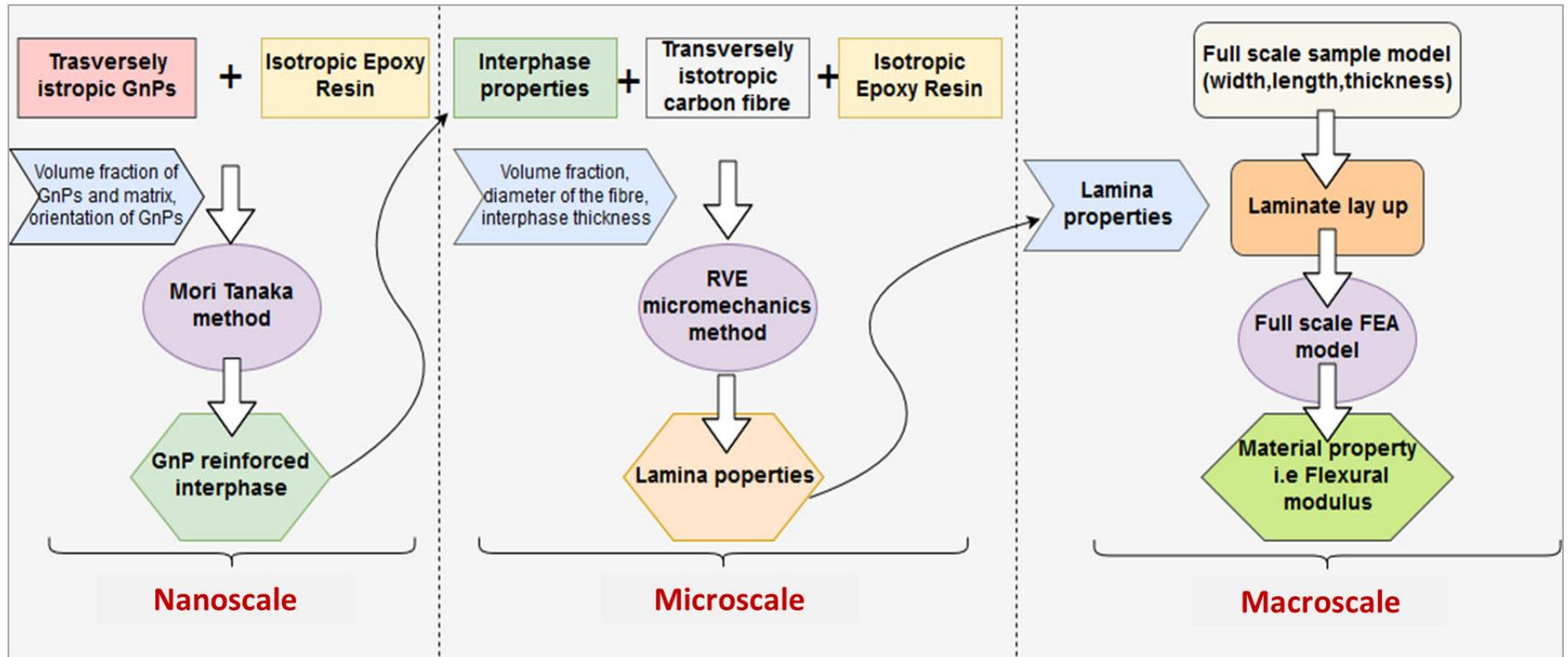


Figure 3-1 Flowchart of a multiscale approach

3.2.1 Nanoscale - Mori Tanaka method

The nano-reinforced phase was the key to successful prediction of this carbon fibre reinforced polymer. In this work, the GNPs reinforced interphase were determined using Mori-Tanka method (Mori and Tanaka, 1973; Ji, Cao and Feng, 2010). This method was traditionally used to estimate properties of nanocomposite (Shokrieh and Rafiee, 2010; Shokrieh *et al.*, 2014). However, it was also exploited to predict properties of the CNTs (Kundalwal and Ray, 2012) and the graphene (Sabuncuoglu, Gorbatikh and Lomov, 2018) reinforced interphase in fibre reinforced composites.

3.2.1.1 Hills parameters

Hills' parameters: k , l , n , m and p were applied to simplify mathematical calculations of Mori-Tanaka presented in subchapter 2.2. The stiffness tensor C can be expressed in terms of Hill's parameters. Following the local coordinate system for GNPs (**Figure 3-2**), the stiffness tensor for this transversely isotropic material is written as:

$$C = \begin{bmatrix} k + m & k - m & l & 0 & 0 & 0 \\ k - m & k + m & l & 0 & 0 & 0 \\ l & l & n & 0 & 0 & 0 \\ 0 & 0 & 0 & p & 0 & 0 \\ 0 & 0 & 0 & 0 & p & 0 \\ 0 & 0 & 0 & 0 & 0 & m \end{bmatrix} \quad 3-1$$

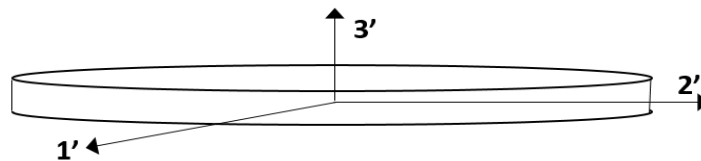


Figure 3-2 Local coordinates system of single graphene nanoplatelet.

For each constituent or the whole mixture, the Hill's parameters can be interconverted to constants of stiffness matrix or elastic properties. For example, properties of transversely isotropic graphene nanoplatelets are expressed in Hill's parameters by equation 3-2. Note that throughout the project subscripts, r and m , mean GNPs reinforcement and matrix respectively and superscript I denotes interphase.

$$E_{1'}^{GNP} = \frac{4m_r(k_r n_r - l_r^2)}{(k_r + m_r)n_r - l_r^2}, \quad 3-2$$

$$E_{3'}^{GNP} = n_r - \frac{l_r^2}{k_r},$$

$$G_{1'3'}^{GNP} = p_r,$$

$$v_{1'2'}^{GNP} = \frac{(k_r - m_r)n_r - l_r^2}{(k_r + m_r)n_r - l_r^2},$$

$$v_{1'3'}^{GNP} = \frac{l_r}{2k_r}$$

For the isotropic epoxy resin in this project, the Hill's parameters can be related to elastic properties in equation 3-5.

$$k_m = \frac{E^m}{2(1+\nu^m)(1-2\nu^m)} \quad 3-3$$

$$l_m = \frac{\nu^m E^m}{(1+\nu^m)(1-2\nu^m)},$$

$$m_m = p_m = \frac{E^m}{2(1+\nu^m)},$$

$$n_m = \frac{(1-\nu^m)E^m}{(1+\nu^m)(1-2\nu^m)}.$$

The interphase properties will be very much dependent on the orientation of nanofillers. The various orientation of nanofillers may occur due to the different techniques of GNPs coating onto the fibre surface. For example, the electrophoretic deposition process tends to make GNPs more wrapped along the fibre surface. Whereas due to the dip coating, GNPs are more likely to end in the random orientation. Here, these two extreme cases of orientation are considered as presented in **Figure 3-3**. All GNPs assume even distribution in the reinforced interphase; thus, the interphase is homogenous. Once GNPs and matrix Hill's parameters are known, the properties of the GNPs reinforced interphase can be calculated in different ways depending on the orientation of GNPs.

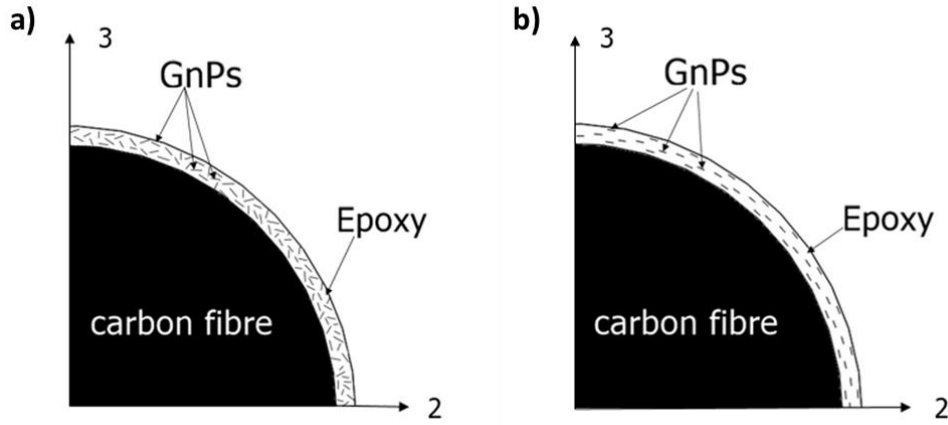


Figure 3-3 Quarter of cross-section view of carbon fibre with (a) randomly orientated GNPs and (b) aligned GNPs within the reinforced interphase. Global coordinate system (1-2-3) is used as shown.

3.2.1.2 Randomly orientated GNPs in the reinforced interphase

When GNPs are randomly distributed in the carbon fibre coating (see **Figure 3-3a**), the GNPs reinforced interphase behaves isotropically even GNPs are transversely isotropic. As a result, its material properties can be entirely determined by two parameters (E^I, ν^I). Following the Mori-Tanka method together with Hill's parameters for GNPs and matrix, the intermediate variables ($\alpha, \beta, \delta, \eta$) for the mixture can be found, where V_r and V_m represent volume fraction of GNPs and matrix respectively.

$$\alpha = \frac{3k_m + 2n_r - 2l_r}{3n_r} \quad 3-4$$

$$\beta = \frac{4\mu_m + 7n_r + 2l_r}{15n_r} + \frac{2\mu^m}{5p_r}$$

$$\delta = \frac{3k_m(n_r + 2l_r) + 4(k_r n_r - l_r^2)}{3n_r}$$

$$\eta = \frac{2}{15} \left(k_r + 6m_r + 8\mu^m - \frac{l_r^2 + 2\mu^m l_r}{n_r} \right)$$

Substituting these variables in equation 3-5, bulk (κ^I) and shear (μ^I) moduli of the interphase can be found as follows:

$$\kappa^I = \kappa^m + \frac{V_r(\delta - 3\kappa^m\alpha)}{3(V_m + V_r\beta)} \quad 3-5$$

$$\mu^I = \mu^m + \frac{V_r(\eta - 2\mu^m\beta)}{2(V_m + V_r\beta)}$$

Furthermore, bulk (κ^I) and shear (μ^I) moduli can be converted to Young's modulus (E^I) and Poisson's ratio of the GNPs reinforced interphase accordingly.

$$E^I = \frac{9\kappa^I\mu^I}{3\kappa^I + \mu^I} \quad 3-6$$

$$\nu^I = \frac{3\kappa^I - E^I}{6\kappa^I}$$

3.2.1.3 Aligned GNPs in the reinforced interphase

The aligned orientation of the GNPs assumes that 2D nanoplatelets are located parallel to the fibre surface - wrapped around the fibre (see **Figure 3-3b**). This orientation causes the GNPs reinforced interphase behaves in a transversely isotropic manner. Following the Mori-Tanaka method, the Hill's parameter of the interphase can be calculated as follows.

$$k = V_r k_r + V_m k_m - \frac{V_m V_r (l_r - l_m)^2}{V_r n_m + V_m n_r} \quad 3-7$$

$$l = \frac{V_r l_r n_m + V_m l_m n_r}{n_r V_m + n_m V_r}$$

$$m = V_r m_r + V_m m_m$$

$$n = \frac{n_m n_r}{V_r n_m + V_m n_r}$$

$$p = \frac{p_m p_r}{V_r p_m + V_m p_r}$$

Stiffness tensor of the aligned GNPs in the reinforced interphase follows the same coordinate system as for single GNP (see equation **3-1**); therefore, the interphase parameters can be determined according to equation **3-8**.

$$E_{1'}^I = \frac{4m(kn - l^2)}{(k+m)n - l^2}, \quad 3-8$$

$$E_{3'}^I = n - \frac{l^2}{k},$$

$$G_{1'3'}^I = p,$$

$$\nu_{1'2'}^I = \frac{(k-m)n - l^2}{(k+m)n - l^2},$$

$$v_{1'3'}^I = \frac{l}{2k}$$

Where: $E_{1'}^I, E_{3'}^I, G_{1'3'}^I, v_{1'3'}^I, v_{1'2'}^I$ are defined as in-plane elastic modulus, out-of-plane elastic modulus, out-of-plane shear modulus, out-of-plane Poisson's ratio, in-plane Poisson's ratio of the interphase respectively.

3.2.2 Microscale – RVE methods

3.2.2.1 RVE model

RVE model was adopted to investigate the effects of the nano-reinforced interphase on the lamina properties. In this model, the smallest volume was selected over which predicted properties yielded representative values of the entire lamina. Cylindrical continuous fibres were assumed to be uniformly embedded in an elastic matrix (**Figure 3-4a**). In manufactured FRPs, the real fibre distribution is often less regular across the cross-section as explained in section 2.2.2. Most micromechanical modelling works assume a periodic fibre arrangement then a simplified 3D representative volume element can be determined as shown in **Figure 3-4b** (Ruchevskis S., 2002; Wang, Crouch and Mogilevskaya, 2006; Kumar, Chandra and Singh, 2010; Maligno, Warrior and Long, 2010; Xu *et al.*, 2012). The RVE model in this work adopted a hexagonal array of fibre sequence, which represented a single lamina of transversely isotropic properties.

The size of RVE is calculated based on the volume fraction of the fibre (v_f) and diameter (d_f) of the fibre according to the equation **3-9**. Symbols a_1, a_2, a_3 represent the thickness, width and height of the RVE model respectively as highlighted in **Figure 3-4b**.

$$v_f = \frac{\pi(d_f/2)^2}{2a_2a_3}, a_3 = \sqrt{3}a_2, a_1 = a_2/4 \quad \mathbf{3-9}$$

The prediction of elastic constants of the fibre-reinforced composite is based on Hooke's law for transversely isotropic materials (equation **3-10**), where C_{ijkl} is a stiffness matrix, and $\bar{\sigma}_{ij}$ and $\bar{\epsilon}_{ij}$ are the volume average stresses and strains respectively. The 1-axis is aligned with the fibre direction (see **Figure 3-4a**).

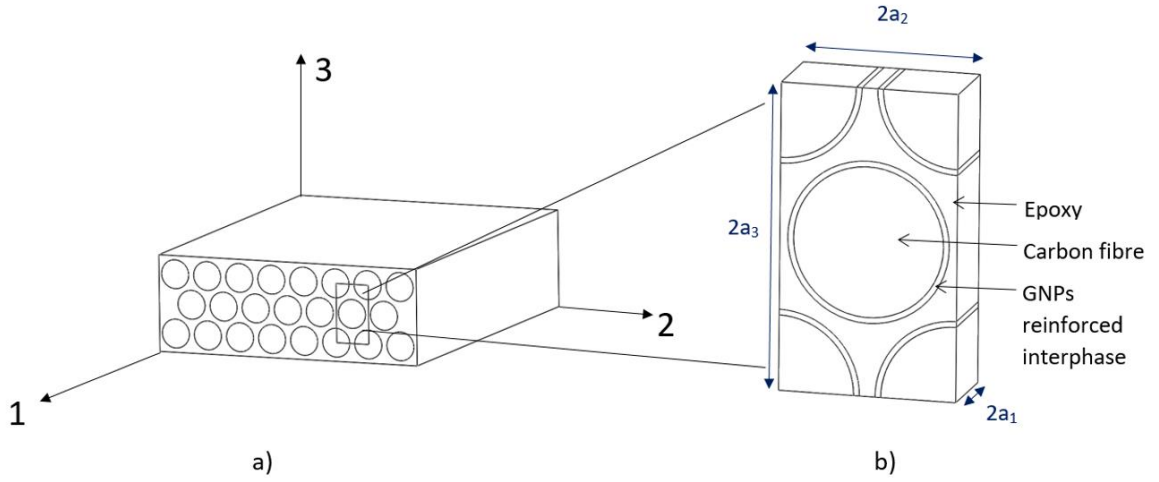


Figure 3-4 Schematic drawings of (a) CFRP lamina and (b) its three-phase representative volume element with the reinforced interphase. The 1-2-3 coordinate system is added to define the material property.

$$\begin{Bmatrix} \bar{\sigma}_1 \\ \bar{\sigma}_2 \\ \bar{\sigma}_3 \\ \bar{\tau}_4 \\ \bar{\tau}_5 \\ \bar{\tau}_6 \end{Bmatrix} = \begin{bmatrix} C_{11} & C_{12} & C_{12} & 0 & 0 & 0 \\ C_{12} & C_{22} & C_{23} & 0 & 0 & 0 \\ C_{12} & C_{23} & C_{22} & 0 & 0 & 0 \\ 0 & 0 & 0 & \frac{1}{2}(C_{22} - C_{23}) & 0 & 0 \\ 0 & 0 & 0 & 0 & C_{66} & 0 \\ 0 & 0 & 0 & 0 & 0 & C_{66} \end{bmatrix} \begin{Bmatrix} \bar{\varepsilon}_1 \\ \bar{\varepsilon}_2 \\ \bar{\varepsilon}_3 \\ \bar{\gamma}_4 \\ \bar{\gamma}_5 \\ \bar{\gamma}_6 \end{Bmatrix} \quad 3-10$$

Determination of the stiffness matrix requires the RVE to be loaded in different ways subjected to periodic boundary condition. The periodic boundary conditions are applied to the RVE model to compute stresses, strains and calculate the overall elastic matrix, C_{ijkl} . The volume average strains and stresses are calculated by equation 3-11, where V is the volume of the RVE model.

$$\bar{\varepsilon}_{ij} = \frac{1}{V} \int_V \varepsilon_{ij} dV \quad 3-11$$

$$\bar{\sigma}_{ij} = \frac{1}{V} \int_V \sigma_{ij} dV$$

Stiffness matrix constants can be readily converted to common elastic properties of the CFRP: E_1 and E_2 represent the longitudinal and transverse moduli, G_{12} and G_{23} are longitudinal and transverse shear moduli, ν_{12} is longitudinal Poisson's ratio respectively (equation 3-12). The comprehensive descriptions on RVE methods can be found elsewhere (Sun and Vaidya, 1996; Luciano, 1998; Barbero, 2014).

$$E_1 = C_{11} - 2C_{12}^2/(C_{22} + C_{23}) \quad 3-12$$

$$E_2 = [C_{11}(C_{22} + C_{23}) - 2C_{12}^2](C_{22} - C_{23})/(C_{11}C_{22} - C_{12}^2)$$

$$\nu_{12} = C_{12}/(C_{22} + C_{23})$$

$$\nu_{23} = [C_{11}C_{23} - C_{12}^2]/(C_{11}C_{22} - C_{12}^2)$$

$$G_{12} = C_{66}$$

3.2.2.2 Implementation in ANSYS APDL

Although ANSYS Workbench has a more intuitive graphical user interface (GUI), the RVE analysis was purposely implemented in ANSYS Design Parametric Language (APDL) module of ANSYS 17.2 software. The simulations in APDL can be executed entirely using commands; the commands collection file can be easily modified which can maximise the operating efficiency of a large number of simulations. *Appendix A* presents an example of the APDL input file motivated by (Barbero, Cosso and Campo, 2013). In this work, parameters such as carbon fibre volume fraction, materials properties, interphase thickness, size of RVE were adjusted by updating the APDL input file according to the particular case. This way reduces the time of setting up new analyses significantly.

Figure 3-5 presents the excerpt of the input file of the three-phase RVE model. The size of RVE calculated by equation 3-9 and together with a radius of the fibre serves as parameters to create the model. Three material models were selected in pre-processor, where 1 represented transversely isotropic carbon fibre, 2 and 3 were an isotropic epoxy matrix and interphase respectively. The x-y-z Cartesian coordinate system is used ANSYS APDL, corresponding to 1-2-3 coordinates in the input file. Next, the element type of the model was selected. The rest of the input files includes the RVE volume generation presented in Appendix A. Note that, great care must be taken while assigning materials properties and creating the model to ensure the consistency between them.

```

/TITLE, Full Model of RVE, hexagonal array

rf=3.55      ! Radius fiber in microns
a2=4.224     ! x2 length in microns
a3=7.307     ! x3 length in microns
a1=1.0561    ! x1 length in microns

/PREP7       ! Pre-processor module (Material properties in TPa)
MP,EX,1,17.2e-3 ! Transverse modulus of Carbon Fibre (E_2_f)
MP,EY,1,17.2E-3 ! Transverse modulus of Carbon Fibre (E_3_f)
MP,EZ,1,224E-3  ! Longitudianl modulus of Carbon Fibre (E_1_f)
MP,NUXY,1,0.5   ! Transverse Poisson's ratio of Carbon Fibre (v_23_f)
MP,NUYZ,1,0.2   ! Longitudinal Poisson's ration of Carbon Fibre (v_13_f)
MP,NUXZ,1,0.2   ! Longitudinal Poisson's ration of Carbon Fibre (v_12_f)
MP,GXY,1,5.73E-3 ! Transverse Shear Modulus of Carbon Fibre (G_23_f)
MP,GYZ,1,27.6E-3 ! Longitudinal Shear Modulus of Carbon Fibre (G_13_f)
MP,GXZ,1,27.6E-3 ! Longitudinal Shear Modulus of Carbon Fibre (G_13_f)
MP,EX,2,3.45E-3 ! Young's modulus of matrix (E_m)
MP,PRXY,2,0.34  ! Poisson's ratio of matrix (v_m)
MP,EX,3,3.45e-3 ! Young's modulus of isotropic interphase (E_i)
MP,PRXY,3,0.34  ! Poisson's ratio of isotropic interphase (v_i)

ET,1,SOLID186   ! Choose SOLID186 element type

```

Figure 3-5 Implementation of the material properties of the three-phase RVE model - an excerpt of an exemplary APDL input file.

Once the RVE model was created, the next step was to generate a mesh. Carbon fibre and the interphase volumes meshes were generated with mapped VMESH command. VSWEEP options meshed the surrounding matrix. To eliminate the influence of mesh density on the simulated properties, mesh independent study was performed. **Figure 3-6** presents the effects of the number of elements on the calculated longitudinal Young's modulus. The mesh was refined by increasing the number of divisions of individual line in the RVE model. A small variation of 0.01 GPa in Young's modulus was found for all the tests. The value remained little changed when the number of elements increased to 6000.

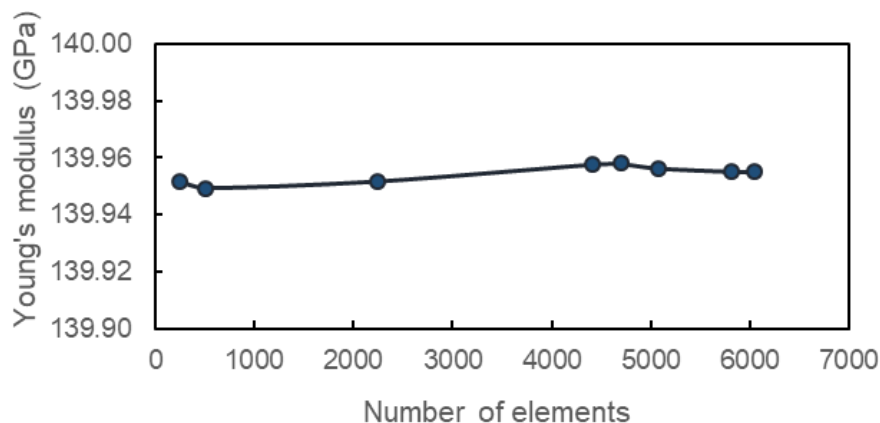


Figure 3-6 Mesh independent study for 3 phase RVE model.

In the next step, periodic boundary conditions were applied to the model to evaluate the overall elastic matrix C of the composite lamina. For a periodic structure consisting of a periodic array of repeated RVE models, the displacement field for this structure can be expressed as:

$$u_i(x_1, x_2, x_3) = \varepsilon_{ij}^0 x_j + u_i^*(x_1, x_2, x_3) \quad 3-13$$

where, ε_{ij}^0 is the global (average) strain tensor of the periodic structure, left term of the equation represents a linear distributed displacement field. The term, $u_i^*(x_1, x_2, x_3)$, is a periodic function from one unit cell to another, and represents a modification to the linear displacement field due to the heterogeneous structure of the composites.

In this RVE model, periodic boundary conditions as presented in equation 3-14 were applied. $2a_j \varepsilon_{ij}^0$ is the displacement needed to enforce a strain ε_{ij}^0 over the distance $2a_j$ (see Figure 3-4b).

$$u_i(a_1, x_2, x_3) - u_i(-a_1, x_2, x_3) = 2a_1 \varepsilon_{i1}^0 \quad \begin{array}{l} -a_2 \leq x_2 \leq a_2 \\ -a_3 \leq x_3 \leq a_3 \end{array} \quad 3-14$$

$$u_i(x_1, a_2, x_3) - u_i(x_1, -a_2, x_3) = 2a_2 \varepsilon_{i2}^0 \quad \begin{array}{l} -a_1 \leq x_1 \leq a_1 \\ -a_3 \leq x_3 \leq a_3 \end{array}$$

$$u_i(x_1, x_2, a_3) - u_i(x_1, x_2, -a_3) = 2a_3 \varepsilon_{i3}^0 \quad \begin{array}{l} -a_1 \leq x_1 \leq a_1 \\ -a_2 \leq x_2 \leq a_2 \end{array}$$

The strain ε_{ij}^0 applied on the boundary by equation 3-14 produces a complex state of strain inside the RVE. However, the average strain in the RVE equals to the applied strain following equation 3-15.

$$\bar{\varepsilon}_{ij} = \frac{1}{V} \int_V \varepsilon_{ij} dV = \varepsilon_{ij}^0 \quad 3-15$$

The relationship between average stress and strain, where $i, j = 1 \dots 3$ and $\alpha, \beta = 1 \dots 6$ is shown in expression 3-16. To determine the components of the tensor C , six modelling of the RVE subjected to periodic boundary conditions (equation 3-14) need to be solved. For each of the six problems only one component of the strain ε_{β}^0 is non-zero.

$$\bar{\sigma}_\alpha = C_{\alpha\beta} \bar{\epsilon}_\beta$$

3-16

The details of the code and further explanation of these periodic boundary conditions are provided in *Appendix A*. Once the coefficients of the overall elastic were calculated, they were converted to elastic constants of lamina according to equation **3-12**.

3.2.3 Macroscale simulation

The microscale simulation is the final step of the multiscale modelling framework, where the laminate was studied. The purpose was to investigate the effects of the predicted lamina properties on the bending behaviour of the unidirectional laminate under the three-point bending conditions. Simulations of fibre-reinforced laminate involve complex definitions including numerous layers, materials, thicknesses and orientations. ANSYS software offers two ways to define laminated composites namely layer section command integrated with ANSYS Workbench, or stand-alone module ANSYS Composite Prep/Post (ACP). In this project, the layer section command was selected in Static Structural Component of Ansys Workbench. This command supports well simple geometries like a rectangular beam. Whereas, in the case of complex geometries or curved shapes it is advisable to use ACP.

Simulating the three-point bending test for a laminate specimen at the macroscale follows this procedure:

- i. CAD model of the specimen was created in Space Claim software. The rectangular sketch was extruded using surface command; thus, the specimen was a 2D shell element. According to the standard BS EN ISO 14125 (1998), the length and width of the specimen were 100, and 12.7 mm respectively. The CAD model was later imported to the ANSYS Static structural component.
- ii. In the Engineering Data library, custom properties were created for the single unidirectional lamina, which is transversely isotropic as presented in **Figure 3-7**. These properties values were predicted from the RVE modelling mentioned above. Extra care on the orientation of the fibres and lamina coordinate system must be taken during assigning properties. These properties are related to a global coordinate system of the CAD model. Note that in this case, longitudinal modulus of the lamina corresponds to the x-direction, and y and z directions represented transverse properties of the lamina.

- iii. After transversely isotropic properties were assigned to each lamina layer, the laminate was built using layer command. This command opens the worksheet window and enables to select a number of layers, the thickness of single ply and fibre orientation. For example, **Figure 3-8** presents one exemplary worksheet to create a 12-layers unidirectional laminate with all fibres orientated in 90°. The total thickness of the laminate was 2.3 mm. Note that z-direction is used to build the laminate; thus, it has to line up with the thickness direction of the model. Layer command assumes perfect bonding conditions between each lamina.
- iv. The automatic meshing was applied with the selected option of fine relevance centre. The whole model contained 1000 elements and 1102 nodes. The average mesh quality was 0.99, where mesh quality of 1.0 corresponds to the best quality.

| | A | B | C | D | E |
|----|-----------------------------|-----------|------|---|---|
| 1 | Property | Value | Unit | | |
| 2 | Material Field Variables | Table | | | |
| 3 | Orthotropic Elasticity | | | | |
| 4 | Young's Modulus X direction | 1.497E+07 | MPa | | |
| 5 | Young's Modulus Y direction | 8950 | MPa | | |
| 6 | Young's Modulus Z direction | 8950 | MPa | | |
| 7 | Poisson's Ratio XY | 0.24 | | | |
| 8 | Poisson's Ratio YZ | 0.48 | | | |
| 9 | Poisson's Ratio XZ | 0.24 | | | |
| 10 | Shear Modulus XY | 5080 | MPa | | |
| 11 | Shear Modulus YZ | 3024 | MPa | | |
| 12 | Shear Modulus XZ | 5080 | MPa | | |

Figure 3-7 Orthotropic elastic properties assigned to the lamina (note that x-direction is aligned with fibre direction). Image used courtesy of ANSYS, Inc.

- v. Then, boundary conditions to reproduce the three-point bending test were assigned (**Figure 3-9**). The sample was placed in a global x-y-z coordinate system, where z was thickness direction. Force in z-direction was applied to the middle of the sample using a time-stepping function to mimic the crosshead speed of real testing conditions. The specimen was imposed by 'simply supported' boundary condition at prescribed span length between supports.

| Layer | Material | Thickness (mm) | Angle (°) |
|-------|--------------|----------------|-----------|
| (+Z) | | | |
| 12 | carbon epoxy | 0.191 | 90 |
| 11 | carbon epoxy | 0.191 | 90 |
| 10 | carbon epoxy | 0.191 | 90 |
| 9 | carbon epoxy | 0.191 | 90 |
| 8 | carbon epoxy | 0.191 | 90 |
| 7 | carbon epoxy | 0.191 | 90 |
| 6 | carbon epoxy | 0.191 | 90 |
| 5 | carbon epoxy | 0.191 | 90 |
| 4 | carbon epoxy | 0.191 | 90 |
| 3 | carbon epoxy | 0.191 | 90 |
| 2 | carbon epoxy | 0.191 | 90 |
| 1 | carbon epoxy | 0.191 | 90 |
| (-Z) | | | |

Figure 3-8 Example of layered section command ANSYS created for 12 layers unidirectional specimen, with fibres orientated in 90° direction. Image used courtesy of ANSYS, Inc.

vi. Force reaction, displacement, stresses and strains were recorded and analysed.

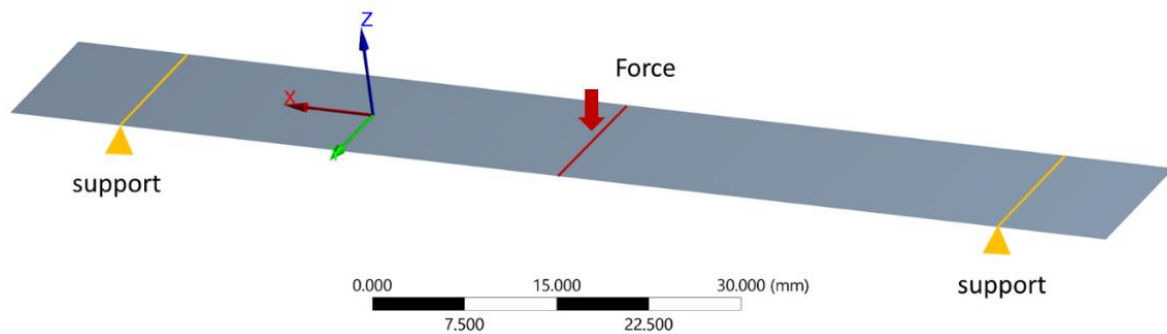


Figure 3-9 FEA model of the three-point bending test of a laminate specimen. Boundary conditions assigned in ANSYS workbench.

3.3 Experimental work

Many techniques have been developed to introduce nanofillers to the FRPs. Researchers are continually trying to improve these processes and seek cheap, effective and scalable alternatives. In the experimental part of this work, nano-reinforced FRP was prepared by spraying GNPs and CNTs. Two types of materials were manufactured: (1) unidirectional carbon fibre-epoxy prepreg was sprayed with nanofillers, laid-up and autoclave cured, (2) carbon fibre fabric sprayed with GNPs/ethanol/epoxy solution, impregnated with resin, wet

laid-up and cured at room temperature. This section provides the details on applied materials, manufacturing processes and samples inspection.

3.3.1 Materials

The materials used in the prepreg lay-up process was unidirectional MTC801-UD125-T700-32%RW-600-P carbon fibre/epoxy roll kindly donated by SHD Composites (Sleaford, UK). This prepreg material is composed of the carbon fibre T700, which is a high strength (4.9 GPa) and standard modulus (230 GPa) fibre with the diameter of 7 μm . Whereas, the MTC801 is a toughened resin system designed to produce components with an excellent surface finish. Tg temperature of this resin system is 120 °C. This prepreg material is designed for autoclave, oven and press manufacturing processes. The density of the carbon fibre (ρ_f) and epoxy resin (ρ_r) are 1.80 and 1.21 g/cm³ respectively. The weight of the prepreg is 184 g/m² where the fabric is 125g/m² (M_f) and the epoxy resin is 59g/m² (M_r). The nominal volume fraction (V_f) of carbon fibre is calculated as 58.82% (according to equation 3-17).

$$V_f = \frac{\frac{M_f}{\rho_f}}{\frac{M_f}{\rho_f} + \frac{M_r}{\rho_r}} \quad 3-17$$

For the wet lay-up manufacturing process, the carbon fibre unidirectional fabric and IN2 infusion epoxy resin were purchased from Easy Composite (Longton, UK). The thickness and weight of the single layer of fabric are 0.22 mm and 250g/m² respectively. The carbon fibre is TR50S 15K has a tensile strength of 5 GPa, tensile modulus 240 GPa, the density of 1.82 g/cm³, and a diameter of 7 μm . The IN2 epoxy resin is high performance ultra-low viscosity resin, which is composed of epoxy resin and slow hardener AT30. The mixing ratio of resin to hardener is 100:30. This mixture has a pot life around 80 - 100 minutes and a low viscosity of 200 - 450 mPa.s at 20°C. Optimal curing time of this epoxy is 7 days at 25°C. The maximum Tg temperature of the cured resin is 98 °C.

Multi-walled CNTs and GNPs are purchased in the form of powder (Sigma Aldrich, Dorset, UK). The average size of a single CNT is 10 μm in length and 12 nm diameter. The average number of layers varies from 7 to 13. Surface area of these MWCNTs is approximately 220 m²/g and density 2.1 g/mL. Whereas, GNPs (xGnP Graphene Nanoplatelet – Grade C750) have a thickness of few nm, surface area of 750 m²/g, bulk density of 0.2-0.4 g/mL.

Non-perforated PTFE film of the thickness of $12\ \mu\text{m}$ used for double cantilever beam test was purchased from VAC innovation (Hinckley, UK). Solvent to spraying process such as 99.5%, extra dry, absolute ethanol and methanol were purchased from Fisher Chemicals (Loughborough, UK). Remaining consumables needed for prepreg lay-up and wet lay-up, Easy Lease release agent and acetone were bought from Easy Composite (Longton, UK).

3.3.2 Spraying nanofillers on the prepreg

3.3.2.1 Nanofillers (CNTs or GNPs) solution

Before spraying process, it is essential to obtain a stable well-dispersed solution. Different solvents such as acetone, methanol and ethanol along with two surfactants: cationic CTAB (Cetyltrimethylammonium bromide) and non-ionic Polyvinylpyrrolidone (PVP) were tested. The powder surfactant was firstly diluted in distilled water at concentration 20g/L. The same amount of nanofillers was dissolved in a solvent with a surfactant solution. The solution was mixed for 30 minutes using magnetic stirrer IKA C-Mag HS 7 followed by another five minutes in the ultrasonic bath. Solutions were inspected at two-time points: immediately after mixing and 48 hours later.

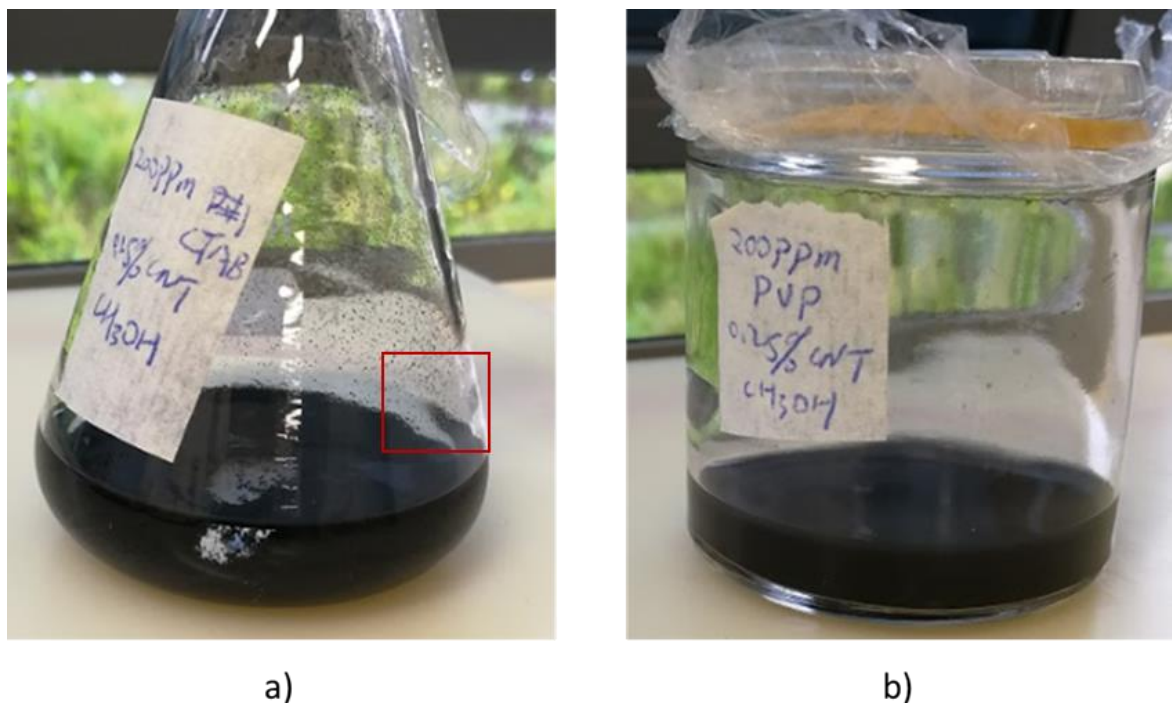


Figure 3-10 Comparison of two solution mixtures of methanol and CNTs at a concentration of 0.25 wt% with two different surfactants (a) CTAB (b) PVP immediately after mixing.

Figure 3-10 presents the sample of prepared solutions of a) CNTs-methanol-CTAB and b) CNTs-methanol-PVP. It can be seen that CNTs sank to the bottom of the flask when cationic surfactant C-TAB was used. On the contrary, PVP maintained the dispersion of GNPs or CNTs, which is in agreement with previous findings (Johnson, Dobson and Coleman, 2015). The inspection was repeated after 48 hours and results are summarised in **Table 3-1**. Both methanol and ethanol with the addition of PVP found to disperse nanofillers well. However, because methanol is toxic, the ethanol was finally selected for the spraying process.

Table 3-1 Comparison between different solvents and surfactants and their effects on the dispersion with nanofillers 48 hours after the mixing process.

| Solution ID | Solvent | Surfactant | Well Dispersed | CNTs/GNPs |
|-------------|----------|------------|----------------|-----------|
| 1 | Acetone | CTAB | No | ✓ |
| 2 | Acetone | PVP | No | ✓ |
| 3 | Ethanol | CTAB | No | ✓ |
| 4 | Ethanol | PVP | Yes | ✓ |
| 5 | Methanol | CTAB | No | ✓ |
| 6 | Methanol | PVP | Yes | ✓ |

3.3.2.2 Lay-up Process

An aluminium plate of dimension 350 mm x 400 mm was used as a mould. Before laminating, the aluminium plate was coated with a non-porous PTFE coated woven glass fabric self-adhesive film (Vac Slip 05SA1-15, VAC innovations, Hinckley, UK). Following the procedure, the vacuum pressure of 1.0 bar was applied for 10 minutes to remove any trapped air between aluminium plate and film. This coating acts as a tool-surface release ply and is applicable for various types of prepreg. Square carbon fibre prepregs of dimensions 300 mm by 300 mm were cut from the unidirectional prepreg roll. The thickness of cured ply (CPT) was calculated as 0.12 mm according to equation **3-18**.

$$CPT(mm) = \frac{W_f}{\rho_f \times V_f \times 1000} \quad 3-18$$

where W_f is the fibre areal weight (g/m^2), ρ_f is fibre density (g/cm^3), and V_f is the volume fraction of the fibre. The number of plies was determined according to the desired thickness of the samples. All plies were placed layer by layer in the same fibre direction creating unidirectional laminate (**Figure 3-11a**). De-bulking process during the lay-up was applied to

reduce the voids and wrinkles as shown in **Figure 3-11b**. Mould together with prepreg was covered with a perforated release film, breather cloth and sealed in a vacuum bag. The vacuum pressure of 1 bar was applied the vacuum port and maintained for 10 minutes. This de-bulking process was repeated every four plies of prepreg.

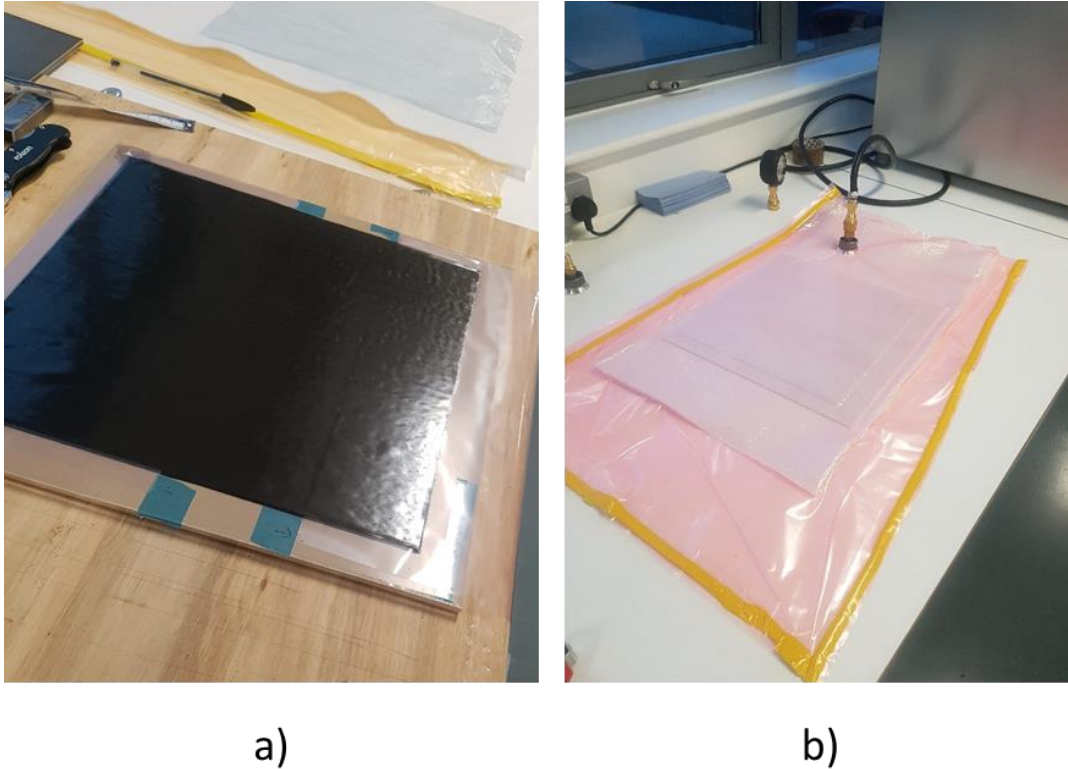


Figure 3-11 Laminate preparation for a 28 layer sample by hand lay-up process (14th layer of DCB panel with PTFE film inserted) (a) and de-bulking process for a certain number of layer (b).

3.3.2.3 Spraying process

Nanofillers (CNTs or GNPs) were applied to the carbon fibre prepreg by spraying technique (Zhang *et al.*, 2015). The schematic of the process is provided in **Figure 3-12**. Prior to spraying, the nanofillers solution was freshly prepared as described in 3.3.2.1. Dual action High-Performance C Plus airbrush (Iwata, Japan) was connected to the in-house compressor. The nanofillers solution was fed to the airbrush using dosing pipette. Spraying conditions were optimised after various trials. The distance between nozzle and prepreg during the spraying process was kept at 20 cm. The prepreg with spraying treatment was left to dry for 20 minutes, and the solvent evaporation was confirmed by visual inspection. The whole process was performed in the fume cupboard.

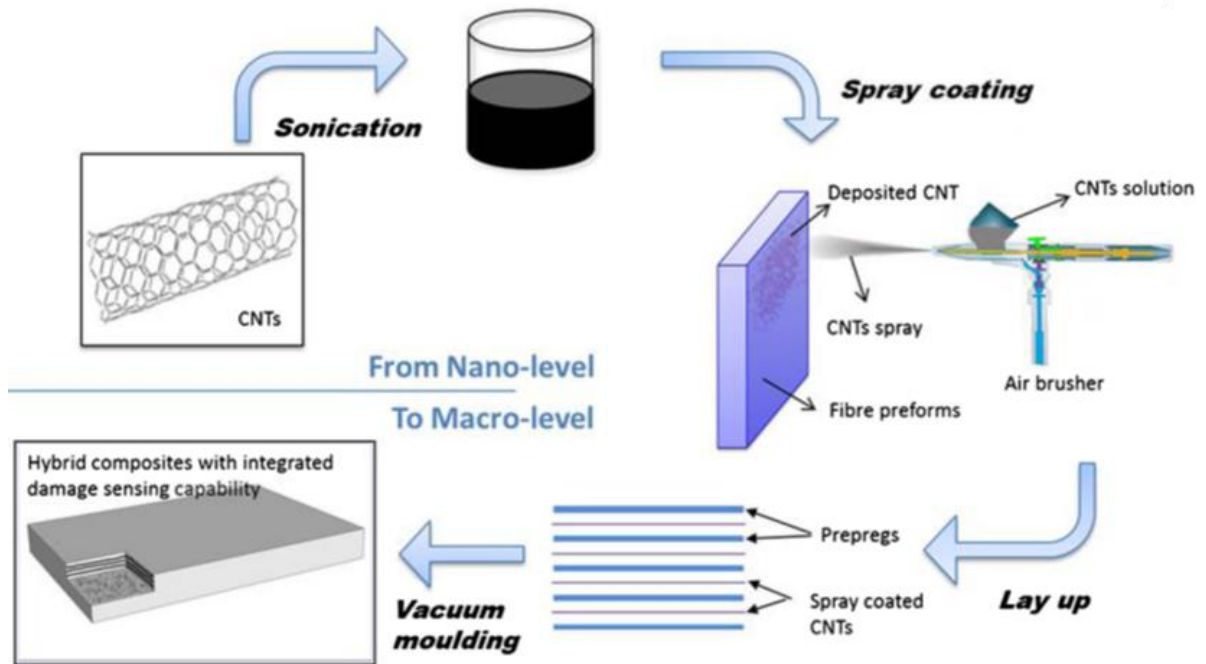


Figure 3-12 Schematic illustration of the spraying process. Reproduced with permission from Zhang et al., 2015.

3.3.2.4 Three-point bending and short beam tests specimens – manufacturing process

Testing standards for three-point bending test (ISO 14125) and short beam test (ISO 14130) require the sample of the thickness 2 mm. According to the estimation of cured ply thickness (equation 3-18), sixteen layers are needed to meet this requirement. Laminae of dimensions 300 mm by 300 mm were laid-up to create sixteen layers unidirectional laminate. The laminate was divided into two parts: part I was sprayed with the nanofillers solutions whereas, part II as control was not treated (see **Figure 3-13a**). GNPs/CNTs solution was sprayed on the top surface of 15 layers so that the sprayed nanofillers were located between the plies. **Figure 3-13b** presents the schematic of the cross-section of the laminate I after spraying treatment. Yellow colours represent layers of sprayed GNPs/CNTs solution. The concentration of the nanofillers in the solution was 0.16 wt% for GNPs and 0.25 wt% for CNTs. After the spraying process, prepreg remained in the fume cupboard for 20 minutes to evaporate the solvent. The total weight percentage of nanofillers amounted to 0.0016% while the ratio of the weight of GNPs to CNTs was 4:6.

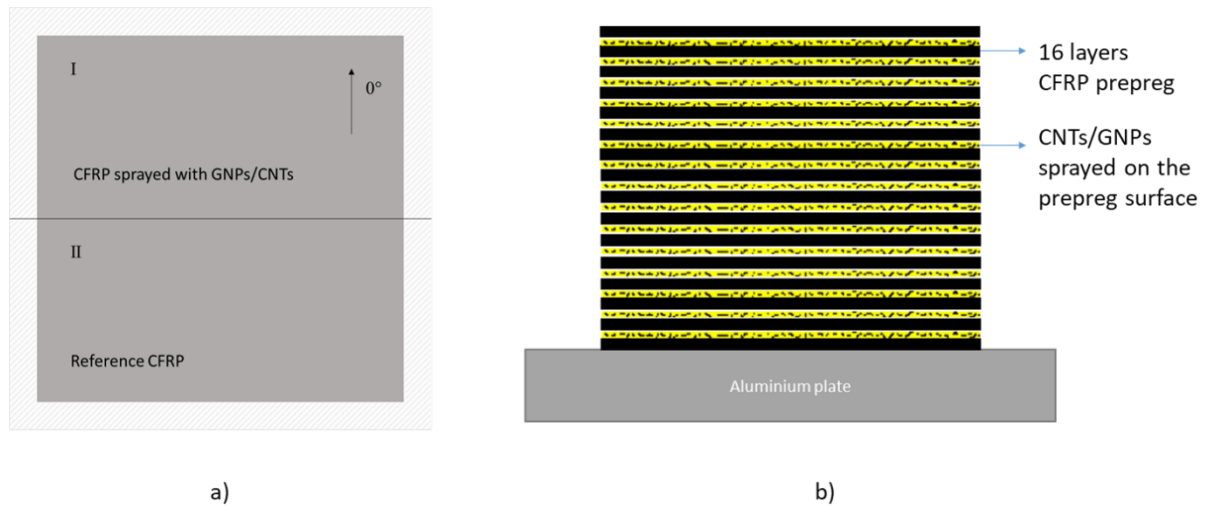


Figure 3-13 Schematic representation of (a) top view of unidirectional laminate manufactured for 3PB and SBT (part I sprayed with nanofillers, and part II control CFRP) (b) Cross-section view of laminate sprayed with nanofillers (part I)

3.3.2.5 Fracture toughness test specimens- manufacturing process

The desired thickness of the specimen for the Double Cantilever Beam (DCB) test is between 3 to 5 mm according to standards (ASTM D5528). Based on the cured ply thickness, it was determined that laminate composing of twenty-eight layers of the unidirectional prepreg is sufficient to achieve this thickness. Twenty-eight layers of dimensions 300 mm by 300 mm were stacked up along the sample fibre direction to create the unidirectional laminate. The laminate was divided into four parts. Each quadrant of the laminate differed from the concentration and type of nanofillers. Quadrant Ia was a reference CFRP; quadrant IIb was sprayed with the CNTs solutions; quadrant IIIc and IVd sprayed with two different wt% of GNP solution (see **Figure 3-14a**).

To prepare this CFRP laminate 14 layers of prepreg were laid-up according to the procedure presented in section 3.3.3. Artificial crack required for the DCB test was created by inserting a 12 μm thickness PTFE film between 14th and 15th ply. Two rectangular pieces of film of dimensions of 85 mm by 320 mm were placed on both ends of the laminate (as indicated in **Figure 3-14a**). White region in this schematic drawing represents the material reserved for sizing cut. The length of the initial crack after cutting samples was designed to be 73 mm.

Two types of solution were prepared for spraying treatment. GNP were mixed with ethanol and PVP at the concentration of 0.16 wt% of GNP. Whereas, CNTs/ethanol/PVP solution had a concentration of 0.25wt% of CNTs. The mid-plane of the laminate (14th layer)

was sprayed with nanofillers. The cross-section view of sprayed part of the laminate is shown in **Figure 3-14b**. Subsequently remaining 14 layers were stacked-up. The total wt % of nanofillers was based on the weight of laminate and sprayed nanofillers. Panels Ia, IIb, IIIc and IVd had a wt % of nanofillers 0, 0.00035, 0.00065, 0.00044% respectively.

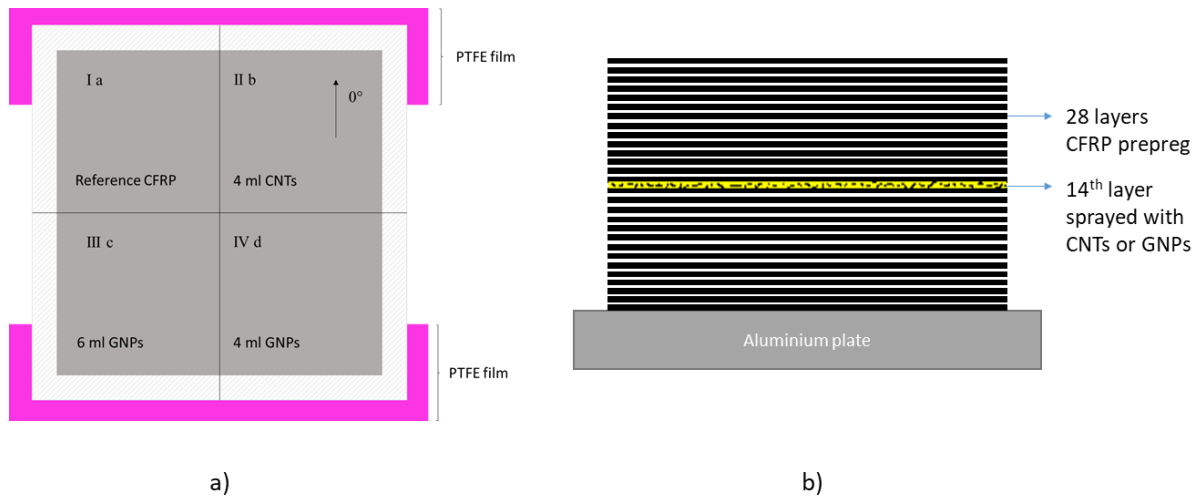


Figure 3-14 Schematic representation of (a) top view laminate manufactured for DCB test (part Ia –pure CFRP, part II b – 0.00035 wt% of CNTs, part III c- 0.00065 wt% of GNPs, part IV d - 0.00044 wt%) (b) Cross-section view of laminate sprayed with nanofillers.

3.3.2.6 Curing laminates

All laminates (3.3.2.4 and 3.3.2.5) were cured using the vacuum bagging process as shown **Figure 3-15**. A solid release film was placed on the top of the laminate ready to cure. The top side of the laminate was covered with the caul plate in order to obtain a better surface finish. The flash tape was applied to secure the caul plate from moving. The mould was wrapped with the breather material, put in a nylon bag and securely sealed.

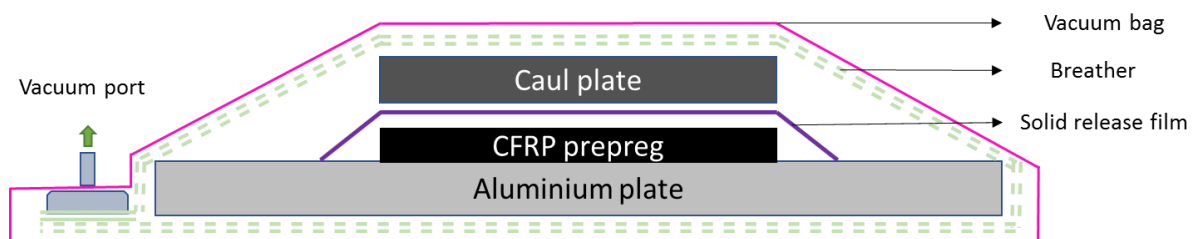


Figure 3-15 Schematic representation of the vacuum bagging process.

The vacuum of 1.0 bar was applied via vacuum line. It was continuously monitored by pressure gauge to make sure there is no leakage. Finally, the laminate was cured in the autoclave in SHD company (Sleaford, UK). The curing cycle is presented in **Figure 3-16** following the recommendation provided by the supplier. The room temperature was 20 °C, and the oven was heated up to 80°C with a 2°C/minute ramp rate. Autoclave pressure was kept at 5 bars during curing. Panels were cured at that temperature for 10 minutes, followed by 1-hour curing cycle at 120 °C and cooled down to room temperature for a further hour.

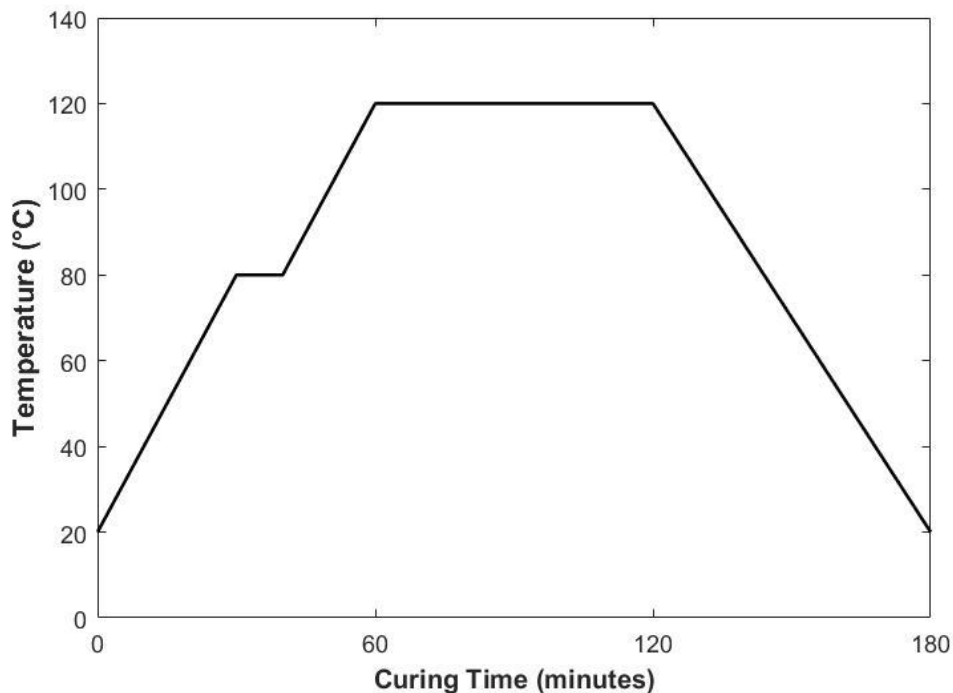


Figure 3-16 *Curing cycle of the MTC801 unidirectional laminate.*

3.3.2.7 Cutting Samples

Materials were cut in SHD company (Sleaford, UK) with COMPCUT 200 (Compact, Devon, UK) advanced composite plate saw with a diamond blade (see **Figure 3-17**). For the sixteen layers unidirectional laminate, samples were prepared for three-point bending and short beam test (section 3.3.2.4). The laminate had a thickness of 1.99 ± 0.06 mm. Twenty rectangular samples of the dimensions 100 mm in length and 15 mm in width were cut from the laminate; five samples from panels I and II in 0° and 90° for each configuration respectively and tested in the three-point bending experiment. Ten sample of the dimensions 20 mm in length and 10 mm in width were prepared from the panel I and II in 0° for short beam test configuration.



Figure 3-17 Illustration of the cutting process using COMPCUT 200.

Twenty-eight layers unidirectional laminate (section 3.3.2.5) had a thickness of 3.38 ± 0.04 mm. After trimming cut, five samples of dimensions 140 mm long, 25 mm wide and 73 mm initial crack length were obtained from each panel Ia and II b. Whereas from panel III c and IV d 10 samples had dimensions of 131.8 in length and 25 mm in width, and 65 mm initial crack length.

3.3.3 Spraying nanofillers solution on carbon fibre fabric – wet lay-up process

Section 3.3.2 has presented the introduction of spraying nanofillers to prepreg. A different way to introduce this nano-reinforcement is to apply nanofillers to fibre surface directly. This process is usually achieved by the dip coating method (Zhang *et al.*, 2012; L. Chen *et al.*, 2014; Qin *et al.*, 2015). As an alternative, spraying nanofillers on the carbon fibre fabric can be adapted. The novelty of this method is that we sprayed nanofillers solution prepared based on the solution used in dip coating processes. Two types of laminates: control CFRP and CFRP with GNPs epoxy solution sprayed on the fibre fabric were manufactured. Wet lay-up technique was used to impregnate the carbon fibre fabric. Mechanical tests such as three-point bending and short beam tests were conducted to investigate the effects of the spraying treatment.

3.3.3.1 Wet lay-up – reference CFRP

To achieve the required thickness of the laminate (2 mm) (ISO 14125, ISO 14130), ten layers of fabric are needed. 240 mm x 240 mm rectangles fabric were cut from the roll to prepare reference CFRP. Before laminating, the aluminium plate was coated with Easy Lease Chemical release agent (EasyComposites, Longton, UK). Epoxy resin and hardener measured with the ratio of 100:30 were mixed using a spatula for 2 minutes. The mixture was degassed using a vacuum chamber at 1 bar for 20 minutes in order to remove trapped air caused by the mixing process (**Figure 3-18a**).

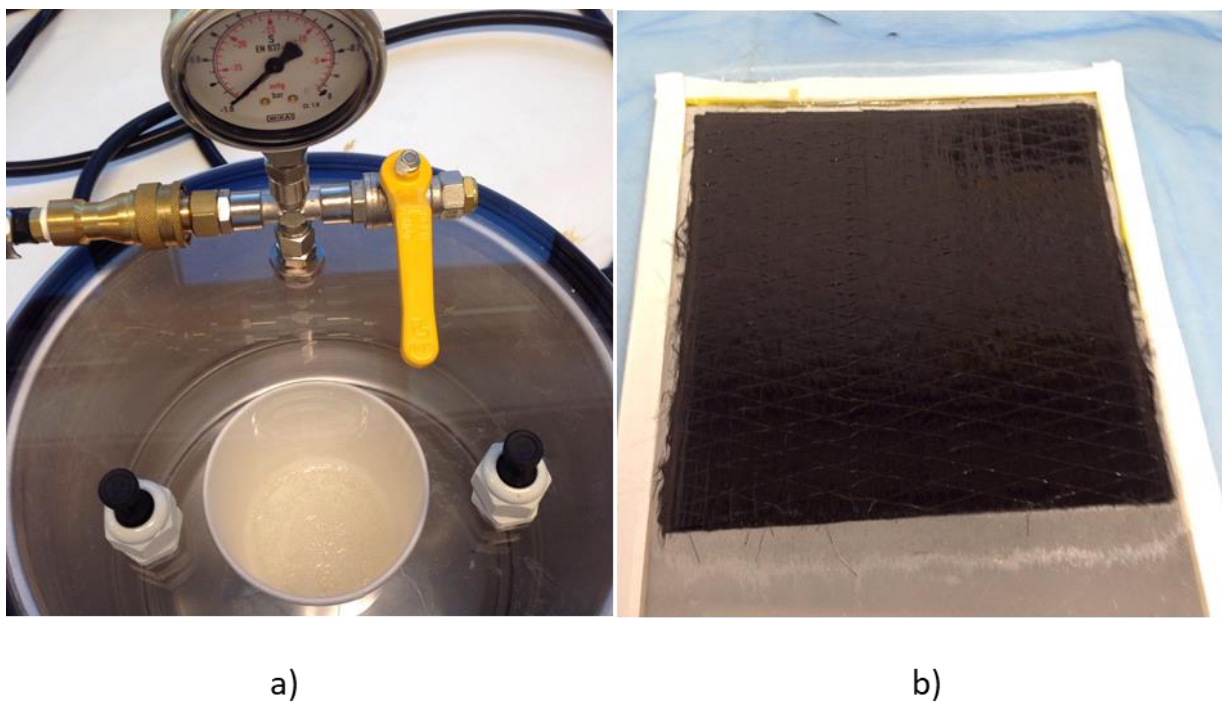


Figure 3-18 Wet lay-up process: (a) epoxy degassing using vacuum chamber at 1 bar for 20 minutes, (b) Impregnating unidirectional carbon fibre fabric with epoxy resin.

Upon the completion of the degassing, the aluminium plate was covered with a layer of resin using a brush then the first layer of fabric was placed on it. The pressure was applied by a roller to impregnate the fabric and remove the air. Then, more resin was brushed to cover the existing layer and the second ply was laid down along the same carbon fibre direction. Subsequently, each layer of fabric was impregnated using hand brush and roller (**Figure 3-18b**). On the 10th layer, peel ply was applied followed by perforated release film and fabric breather. Then, the laminate was sealed in the vacuum bag to remove excess of the resin and remove the trapped air.

3.3.3.2 *Spraying nanofillers solution*

The desired weight percentage of GNPs in this material was established to be 0.5 wt%. Before preparation of the solution, the weight of the fabric and resin was calculated. Considering that the laminate contained ten layers, each of them was squares of the size of 240 by 240 mm, the area of material needed was $0.576 m^2$. According to the datasheet, one square metre of this fabric weight is 250 grams; therefore, the applied layer in this process was 144 grams. The weight ratio of the fibre to resin selected for this material was 1:1. As a result, assumed that fabric impregnated with resin is expected to weight of 288 grams. To achieve 0.5 wt% of GNPs in the composite 1.45 gram of GNPs according to equation 3-19.

$$0.5 \text{ wt}\% = \frac{x}{(x+288)} \quad 3-19$$

The solution was prepared similarly to the procedure reported elsewhere (Qin *et al.*, 2015) where N-Methyl-2-pyrrolidone (NMP) was used as a solvent. Given a large amount of the solvent is required for the process, cheap and environmental alternative solvent is preferred. Here, GNPs were dissolved in a solution of ethanol and deionised water in volume ratio 7:3 (Liu *et al.*, 2012). 35 ml of ethanol was mixed with 15 ml of deionised water, then 0.5 grams of GNPs and 0.3 ml of PVP were added to the solution. The solution was mixed for 30 minutes using magnetic stirrer followed by the ultrasonic bath for 5 minutes. 0.1 gram of hardener and 0.7 gram of epoxy resin was later added to the mixture. The solution was further mixed for 30 minutes with magnetic stirring and 5 minutes using an ultrasonic bath. The prepared nanofillers solution was sprayed on both sides of each ply of fabric using airbrush as explained in section 3.3.2.3. Because a small amount of the hardener and epoxy were added, the solution viscosity was increasing with time which made spraying process difficult. To avoid this issue, we prepared the solution in 3 batches consequently. Each batch was adequate to spray 3 or 4 plies of fabric. In total 10 layers of fabric were sprayed (**Figure 3-19a**). The total weight of the sprayed graphene was approximately 1.5 grams. The fabric was placed in the oven for 3 hours at 60° to enhance the evaporation of the solvent (**Figure 3-19b**). After nanofillers sprayed fabric plies were dried and removed from the oven, they were wet laid-up to make unidirectional laminate using the same procedure as in 3.3.3.1. 148.0 or so grams of resin was used in total. The vacuum pressure of one bar was applied, and the excess resin was squeezed through peel ply.

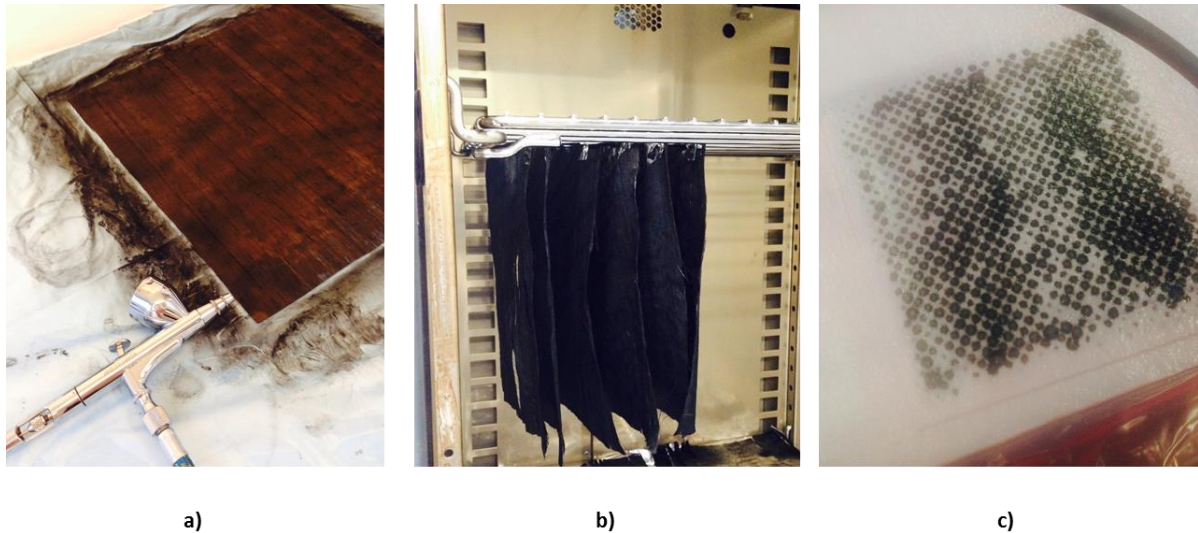


Figure 3-19 (a) *Spraying process of GNP/epoxy/ethanol solution using an airbrush,* (b) *Evaporating the solvent under 60° for 2 hours,* (c) *Curing sprayed laminate under vacuum.*

It is worth mentioning that the resin used in this project was transparent. Nevertheless, excessing resin on the breather cloth appeared black, which indicate some GNPs were carried away from fabric (**Figure 3-19c**). Therefore, the final wt% of GNPs was less than 0.5%. The calculated volume fraction based on the amount of the material used corresponded to 38% of carbon fibre.

3.3.3.3 *Curing and cutting process*

Both panels were cured using vacuum bagging technique under 1.0 bar pressure in the room temperature for 24 hours. The thickness of cured reference and sprayed panels were 2.51 ± 0.04 mm and 2.74 ± 0.03 mm respectively. The small increase in thickness of nano-reinforced laminate could be caused by more resin and the presence of GNPs. Laminates were cut using in-house Ryomi circular saw. Sides of the sample were polished with SiC abrasive paper grid 320. Ten three-point bending test samples of dimensions, 100 mm and 15 mm were cut from control and nano-reinforced laminates. They were either 0 or 90° fibres direction. Twelve short beam test samples of dimensions 21 mm by 15 mm were prepared.

3.3.4 **Sample inspection**

Manufacturing defects are unavoidable in FRPs such as fibre waviness, misalignment, improper fibre distribution, voids, matrix cracks, resin rich area, fibre/matrix de-bonding.

Voids are one of the most common imperfections, which are caused by the trapped air in the matrix. The void content can vary from around 1 % to up to several percents and depends on the manufacturing technique and process conditions like pressure, curing conditions, debulking process. Voids have a significant influence on the composite mechanical properties. Some qualitative measurements on voids like size, shape were conducted for these CFRP.

An optical microscope was used to check the existence of voids (**Figure 3-20**). A small section of the sample was encapsulated in Epo Mount 5F (mounting compound) using hot mounting press ATA Opal 410 (ATA GmbH, Germany). Samples were polished using ATA Saphir 520 (ATA GmbH, Germany) grinding/polishing machine following the recommended procedure (see *Appendix B*).

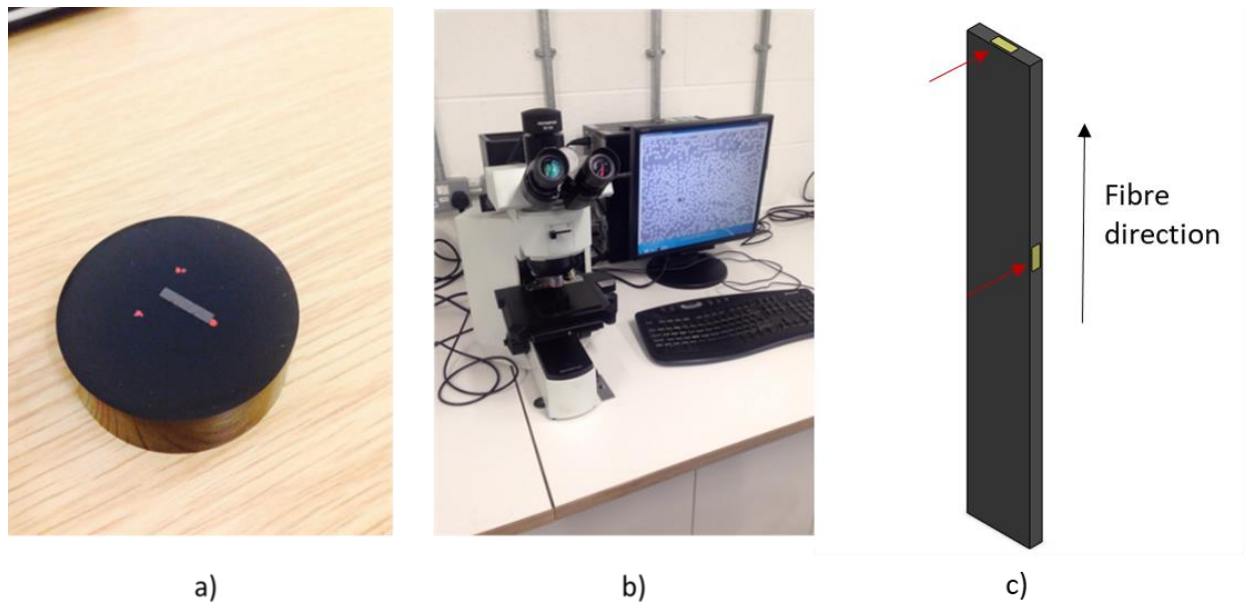


Figure 3-20 (a) Preparation of the polished specimen for the microscope study, (b) Images extract using optical microscope and data processing (c) Cutting microscope samples.

The primary grinding stage was accomplished with abrasive paper P320 for 5 minutes followed by additional grinding stages using Piano cloth H and 9 μm diamond solution for 5 minutes. The final polishing stage was completed with Multicloth and 0.06 μm Silco solution. Polished samples, as shown in **Figure 3-20a**, were inspected by the Olympus SC100 optical microscope (50 times magnification). Digital images were taken during the inspection and later post-processed by Olympus Stream software.

i. Hand lay-up of carbon fibre prepreg

Figure 3-21 presents the cross-sectional view of the 16 layers unidirectional CFRP laminate. Circular shapes represent the cross-section of carbon fibre, and darker colour shows the epoxy resin. Overall fibres were well distributed over the lamina region. There was some irregular distribution of the fibre and resin rich areas that is speculated to concentrate in interlayer region. Some voids were also found (see black colour in **Figure 3-21**).

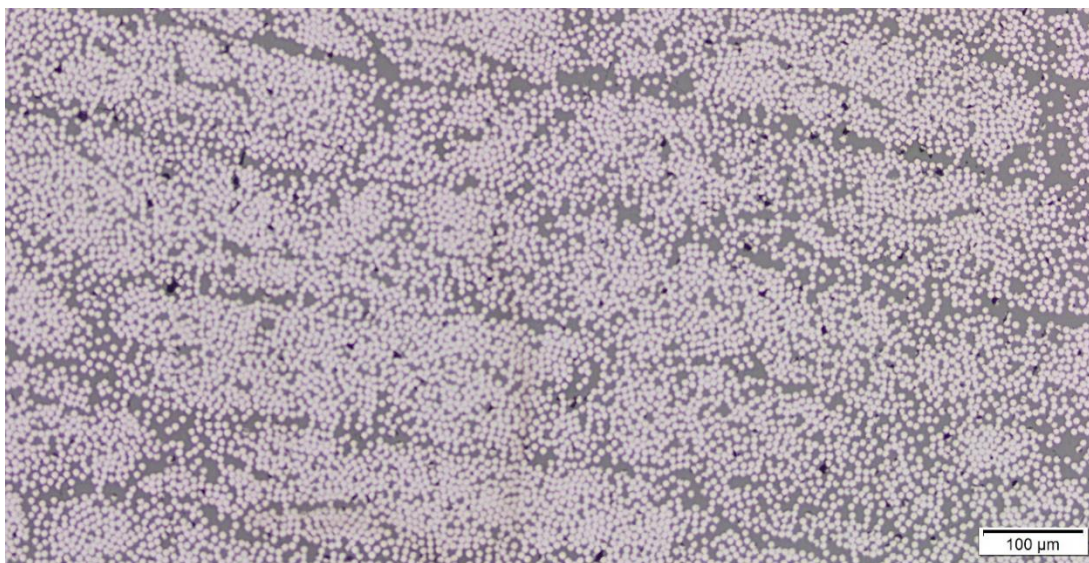


Figure 3-21 *Cross-sectional view of the unidirectional laminate CFRP with sprayed CNTs and GNPs.*

The microstructure was further inspected with higher magnification as presented in **Figure 3-22**. Some resin rich areas were found (as seen in **Figure 3-22a**) and represented regions where there were fewer fibres. Some voids were also noticed across the microstructure. At this magnification, voids showed different more reflective colour comparing to **Figure 3-21**. The presence of these voids may be caused by several factors: such as effects of sprayed solvent, the moisture of the resin and prepreg surface roughness. If the voids quantification is needed acid digestion or resin burn off methods could be used. In such high magnification view, the fibre distribution can be more precisely assessed. The somewhat irregular packaging of fibres was observed, but most common packaging arrays; hexagonal and square were also presented (**Figure 3-22b**). Fibre diameter was also measured to be $7.0 \mu\text{m}$, which is of the range given by material suppliers.

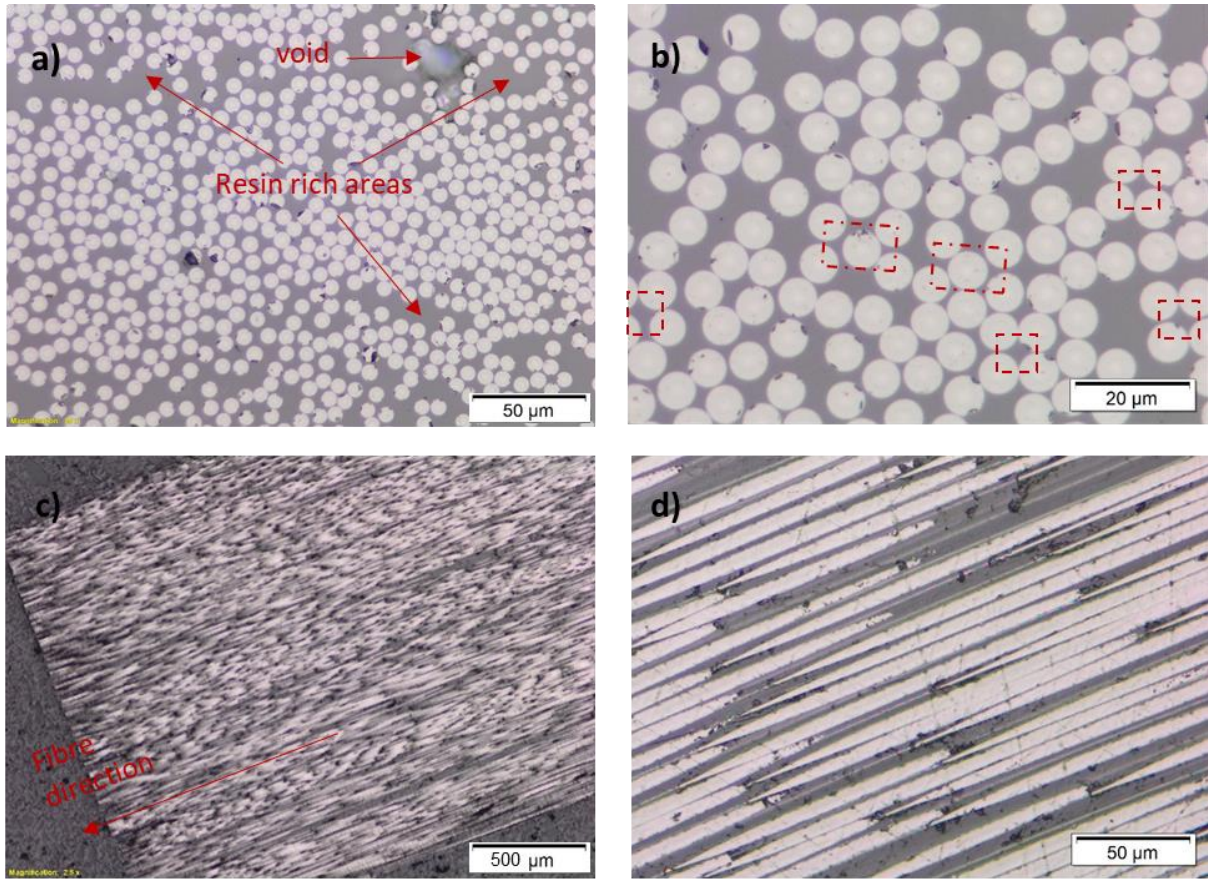


Figure 3-22 *Optical micrographs of unidirectional laminate (manufactured by prepreg hand lay-up method) (a) cross-section view of the sample in the direction parallel to fibres (b) carbon fibre distribution- examples of packaging arrays: hexagonal and square (c) and (d) side view of the specimen in direction perpendicular to fibres.*

The observation of the samples from the side view – in the direction parallel to fibre were also taken. **Figure 3-22c** and **3-22d** show typical micrographs where fibres are parallel to each other. Similar microscopic observation of the very similar carbon fibre unidirectional composite (T700SC /MCP 939) was presented by (Ma *et al.*, 2017).

ii. Wet lay-up

The samples prepared by the wet lay-up method were inspected similarly. Preparation of the encapsulated specimen was more challenging as was caused by the non-planar surface of the specimen produced by the in-house cutting machine. Obtained images were blurred, even the same polished procedure was followed. Regarding the microstructure, the cross-sectional

view (**Figure 3-23a**) shows some resin rich areas. The magnification of this image allows for identification of the fibre distribution. The typical periodic packaging of fibres like square and hexagonal exist (**Figure 3-23b**). The diameter of fibre was also measured as averaged of $7.0\ \mu\text{m}$ over several places. Unlike prepreg there is no clear boundary between interplay; this may be caused by the method of preparation of these samples (**Figure 3-23c and d**).

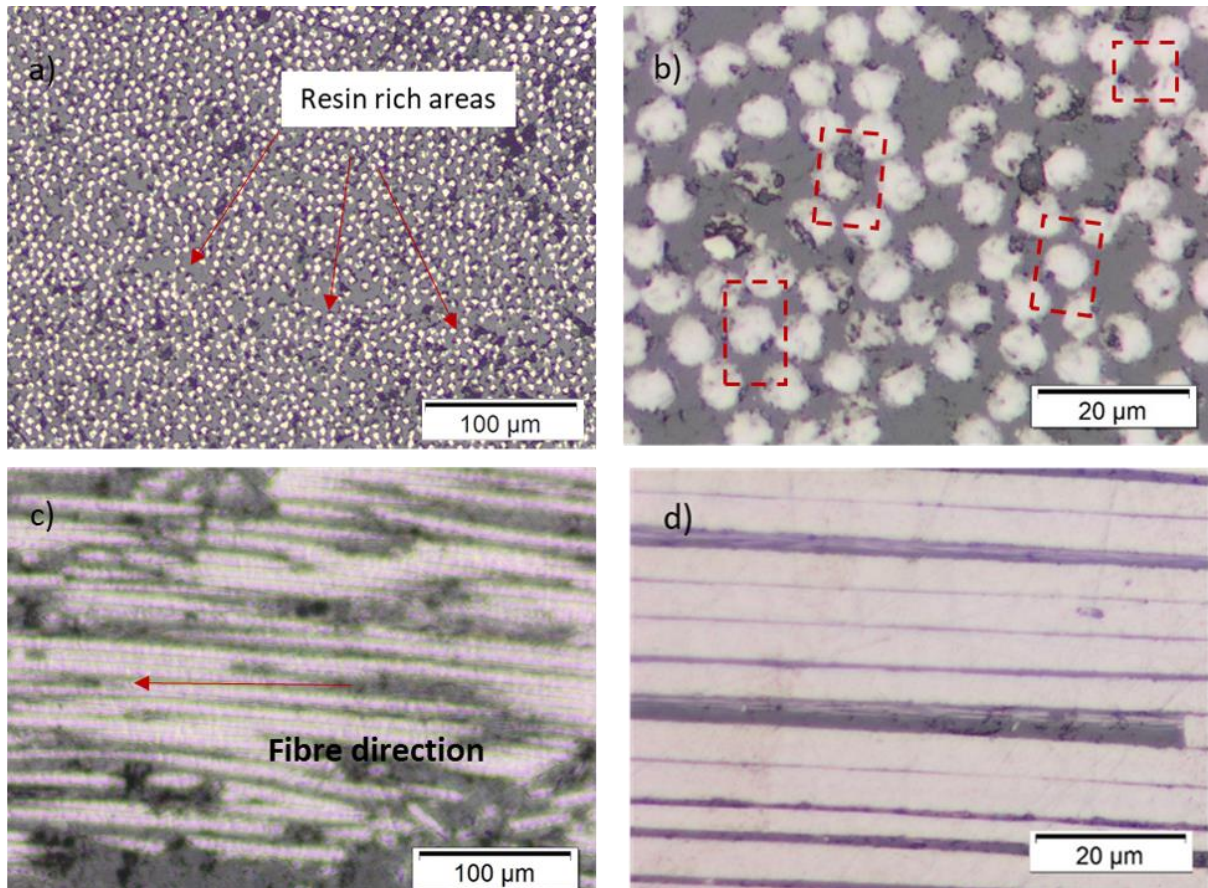


Figure 3-23 Optical microscope images of unidirectional laminate (manufacture by wet lay-up) (a) cross sample view of the specimen in the direction parallel to the fibre (b) carbon fibre distribution- examples of packaging arrays: hexagonal and square (c) side view of the side of the specimen in direction perpendicular to fibres, (d) side view of the side of the specimen in direction perpendicular to fibres.

iii. Scanning Electron Microscopy

The Scanning Electron Microscopy (SEM) was used to investigate effects of nanofillers on fracture mechanism. SEM uses a focused beam of high-energy electrons to produce a magnified image of specimen. The main SEM components are source of electrons, electron lenses, sample chamber with stage, detector for all signals of interest, display device to view

the images. Accelerated electrons in the SEM carry large amounts of kinetic energy, which is dissipated as variety of signals produced by electron-sample interactions. When electrons interact with the sample, secondary electrons, backscattered electrons and X-rays characteristics are produced. These signals are collected by detectors to form images.

iv. Dynamic Mechanical Analysis

Dynamic Mechanical Analysis (DMA) was used to investigate the glass transition temperature of manufactured laminates. The samples was clamped in measurement head using single cantilever beam set-up. DMA applies a small sinusoidal deformation to a sample of known geometry. A force motor is used to generate a sinusoidal wave, which is transmitted to the sample. Sample can be subjected to the range of the temperature. Stiffness and damping of the sample are reported as modulus and tan delta. As the force is applied in cyclic manner, in-phase component (storage modulus) and out of phase (loss modulus) are measured. The ratio of the loss to the storage moduli is represented by tan delta peak and it is related to the glass transition temperature of material.

3.4 Inverse analysis

3.4.1 ANSYS DesignXplorer

The inverse analysis was used to determine some unknown material properties. Interphase properties are particularly difficult to measure due to its small dimension. The interphase's thickness was never accurately measured not mentioning its properties. In this analysis, three parameters namely: interphase modulus, Poisson's ratio and thickness are of interest. Because the interphase between the fibre and matrix is not present in the macroscale model, the developed optimisation process was divided into two scale using macro and microscale simulations.

This study was executed with ANSYS Design Explorer module. This application is integrated with ANSYS Workbench and allows parametric analyses to explore, understand and optimise the design conveniently. ANSYS Design Xplorer includes components such as parameters correlations, direct optimisation, and response surface creation. The optimisation process starts from parameters correlations component, which provides an insight into how outputs parameters are related to inputs parameters. This analysis enables users to filter out less

sensitive parameters and focus on most relevant design inputs. Afterwards, the goal-driven optimisation is performed considering various approaches for multi-objective optimisation, for example, Screening, Multi-Objective Genetic Algorithm (MOGA) or Adaptive Multi-objective Optimisation Algorithm (AMO). The Screening approach is a non-iterative direct sampling method through a quasi-random number generator based on the Hammersley algorithm. The MOGA approach is a hybrid variant of the popular Non-dominated Sorted Genetic Algorithm (NSGA-II) based on controlled elitism concepts. Whereas, AMO is an approach that combines a Kriging response surface and the MOGA optimisation algorithm. Screening is usually used for preliminary design followed by MOGA or AMO to refine optimisation results. Results are provided in the form of charts and tables, which enable to evaluate trade-offs and select the best candidates.

3.4.2 Inverse analysis methodology to determine interphase properties

The inverse analysis combined numerical simulations of the model described in section 3.2.3 and three-point bending experimental data (Qin *et al.*, 2015). Three types of carbon fibre reinforced polymer 1) non-coated CFRP, 2) epoxy-coated CFRP and 3) GNPs coated CFRP were investigated. The procedure of the two-scale optimisation process is discussed below.

3.4.2.1 Macroscale optimisation

Macroscale simulations aimed to optimise lamina properties so that numerical simulations results matched the experimental one. Forward simulations of the model were performed in the Static Structural module of ANSYS Workbench 17.2 software following the procedure provided in chapter 3.2.3. Initial input lamina elastic constants were selected based on the properties predicted by RVE micromodelling simulations and input to the Engineering Database. All input lamina properties were parametrised. The displacement of the beam generated by bending force was chosen as an output parameter in numerical simulations. Experimental displacement was calculated based on the flexural modulus. The objective of this macroscale optimisation was to find the new input parameters, so the output deformation matched sought target (see **Figure 3-24**). The sought target was the displacement determined from experimental flexural modulus. Note that simulation negative displacement value is due to the assigned coordinate system (**Figure 3-9**).

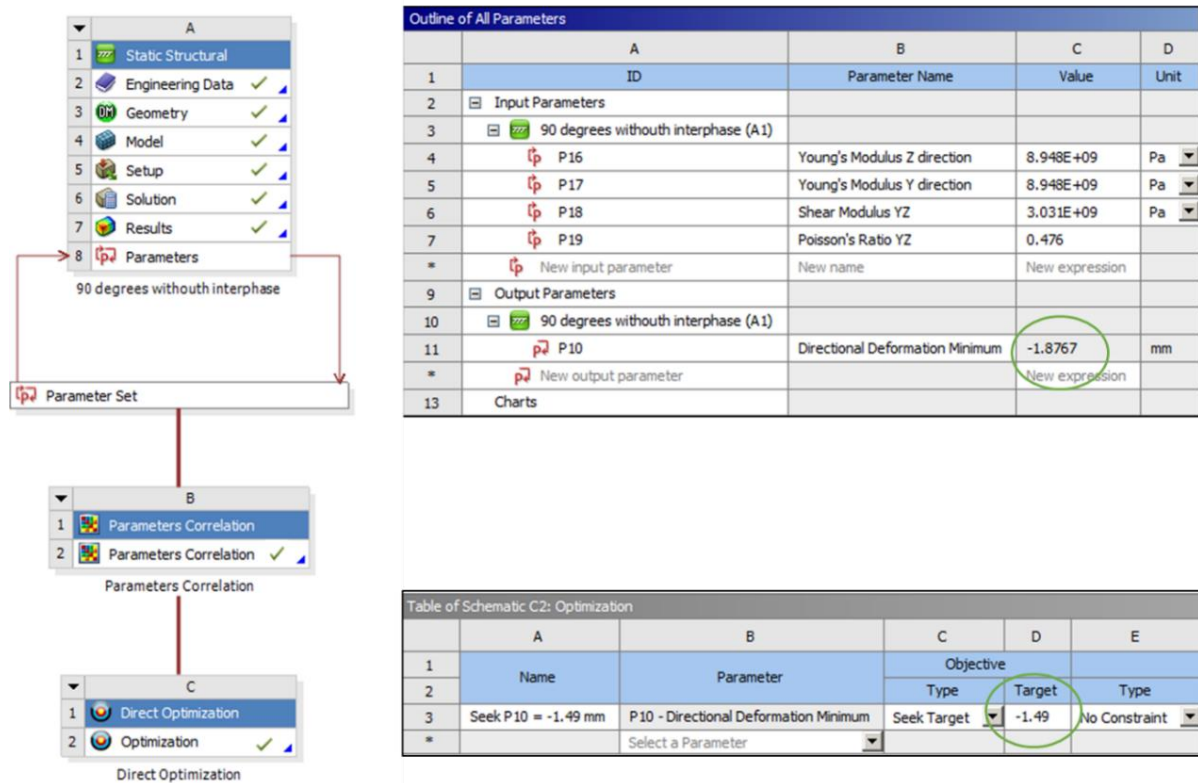


Figure 3-24 Schematic of the macroscale optimisation process performed in ANSYS Design Explorer. Image used courtesy of ANSYS, Inc.

Direct optimisation component in ANSYS Workbench was selected together with the Adaptive Multiple-Objective optimisation algorithm (see **Figure 3-25**). This algorithm supports multiple objectives and constraints to find the global optimum. Optimisation process ended when the solution converged, and candidate points meet the required objectives and constraints. In this case when calculated displacement matches the experimental one.

3.4.2.2 Microscale optimisation

In this microscale optimisation a methodology, which combines three-phase RVE modelling simulations and experimental lamina properties (predicted from macroscale optimisation) is proposed. Interphase is described by modulus (E_i), Poisson's ratio (ν_i) and thickness of the interphase (t_i). Each FEA analysis was controlled by ADPL scripts, which called for the evaluation of the elastic constant of the lamina. The input parameters E_i , ν_i , t_i were defined in APDL script as input parameters as seen in **Figure 3-26**. Note that the thickness of the interphase is represented as a difference of interphase (r_i) and fibre (r_f) radii.

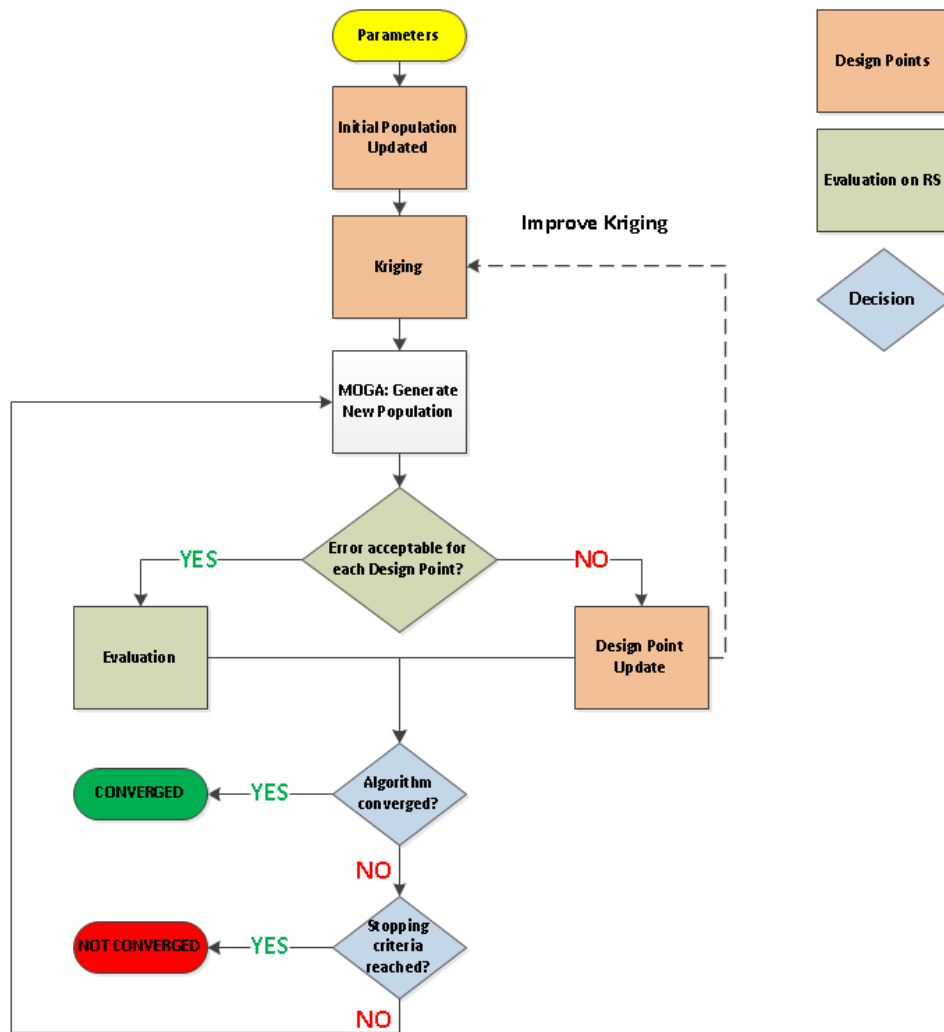


Figure 3-25 Framework of Adoptive Multi-Objective Optimisation Algorithm (ANSYS, 2018). Image used courtesy of ANSYS, Inc.

```

/TITLE, Full Model of RVE, hexagonal array

rf=3.55      ! Radius fiber in microns
a2=4.224    ! x2 length in microns
a3=7.307    ! x3 length in microns
a1=1.0561   ! x1 length in microns
Ei=3.45e-3  ! Interphase elastic modulus in TPa
vi=0.34     ! Poisson's ratio
ri=3.58     ! Interphase thickness in microns t=ri-rf
  
```

Figure 3-26 Initial input parameters defined in ANSYS APDL

These interphase input parameters were then recalled in the material properties and RVE modelling sections as shown in **Figure 3-27**. Remaining material parameters such as fibre diameter, RVE dimensions, carbon fibre and matrix material properties were fixed. In the next step, APDL file was loaded to the Mechanical Component in ANSYS Workbench, and input and output parameters were selected (**Figure 3-28**). Input parameters were represented by E_i, ν_i, r_i , whereas output parameters were transversely elastic constants of lamina ($E_1, E_2, \nu_{12}, \nu_{23}, G_{12}$). Microscale optimisation were used here to minimize the error between numerical and experimental data by adjusting interphase properties. The objective of this optimisation was that output parameters seek the lamina properties values predicted from macroscale simulations. In such way by combining this two-step optimisation process, the final values of the interphase input parameters represent the interphase properties of this material system, which are often impossible to measure experimentally.

```

/PREP7                ! Pre-processor module
MP,EX,1,17.2e-3
MP,EY,1,17.2E-3
MP,EZ,1,224E-3
MP,NUXY,1,0.5
MP,NUYZ,1,0.2
MP,NUXZ,1,0.2
MP,GXY,1,5.73E-3
MP,GYZ,1,27.6E-3
MP,GXZ,1,27.6E-3
MP,EX,2,3.45E-3
MP,PRXY,2,0.34
MP,EX,3,E1
MP,PRXY,3,vi
ET,1,SOLID186        ! Choose SOLID186 element type

BLOCK,-A2,A2,-A3,A3,-A1,A1,
CYLIND,r,f,,-A1,A1, 0, 90,
CYLIND,r,f,,-A1,A1, 90,180,
CYLIND,r,f,,-A1,A1,180,270,
CYLIND,r,f,,-A1,A1,270,360,
CYLIND,r,f,,-A1,A1, 0, 90,
CYLIND,r,f,,-A1,A1, 90,180,
CYLIND,r,f,,-A1,A1,180,270,
CYLIND,r,f,,-A1,A1,270,360,
VGEN,1,6,,, -A2,-A3,,,,1
VGEN,1,7,,, A2,-A3,,,,1
VGEN,1,8,,, A2, A3,,,,1
VGEN,1,9,,, -A2, A3,,,,1
CYLIND,ri,,-A1,A1, 0, 90,
CYLIND,ri,,-A1,A1, 90,180,
CYLIND,ri,,-A1,A1,180,270,
CYLIND,ri,,-A1,A1,270,360,
CYLIND,ri,,-A1,A1, 0, 90,
CYLIND,ri,,-A1,A1, 90,180,
CYLIND,ri,,-A1,A1,180,270,
CYLIND,ri,,-A1,A1,270,360,
VGEN,1,14,,, -A2,-A3,,,,1
VGEN,1,15,,, A2,-A3,,,,1
VGEN,1,16,,, A2, A3,,,,1
VGEN,1,17,,, -A2, A3,,,,1
ALLSEL,ALL
VOVLAP,all          ! Overlap volumes|
NUMCMP,all          ! Renumbering all volumes, volume 9 is the matrix
/DEVICE,VECTOR,1
/VIEW,1,1,2,3
/ANG,1
/PNUM,VOLU,1
/PNUM,MAT,1
/REPLOT

```

Figure 3-27 Parameterisation of interphase properties in the RVE modelling – excerpt of APDL script.

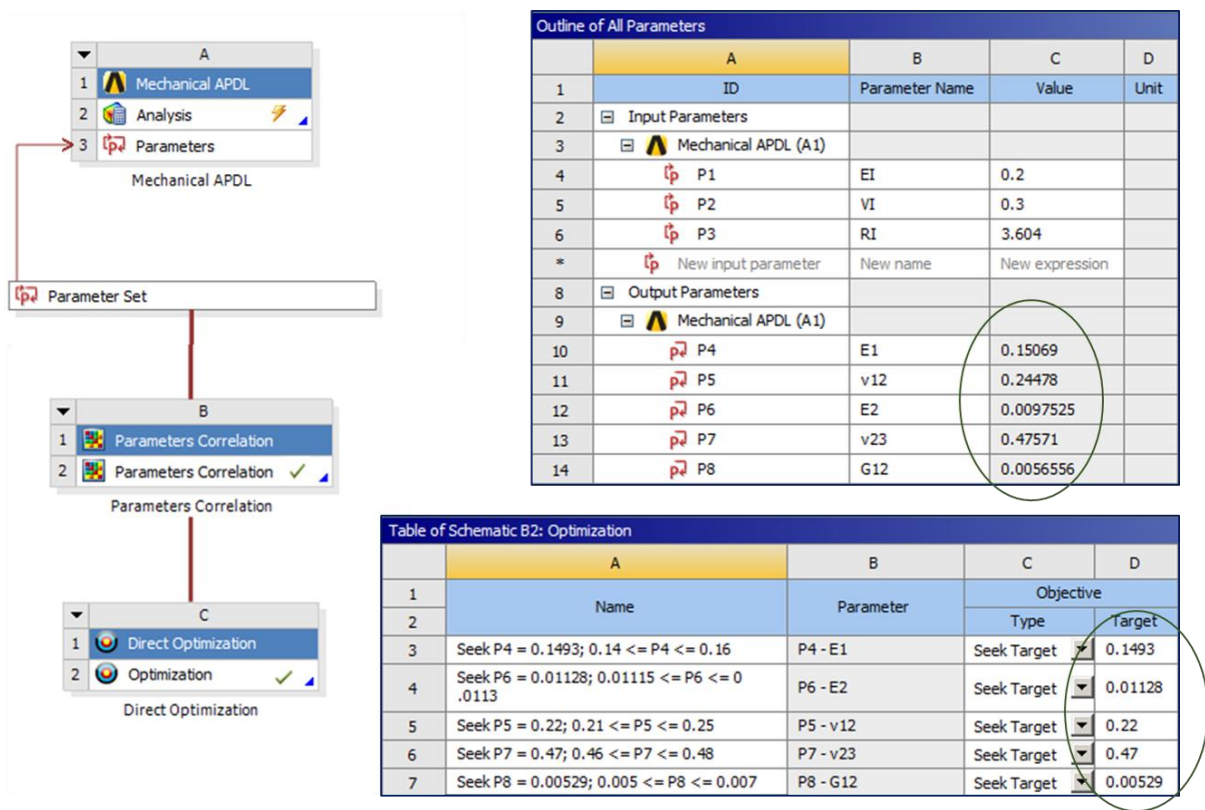


Figure 3-28 Structure of the microscale optimisation process performed in ANSYS Design Xplorer. Image used courtesy of ANSYS, Inc.

3.5 Summary

This chapter has presented the outline of numerical and experimental research methods to investigate the effects of the GNPs on mechanical properties of CFRP.

The first section has described in details multiscale framework to study CFRPs with the GNPs reinforced interphase. This method has included investigation of the material at various scale: nanoscale, microscale, and macroscale. At the nanoscale, the approach to estimate the properties of the GNPs reinforced interphase using Mori-Tanaka method has been proposed. Two types of GNPs orientations were considered. At the microscale, three-phase RVE element to predict lamina properties has been presented. The final macroscale has shown modelling methodology of the 12 layers unidirectional laminate simulated in the three-point bending test.

The second part of this chapter has dealt with materials and experimental methods. Spraying technique has been explored to introduce nanofillers into CFRPs. Preparation of

nanofillers solutions and types of manufacturing methods including hand lay-up and wet lay-up have been discussed. The details on curing and cutting samples as well as inspection using an optical microscope can be found there.

Finally, the two-scale optimisation methods using ANSYS Design Explorer have been explained. This optimisation process has included numerical simulations at macro and microscale to indirectly determined interphase properties and thickness. Details on the design of experiments including a selection of input, output parameters, objectives and constraints and optimisation details have been given here.

4 Influence of Graphene nanoplatelets reinforced interphase on the CFRPs elastic constants

4.1 Introduction

The fibre-matrix interphase heavily influences the mechanical properties of carbon fibre reinforced polymer (CFRPs) (Kim and Mai, 1998). Nanofillers show a potential to improve the strength of the interphase. Graphene and its derivatives have been applied to the fibre surface by dip coating (Knoll *et al.*, 2014; Ashori, Rahmani and Bahrami, 2015; Qin *et al.*, 2015), electrophoretic deposition (Deng *et al.*, 2015; Wang *et al.*, 2016; Mahmood *et al.*, 2018) or chemical grafting (R. L. Zhang *et al.*, 2016). These methods make the interphase layer distinctive from matrix and fibre regarding its mechanical properties (Dai and Mishnaevsky, 2014b). Interphase is directly affected by the method of production, which causes the variation of dispersion, orientation and volume fraction of graphene within the interphase (Atif and Inam, 2016). For example, dip coating of fibres in graphene-epoxy solution tends to create a random orientation of graphene in the interphase, whereas electrophoretic deposition or chemical grafting will make graphene more aligned along the fibre surface. This graphene reinforced interphase has been speculated to improve adhesion between matrix and fibres and consequently to enhance mechanical properties. In this study, author investigates how volume fraction and orientation of GNPs in the interphase influence on the extent of improvement of mechanical properties of CFRP using multiscale modelling framework.

Because interphase's properties are difficult to measure directly through experiment, many researchers used numerical simulations as an alternative to predict the properties of this interphase (Ruchevskis S., 2002; Kari *et al.*, 2008; Wang *et al.*, 2011; Y Liu *et al.*, 2012). Finite element analysis (FEA) enable to study different combinations of parameters and their effects on material behaviour resulting in a less expensive design cycle. In the case of the graphene-reinforced composite, numerical studies were reported on the nanocomposites (Shokrieh *et al.*, 2014), where graphene directly reinforced polymer. A few articles on the numerical simulations of 2-D particles in FRPs were published. For example, GNPs were directly introduced to the resin matrix then carbon fibre reinforced hybrid composites was formed (Hadden *et al.*, 2015; Aluko, Gowtham and Odegard, 2017). Both longitudinal and transverse moduli of CFRPs were significantly enhanced with the increase of GNPs volume fraction. Dai

and Mishnaevsky (2014a) analysed fatigue damage of fibre reinforced polymer reinforced with nanoclay particles. Nanoclay were introduced to modify either matrix or fibre/matrix interphase. The highest improvement in fatigue life was observed when thoroughly exfoliated nanoclay was located in the interphase between fibre and matrix. Sabuncuoglu et al. (2018a) studied steel fibre composite with nano-reinforced interphase was simulated under transverse loading to report the stress concentration. The primary challenge of the FEA of the FRPs reinforced with graphene is the necessity to simulate behaviour at the multiple scales. The difference in dimensions of nanoscale graphene, microscale fibre, and macroscale lamina increases the complexity of the analysis drastically.

This chapter aims to develop the multiscale framework to investigate the influence of the GNPs coated on fibre surface on mechanical properties of CFRP. Firstly, the properties of the GNPs reinforced interphase were predicted using the Mori-Tanaka method. Various volume fraction and different orientation of GNPs within the interphase were examined. Secondly, the predicted properties of the GNPs interphase are input to the RVE model to predict the properties of the unidirectional lamina. Finally, a macroscale model of three-point bending test is attempted.

4.2 Properties of GNPs reinforced interphase

4.2.1 Properties of the GNPs and Matrix

Single GNP is flake shape and behaves transversely isotropic. Local coordinates system was used to annotate material properties with the 1'-2' plane of isotropy and axis 3' being the thickness direction of GNPs (see **Table 4-2**). Mechanical properties of GNPs are difficult to quantify accurately. There exists a wide range of variations in properties of GNPs and graphene sheets in the literature (Cho, Chen and Daniel, 2007; Lee, Wei, Jeffrey W Kysar, *et al.*, 2008; Dai and Mishnaevsky, 2014a, 2014b; Giannopoulos and Kallivokas, 2014; Shokrieh *et al.*, 2014; Hadden *et al.*, 2015; Pontefisso and Mishnaevsky, 2016; Sabuncuoglu, Gorbatiikh and Lomov, 2018). In-plane properties of graphene are usually measured by nanoindentation with the aid of Atomistic Force Microscopy. Graphene in-plane elastic modulus ranges from 300 GPa (Nicholl *et al.*, 2015) to 1.0 TPa (Lee, Wei, Jeffrey W Kysar, *et al.*, 2008). However, determination of graphene properties in the thickness direction remains a big challenge. Out-of-plane graphene properties are not provided by material suppliers (*STREM Graphene Nanoplatelet*). To evaluate transversely isotropic properties of graphene, researchers employed

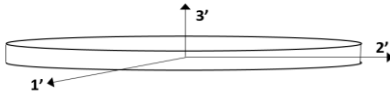
nano-scale simulations like molecular dynamics or atomistic modelling as summarised in **Table 4-1**.

Table 4-1 Exemplar graphene properties taken from the literature.

| Reference | Method | $E_{1'}^r$ (GPa) | $E_{2'}^r$ (GPa) | $E_{3'}^r$ (GPa) | $G_{12'}^r$ (GPa) | $G_{13'}^r$ (GPa) | $G_{23'}^r$ (GPa) | $\nu_{12'}^r$ | $\nu_{13'}^r$ | $\nu_{23'}^r$ |
|-------------------------------------|--|---------------------|---------------------|---------------------|----------------------|----------------------|----------------------|---------------|---------------|---------------|
| (Shokrieh <i>et al.</i> , 2014) | MD | 770 | 610 | 400 | n/a | 78 | n/a | 0.03 | 0.81 | n/a |
| (Spanos <i>et al.</i> , 2015) | Spring-based FEA | 730 | 709 | 58.5 | 436 | 3.32 | 3.45 | n/a | n/a | n/a |
| (Cho <i>et al.</i> , 2007) | MD | 1153 | 1153 | 39.51 | 482 | 0.268 | 0.268 | 0.195 | 0.006 | 0.006 |
| (Giannopoulos <i>et al.</i> , 2014) | Atomistic, continuum formulation | 722 | 738 | n/a | 444 | n/a | n/a | 0.463 | n/a | n/a |

Unlike many previous micromechanical models assuming graphene isotropic (Dai and Mishnaevsky, 2014a; Pontefisso and Mishnaevsky, 2016), this study takes the transversely isotropic features of the graphene into account to more realistically represent the effects of the GNPs reinforced interphase. The properties of GNPs used in this study were adopted from (Shokrieh *et al.*, 2014) shown in **Table 4-2**. The properties of isotropic epoxy resin 828 were taken from literature (Zhiye Li *et al.*, 2016) (see **Table 4-3**).

Table 4-2 Properties of graphene nanoplatelet in the local coordinate system ($1'-2'-3'$)
(Shokrieh *et al.*, 2014)

| Graphene nanoplatelet | | |
|--|-------|------|
|  | | |
| In- Plane modulus, $E_{1'}^r$ | (TPa) | 0.77 |
| Out-of-plane modulus, $E_{3'}^r$ | (TPa) | 0.40 |
| Out-of-plane shear modulus, $G_{1'3'}^r$ | (GPa) | 78 |
| In-plane Poisson's ratio, $\nu_{1'2'}^r$ | | 0.03 |
| Out-of-plane Poisson's ratio, $\nu_{1'3'}^r$ | | 0.81 |

Within this interphase, the volume fraction of GNPs varies from 0 to 60% in the parametric study. It is incredibly challenging if not impossible to measure the local volume

fraction of nanofillers at the interphase experimentally. A range of local volume fractions of CNTs from 0 to 80 % was used by another numerical parametric study (Chatzigeorgiou, Seidel and Lagoudas, 2012). The highest volume fraction of GNPs is assumed at 60% in present studies, interaction among GNPs was not considered at this stage.

4.2.2 Results

The elastic constants of the interphase were calculated according to the Mori-Tanaka method. Two types of GNPs orientation as shown in **Figure 4-1** were considered: randomly orientated and aligned GNPs. According to the Mori-Tanaka formulation, the randomly distributed inclusion in the infinitive matrix can be treated as homogeneous, isotropic material. Therefore, the GNPs randomly oriented in the interphase (**Figure 4-1a**) are described by any combination of two parameters such as Young's modulus (E^I) and Poisson's ratio (ν^I), where superscript 'I' represents interphase. On the other hand, when GNPs are aligned parallel to the fibre surface (**Figure 4-1b**), the GNPs reinforced interphase is transversely isotropic and expressed by: $E_1^I, E_3^I, G_{13}^I, G_{12}^I$. As a result, GNPs uniformly wrap up each carbon fibre. Based on the volume fraction and material properties of GNPs and epoxy, the interphase properties were determined following the equations 3-1 to 3-8.

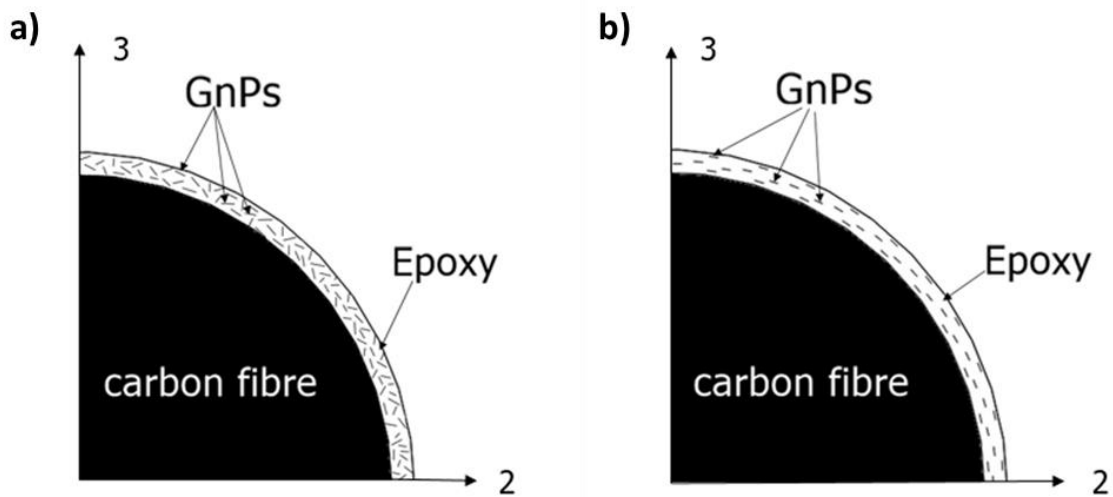


Figure 4-1 The cross-section views of the carbon fibre coated with GNPs following 1-2-3 global coordinate system (a) randomly orientated (b) aligned.

i. Randomly orientated GNPs in the reinforced interphase

Figure 4-2 presents the relationship between the interphase's Young's modulus against the volume fraction of GNPs within the interphase. When the volume fraction of GNPs is nil,

the interphase's Young's modulus is equal to that of the pure resin matrix, i.e. 3.45 GPa. In the presence of randomly distributed GNPs, Young's modulus of the interphase increases monotonically with the volume fraction of GNPs. For the maximum GNPs volume fraction, 60%, Young's modulus of the interphase is 370.5 GPa

When the volume fraction of GNPs is nil, the Poisson's ratio equals 0.34. Up to 9% GNPs volume fraction in the reinforced interphase, the Poisson's ratio decreases to 0.19 (Figure 4-3). Then increases monotonically with the volume fraction. For the highest volume fraction 60% of GNPs being studied, the interphase the Poisson's ratio is 0.42.

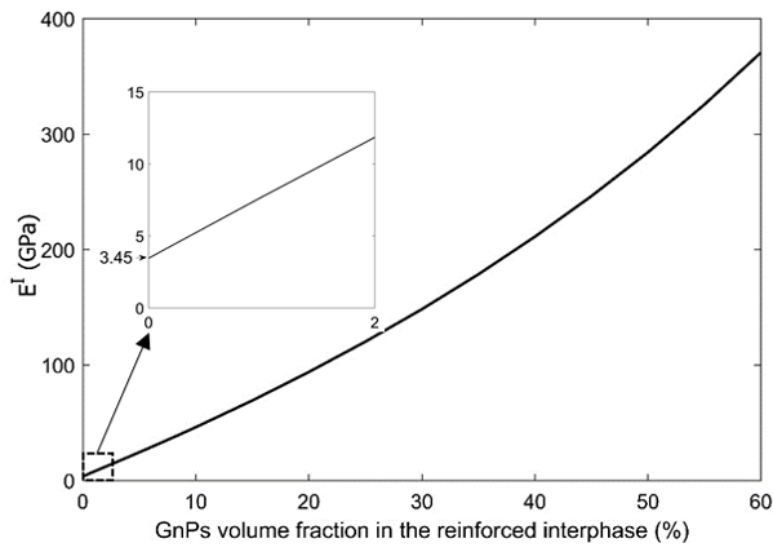


Figure 4-2 Elastic Modulus of the reinforced interphase with randomly orientated GNPs as a function of the volume fraction of GNPs in the interphase.

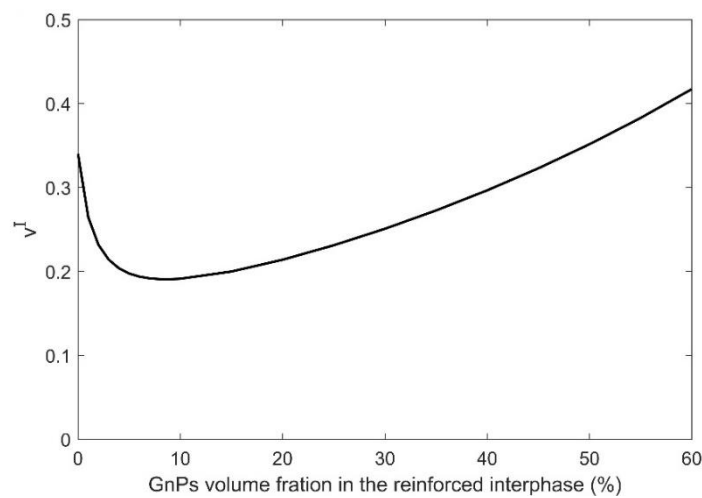


Figure 4-3 Poisson's ratio of the reinforced interphase with randomly orientated GNPs as a function of the volume fraction of GNPs in the interphase.

ii. Aligned GNPs in the reinforced interphase

When GNPs are perfectly aligned in the interphase parallel to the fibre direction, the interphase is transversely isotropic. The in-plane elastic modulus of the interphase increases quasi-linearly with the volume fraction of GNPs. For 0% GNPs volume fraction, the modulus equals 3.4 GPa and corresponding to the pure matrix. For the maximum concentration of GNPs, the in-plane elastic modulus amounts to 463.12 GPa. Comparing two orientations of GNPs reinforced interphase, the increase of this modulus is continuously higher than the interphase with GNPs random distribution. The ratio of in-plane Young's modulus between aligned interphase to randomly orientated interphase varies from 1.75 to 1.25 in the range of volume fraction (10 - 60%) of GNPs being tested.

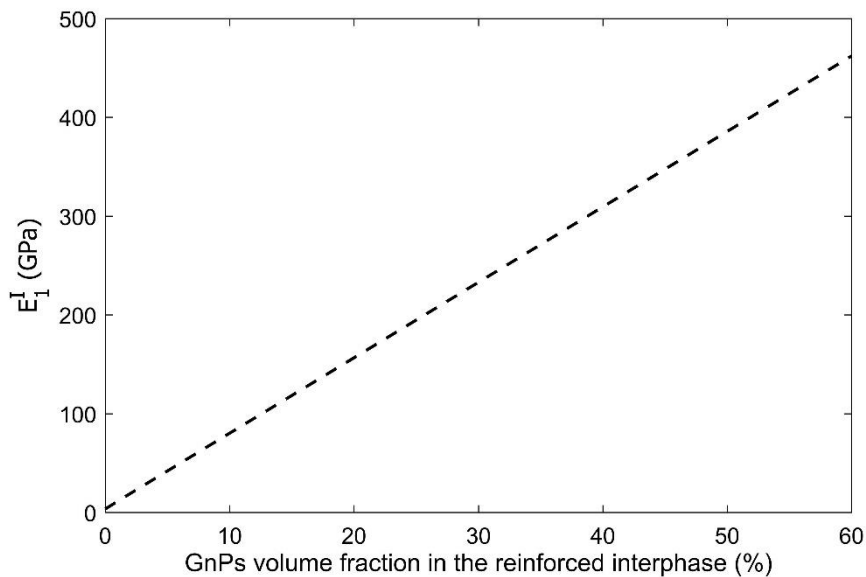


Figure 4-4 *In-plane elastic modulus of the reinforced interphase with aligned GNPs as a function of the volume fraction of GNPs in the interphase.*

The in-plane shear modulus (**Figure 4-5**) of this interphase exhibits nearly linear increase with the GNPs volume fraction. When GNPs volume fraction is nil, the in-plane shear modulus of the interphase is 1.28 GPa. Reaching the maximum concertation of GNPs, this modulus increases up to 224 GPa.

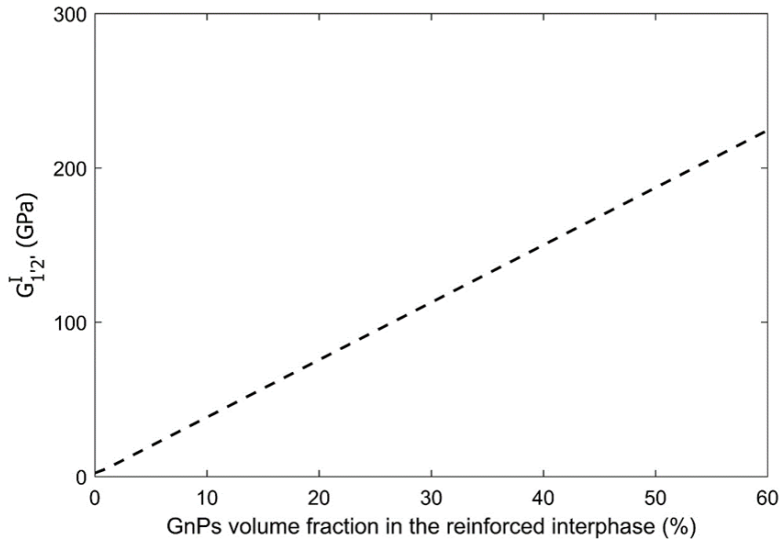


Figure 4-5 *In-plane shear modulus of the reinforced interphase with aligned GNPs as a function of the volume fraction of GNPs in the interphase.*

The out-of-plane elastic modulus of the interphase exhibits a sigma-like increase with the volume fraction of GNPs as shown in **Figure 4-6**. This modulus increases from 3.45 GPa for pure matrix up to 12.7 GPa for the 60% volume fraction of GNPs. Out-of-plane elastic modulus can be correlated with the modulus of the interphase reinforced with randomly orientated GNPs. The elastic modulus of aligned GNPs in the interphase is nearly two-order magnitude lower.

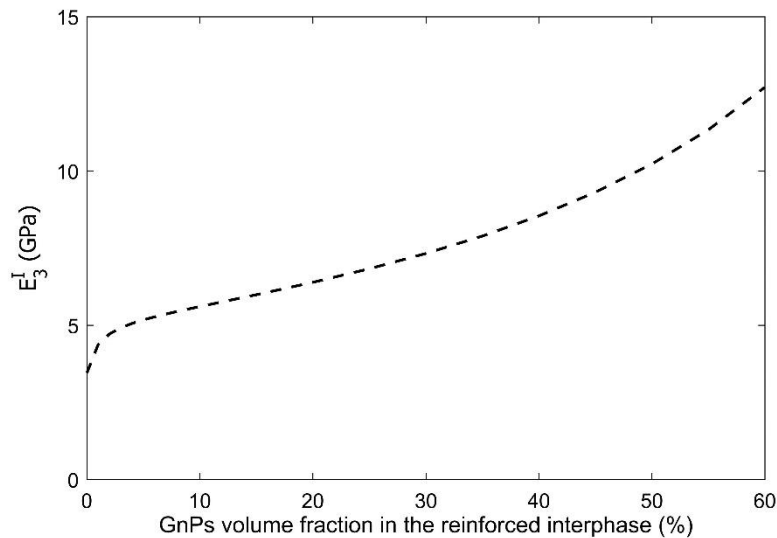


Figure 4-6 *Out-of-plane elastic modulus of the reinforced interphase with aligned GNPs as a function of the volume fraction of GNPs in the interphase.*

The out-of-plane shear modulus increases slowly in a non-linear manner (**Figure 4-7**). Values for this modulus vary from 1.28 GPa to 3.1 GPa for given volume fraction range. The out-plane-shear modulus is nearly two-order of magnitude lower than its in-plane counterpart.

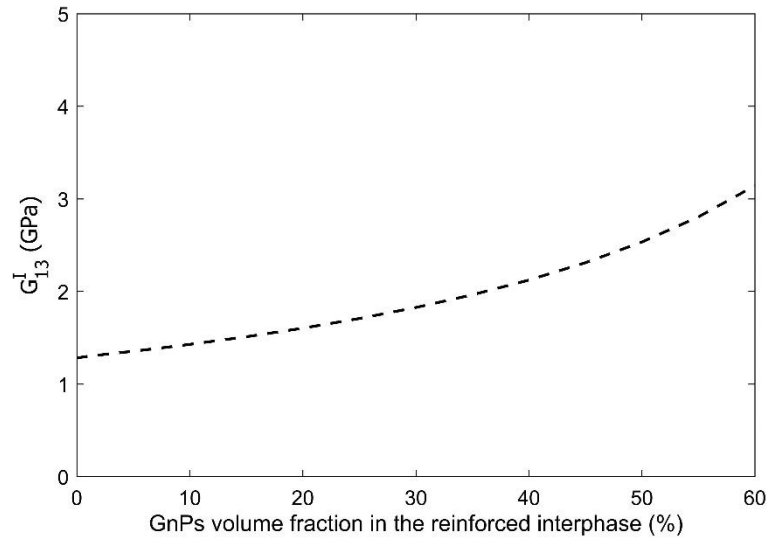


Figure 4-7 Out-of-plane shear modulus of the reinforced interphase with aligned GNPs as a function of the volume fraction of GNPs in the interphase.

4.3 Elastic constants of the lamina with the GNPs reinforced interphase

4.3.1 RVE modelling

The properties of a single lamina were predicted using micromechanical mechanics. The RVE model contains three phases: carbon fibre, epoxy resin and the GNPs reinforced interphase. This example has investigated commonly used carbon fibre/epoxy system with well-established properties. Properties of transversely isotropic carbon fibre T300 and isotropic epoxy resin 828 are summarised in **Table 4-3** and adopted from literature (Soden, Hinton and Kaddour, 2004; Zhiye Li *et al.*, 2016).

The size of the RVE model was calculated based on carbon fibre diameter ($7.1\mu\text{m}$) and volume fraction of 65%. Height, width and thickness of the RVE model dimension were 7.26, 4.19 and $1.05\mu\text{m}$ respectively (according to equation **3-9**). For detailed calculations, see *Appendix A*. In line with direct measurement of the GNPs reinforced interphase, the thickness was set to 54 nm. This interphase corresponded to 2% of the volume fraction of the whole RVE model. The volume fractions of the particular constituents of RVE models were 65%, 33% and

2% for carbon fibre, epoxy and GNPs reinforced interphase respectively. The model was implemented in ANSYS APDL 17.2 using 20-node 3-D solid elements (SOLID186).

Table 4-3 Properties of carbon fibre and matrix in the global coordinate system (1-2-3).

| Carbon Fibre | | Epoxy Resin | |
|--|------|--------------------------------|------|
| Longitudinal modulus, E_1^f (GPa) | 230 | Modulus, E^m (GPa) | 3.45 |
| Transverse modulus, E_2^f (GPa) | 15 | Poisson's ratio, ν^m | 0.34 |
| Longitudinal shear modulus, G_{12}^f (GPa) | 15 | Bulk modulus, κ^m (GPa) | 3.59 |
| Transverse shear modulus, G_{23}^f (GPa) | 7 | Shear modulus, μ^m (GPa) | 1.28 |
| Longitudinal Poisson's ratio ν_{12}^f | 0.2 | | |
| Transverse Poisson's ratio ν_{23}^f | 0.07 | | |
| Diameter (μm) | 7.1 | | |

The interphase properties obtained in section 4.2 were input to this RVE model. The volume fraction of GNPs varied from 0 to 60% parametrically, which was relative to the interphase only. Two orientations of GNPs (random and aligned) were compared in order to illustrate the influence of the GNPs on the reinforced interphase. The implementation of the transversely isotropic properties of the interphase with aligned GNPs was challenging. To solve that problem, “VEORIENT” command was adopted to specify bricks element orientation for meshed volume. The element orientation was determined by the line option, which was chosen along the circumference of the carbon fibre (see **Figure 4-8**). The normal direction of elements followed the direction of the line (ANSYS, 2018). The example of VEORIENT command is provided in the RVE script in *Appendix C*.

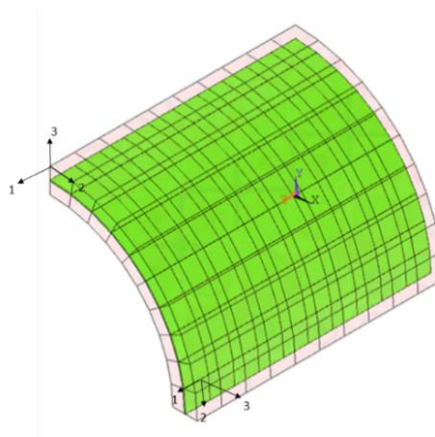


Figure 4-8 VEORIENT command applied to the transversely isotropic interphase. Image used courtesy of ANSYS, Inc.

4.3.2 Longitudinal and transverse elastic moduli.

Figure 4-9 shows the results of the lamina elastic moduli along the longitudinal direction. The interphase properties equal to the epoxy resin properties for 0% graphene volume fraction. Therefore, the longitudinal and transverse Young's moduli of the 65% carbon and 35% epoxy resin are 150.9 and 8.57 GPa respectively. This acts as the baseline of CFRP.

Both aligned and randomly orientated GNPs coatings moderately improve longitudinal Young's modulus (E_1). E_1 increases nearly linearly with the volume fraction of GNPs for the case of aligned GNPs within interphase. While the case of randomly orientated GNPs presents a somewhat nonlinear increase of E_1 . The improvement is a bit higher for aligned GNPs in the interphase, but the difference in the enhancement between aligned and randomly orientated GNPs is no more than 2 GPa. For example, the longitudinal modulus increases from 150.9 GPa for the pure CFRP to 160.3 GPa for 60% aligned GNPs in the reinforced interphase. For the same volume fraction of randomly orientated GNPs, the enhancement is 1.8 GPa lower.

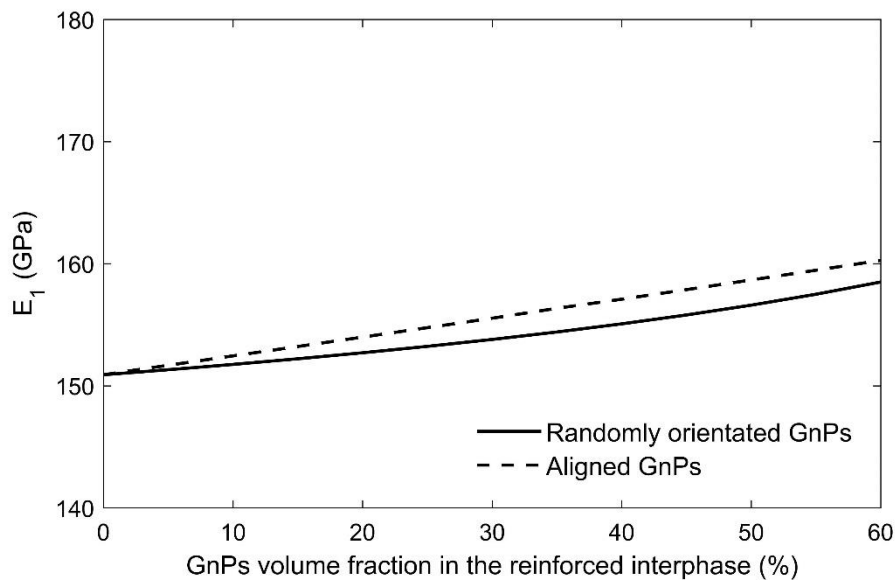


Figure 4-9 Effects of the volume fraction of GNPs in the reinforced interphase on the longitudinal elastic modulus of the unidirectional lamina.

Figure 4-10 presents the relation between lamina transverse modulus (E_2) versus GNPs volume fraction within the interphase. When GNPs are aligned in the reinforced interphase, a brisk improvement of 3% is observed at as low as 4% of GNPs volume fraction. Further increase of GNPs volume fraction yields little enhancement. On the other hand, randomly orientated GNPs in the interphase show similar increase to the aligned case for up to

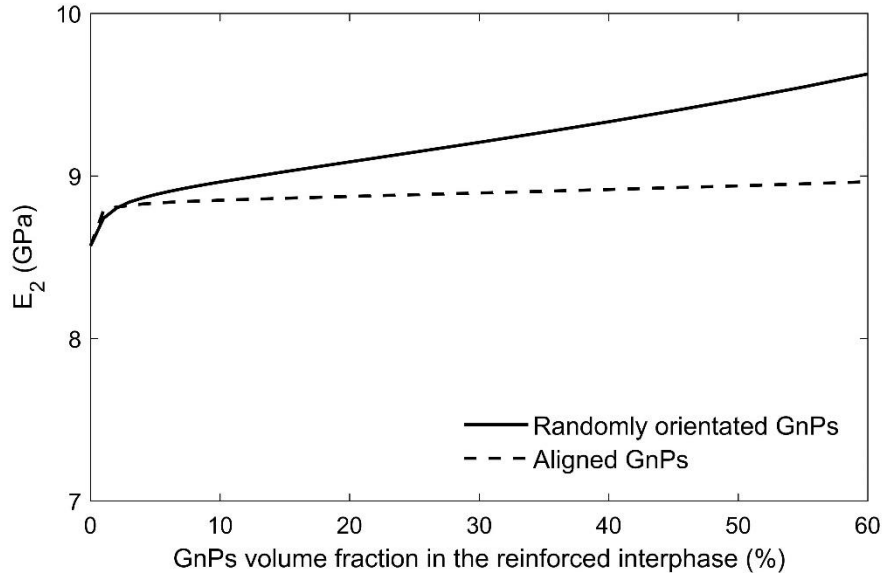


Figure 4-10 Effects of the volume fraction of GNPs in the reinforced interphase on the transverse elastic modulus of the unidirectional lamina.

4% of GNPs volume fraction. Above this value, a continuously noticeable linear growth of E_2 with the GNPs content is found. For 60% GNPs in the reinforced interphase, lamina transverse modulus increases from 8.57 GPa for the pure CFRP to 9.63 GPa and 8.96 GPa for randomly orientated and aligned cases respectively.

4.3.3 Longitudinal and transverse shear moduli

Both shear moduli were enhanced due to the introduction of GNPs in the interphase (**Figure 4-11, 4-12**). GNPs orientations affect the changing trend of shear moduli. For aligned and randomly orientated GNPs in the reinforced interphase, up to 2% volume fraction brisk growth of shear moduli is observed. After that, the aligned GNPs case shows little change with the further increase of the volume fraction of GNPs. On the contrary, the randomly orientated case has shown continuously although slow increments of moduli. G_{12} increases from 4.43 GPa (0% GNPs volume fraction) to 4.84 GPa (60% GNPs volume fraction). The difference between randomly orientated and aligned GNPs G_{12} values for 60% volume fraction is 0.15 GPa. Transverse shear modulus (G_{23}) increase from 3.31 GPa (pure CFRP) to 3.57 GPa and 3.51 GPa for 60% randomly orientated and aligned GNPs respectively.

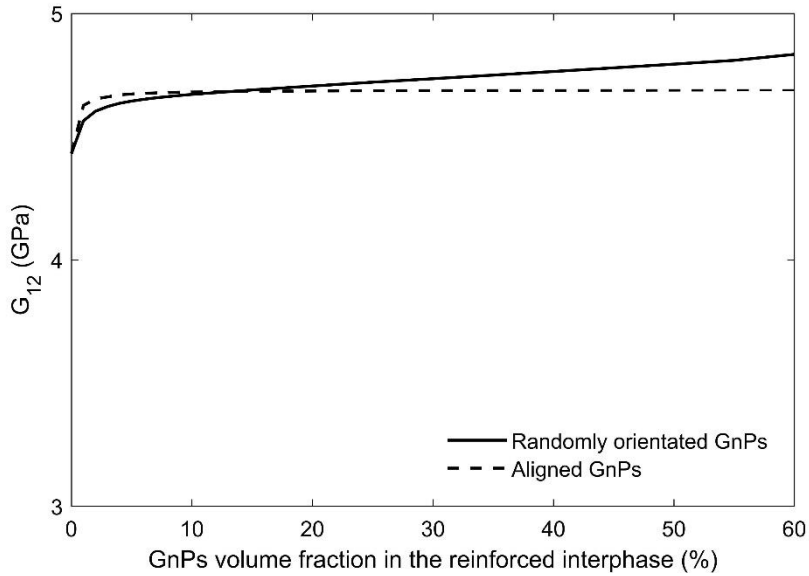


Figure 4-11 Effects of the volume fraction of GNPs in the reinforced interphase on the longitudinal shear modulus of the unidirectional lamina.

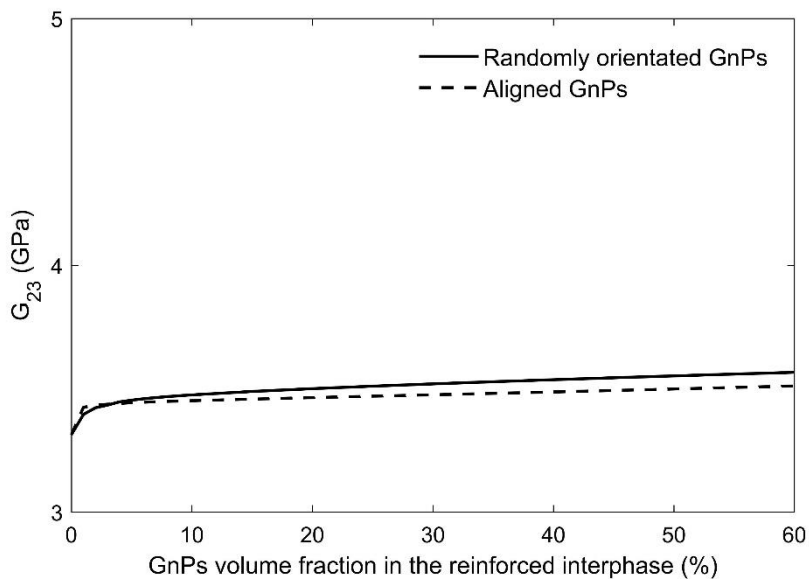


Figure 4-12 Effects of the volume fraction of GNPs in the reinforced interphase on the transverse shear modulus of the unidirectional lamina.

4.3.4 Poisson's ratio

For the completeness of results, **Figure 4-13** presents effects of the GNPs reinforced interphase on the Poisson's ratio of the unidirectional lamina. For aligned GNPs, ν_{12} of the lamina yields little difference in comparison to the Poisson's ratio of pure CFRP.

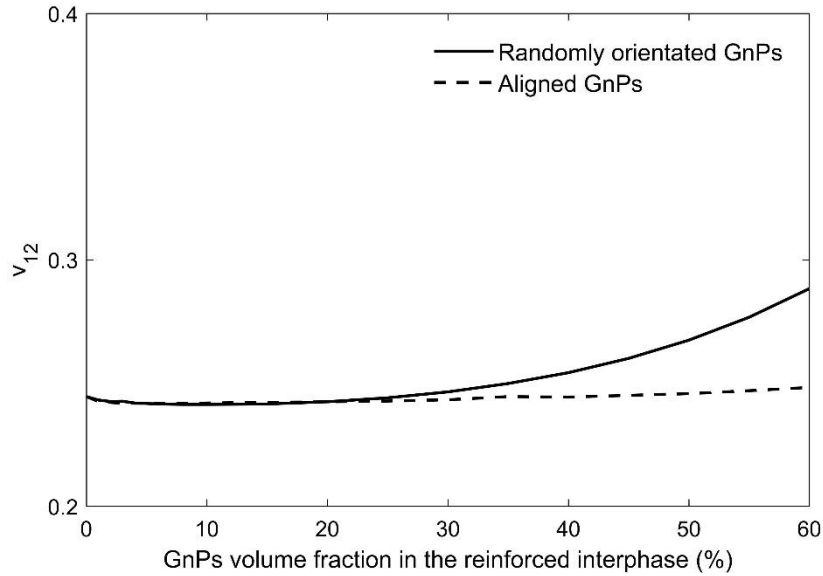


Figure 4-13 Effects of the volume fraction of GNPs in the reinforced interphase on longitudinal Poisson's ratio of the unidirectional lamina.

Longitudinal Poisson's ratio for randomly orientated remains unchanged up to 20 % of GNPs in the interphase and starts growing gradually with the further increase of volume fraction of GNPs.

4.4 Macroscale model

4.4.1 Prediction of CFRP laminate properties

Prediction of the mechanical properties of carbon fibre reinforced laminate requires simulations at the macroscale. To truly reflect the behaviour of CFRP, one must consider various factors including properties of each lamina, their stacking sequence and interaction between them. Three-point bending test was simulated to study the effects on the lamina properties and fibre orientation on the flexural modulus of the CFRP following the experiment performed by Qin *et al.* (2015). The model was simulated in the three-point bending test using ANSYS 17.2 Workbench software. Examination of the microstructure of the GNPs reinforced interphase exhibited a very high density of well homogenously dispersed GNPs at the carbon fibre surface. Therefore, the randomly orientated case of Mori-Tanaka prediction was selected for this type of coating. Based on the available sample preparation quantitative details, the local volume fraction of GNPs in the reinforced interphase was estimated to be 40%. Properties of the single lamina with and without GNPs reinforced interphase were calculated using the RVE

method. The material properties of carbon fibre AS4 (Ding *et al.*, 2016), epoxy resin (**Table 4-2**) and interphase properties predicted in section 4.2 were applied in the RVE modelling. Predicted lamina properties are provided in **Table 4-3**.

Table 4-4 Properties of the single lamina with and without graphene reinforced interphase.

| Fibre direction | Carbon fibre AS4 | Epoxy matrix | GNPs reinforced interphase | E_1 (GPa) | E_2 (GPa) | ν_{12} | ν_{23} | G_{12} (GPa) |
|-----------------|------------------|--------------|----------------------------|-------------|-------------|------------|------------|----------------|
| 0° | 65% | 35% | 0% | 149.70 | 8.95 | 0.24 | 0.48 | 5.08 |
| 0° | 66% | 32% | 2% | 156.01 | 9.80 | 0.25 | 0.48 | 5.60 |

The dimensions of the sample were 12.7 mm, 100 mm and 2.3 mm indicating width, length and thickness respectively. The model was created using ANSYS SpaceClaim by extracting a thin surface from a rectangular shape. This step enables to use a layer structure command, which is only applicable for shell elements as explained in 3.2.3. The boundary conditions as presented in **Figure 4-14** were applied. The vertical component of force was selected in the middle of the sample. As a support, the simply supported boundary conditions were selected. The distance (span length) between supports was 80 mm. Maximum displacement was recorded in the middle of the sample span.

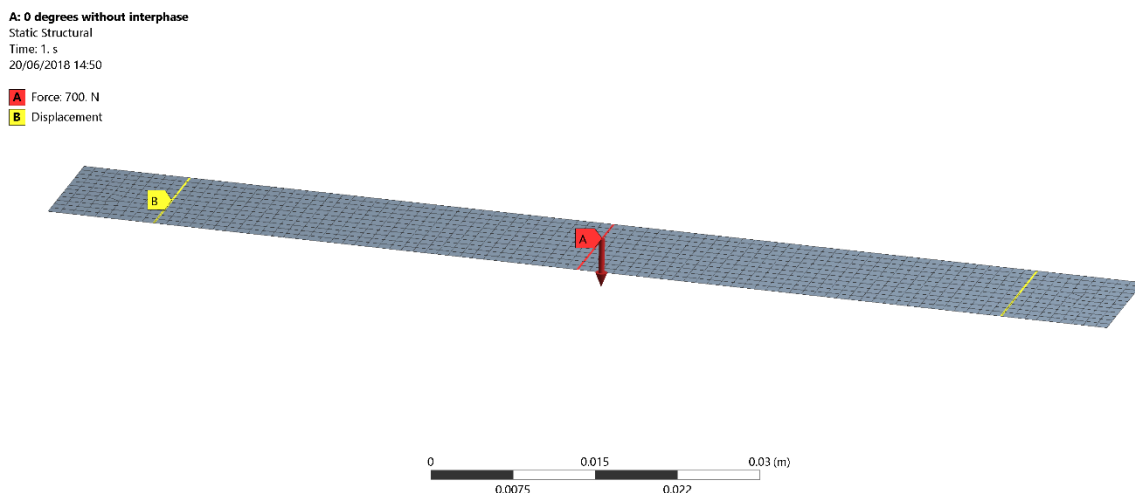


Figure 4-14 Boundary conditions for a meshed model of 0° sample without interphase. Image used courtesy of ANSYS, Inc.

4.4.2 Results

Four different laminates made of 12 unidirectional plies were numerically tested to represent the three-point bending experiment. Sample dimensions, force and corresponding maximum displacement were substituted to the equation 4-1 to calculate flexural modulus (E_f). The comparison between predicted E_f using the present methodology and experimental data (Qin *et al.*, 2015) is provided in **Table 4-4**. The numerical modelling has been able to predict flexural modulus of CFRP material satisfactorily. The average percentage error in flexural modulus is below 5%.

$$E_f = \frac{L^3}{4bh^3} \left(\frac{\Delta F}{\Delta s} \right) \quad 4-1$$

Table 4-5 Comparison between the flexural modulus predicted by present multiscale modelling and experimental data.

| Fibre direction | Presence of GNPs reinforced interphase | Span length L (mm) | Force F (N) | Deflection s (mm) | Calculated E_f (GPa) | Mean measured E_f (GPa) [10] | Percentage error (%) |
|-----------------|--|----------------------------|---------------------|---------------------------|------------------------------|---|----------------------|
| 0° | No | 80 | 700 | 4.05 | 143.18 | 139±3.0 | +2.92 |
| 0° | Yes | 80 | 700 | 3.88 | 149.45 | 143±9.0 | +4.45 |
| 90° | No | 80 | 20 | 1.9 | 8.72 | 8.8±0.3 | -0.81 |
| 90° | Yes | 80 | 20 | 1.72 | 9.74 | 11±0.3 | -13.01 |

The accuracy of this analysis depends on many factors, but mainly on the material properties input to the software. Both samples without GNPs reinforced interphase shows close correlation with experimental results. The highest discrepancy occurred for the 90° flexural modulus as the numerical prediction slightly underestimated this value. This may be attributed to the imprecise estimation of the interphase properties or thickness.

4.5 Discussion

Elastic constants of CFRP were enhanced by the presence of the GNPs reinforced interphase. The interphase properties are crucial in the successful determination of CFRP

behaviour. This was for the first time to quantify the effects of volume fraction, and orientation of GNPs deposited on the fibre surface on the elastic constants of CFRP.

Generally speaking, the distribution of GNPs in the coating is affected by many factors such as methods of introducing GNPs, the interaction between them and local volume fraction (Zhang *et al.*, 2012). In this study, all GNPs assumed either aligned or randomly orientated. The interphase made of resin and GNPs is essentially a thin layer of GNPs reinforced nanocomposite, but at a higher volume fraction. The main difference is that in the present RVE model, GNPs are concentrated on the fibre surface and reinforce the interphase layer only. Considering the volume fraction of the whole composite the interphase is only 2%. The maximum volume fraction of GNPs, i.e. 60 % is equivalent to 1.2 % for the whole composite. A similar amount of GNPs has been applied to traditional nanocomposites (R. L. Zhang *et al.*, 2016).

Direct comparison to the experimental studies is very challenging. Numerical modelling requires parameters, which are not usually directly measured in experiments including, for example, the interphase thickness, the local volume fraction of nanofillers in the interphase, the orientation of nanofillers and interphase properties. Due to the nature of the coating process, these conditions are also difficult to control. Most of the present experimental studies focus on the influence of graphene or CNTs on the overall laminate properties. Nevertheless, numerical studies require many steps trying to reproduce the experimental data. For the typical CFRP system data sheets are widely available. However, for this new type of CFRP reinforced graphene the lamina properties have not been experimentally tested yet. Therefore, the interphase properties at the nanoscale and lamina properties at microscale are compared here with available numerical models.

Interphase properties for aligned and random orientated cases can be correlated with published nanocomposites properties (Ji, Cao and Feng, 2010; Shokrieh and Rafiee, 2010). In the GNPs reinforced nanocomposite, the elastic modulus of randomly orientated GNPs is 0.53 of that of the aligned case at the low volume fraction of GNPs (Zheling Li *et al.*, 2016). The ratio of the elastic modulus in the present study is found acceptably close to this value. It is worth mentioning that all elastic properties of transversely isotropic interphase were predicted in the present work, while most nanocomposite modelling only focused on the elastic modulus.

Improvement of unidirectional lamina properties with the GNPs reinforced interphase was quantified for different conditions. This extent of the enhancement depends highly on the

orientation of GNPs within the interphase. CFRP always exhibits extraordinary properties in the fibre direction due to the high longitudinal modulus of fibres. GNPs coating on the fibre improved longitudinal elastic modulus (E_1) of the CFRP lamina moderately. When all GNPs at a volume fraction of 60% were aligned in the interphase, the increase in E_1 was 6.2%. It was higher than that of 5% observed for the same volume fraction of randomly orientated GNPs. This larger enhancement was attributed to the higher transversely isotropic properties possessed by the interphase, which resulted from the parallel orientation of GNPs along the fibre surface, and exceptionally high in-plane modulus of GNPs.

Unlike the moderate effects of longitudinal modulus, the increase of transverse modulus E_2 was noticeably affected by the orientation of GNPs in the interphase. When the graphene content reached 60%, the increase of E_2 for randomly orientated GNPs in the interphase was as high as 12.3%. For the same volume fraction but aligned GNPs case, the enhancement was only 4.5%. Randomly orientated GNPs in the interphase endows the interphase isotropic properties. Therefore, GNPs remarkable in-plane properties were utilised in all directions. On the contrary, in the case of aligned GNPs, the out-of-plane properties of the interphase were much weaker. This indicates that unifying GNPs orientation parallel to the fibre surface may not yield maximum beneficial improvement in the transverse material properties.

The GNPs reinforced CFRP adopted in this study is similar to the fuzzy fibre reinforced composite. Both make use of graphene reinforcement in the interphase. Results from the present study were correlated with numerical models of fuzzy fibre reinforced composites. Chatzigeorgiou et al. (2012) observed that the reinforced interphase did not change the axial properties, but improved the transverse properties of fuzzy fibre reinforced composite significantly. More than 200% of enhancement in composite moduli was found in the transverse direction. This interphase is efficiently reinforced as the axial direction of CNTs growing on the fibre surface is in line with the fibre transverse direction. This may represent the maximum enhancement possible for this type of interphase. This interphase is as thick as 2 μm , which is dictated by the length of the CNTs. This thickness is significantly higher than GNPs reinforced interphase in the present study. Following the same principle, maximum GNPs reinforcement to CFRP may be achieved at the orientation of GNPs perpendicular to the fibre surface. This type of graphene alignment has been already implemented in sensors, fuel cells and supercapacitors (Junhong, Zheng and Lu, 2015).

The validity of the present numerical simulation was further investigated by comparing with experimental work at the macroscale. A 12 layers unidirectional laminate with carbon fibres coated with GNPs in 0° was performed in three-point bending test (Qin *et al.*, 2015). Random orientation of GNPs was indirectly derived from the image analysis of samples. The flexural modulus calculated in this analysis was 149.45 GPa and matched well the range of experimental data. Based on the same numerical approach the flexural modulus of the sample in the absence of the GNPs was predicted at 142.2 GPa. This amounts to 5 % improvement in flexural modulus due to the presence of the GNPs reinforced interphase which is close to the results given by (Qin *et al.*, 2015). This multiscale modelling approach shows a potential to reproduce experimental measurements.

Besides the improvement in elastic properties of CFRP as shown in this study, the GNPs coating will increase other mechanical properties such as fracture toughness, interfacial and interlaminar shear strength (Deng *et al.*, 2015; Qin *et al.*, 2015; Mahmood *et al.*, 2018). Strengthening the bonding between the matrix and fibre is caused by chemical reactions and mechanical interlocking processes. Fibre coated with graphene increases its surface roughness and surface morphologies (Deng *et al.*, 2015). Those properties are not directly investigated in this study.

There are some other limitations to this work. The GNPs are assumed perfectly straight and evenly distributed in the interphase. However, GNPs agglomeration due to the Van der Waals forces (Atif and Inam, 2016) will become non-negligible as the local volume fraction of GNPs increases. When the GNPs volume fraction reaches a high value, the interaction between GNPs should be taken into account. During the manufacturing process, some imperfections are unavoidable. This approach neglects the production flaws such as voids, cracks and delamination. Future improvement in this modelling work needs to address these issues.

4.6 Summary

In conclusion, the effects of the GNPs reinforced interphase on elastic constants of CFRP using three-phase RVE model have been studied. The effective material properties of the reinforced interphase have been determined by considering transversely isotropic features of GNPs. The presence of GNPs in the interphase enhances elastic properties of CFRP lamina and the enhancement depends on its volume fraction. The random and aligned orientation of GNPs in the reinforced interphase have been compared. Randomly orientated GNPs in the interphase yields a higher improvement in transverse properties of the composite. The

determined elastic properties of GNPs reinforced CFRP lamina has been successfully used to reproduce experimental flexural modulus of CFRP laminate.

5 Fuzzy Fibre Reinforced Polymer – numerical modelling

5.1 Introduction to fuzzy fibre reinforced polymer (FFRP)

The enhancement of the CFRP elastic properties through the GNPs reinforced interphase has been explained in Chapter 4. Here, the author focuses on numerical simulations of FRPs with another type of commonly used nano-reinforcement – carbon nanotubes (CNTs). CNTs are essentially graphene sheets rolled into the tubular shape. These nanofillers have been applied in FRPs by growing on the fibre surface (Sager *et al.*, 2009; Wood *et al.*, 2012; Jin, Young and Eichhorn, 2014)(see **Figure 5-1**). Coated with radially orientated CNTs fibres are embedded in the polymeric matrix forming fuzzy fibre reinforced polymer (FFRP). The purpose of this coating is to increase the bonding strength between fibre and matrix. Experimental studies found that the presence of CNTs on fibre surface increased mechanical properties, for example, interfacial shear strength (Thostenson *et al.*, 2002) or flexural modulus (Mathur, Chatterjee and Singh, 2008).

The improvement in mechanical properties of FFRP has drawn the interest of researchers in developing numerical and theoretical approaches to study the behaviour of this material (Kulkarni *et al.*, 2010; Kundalwal and Ray, 2011, 2012; Rafiee and Ghorbanhosseini, 2017a). The numerical simulations of FFRP employ a similar concept of multiscale modelling as described in Chapter 4. A micromechanical model of FFRP distinguished three phases like fibre, the nano-reinforced interlayer (matrix and CNTs) and pure matrix. To study this model, the nano-scale simulations of the CNTs reinforced layer are essential. This can be achieved by simulating RVE model consist of CNTs and matrix (Kulkarni *et al.*, 2010) or with the aid of theoretical models such composite cylinder methods (Chatzigeorgiou, Seidel and Lagoudas, 2012). Simulation results of FFRP summarised that the transverse properties of the composites are remarkably improved because of the unique orientation and exceptional high axial modulus of CNTs (Kulkarni *et al.*, 2010; Chatzigeorgiou, Seidel and Lagoudas, 2012).

This chapter presents the results of the multiscale analysis to investigate the properties of the FFRP. FFRP was used as the validation of the developed multiscale model due to availability of numerical results. The composite being studied contains three phases, namely: the T650 carbon fibre, the CNTs reinforced interphase and the epoxy resin EPIKOTE 862. Firstly, the Mori-Tanaka method is adopted to estimate the properties of aligned CNTs in the reinforced interphase. Then, the RVE with hexagonal fibres array is used for numerical

simulation to predict the properties of the fibre-reinforced polymer with the concept of the CNTs reinforced interphase. The influence of the interphase properties on the response of the FFRP is analysed for a various carbon fibre volume fraction. Two types of models: with and without the CNTs reinforced interphase are compared to highlight its influence on material properties. The results predicted by RVE micromechanical models are compared with published results of FFRP (Chatzigeorgiou et al.,2012). CNTs present in the interphase and their effects on the lamina properties of CFRP were critically analysed and compared to GNPs reinforced interphase. The developed multiscale model can do any orientation for CNTs enhancement in CFRP.

Figure 5-1 is unavailable due to copyright restrictions.

Figure 5-1 Schematic of a fuzzy fibre consisting of fibre which is coated with radially aligned CNTs (Kundalwal *et al.*, 2011).

5.2 CNTs reinforced interphase properties – Mori Tanaka method

Fuzzy fibre results from the introduction of CNTs in the fibre surface forming a separate layer of the nanocomposite. Mori-Tanaka method was employed to predict the CNTs reinforced interphase properties, (Shi *et al.*, 2004). The interphase was assumed to behave as a layer of nanocomposite with aligned CNTs. The local 1'-2'-3' coordinates describes the CNTs properties, where 1' is CNTs axial direction (see **Figure 5-2b**). The stiffness tensor \mathbf{C} of CNTs reinforced material can be expressed in terms of Hill's elastic parameters: k , l , n , m and p by equation (5-1), which simplified mathematical calculations of Mori-Tanaka method. The properties of transversely isotropic CNT and isotropic epoxy resin are provided in **Table 5-1**. The expressions of Hill's parameters are related to the material properties of CNTs and matrix and their volume fractions, and the plane of isotropy. In this modelling exercise, the CNTs volume fraction was fixed at 42.17 % and remaining volume fraction was resin.

$$\mathbf{C} = \begin{bmatrix} n & l & l & 0 & 0 & 0 \\ l & k+m & k+m & 0 & 0 & 0 \\ l & k+m & k+m & 0 & 0 & 0 \\ 0 & 0 & 0 & m & 0 & 0 \\ 0 & 0 & 0 & 0 & p & 0 \\ 0 & 0 & 0 & 0 & 0 & p \end{bmatrix} \quad 5-1$$

$$k = \frac{E_m \{E_m c_m + 2k_r(1+v_m)[1+c_r(1-2v_m)]\}}{2(1+v_m)[E_m(1+c_r-2v_m) + 2c_m k_r(1-v_m-2v_m^2)]} \quad 5-2$$

$$l = \frac{E_m \{c_m v_m [E_m + 2k_r(1+v_m)] + 2c_r l_r(1-v_m^2)\}}{(1+v_m)[2c_m k_r(1-v_m-2v_m^2) + E_m(1+c_r-2v_m)]}$$

$$p = \frac{E_m [E_m c_m + 2(1+c_r)p_r(1+v_m)]}{2(1+v_m)[E_m(1+c_r) + 2c_m p_r(1+v_m)]}$$

$$n = \frac{E_m^2 c_m(1+c_r-c_m v_m) + 2c_m c_r(k_r n_r - l_r^2)(1+v_m)^2(1-2v_m)}{(1+v_m)[2c_m k_r(1-v_m-2v_m^2) + E_m(1+c_r-2v_m)]} +$$

$$\frac{E_m [2c_m^2 k_r(1-v_m) + c_r n_r(1-2v_m+c_r) - 4c_m l_r v_m]}{2c_m k_r(1-v_m-2v_m^2) + E_m(1+c_r-2v_m)}$$

$$m = \frac{E_m [E_m c_m + 2m_r(1+v_m)(3+c_r-4v_m)]}{2(1+v_m)\{E_m [c_m + 4c_r(1-v_m)] + 2c_m m_r(3-v_m-4v_m^2)\}}$$

Table 5-1 Mechanical properties of SWCNT and epoxy resin (Seidel and Lagoudas, 2006).

| Nanofiller: SWCNT | Matrix: EPIKOTE Resin | | |
|---|-----------------------|--------------------------|----------|
| Longitudinal modulus, $E_{1'}^{CNT}$ | 704 GPa | Modulus, E^m | 3.07 GPa |
| Transverse modulus, $E_{2'}^{CNT}$ | 345 GPa | Poisson's ratio, ν^m | 0.3 |
| In-plane shear modulus, $G_{12'}^{CNT}$ | 227 GPa | | |
| In-plane Poisson's ratio, $\nu_{12'}^{CNT}$ | 0.14 | | |
| Out-of-plane Poisson's ratio, $\nu_{23'}^{CNT}$ | 0.3764 | | |

$$E_{2'}^{CNT} = \frac{4m_r(k_r n_r - l_r^2)}{(k_r + m_r)n_r - l_r^2}, \quad 5-3$$

$$E_{1'}^{CNT} = n_r - \frac{l_r^2}{k_r},$$

$$G_{12'}^{CNT} = p_r,$$

$$v_{23'}^{CNT} = \frac{(k_r - m_r)n_r - l_r^2}{(k_r + m_r)n_r - l_r^2},$$

$$v_{12'}^{CNT} = \frac{l_r}{2k_r}.$$

To predict the properties of CNTs reinforced layer, transversely isotropic properties of individual nanotubes need to be also represented with Hill's elastic constants. This can be achieved by solving simultaneous equations (5-3) which describes the relations between CNTs properties and Hill's parameters. Therefore, Hill's parameters for CNTs were calculated as: $k_r = 285.41 \text{ GPa}$, $l_r = 79.9 \text{ GPa}$, $n_r = 726.38 \text{ GPa}$, $m_r = 125.33 \text{ GPa}$, $p_r = 227 \text{ GPa}$. These values together with epoxy resin properties (E^m , v^m) were subsequently inputted to the equations 5-2. The terms c_r and c_m are the volume fraction of CNTs and matrix respectively. Once the Hill's parameters of the mixture of CNTs and matrix are known, the elastic constants of the nano-reinforced layer are calculated as follows:

$$E_{2'} = \frac{4m(kn - l^2)}{(k+m)n - l^2}, \quad 5-4$$

$$E_{1'} = n - \frac{l^2}{k},$$

$$G_{12'} = p,$$

$$v_{23'} = \frac{(k-m)n - l^2}{(k+m)n - l^2},$$

$$v_{12'} = \frac{l}{2k}.$$

Table 5-2 presents the comparison between the CNTs reinforced interphase given by Chatzigeorgiou, Seidel and Lagoudas (2012) and the present method. The interphase reinforced with CNTs behaves transversely isotropic. Longitudinal modulus, $E_{1'}$, of the interphase is 297.29 GPa. This high value is attributed to the exceptionally high axial modulus of individual CNTs ($E_{1'}^{CNT}$). On the other hand, in the direction transverse to the axis of CNT direction, the transverse modulus ($E_{2'}$) of material is only 6.99 GPa. Both shear moduli ($G_{12'}$, and $G_{23'}$) were 2.87 and 2.49 GPa. Predicted interphase results are in very good agreement with the properties of the same material and volume fraction given calculated by self-consistent method. The interphase properties predicted by the Mori-Tanaka method became input properties to the microscale three-phase RVE model of FFRP.

Table 5-2 Comparison between the properties of the CNTs reinforced interphase predicted by self-consistent method and present Mori-Tanaka approach.

| Interphase: CNTs reinforced interphase | | | |
|--|-------------------------------|-----------------|---------------------|
| | Chatzigeorgiou et al. 2012 | Present work | Percentage Error |
| Longitudinal modulus, $E_{1,}$ | 298.64 GPa | 297.29 GPa | -0.4 % |
| Transverse modulus, $E_{2,}$ | 7.01 GPa | 6.99 GPa | -0.3 % |
| In-plane shear modulus, $G_{12,}$ | 2.81 GPa | 2.87 GPa | +2% |
| Transverse shear modulus, $G_{23,}$ | 2.52 GPa | 2.49 GPa | -1% |

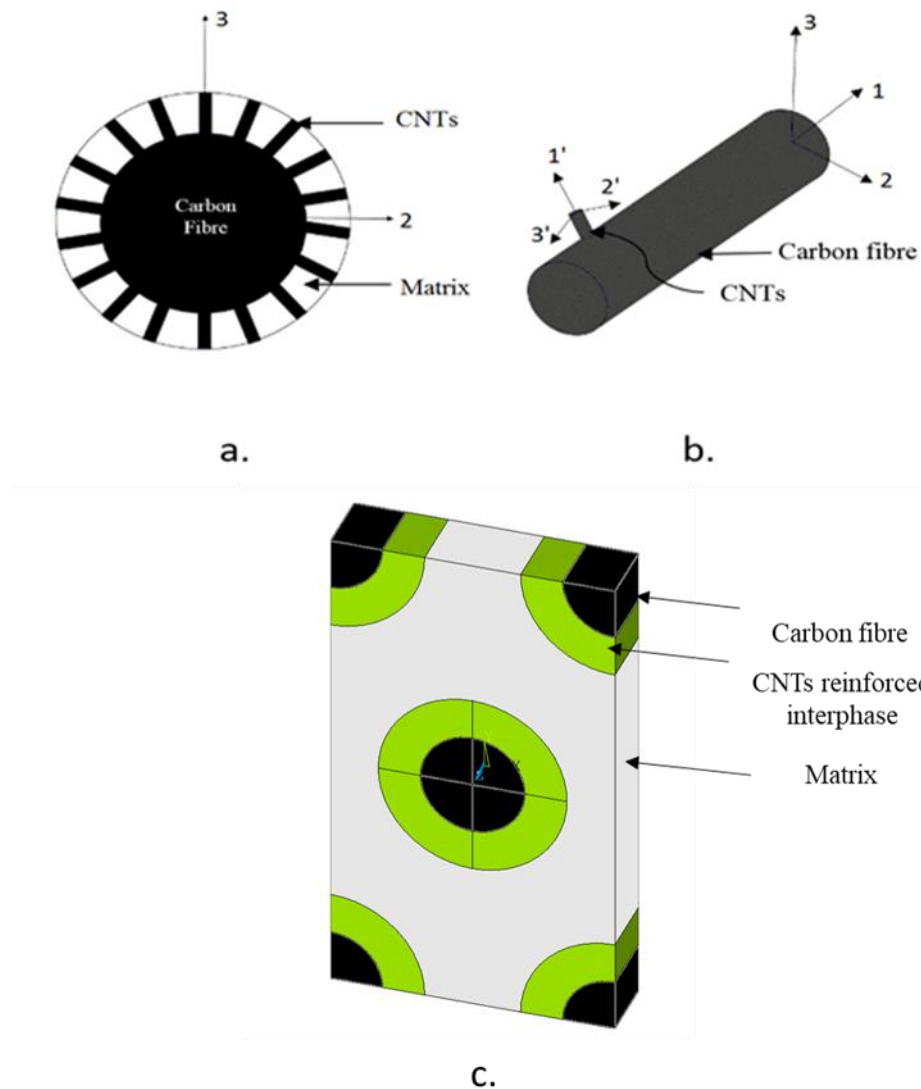


Figure 5-2 Schematic illustrations of (a) Cross-section view of the fuzzy fibre, (b) Perspective view of the fuzzy fibre, (c) Hexagonal RVE model of FFRP RVE model.

5.2.1 RVE models

The mechanical behaviour of FFRP lamina was effectively studied using the hexagonal RVE model as presented in **Figure 5-2c**. Two types of RVE models with and without CNTs reinforced interphase were studied. The two-phase model contained carbon fibre together with interphase and throughout results section being described as carbon fibre composite. Whereas, the three-phase RVE model contained an extra phase namely the CNTs reinforced interphase and referred to fuzzy fibre composite. In the FFRP, CNTs are radially grown on the surface of the carbon fibre (**Figure 5-2a**); extra care must be taken while assigning materials properties. This type of material is usually simulated in the cylindrical coordinates system (Kundalwal and Ray 2012, Chatzigeorgiou et al. 2012). Here, two Cartesian coordinates systems are appointed. Local coordinates system 1'-2'-3' presented in **Figure 5-2b** describes the CNTs reinforced interphase (where 1' aligns with CNTs axial direction). Fuzzy fibres are arranged in the unidirectional lamina and follow global coordinate system with axes denoted by 1-2-3, where, 1 is the carbon fibre direction.

5.2.2 Material properties of each phase

Two-phase and three-phase models are compared to highlight the effects of the CNTs-reinforced interphase on the mechanical properties of the FFRP. In the two-phase model, the mechanical properties of the transversely isotropic T650 carbon fibre and the isotropic EPIKOTE epoxy resin were selected (**Table 5-1, Table 5-3**). Properties of the transversely isotropic carbon fibre were assigned according to the lamina coordinate system (see **Figure 5-2**). Dimensions of the RVE were calculated based on the fibre volume fraction and fibre diameter (5 µm). The carbon fibre volume fraction varies from 0 to 25%. For example, for 25% of carbon fibre volume fraction, height, width and thickness are 8.23, 4.76 and 1.19 µm respectively.

The three-phase model additionally included the CNTs reinforced interphase with a thickness of 2 µm. The "VEORIENT" command was applied to the RVE model to define the orientation of CNTs. This command allowed specifying element orientation to control transversely isotropic material properties direction. As a result, of CNTs mechanical characteristics and orientation, the interphase was transversely isotropic. The material properties of the CNTs reinforced interphase were calculated based on the Mori-Tanaka method and provided in **Table 5-2**. For the completeness of material properties input

parameters, in-plane Poisson's ratio ($\nu_{12'}$) and out-of-plane Poisson's ratio, ($\nu_{23'}$) were 0.1 and 0.29 respectively.

Both models were simulated using ANSYS APDL 17.2. Perfect bonding conditions between each phase were assumed. The mesh types for the models adopted 20-node 3-D solid elements (SOLID186). Mesh independent test was accomplished to eliminate the influence of mesh density on the accuracy of the results (see 3.2.2). The whole meshed model contained approximately 7000 elements. In the parametric study, material properties and dimensions for all constituents were kept constant, except that the volume fraction of carbon fibre range from 0 to 25% for both two and three-phase models.

Table 5-3 *Transversely isotropic material properties of carbon fibre T650.*

| Fibre: Carbon fibre T650 | |
|---------------------------------------|-----------------|
| Longitudinal modulus, E_{f1} | 241 GPa |
| Transverse modulus, E_{f2} | 14.5 GPa |
| In-plane shear modulus, G_{f12} | 22.8 GPa |
| Transverse shear modulus, G_{f23} | 4.8 GPa |
| In-plane Poisson's ratio, ν_{f12} | 0.27 |
| Diameter | 5 μm |

5.3 Results

This section presents the results of micromechanical simulations of two-phase (carbon fibre composite) and three-phase (fuzzy fibre composite) RVE models. The effects of CNTs reinforced on elastic constants of carbon fibre reinforced polymers were investigated. Moreover, the influence of carbon fibre volume fraction on the elastic properties was parametrically studied. Results were compared to the analytical prediction of composite cylinder method (Chatzigeorgiou et al. 2012) which can be found in *Appendix C*.

5.3.1 Longitudinal modulus of CFRP and FFRP

Figure 5-3 presents lamina longitudinal modulus, E_1 , versus carbon fibre volume fraction of fuzzy fibre and carbon fibre composites. In both cases, for 0% carbon volume fraction results start from 3 GPa, which corresponds to the modulus of the pure matrix. The nearly linear relationship between the modulus and volume fraction is observed for both two-phase and three-phase RVE models. For the maximum carbon fibre volume fraction, 25%, the longitudinal modulus of carbon fibre composite increased slightly from 61.7 GPa to 65 GPa for FFRP. The difference between carbon fibre and fuzzy fibre composites is small. Both curves for CF composite and fuzzy fibre composite agreed well with published data.

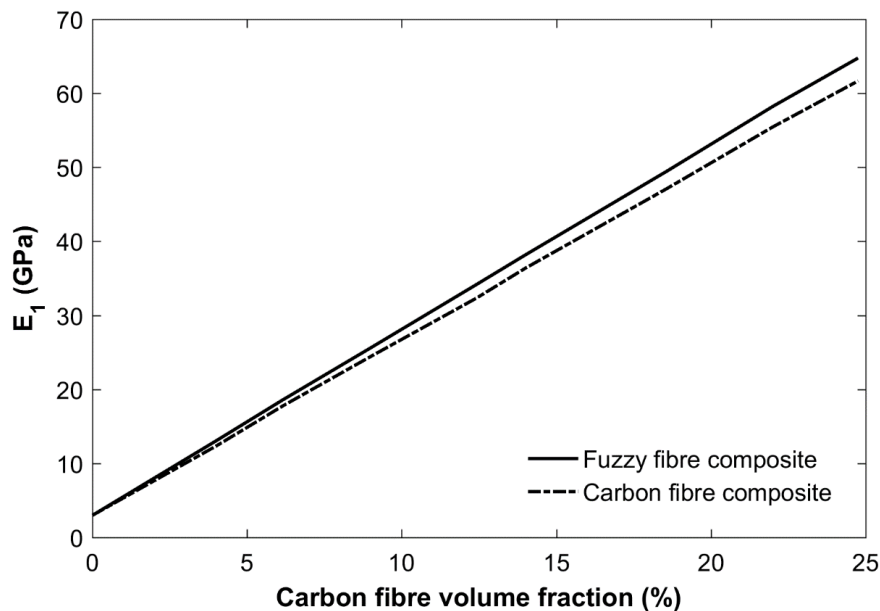


Figure 5-3 Longitudinal modulus of carbon fibre reinforced polymer versus carbon fibre volume fraction - the influence on the presence of CNTs interphase.

5.3.2 Transverse modulus of CFRP and FFRP

Transverse modulus, E_2 , for the two-phase model is almost insensitive to the increment of carbon fibre volume fraction (**Figure 5-4**). However, the significant increase was observed for the FFRP. Transverse modulus increased from 3 GPa, for 0% volume fraction, up to 10.4 GPa for 25% of carbon fibre volume fraction. In comparison to the two-phase composite, the presence of CNTs interphase increased transverse modulus of FFRP more than 200%, when the volume fraction reached above 20%.

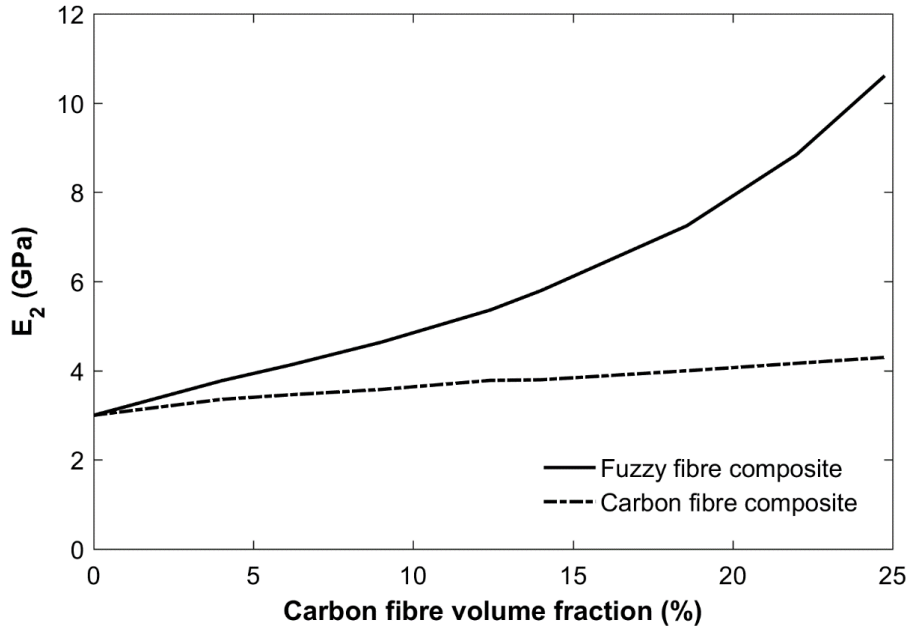


Figure 5-4 Transverse modulus of carbon fibre reinforced polymer versus carbon fibre volume fraction - the influence on the presence of CNTs interphase.

5.3.3 In-Plane Shear modulus of CFRP and FFRP

The relationship between in-plane shear modulus and carbon fibre volume fraction is shown in **Figure 5-5**. For 0% carbon fibre volume fraction, the shear modulus equals to the shear modulus of pure matrix. In the case of two-phase carbon fibre composite, slow and almost linear growth of the G_{12} is observed. In-plane shear modulus for FFRP increase in curvilinear and steeper manner with the carbon fibre volume fraction. For the maximum volume fraction of carbon fibre, the enhancement in shear modulus is almost double. No difference between results from present model and published data is observed.

5.3.4 Out-of-Plane Shear Modulus of CFRP and FFRP

Figure 5-6 presents the effects of the CNTs reinforced interphase and volume fraction on the out-of-plane shear modulus G_{23} . It is found that shear moduli values for carbon fibre composite model are nearly insensitive to the change of the carbon fibre volume fraction. Significant increases were observed in the case of the fuzzy fibre. This model represents the exponential growth of shear moduli. For 25 % of carbon fibre volume fraction, shear moduli enhanced more than 200%. These findings are in very good agreement with the available analytical model.

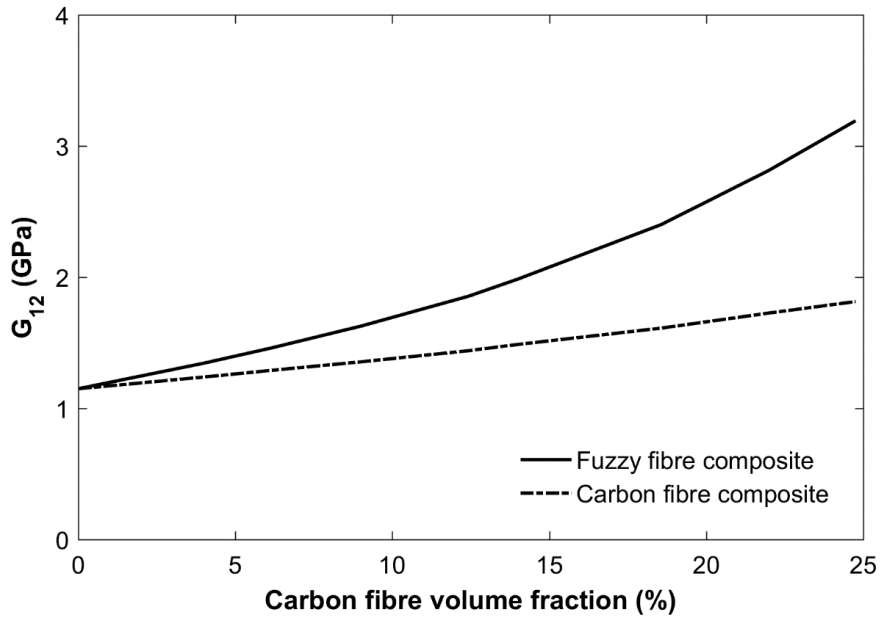


Figure 5-5 *In-plane shear modulus of carbon fibre reinforced polymer versus carbon fibre volume fraction - the influence on the presence of CNTs interphase.*

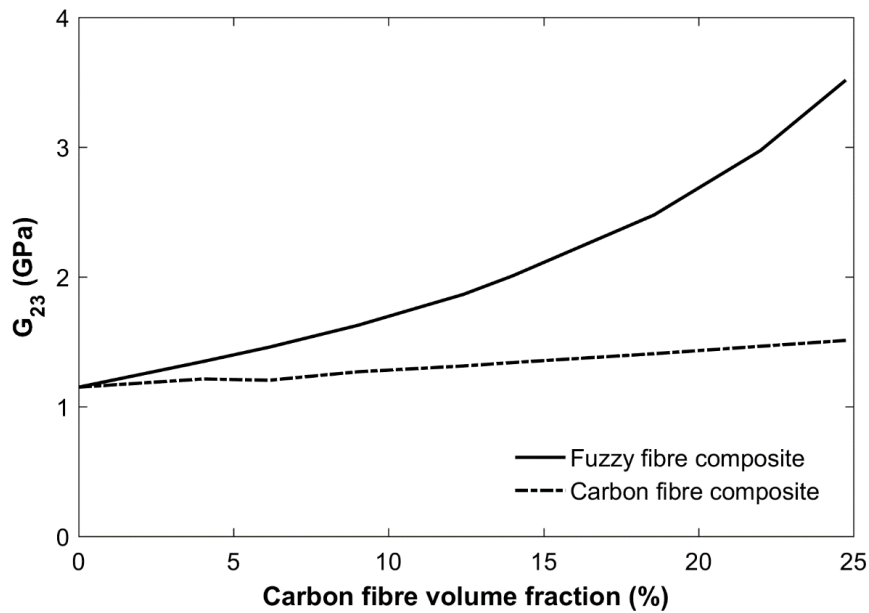


Figure 5-6 *In-plane shear modulus of carbon fibre reinforced polymer versus carbon fibre volume fraction - the influence on the presence of CNTs interphase.*

5.4 Discussion

The purpose of coating fibres with nanofillers is to strengthen the interphase between the fibre and matrix. Numerical results have shown a significant improvement of properties in the lamina transverse direction. Transverse properties of the carbon fibre-reinforced composites are dominated by matrix properties and are considerably lower in comparison to longitudinal properties, which are governed by carbon fibre. The presence of CNTs in the matrix surrounding the carbon fibre enhances the performance of the FFRP. This enhancement is attributed to the unique orientation where the axial direction of the CNT is aligned with the transverse direction of the carbon fibre.

These numerical results were compared with analytical results for the same type of material given by the Chatzigeorgiou et al., 2012. Firstly, the CNTs reinforced interphase properties predicted with Mori-Tanaka agreed well with the published data. Moreover, numerical results predicted by the hexagonal RVE perfectly matched analytical results calculated by composite cylinders method (Chatzigeorgiou et al., 2012), which are not shown on the graphs (*see Appendix C*). Composite cylinders method uses the cylindrical coordinate system to describe the orientation of the interphase and make the analytical way possible. This method is commonly used to simulate FFRP due to the axisymmetric nature of the interphase (Kulkarni et al., 2010; Chatzigeorgiou, Seidel and Lagoudas, 2012). However, the present hexagonal RVE model frees us from the cylindrical coordinate system thanks to the application of the VEORIENT command. This model enables to efficiently study a various distribution and directions of nanofillers, for example, the graphene sheets parallel aligned to the fibre surface or randomly distributed in the reinforced interphase (Pawlik, Dean and Lu, 2017).

The unique radial orientation of CNTs on carbon fibre surface presented a significant improvement in matrix dominated lamina properties like transverse elastic modulus and both shear moduli. These findings were also supported by the experimental study. (Yu *et al.*, 2000). According to Kulkarni *et al.*, (2010), the transverse elastic modulus of FFRP can generally be improved about three times with respect to the value of the pure matrix. In this study, for 25 % carbon fibre volume fraction, the transverse modulus increased more than twice. However, the possible increase in properties depends on factors like the volume fraction, size and properties of the CNTs, which will, in turn, affect the interphase properties.

Contrarily, the presence of the CNTs radially grown on the surface of carbon fibre has negligible influence on the longitudinal modulus of the fuzzy fibre composite. The highest

improvement of longitudinal modulus was observed for the 25% carbon fibre volume fraction and results in a 5% increase. This lower increase was associated with weaker properties of the interphase in the carbon fibre direction (1-direction in global coordinate system) which were caused by lower transverse properties of the single nanotube.

The amount of increase of the elastic constants is also highly dependent on the interphase dimensions. When comparing FFRP to FRP with GNPs coated on fibre, one must notice that there is a significant difference in thickness between two nano-reinforced interphases. In this case, the interphase had a relatively high thickness of 2 μm , which was dictated by the length of CNTs radially grown on the carbon fibre. Whereas, the GNPs reinforced interphase was estimated as only 54 nm. The thickness of the interphase influences on the maximum volume fraction of carbon fibre. For this particular case, introducing CNTs into the FRP restricted the maximum volume fraction of carbon fibre to 25%. Because of CNTs are radially grown on the CF, the diameter increased from 5 microns for CF to 9 microns for Fuzzy Fibre (CF+ CNTs reinforced interphase). Thus for 25% of carbon fibre, the total volume fraction of fuzzy fibre was 81%.

The 200% enhancement of the transverse elastic modulus of lamina was related to both the interphase properties and interphase thickness. While the introduction of CNTs has a positive influence on the transverse properties of the lamina, there are significant limitations of the longitudinal properties caused by the lower volume fraction of the carbon fibre. Because of the orientation of the CNTs, the longitudinal properties of the FFRP remains almost insensitive to the presence of interphase. These longitudinal properties are dictated by the carbon fibre properties and volume fraction. It can be concluded that the thickness of the interphase is related to the type of the nanofillers and the method of the introduction, which indeed relates to the orientation.

The main limitation of this study is the assumption of perfectly straight CNTs, evenly distributed on the fibre surface. In reality, during the manufacturing process, some defects may occur. Moreover, the thickness of CNTs interphase may not be uniform throughout the fibre. Besides, these micromechanical models are simulated in elastic region of the material behaviour. It would also be beneficial to simulate the designed model to predict the influence of the CNTs on the FFRP material strength. These problems will be considered in future work.

5.5 Summary

To sum up, this chapter has studied the effects of the CNTs interphase on the fuzzy fibre composite using computational micromechanics. Mori-Tanaka model has successfully estimated the CNTs reinforced properties. The predicted CNTs interphase properties agreed well with the one predicted with self-consistent method (Chatzigeorgiou et al. 2012). The RVE with hexagonal fibre array has successfully predicted elastic constants of the fuzzy fibre composite. The results have indicated that CNTs have a significant influence on the transverse properties of the FFRP. The numerical model has allowed dealing with arbitrary shapes of fibres, which cannot be always tackled analytically. Direction-dependent properties of the interphase and fibres can be readily incorporated. The mechanical properties of FFRP in different conditions can be determined efficiently.

6 Effects of spraying nanofillers on mechanical properties of Fibre Reinforced Polymers - experimental results.

6.1 Introduction

More recently, a spraying technique to introduce CNTs (Mujika *et al.*, 2012; Almuhammadi *et al.*, 2014; Zhang *et al.*, 2015), GNPs (Yavari *et al.*, 2010) or a mixture of CNTs and GO (Rodríguez-González *et al.*, 2018) have drawn increasing attention. It allows for better control of nanofillers and shows a huge potential to scale up to an industrial level. Zhang *et al.* (Zhang *et al.*, 2015) reported a 47 % increase in interlaminar fracture toughness at 0.047 wt% of CNTs sprayed on nine layers woven carbon fibre prepreg. Rodriguez-Gonzalez (Rodríguez-González *et al.*, 2018) investigated the synergistic effects of the MWCNTs/GO sprayed at the midplane of the CFRP laminate. The highest improvement of 17% and 14 % improvement in mode I and mode II strain energy release was reported for the mixture of MWCNTs/GO.

This chapter presents experimental results on two types of laminates - with nanofillers sprayed either on prepreg surface or carbon fibre fabric. Following the procedure described in Chapter 3.3, laminate samples were prepared for testing. Promising results on synergistic effects of the nanofillers (Wang *et al.*, 2015; Kostagiannakopoulou *et al.*, 2017) motivated the author to investigate the influence of spraying CNTs/GNPs to the prepreg on mechanical properties of CFRP Laminates. The first section presents the mechanical properties of CFRP, where CNTs and/or GNPs were sprayed on the prepreg surface. This approach created a nano-reinforced layer, which is located between prepreg plies. The effects of this nano-reinforced layer were investigated by mechanical tests such as three-point bending, short beam test and double cantilever beam tests.

In the second part of the chapter, spraying method of GNPs solution directly on carbon fibre surface was trialled to make a GNPs reinforced interphase. The nanofillers solution usually consists of nanofillers and solvent. Here epoxy/hardener was purposely added to the spraying solution to assist the bonding of the coating to carbon fibre (Qin *et al.*, 2015). Mechanical properties of the CFRP laminates, including flexural modulus, strength and interlaminar shear strength were investigated and compared with untreated samples.

6.2 Experimental results on the carbon fibre prepreg sprayed with nanofillers

6.2.1 Flexural properties

Figure 6-1 presents the experimental set-up of three-point bending test performed using Tinus Olsen mechanical testing machine. Five long beam samples of length (l) 100mm, width (b) 15 mm, and thickness (h) 2 mm for each group of materials were tested. Experiments were conducted according to the BS EN ISO 14125 (1998) standard with test cross-head loading speed of 2 mm/min. The radii of supports and loading cell were 5 mm, and the span length between two supports, (L) was 80 mm.

The flexural strength (σ_f) and flexural modulus (E_f) were calculated as follows:

$$\sigma_f = \frac{3F_{max} L}{2bh^2} \quad 6-1$$

$$E_f = \frac{L^3}{4bh^3} \left(\frac{\Delta F}{\Delta S} \right) \quad 6-2$$

where F_{max} is the maximum load in Newton and $\left(\frac{\Delta F}{\Delta S} \right)$ is the slope of the linear portion of the force displacement graph.

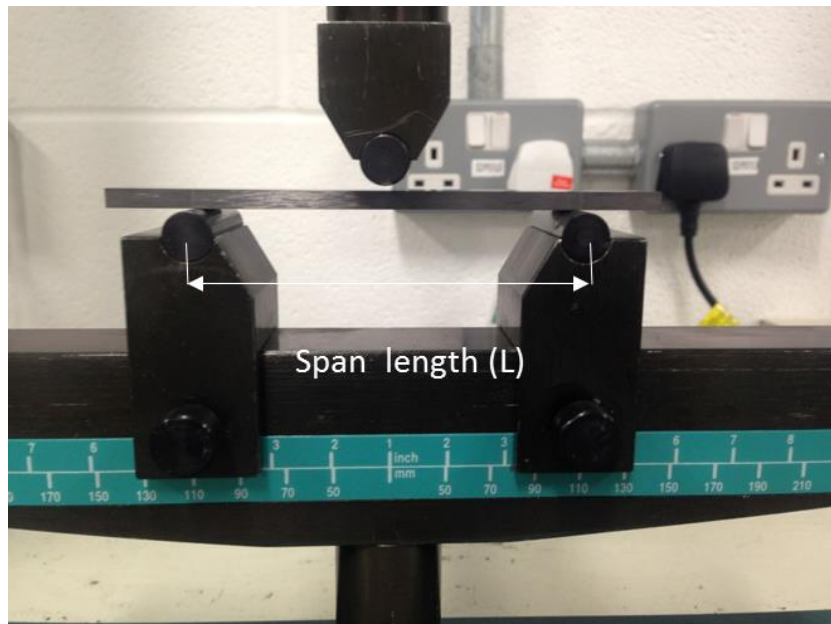


Figure 6-1 Three-point bending test rig according to BS EN ISO 14125 (span length 80mm).

Figure 6-2 presents a typical load-deflection curve for the 90° unidirectional laminate in the three-point bending test. Force increased nearly linearly with the deflection until a rapid drop in force was observed when the sample failed in the middle by the fast fracture. All five samples showed consistent mechanical behaviour and recorded data were used to calculate flexural modulus and strength of this group of samples. Following the same procedure, three other groups of materials including 0° and 90° pure CFRP and 0°CFRP sprayed with GNPs and CNTs were tested.

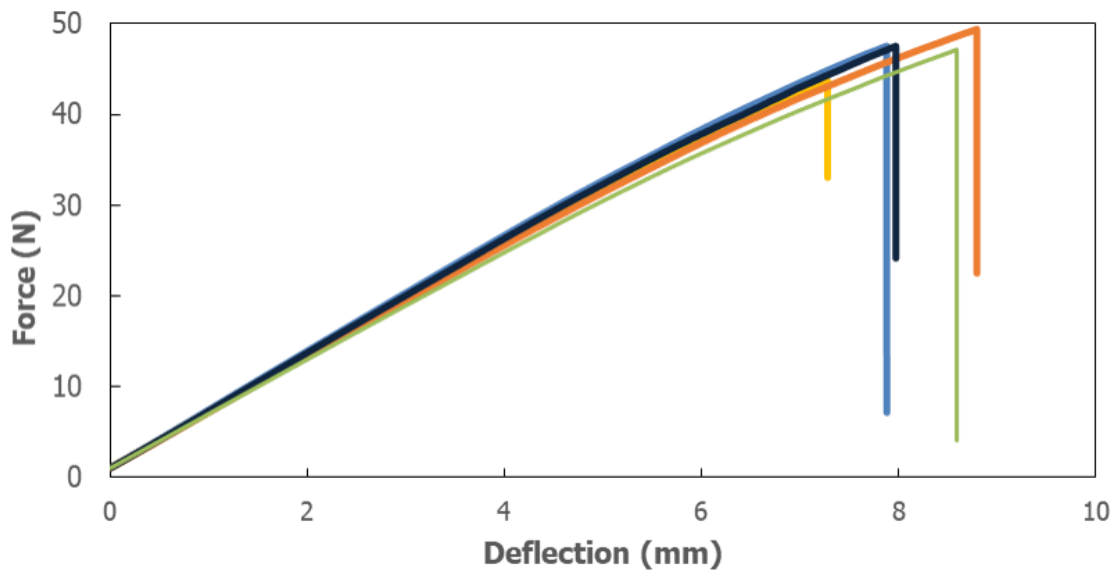


Figure 6-2 Load-deflection curve for UD 90° carbon fibre long beam in the three-point bending test. The laminate sample was prepared from prepreg plies sprayed with nanofillers.

Table 6-1 shows the comparison of long beam flexural results on carbon fibre prepreg subjected to spraying treatment. To the best of author’s knowledge, no flexural results on nanosprayed prepreg have been reported previously. Mean flexural modulus (E_f) of pure UD 0° CFRP increased from 111.25 to 113.25 GPa as a result of spraying nanofillers. The enhancement in E_f was around 2%. Whereas the flexural strength increased by 74.2 MPa, which is equal to a 4.8% increase. Generally, flexural modulus in 0 degrees is mainly driven by exceptionally high tensile properties of fibres. This moderate improvement is attributed to increased resin properties due to the presence of nanofillers. In 90° fibre direction, the flexural modulus of laminate increased by 0.14 GPa due to the spraying method, yielding 1.8% enhancement. On the other hand, a 5.6% decrease in flexural strength was observed. According to Madkuhar and Drzal (1991), the flexural strength of 90° unidirectional laminate is the most

sensitive parameters to the interfacial adhesion between the fibres and matrix in the three-point bending test. Spraying nanofillers on the prepreg were more likely to improve the interlaminar region than the interfacial region between fibres and matrix. Thus, properties such as ILSS or fracture toughness are speculated to show higher improvement. To measure these properties SBT and DCB test were performed and presented in following sections.

Table 6-1 Comparison of 0° and 90° flexural properties of the unidirectional carbon fibre reinforced laminate (pure CFRP and CFRP reinforced with CNTs and GNPs).

| Laminate | UD 0° (Pure CFRP) | UD 0° (CFRP+GNPs +CNTs) | UD 90° (Pure CFRP) | UD 90° (CFRP+GNPs +CNTs) |
|------------------|-------------------|-------------------------|--------------------|--------------------------|
| Length (mm) | 100 | 100 | 100 | 100 |
| Width (mm) | 15.01±0.02 | 15.01±0.03 | 15.01±0.01 | 15.01±0.02 |
| Height (mm) | 1.98±0.03 | 2.00±0.08 | 1.79±0.02 | 1.85±0.03 |
| Span (mm) | 80 | 80 | 80 | 80 |
| F_{max} (N) | 742.4±105 | 792.2±40 | 46±3 | 47±4 |
| S_{max} (mm) | 7.51±0.8 | 7.68±0.72 | 8.91 ±0.88 | 8.09±0.46 |
| E_f (GPa) | 111.25±5.2 | 113.25±6 | 7.66±0.5 | 7.80±0.2 |
| σ_f (MPa) | 1517.4±95 | 1591.6±95 | 116±3 | 109.8 ±7 |

6.2.2 Interlaminar properties

Due to its simplicity and ease of use, short beam test (SBT) is one of the most popular test method to determine interlaminar properties. The principle is the same as the three-point bending test except for the difference in the beam dimensions. In SBT, the length of span, L, is a low multiple of the specimen thickness, t. Span to thickness ratio between 4 and 5 is recommended for all kinds of fibre reinforcements (BS EN ISO 14130, 1998). The main drawback of SBT is that samples do not always fail in the pure shear mode. Some samples may fail by tensile, compressive or plastic deformation (**Figure 6-3**). It is necessary to record the mode of failure. Apparent interlaminar shear stress τ (MPa) is calculated from SBT results in the following formula:

$$\tau = \frac{3}{4} \frac{F}{bh}$$

6-3

where F (N) is the maximum load, b (mm) is the width of the specimen, and h (mm) is its thickness.

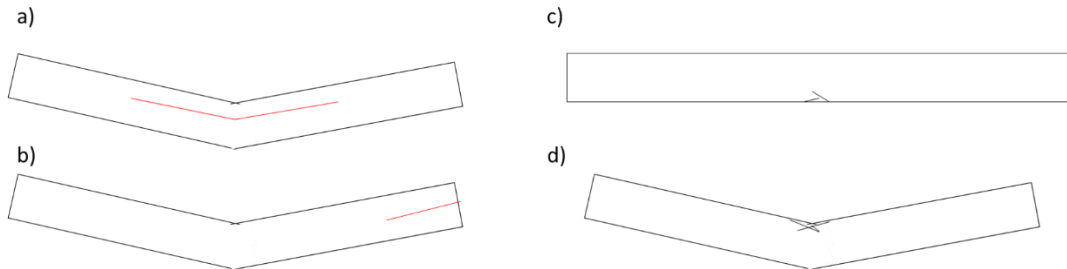


Figure 6-3 Typical failure modes in SBT acceptable single and multiple pure shear failure modes (a,b), unacceptable failure mode: tension (c) and compression (d) (schematic drawing created based on BS EN ISO 14130, 1998).

The experiment was performed using a universal tensile machine with the load cell of 50 kN in room temperature (see **Figure 6-4**). 5 specimen was used for each group, and 10 samples were tested in total. Specimens were 20 mm long, 15 mm wide and 1.87 mm thick. The span length was set to 9.6 mm corresponding to approximately 5:1 span to thickness ratio. The crosshead speed was 1 mm/min. The support and loading radii were 2 mm and 5 mm respectively. **Figure 6-5** presents force-deflection graphs, where black colour represents pure CFRP, and red colour shows CFRP sprayed with nanofillers. Typical SBT result of FRP samples follows a linear relationship with the sudden drop of force. In the present project, all samples exhibited nonlinear behaviour. The maximum value of force was used in the equation 6-3 to calculate apparent interlaminar shear strength (τ).



Figure 6-4 Short beam test experimental set-up (Loading roller diameter =10mm, support diameter=4mm).

The average values of τ were 89.2 and 89.4 MPa for pure CFRP and CFRP reinforced with nanofillers respectively. This relative increase amounted to 1%. Contrary to the expectations, all short beam tests were unable to produce a pure shear between layers. All samples failed in either mixed compression or plastic shear mode. It is imperative to achieve pure shear failure mode to make meaningful SBT. It is thus inconclusive if nanofillers has any influence on the apparent interlaminar shear strength.

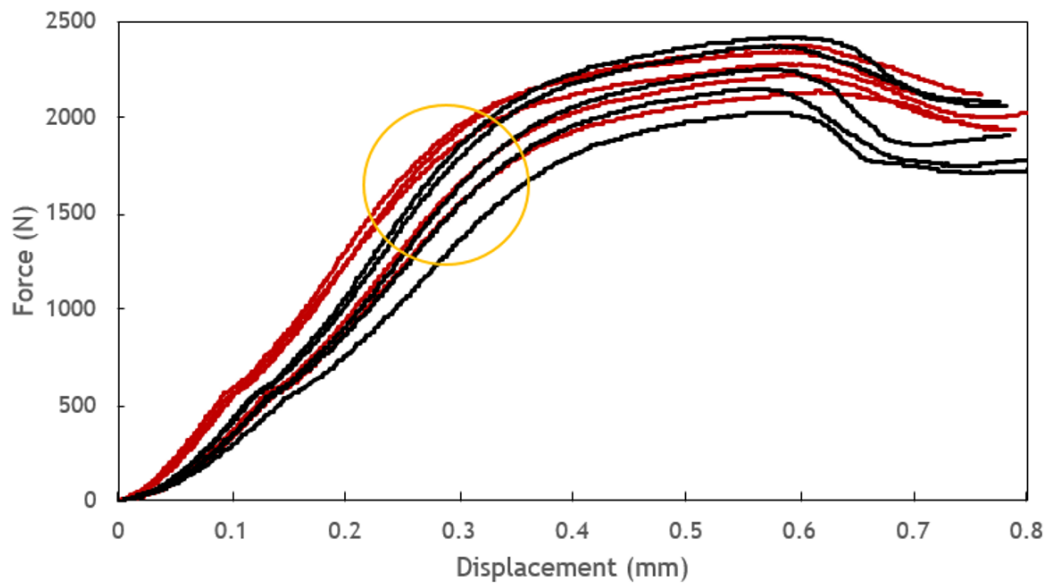


Figure 6-5 Force-deflection results of short beam test (black colour represents pure CFRP, red colour represents CFRP sprayed with nanofillers solution).

Further investigation was undertaken to reveal reasons for causing unacceptable failure mode in short beam test. The following possible issues were identified namely:

- under cured laminate,
- sample dimensions and span to thickness ratio,
- delamination of the sample was not clearly visible with the bare eye.

Glass transition temperature (T_g) was measured using dynamic mechanical analyser (DMA8000 Perkin Elmer). In **Figure 6-6**, peak T_g was measured approximately 135°C and agreed well with the glass transition temperature provided by prepreg datasheet supplier. This experimental result eliminated the possibility of under-cured laminate as a reason for lack of desired pure shear failure mode in SBT.

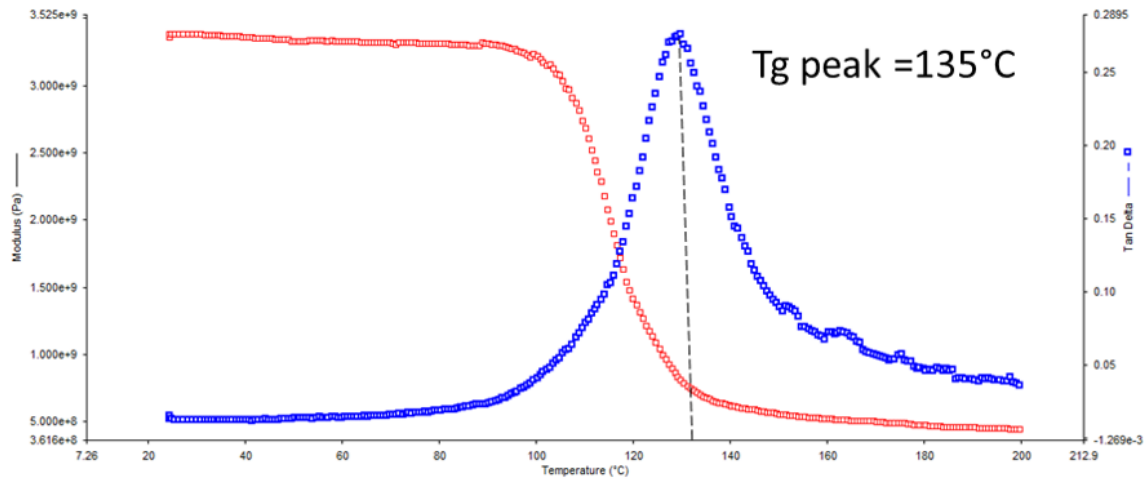


Figure 6-6 Glass transition temperature of MTC801 laminate measured by DMA.

Secondly, the discrepancy in recommended testing conditions between British and American standards exists. ASTM D2344 (2016) standard suggests using three times thicker specimen and loading roller and support of smaller radii 3.0 mm and 1.5 mm respectively. Cui et al. (1994) investigated the influence on the loading diameter and specimen dimensions on ILSS results. It was found that plastic deformation mode, as observed in this study, might be caused by too small space between the loading roller and support rollers. This small space tends to accommodate the specimen plastic deformation so that specimen had been “squashed” before final interlaminar shear failure occurred. Thus, it is advisable to increase the span length between support rollers or use smaller loading roller.

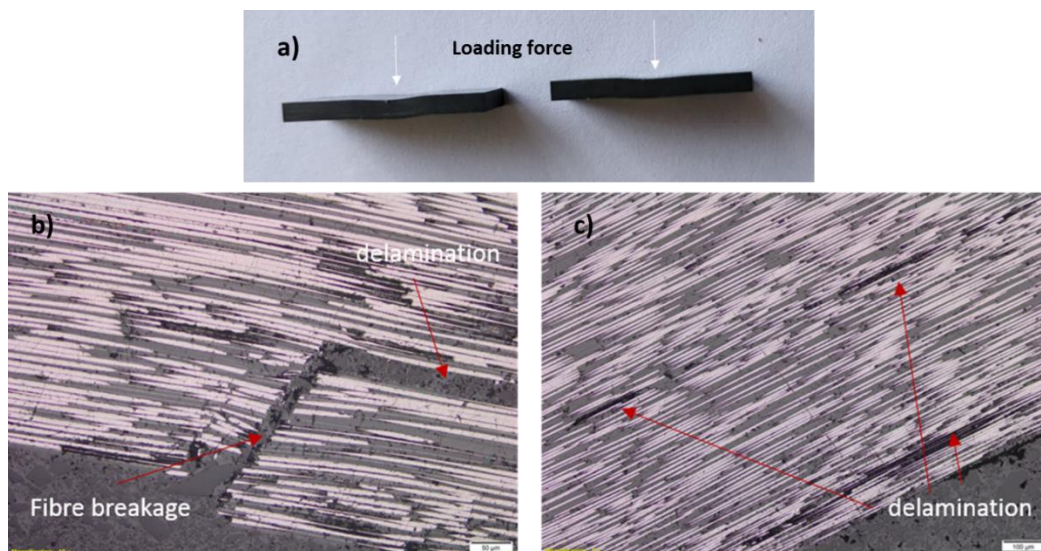


Figure 6-7 Samples inspection after SBT. Digital images of tested samples (a) optical micrographs of the tested sample (b) region near the load cell compression force and (c) delamination observed on the side view of the sample.

Although the final failure mode of this SBT was unacceptable, it is believed that the interlaminar failure could appear before the plastic deformation. Similar conclusions were presented recently by Zhou et al. (2016). This research group investigated the influence of CNTs on the ILSS of six different group of samples: carbon fibre/epoxy composites with and without CNTs in the matrix, with and without CNTs in the fibre coating, with varied wt% of CNTs in both coating and matrix. The thickness of the samples varied from 2.7 to 4.4 mm, whereas the span length remained at 15 mm the corresponding span to thickness ratio value from 3.4 to 5.5. During the SBT, the area in the sample just beneath the loading roller was examined under the SEM. Interestingly, most of the testing samples with CNTs leads to similar non-linear behaviour of the force-deflection curve. However, the force used to calculate interlaminar shear strength was selected based on the observation onset of the delamination. More linear behaviour with a sudden drop of force when the initial delamination occurs was observed for samples with smaller thickness; therefore, larger span to thickness ratio. The behaviour of force-deflection curves also depended on the location of CNTs. More nonlinear behaviour was observed with the sample with CNTs mixed with the resin or both with the resin and fibre coating. Considering the SEM images reported by Zhou et al. (2016), it was found that initial delamination occurred at the various stages of the force-deflection curve for different groups of samples. In the present project, maximum force selected to calculate the ILSS may not represent true initial delamination. According to Zhou et al. (2016) SEM analysis, it can be reasonably speculated that initial delamination happened in the region denoted by a yellow circle (**Figure 6-4**), the improvement in ILSS between pure CFRP and sprayed with nanofillers would be significantly higher.

The designed experiment followed all standard recommendation; presented results yield only moderate enhancement by spraying of nanofiller. The actual effects of sprayed nanofillers on interlaminar properties may be significantly higher with more information on the initiation of delamination. Revising sample dimensions, changing testing conditions and adopting digital image correlation have been considered to improve future experiment. Revised testing conditions were accommodated for the wet lay-up laminate and presented in chapter 6.3.

6.2.3 Fracture toughness

6.2.3.1 Experimental set-up

The double cantilever beam (DCB) test was used to measure the mode I fracture toughness of CFRP. The set-up of this test is presented in **Figure 6-8a** and follows the recommendation given by ASTM D5528.889-1 standard. Prior to testing, samples required some additional preparation (see **Figure 6-8b**). All specimen and hinges were polished with abrasive paper grade 200 and cleaned with acetone. Then, hinges were glued to the pre-cracked side of the sample with two-part epoxy glue Araldite and cured in the room temperature for 24 hours. The specimen side was coated with white correction fluid, which aids the visibility of crack tip propagation. The printed paper scale was attached to the side of the specimen to record the crack propagation. The tip of the crack insert was marked explicitly. After tensile force was applied through the hinges, the crack started to propagate causing delamination of the sample as seen **Figure 6-8c**. A high-resolution Panasonic HC-X920 camera recorded crack propagation with respect to time.

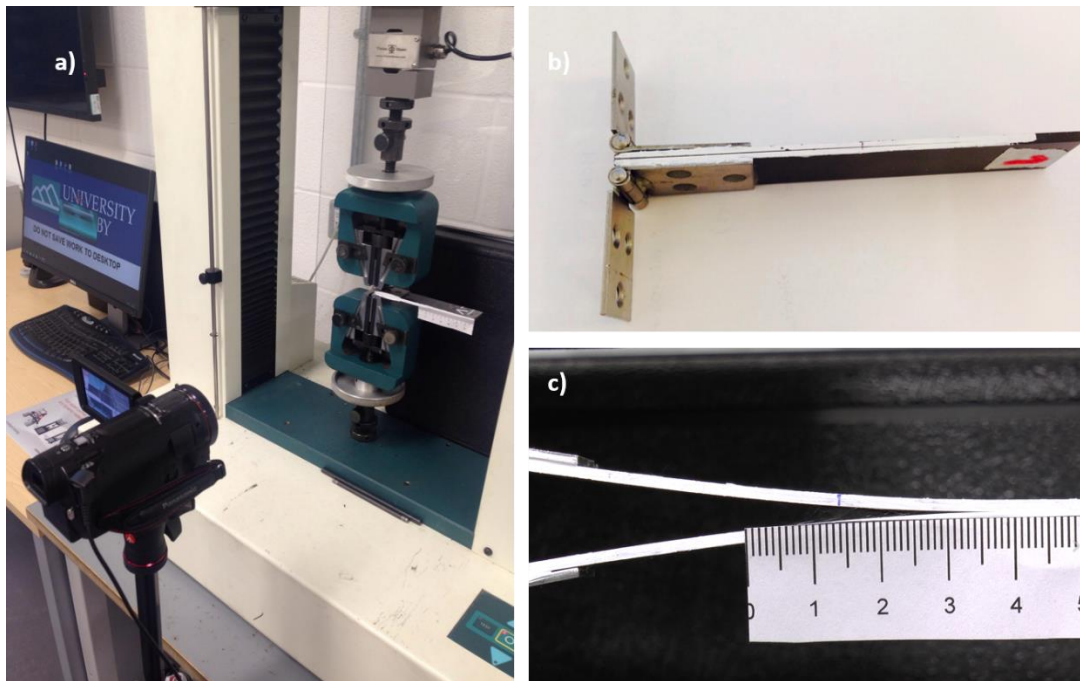


Figure 6-8 Double cantilever beam test (DCB) (a) Experimental set-up (b) Sample preparation (c) Crack propagation recording.

Four groups of CFRP samples (in total 19 specimens) were under DCB testing. The details of the samples were shown in **Table 6-2**. The difference between each group of materials was the amount and type of sprayed nanofillers.

Table 6-2 Dimensions and specifications of specimens prepared for fracture toughness test.

| ID | Description | Length (mm) | Thickness (mm) | Width (mm) | Initial Crack (mm) | Number of specimen | Specimen numbering |
|------|---------------------|-------------------|-------------------|---------------|--------------------------|-----------------------|-----------------------|
| IA | Pure CFRP | 140.09 (±0.05) | 3.43 (±0.06) | 25 | 73 | 3 | 1,2,3,4 |
| IIB | 0.00035 wt% CNTs | 140.15 (±0.2) | 3.36 (±0.12) | 25 | 73 | 5 | 5,6,7,8,9 |
| IIIC | 0.00065 wt% GNPs | 131.83 (±0.06) | 3.39 (±0.08) | 25 | 65 | 5 | 10,11,12,13,14 |
| IVD | 0.00044 wt% GNPs | 131.58 (±0.07) | 3.33 (±0.11) | 25 | 65 | 5 | 15,16,17,18,19 |

6.2.3.2 Initial loading

Firstly, each specimen was loaded with a constant crosshead speed of 4.0 mm/min until the mark on the specimen, where the release film ends and crack initiation begin. The loading was stopped when crack propagated for another 5 mm from the crack insert. The sample was unloaded at the crosshead speed of 15 mm/min, and new crack tip was marked on the side of the sample. **Figure 6-9** presents the force deflection curve during the initial loading across various samples. Sample 3 (dashed line) was selected as an example for post-processing. In the case of the loading curve, almost linear relationship of the force against displacement was observed. When the force reached the value around 47 N, a rapid drop of force (approximately 30%) was noticed, which was caused by an unstable crack growth from the tip of the insert film.

Figure 6-10 presents two timeframes of the recorded video for sample 3, which shows that the initial crack increased rapidly from 73 mm to 80 mm within 1 second. After completing experiment of this sample, further examination of the insert film showed small delamination from the end of the crack insert film (see **Figure 6-10**). The width of this delamination area is 7 mm, which agreed well with the sudden increase in crack length as explained above. ASTM standards suggest that this unstable jump from the insert might be an indication of the problem with the insert. Possible problems causing this behaviour are listed as tear and fold of PTFE film or that the insert was not completely disbanded from the laminate. At this occasion, the

length of the PTFE insert film was also measured and matched the established value (73 mm). This delamination was very likely caused by insufficient pressure applied during the manufacturing process.

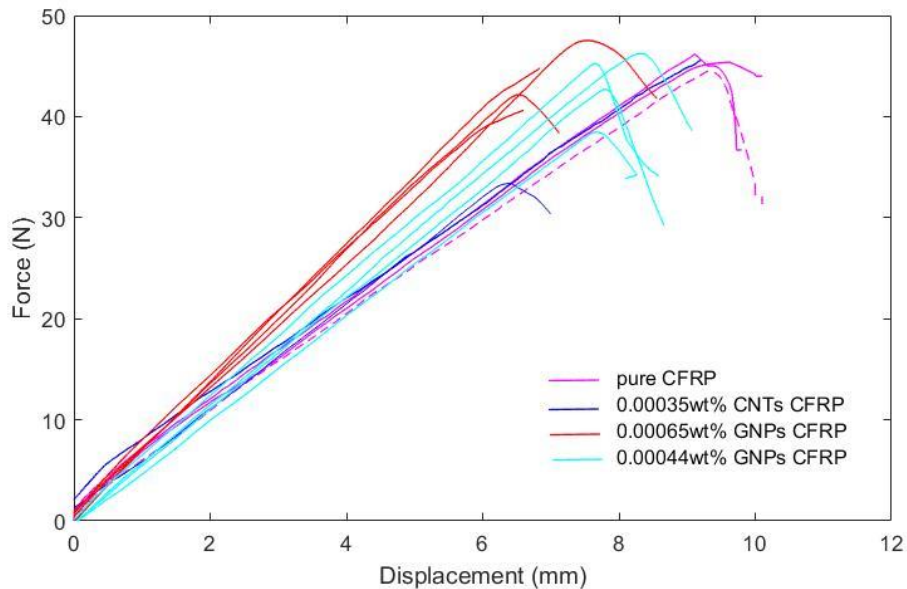


Figure 6-9 Load displacement trace for DCB test – initial loading. Dashed line represents sample 3 (pure CFRP), which has been used for exemplar post-processing.

All of the samples were initially loaded to eliminate the effects on that unstable crack propagation and reloaded to continue the test. Because of this crack behaviour, a new delamination tip point was marked at the position of initial crack arrest, e.g., for the sample 3 it was 80 mm. This procedure induces a natural Mode I pre-crack in the DCB specimen.

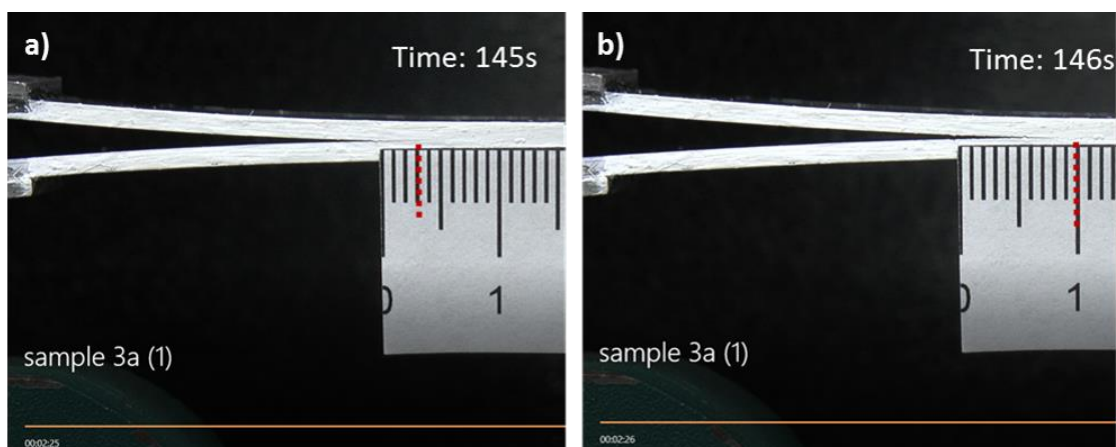


Figure 6-10 Frames from the video recorded during the initial loading of sample 3 (a) crack length at the time of 145 seconds is 74mm (b) rapid unstable crack propagation to 80 mm a second later.

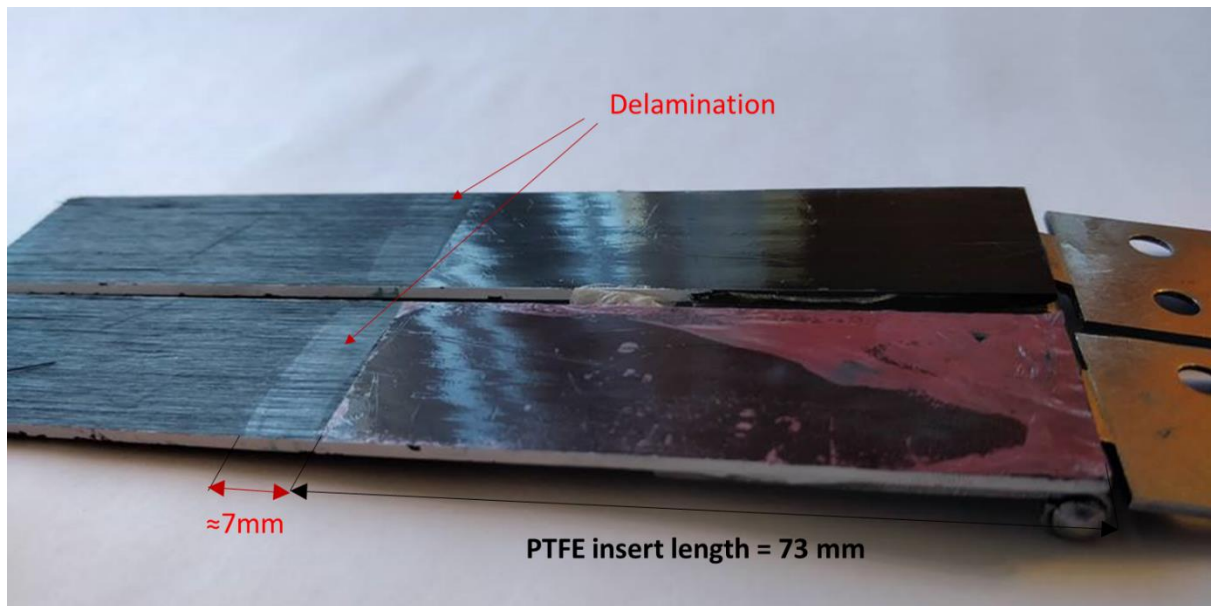


Figure 6-11 PTFE insert film inspection of the sample after the completion of the DCB test.

6.2.3.3 Reloading

After initial loading, each specimen was reloaded at the same constant speed of 4mm/min without stopping until the crack propagated further and reached the value above 45 mm from new marked crack arrest (i.e. 80 mm in the example of sample 3). During the experiment, force against load point displacement along with delamination and time were recorded.

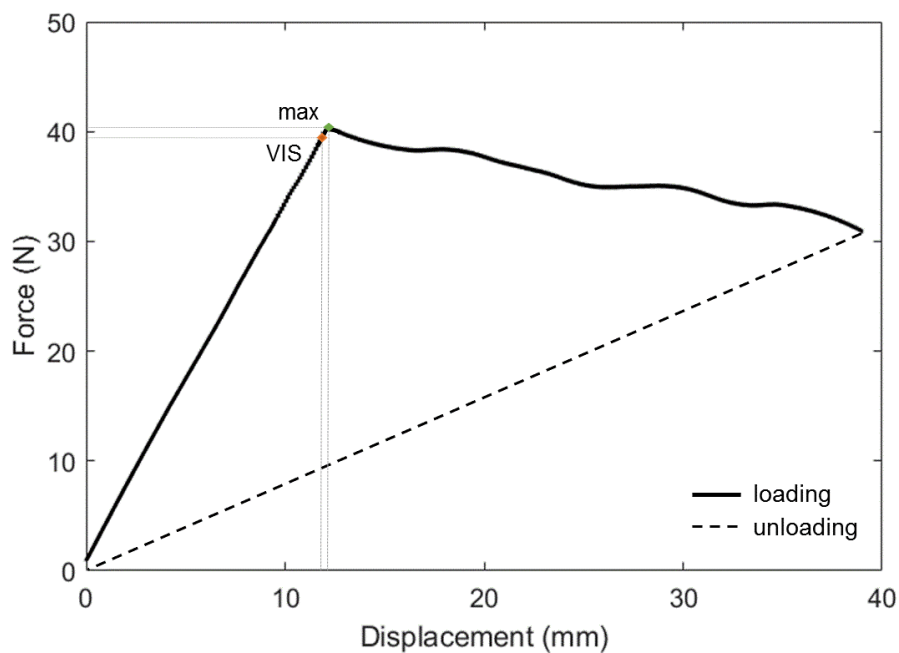


Figure 6-12 Example of the load-displacement trace for DCB test – reloading of sample 3.

The example of the load-displacement trace for reloading of sample 3 was presented in **Figure 6-12**. A linear relationship between force and displacement was observed during the first phase of reloading. When displacement reached around 12 mm, and the maximum corresponding force was equal to 40 N, new crack propagation begins. Force slowly decreases in a non-linear manner. The test was stopped when the total crack length reached 125 mm, which corresponded to 32 N force and 38 mm displacements. Finally, the sample was unloaded at a constant speed of 15 mm/min.

6.2.3.4 Post-processing

In the post-processing, recorded video of crack propagation was converted to timeframes to identify a time for given crack length. Then force and displacement data can be extracted at the same time point. The property measured by the DCB test is G_{IC} called the mode I strain energy release rate and can be found by three different methods such as modified beam theory, compliance calibration method and modified compliance calibration. This subchapter presents example calculations for a set of experimental data from sample 3 (pure CFRP). All calculations were conducted in an excel spreadsheet (*see appendix B*).

i. Modified Beam Theory (MBT)

The strain energy release rate (G_{IC}) of a perfectly built-in (clamped at delamination front) double cantilever follows the expression:

$$G_{IC} = \frac{3P\delta}{2ba} \quad 6-4$$

where: P is the load measured by the load cell of the testing machine, b is the specimen width, a is the crack length, and δ is the displacement of the cross-head testing machine. However, in practice this formula usually overestimate G_{IC} because factors such as rotation may occur at the delamination front. To correct this, the DCB test is treated as if it has a longer delamination ($a+|\Delta|$), where Δ is a correction factor. Consequently G_{IC} is described as equation 6-5.

$$G_{IC} = \frac{3P\delta}{2b(a+|\Delta|)} \quad 6-5$$

The correction factor is determined experimentally by generating a least squares plot of the cube root of compliance $C^{1/3}$ as a function of crack propagation length (**Figure 6-13**).

Where, C is the ratio of load point displacement δ to the applied load P . This method also allows the modulus, E_{1f} to be determined as follows:

$$E_{1f} = \frac{64(a+|\Delta|)^3 P}{\delta b h^3}$$

6-6

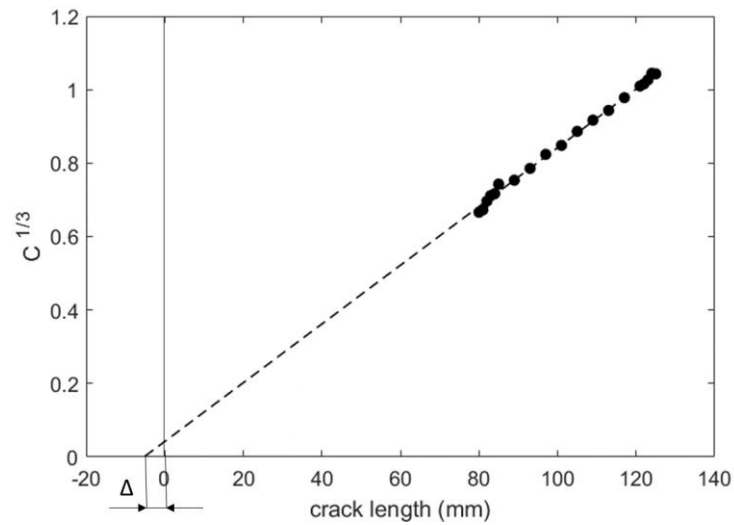


Figure 6-13 Modified Beam Theory – determination of the correction factor for specimen 3.

ii. Compliance Calibration Method (CC)

Calculation of the strain energy release rate (G_{IC}) using compliance calibration (CC) method follows the equation 6-7. To find n component, the least square plot of log compliance C versus log a of all propagation values is generated as presented in **Figure 6-14**. The component n is calculate from the slope of this curve and in this example equals 2.887.

$$G_{IC} = \frac{n P \delta}{2 b a}$$

6-7

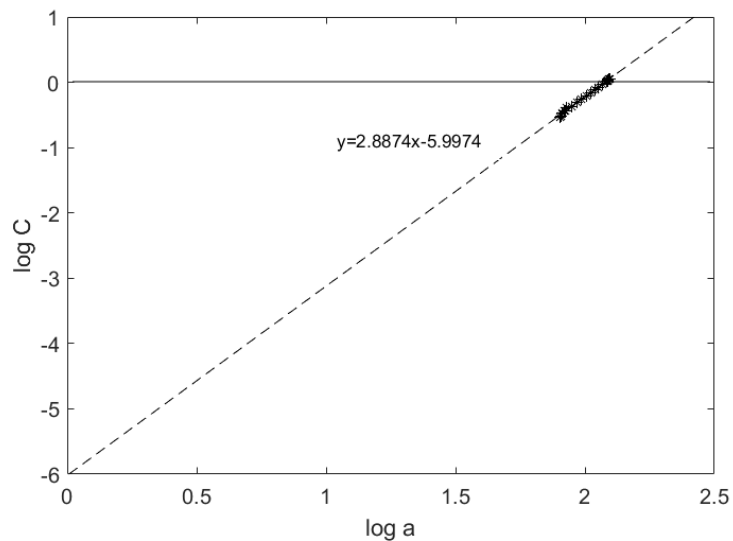


Figure 6-14 Compliance Calibration method – determination of n component for specimen 3.

iii. Modified Compliance Calibration Method (MCC)

The strain energy release rate (G_{IC}) calculated using the Modified Compliance Calibration method (MCC) follows the expression:

$$G_{IC} = \frac{3P^2C^{2/3}}{2A_1bh} \quad 6-8$$

Where: h is the thickness of the sample and A_1 is the slope of the line generated from a least squares plot of the delamination length normalised by specimen thickness (a/h) as a function of the cube root of compliance ($C^{1/3}$). **Figure 6-15** presents an example of modified compliance calibration graph representing sample 3, where A_1 value is 36.49.

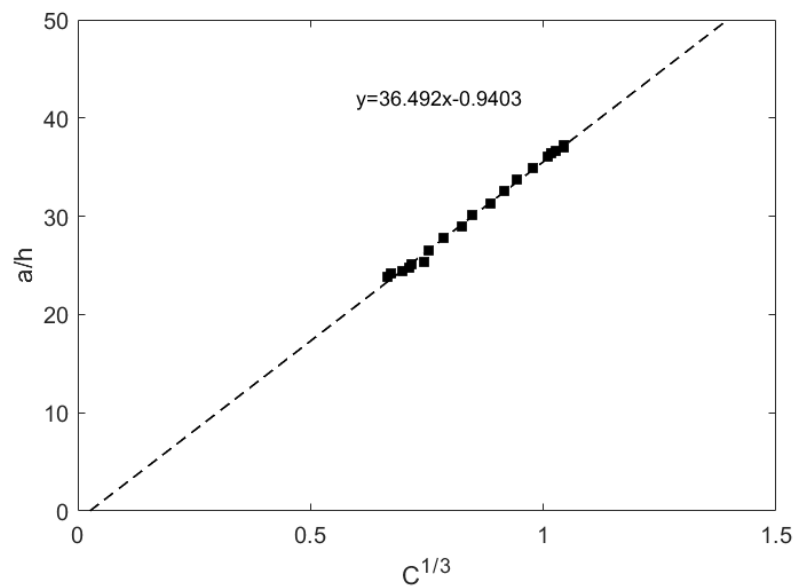


Figure 6-15 Modified Compliance Calibration Method – determination of A_1 component for sample 3.

iv. Comparison of different methods

The comparison of G_{IC} values calculated using the above mentioned methods was presented in **Figure 6-16**. The vertical and horizontal axes represent G_{IC} and delamination length respectively. For the initial crack length, 80 mm, the mode I G_{IC} was approximately 330 Nm/m^2 for all methods. Nonlinear increase of strain energy release rate with delamination length was observed. The difference in average G_{IC} for the same delamination length was less than 1.3% for three different data reduction approaches. This variation range is consistent with the recommendation of ASTM standard. Calculations of G_{IC} for remaining 17 samples follows MBT theory as recommended (O'Brien and Martin, 1993).

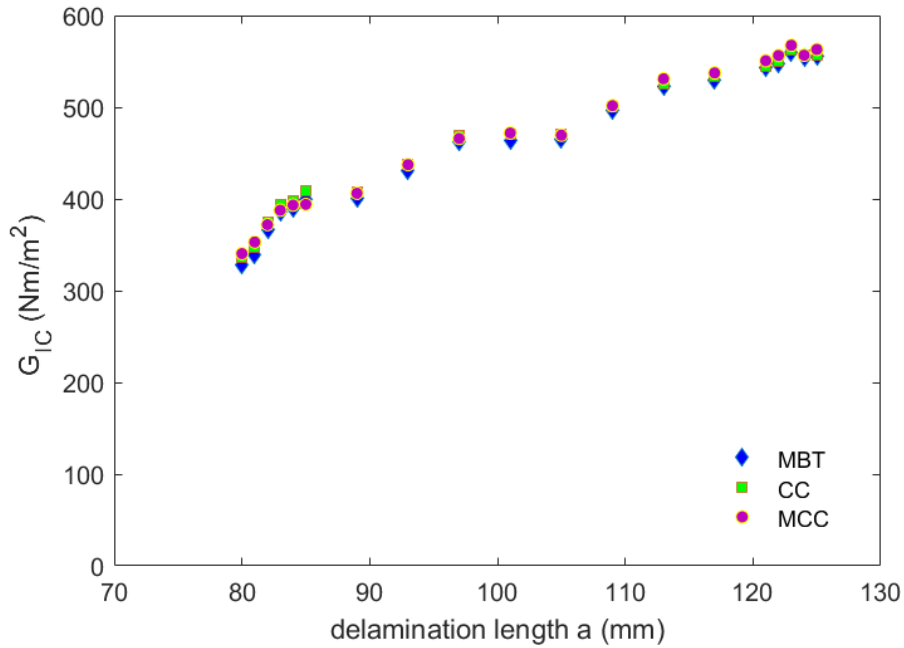


Figure 6-16 Strain energy release rate versus delamination length. Comparison of Modified Beam Theory, Compliance Calibration and Modified Compliance Calibration Methods.

v. Calculation of flexural modulus with DCB test

The MBT theory can also provide the estimation of the flexural modulus of the tested sample. Flexural modulus (E_{1f}) of pure CFRP for sample 3 can be calculated following the equation 6-6. This particular specimen was 25.22 and 3.352 mm for width and thickness respectively. **Table 6-3** presented how flexural modulus changes with the delamination length. In theory, these values should be independent of delamination length; however, some variations were observed due to fibre bridging (Hashemi, Kinloch and Williams, 1989). The average flexural modulus was determined as 112.9 ± 3.6 GPa. Alternatively, the three-point bending test for the same material (0° UD CFRP, **Table 6-1**) yielded the flexural modulus 111.25 ± 5.2 GPa. Both flexural moduli were in good agreement.

vi. Large displacement and end block corrections

Based on the dimensions of the sample and the type of material tested during the DCB test, large displacement may occur. To correct this effect, a parameter F , is introduced which accounts for both the shortening of the moment arm as well as tilting of the end blocks. For piano hinges, G_{IC} is multiplied by F and is expressed by equation 6-9 where t is calculated as shown in **Figure 6-17**. In the case of sample 3, the t was 4.09 mm.

$$F = 1 - \frac{3}{10} \left(\frac{\delta}{a} \right)^2 - \frac{3}{2} \left(\frac{\delta t}{a^2} \right) \tag{6-9}$$

Figure 6-17 is unavailable due to copyright restrictions.

Figure 6-17 *Methods for Introducing Opening load to DCB specimen (large displacement correction) (ASTM D 5528-01, 2009)*

Table 6-3 *DCB post-processing results example for pure CFRP.*

| a (mm) | P (N) | δ (mm) | G_{IC} (Nm/m²) | E_{1f} (GPa) | F | G_{ICcorrected} (Nm/m²) |
|-------------------------|------------------------|-------------------------|--|---------------------------------------|--------------|---|
| 80 | 39.68 | 11.74 | 327.96 | 120.20 | 0.982 | 323.55 |
| 81 | 40.00 | 12.20 | 339.52 | 120.79 | 0.982 | 334.77 |
| 82 | 39.70 | 13.40 | 365.87 | 113.01 | 0.980 | 359.99 |
| 83 | 39.64 | 14.30 | 385.44 | 109.43 | 0.978 | 378.68 |
| 84 | 39.66 | 14.60 | 389.31 | 110.94 | 0.978 | 382.42 |
| 85 | 38.30 | 15.70 | 399.80 | 103.03 | 0.976 | 391.99 |
| 89 | 38.33 | 16.40 | 400.22 | 112.48 | 0.977 | 392.60 |
| 93 | 38.15 | 18.50 | 431.05 | 112.48 | 0.975 | 421.86 |
| 97 | 37.55 | 21.00 | 462.76 | 109.99 | 0.972 | 451.55 |
| 101 | 36.70 | 22.40 | 464.27 | 113.12 | 0.972 | 452.75 |
| 105 | 35.03 | 24.40 | 465.20 | 110.79 | 0.970 | 452.87 |
| 109 | 35.00 | 27.00 | 496.32 | 111.36 | 0.968 | 481.83 |
| 113 | 35.00 | 29.40 | 522.16 | 113.43 | 0.966 | 505.76 |
| 117 | 33.96 | 31.80 | 530.07 | 112.47 | 0.964 | 512.32 |
| 121 | 33.30 | 34.30 | 542.86 | 112.65 | 0.962 | 523.51 |
| 122 | 33.27 | 34.90 | 547.53 | 113.27 | 0.961 | 527.74 |
| 123 | 33.25 | 36.00 | 560.04 | 112.36 | 0.960 | 539.03 |
| 124 | 32.37 | 36.90 | 554.53 | 109.24 | 0.959 | 533.16 |
| 125 | 31.99 | 37.00 | 555.68 | 110.19 | 0.959 | 524.52 |
| Average | | | 460.03 | 112.89 | 0.971 | 446.89 |

The parameter F was determined for different crack length and corresponding displacement as presented in **Table 6-3**. The column named $G_{ICcorrected}$ is the result of multiplication of G_{IC} by this factor F . When F reaches 1, the effects of the large displacement on G_{IC} are not present. From the table, it can be seen that the increase of the delamination length leads to a decrease of the parameter F . For the relatively small delamination length, 80 mm, F equals to 0.982. Thus, the difference between G_{IC} and $G_{ICcorrected}$ is only about 1.3%. However, when the delamination length grow significantly, the maximum variation in mode I strain energy release could increase to almost 6%. In this project, the effects of large deflection criteria is relatively small, this factor was not applied throughout the analysis.

6.2.3.5 Average G_{IC} for the samples sprayed with GNPs

Two sets of samples with a different concentration of GNPs taken from Panel IIIC and IVD were compared. The relationship between the crack length and G_{IC} as well as error bars are shown in **Figure 6-18**. Over the same crack propagation, samples from Panel IIIC with a higher concentration of GNPs of 0.00065 wt % of GNPs exhibited a consistent higher G_{IC} compared to samples of panel IVD, where the concentration of GNPs was only 0.00044 wt %. Both curves also show the error bar with the difference between the lowest and the highest amount of G_{IC} in 5 samples of each set. Larger deviations between average values and maximum/minimum were found for the panel IIIC.

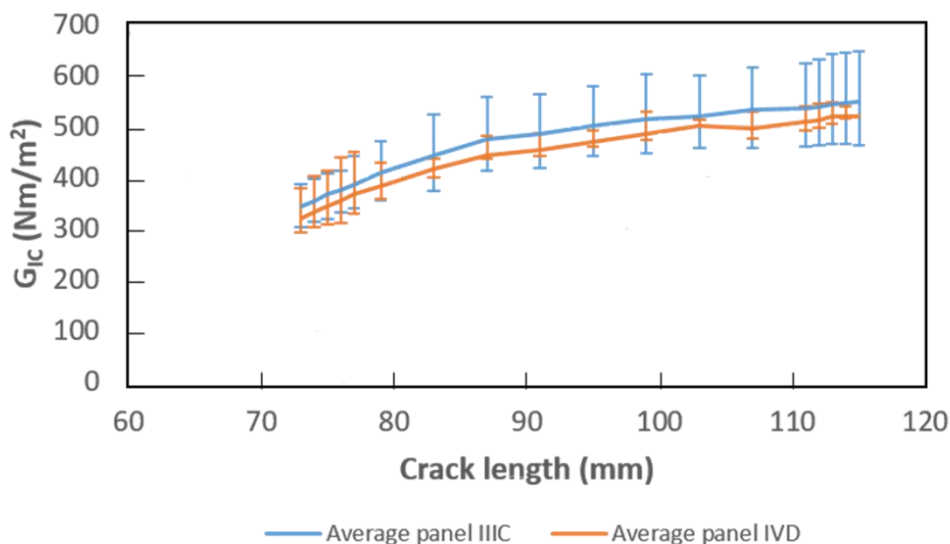


Figure 6-18 Average mode I strain energy release versus crack length (panel IIIC -0.00065 wt% of GNPs, panel IVD 0.00044 wt%)

A comparison between the mode I strain energy release is presented in figure 6-19. Values of crack propagation on horizontal axis were measured from the new crack tip (this is the point, where the unstable crack propagation ended during the initial loading). All of the samples follow nonlinear increase of the G_{Ic} value with respect to the crack propagation. Mode I strain energy release changes in the range of 300 to 560 Nm/m^2 . Results obtained from pure CFRP and CFRP sprayed with 0.00044 wt % of GNPs were close to each other. For samples of CFRP sprayed with 0.00065 wt % of GNPs, a noticeable enhancement was shown (up to 30 mm crack length). On the other hand, the CFRP sprayed with a lower amount of CNTs at the first stages of propagation showed the lowest G_{Ic} values compared to other specimen. When the crack propagation length exceed 10 mm, the increase of G_{Ic} with the crack propagation is fastest and the actual G_{Ic} value became higher than the 0.00044 wt% CFRP results.

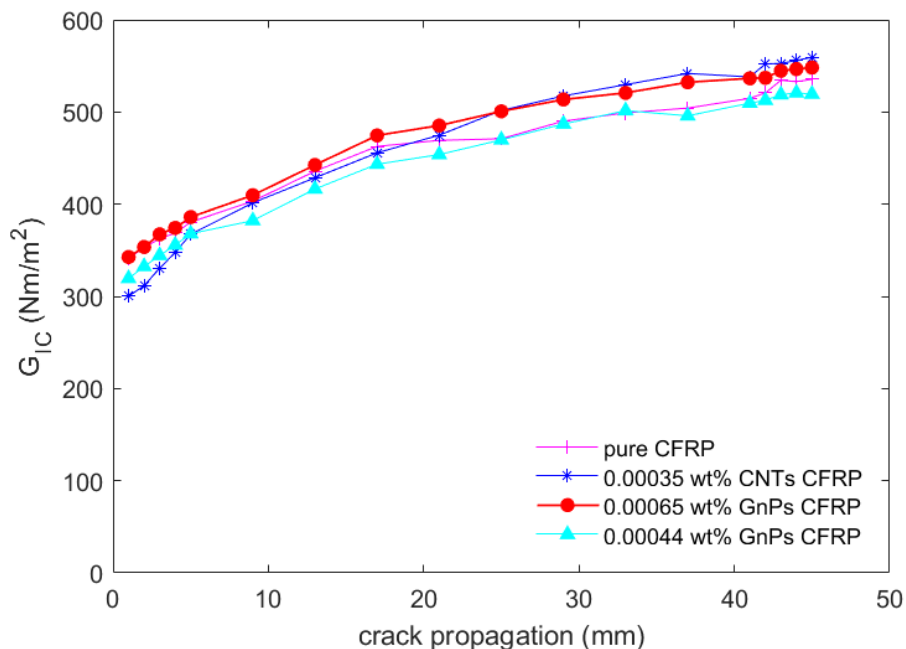


Figure 6-19 Mode I strain energy release versus crack propagation – comparison of average curve of all four group of samples.

The average mode I strain energy release was calculated over all of propagation points for each sample as presented in **Table 6-4**. The pure CFRP sample acted as a reference and its average value of G_{Ic} was 444 Nm/m^2 . When samples were sprayed with 0.00044 wt% GNPs, it showed a close values 441 Nm/m^2 . Samples sprayed with CNTs showed a higher value of 446 Nm/m^2 . The highest average mode I strain energy release 468 Nm/m^2 was exhibited by the CFRP specimens sprayed with 0.00065 wt% GNPs. This corresponds to 5 % increase of the average G_{Ic} in comparison to reference CFRP. Considering the variation of G_{Ic} during the

whole crack propagation process, the maximum difference among different set samples at some points will be higher than the average one shown in the **Table 6-4**. For example, more than 30 Nm/m^2 enhancement between pure CFRP and GNPs reinforced was observed between 20 to 40 mm of crack propagation length, which is equivalent to approximately 7 % of improvement in comparison to pure CFRP.

Table 6-4 Comparison of average mode I strain release energy for various wt % of nanofillers.

| Group ID / Nanofillers wt% | Panel I A 0 wt% | Panel II B CNTs 0.00035 wt% | Panel III C GNPs 0.00065 wt% | Panel IV D GNPs 0.00044wt% |
|----------------------------------|--------------------|-----------------------------------|------------------------------------|----------------------------------|
| Average G_{Ic} (Nm/m^2) | 444 | 446 | 468 | 441 |

6.2.3.6 SEM analysis

In order to investigate the influence of the nanofillers on the crack propagation in unidirectional CFRP, SEM images were taken at various magnifications 200, 500, 7500, 35000 times (15kV). All SEM samples were cut from the crack propagation region in tested samples as shown in **Figure 6-20**. **Figure 6-21** presents the comparison between the fracture surface of the pure CFRP (**a**) and CFRP with sprayed CNTs (**b**) at the magnification of 500 times, where yellow arrows indicate the crack direction. Pure CFRP fracture surface shows a relatively smooth surface of the fibre with little remaining resin. Fibre imprints were visible with rather straight edges without resin cusps. Contrarily, a sample with CNTs clearly exhibited rougher fibre surface, regions with large areas with remaining resin on the fibres (as pointed with red arrows) and resin debris. These observations were in-line with other studies (Almuhammadi *et al.*, 2014).

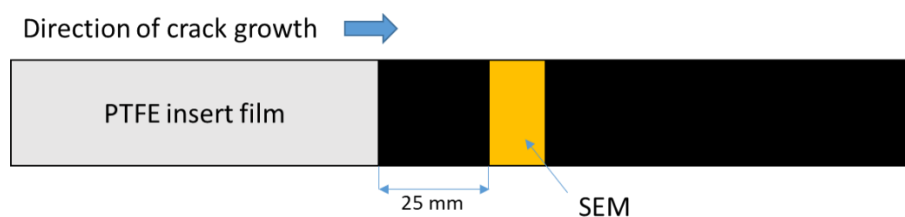


Figure 6-20 Schematic drawing of the tested sample. Yellow area indicates the location where SEM samples were cut– distance from the end of inserted PTFE film (not in scale).

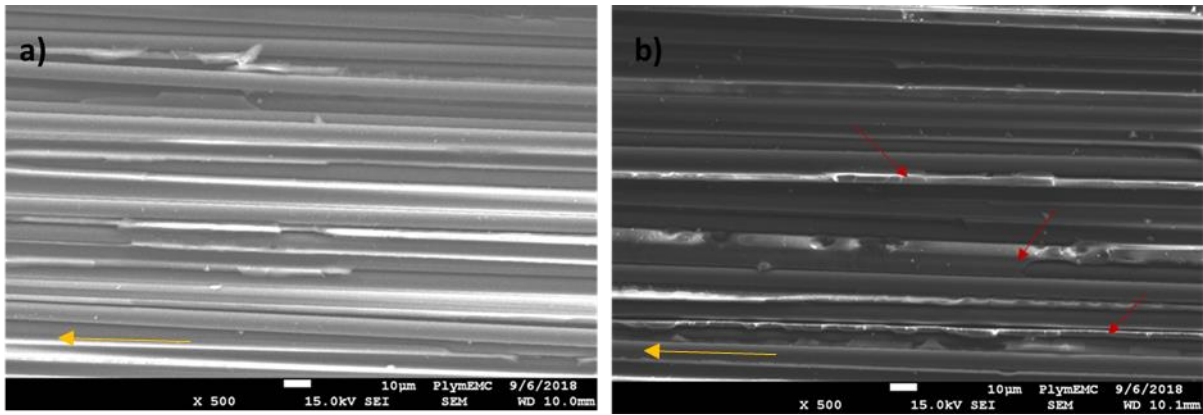


Figure 6-21 SEM images of fracture surface area (a) pure CFRP, (b) 0.00035 wt% of CNTs CFRP (yellow arrows indicate the crack propagation direction).

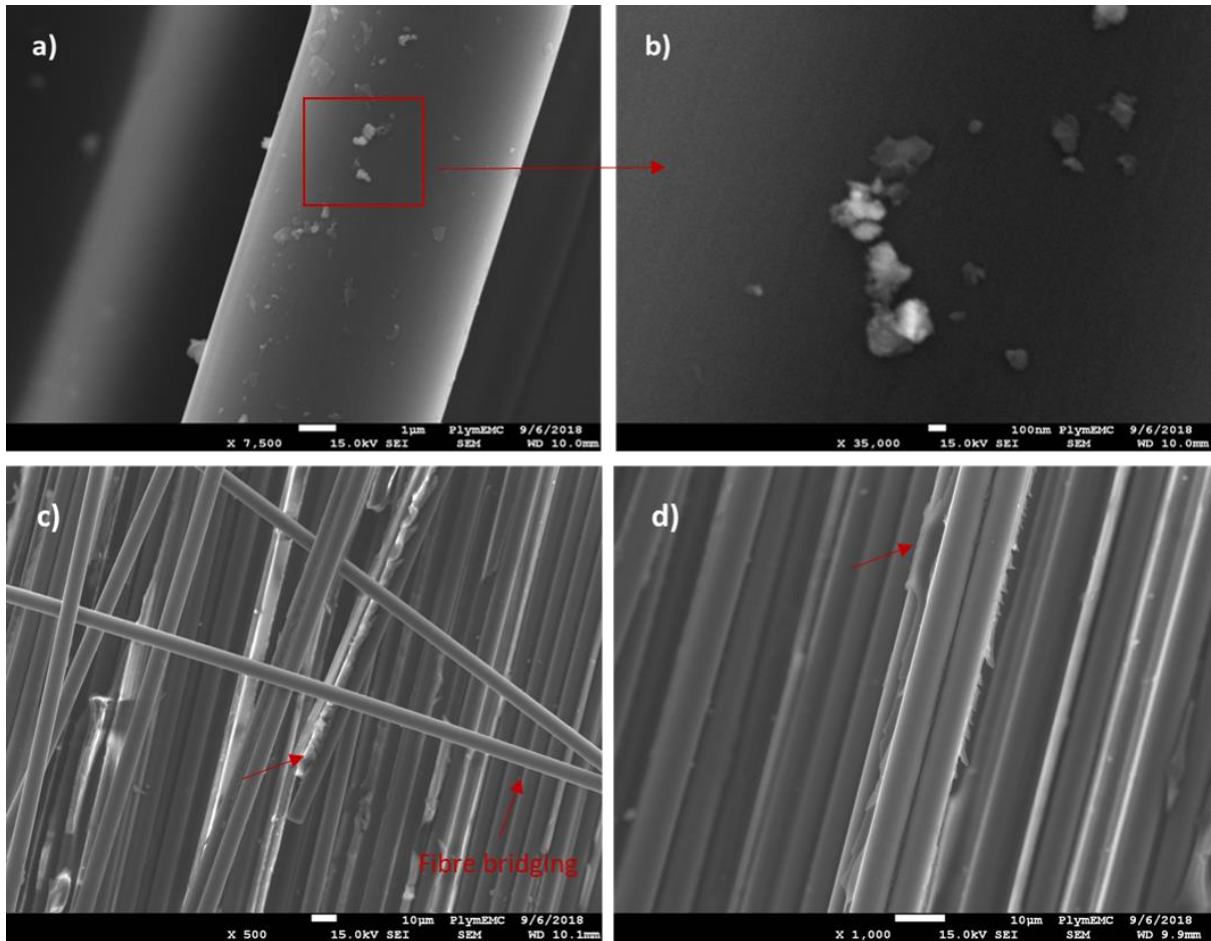


Figure 6-22 SEM images of 0.00065wt% GNPs sprayed CFRP (a) carbon fibre coated with GNPs (b) GNPs (c) fibre bridging and (d) resin cusps on the carbon fibre.

The fracture surface of CFRP samples sprayed with GNPs is presented **Figure 6-22**. The presence of the nanoparticles on the fracture surface was clearly noticeable at 7500 times

magnification (see **Figure 6-22a**). Further magnification of selected area at 35000 times enabled to measure the average size of this type of nanofillers and proved to be less than 300 nm as shown in **Figure 6-22b**. These results matched well those observed in the previous study for the same type of GNPs (Qin *et al.*, 2015). On the other hand, **Figure 6-22c** and **d** display the overall view of the fracture surface at 500 times magnification, where fibre bridging and resin attached to the fibre were present similarly to the SEM image of CNT sprayed sample (indicated by red arrows).

6.2.3.7 Critical analysis

As mentioned in the literature review, nanofillers can increase mechanical properties of CFRP, i.e. fracture toughness by improving the fibre/matrix bonding and delamination resistance. In this study, the G_{Ic} properties of the CFRP sprayed with two type of nanofillers namely CNTs and GNPs were determined from the DCB test. A moderate enhancement of mode I strain energy release was obtained at low wt% of the nanofillers. The extent of improvement depends highly on factors like amount, type of nanofillers, and location of the spraying. It was found that the highest improvement, approximately 7 %, was obtained for 0.00065 wt% of GNPs comparing to the pure CFRP. Interestingly, spraying 0.00044wt% of GNPs slightly decrease the average G_{Ic} . A possible explanation for decreased G_{Ic} value is that the enhancement caused by nanofillers may be overtaken by the negative impact caused by the residual sprayed solvent. In most published work (Zhang *et al.*, 2015; Rodríguez-González *et al.*, 2017) ethanol solvent was also applied to control sample in order to eliminate this extra negative impact given by ethanol solvent, in other words, the effects of ethanol solvent was not considered.

Zhang *et al.* (2015) sprayed nine layers of carbon fibre prepreg with CNTs-methanol solution. Significant improvement as 47 % in mode I strain energy release was found at the CFRP with the addition of 0.047 wt% CNTs. A smaller improvement (22%) was noted for 0.02 wt% concentration. This indicates that increasing the amount of nanofillers could improve the fracture toughness properties even higher. However, increasing the wt % of nanofillers could develop the risk of potential agglomeration effects of nanofillers. It is impossible to make a direct comparison between the present study and Zhang *et al.* (2015). Both studies differ in carbon fibre orientation in the prepreg, and the number of the prepreg plies subjected to spraying process.

Almuhammadi *et al.*, (2014) tested 0° unidirectional carbon fibre composite, where 0.5 wt% of CNTs was sprayed onto the mid-plane prepreg layer. 17 % improvement was found in G_{Ic} . The sample was also inspected using Raman Spectroscopy to identify the location and thickness of the sprayed CNTs, which created a nano-reinforced resin reach layer. The thickness of this layer was approximated to 10 μm . It was also identified that the interlaminar growing crack did not completely propagate through CNTs resin reach layer, what therefore unable to fully exploit the potential of the sprayed CNTs. This also could serve as an explanation why spraying each layer would be more beneficial.

More recently, Rodríguez-González *et al.* (2017) investigated the effects of spraying MWCNTs on unidirectional carbon fibre composite properties. The same amount of the solution, but with different concentrations of CNTs was sprayed on both sides of the mid-plane of the composite. Authors also reported an unstable crack propagation during the loading, however unlikely in our case tests were continued. This violates the recommendation given by ASTM; therefore, these results need to be interpreted with cautions. Force values were taken to calculate the initiation of G_{Ic} (known as VIS during the initial loading) are invalid as followed by unstable crack propagation from the insert. Therefore, only the propagation values are comparable. Authors reported a 15% increase in propagation values for 0.05 wt % of nanofillers, suggesting that this is the optimum concentration of the CNTs in the solution within the range from 0.05 to 0.5 wt%. Direct comparison with this work is impossible due to the lack of given laminate measurements.

In conclusion, the spraying coating process can effectively introduce nanofillers in CFRP and obtain moderate enhancement in mode I strain energy release. This process can be further improved by accounting some factors. Firstly, spraying process conditions may have a significant effect on the extent of the improvement. The discrepancy in the results for G_{Ic} values of Panel IIIC (**Figure 6-18**) may be caused by uneven distribution of the nanofillers. During the spraying process, the operator manually controlled airbrush. Although, every effort were made to ensure repeatable spraying process, errors such a splash of the solution happened occasionally. To eliminate these effects, the automation of the process would be beneficial. Secondly, the increasing the amount of nanofillers in CFRP can potentially lead to higher improvement. Thirdly, nanofillers should be sprayed on more layers to ensure that crack propagate through the nano-reinforced region. Fourthly, the effects of the ethanol should be further investigated. In this case, the very little negative effect of the spraying process was noticed when compared to pure CFRP. During the spraying process, the prepreg material

remained in the fume cupboard to evaporate ethanol. However, placing the prepreg in the oven could be another alternative to solvent evaporation. Finally, the post-processing of the recorded video is very tedious and time-consuming. This method of extracting crack length with respect to time introduce another possible source of errors. Very often crack tip is difficult to precisely identify. Software like video recognition or digital image correlation technique could improve the accuracy of this analysis.

6.3 Experimental results on the carbon fibre fabric sprayed with nanofillers

6.3.1 Flexural properties

Five samples from each group of specimens were tested in three-point bending. The same procedure and testing conditions as in subchapter 6.1.1 were applied. **Table 6-5** presents the average of sample dimensions and obtained experimental results. Two laminates in the presence/absence of GNPs nanofillers were wet laid-up. Pure CFRP material is simply carbon fibre impregnated with resin. In the case of CFRP+GNPs, approximately 0.5 wt% of GNPs was applied to the fibre by a spraying process. The difference in thickness was caused by the amount of resin used during the laminating and possibly by the presence of GNPs.

Table 6-5 Comparison of 0° and 90° flexural properties of the unidirectional carbon fibre reinforced laminate (pure CFRP and CFRP reinforced with 0.5 wt% of GNPs).

| Laminate ID | UD 0° (Pure CFRP) | UD 0° (CFRP+GNPs) | UD 90° (Pure CFRP) | UD 90° (CFRP+GNPs) |
|------------------|----------------------|----------------------|-----------------------|-----------------------|
| Length (mm) | 102±0.4 | 100.9±0.44 | 101.3±1.3 | 100.7±0.44 |
| Width (mm) | 14.3±0.16 | 14.38±0.09 | 14.86±0.1 | 14.43±0.04 |
| Height (mm) | 2.55±0.1 | 2.74±0.11 | 2.51±0.03 | 2.71±0.05 |
| Span (mm) | 80 | 80 | 80 | 80 |
| F_{max} (N) | 513±36 | 546.4±78 | 40±2 | 47±4 |
| E_f (GPa) | 96.6±4.5 | 97.38±2.5 | 6.05±0.2 | 5.6±0.6 |
| σ_f (MPa) | 665.2±8.2 | 632.2±24.6 | 49.04±2.2 | 49.67±4.2 |

The average flexural modulus for 0° unidirectional CFRP increased from 96.6 GPa to 97.38 GPa due to the presence of GNPs. This enhancement corresponds to approximately 1%. On the other hand flexural strength, slightly decrease from 665.2 to 632.2 MPa. In the case of 90° specimens, a slight decrease of flexural modulus was observed for the samples with sprayed GNPs. On the other hand, the flexural strength changed little from 49.05 to 49.67 MPa.

6.3.2 Interlaminar properties

Due to difficulties in obtaining interlaminar shear strength in short beam subchapter 6.1.2, some modifications to testing conditions have been made. During this test, a smaller loading and support rollers of diameters 6 and 4 mm respectively, as according to ASTM D2344 (2016) were used. Sample width and length were approximately 5 and 10 times the thickness of the sample respectively. The loading speed was 1mm/min. 7 sample from the pure CFRP panel and 5 sample from the GNPs reinforced material were tested.

Table 6-6 Specimen dimensions prepared for short beam test.

| Laminate | UD 0° (Pure CFRP) | UD 0° (CFRP+GNPs) |
|-------------------|-------------------|-------------------|
| Length (mm) | 21.33±0.58 | 21.39±0.45 |
| Width (mm) | 14.58±0.07 | 14.3±0.16 |
| Height (mm) | 2.46±0.03 | 2.77±0.02 |
| Number of samples | 7 | 5 |

Firstly, the influence on the span to thickness (s/t) ratio on the material behaviour was evaluated on 4 sample from pure CFRP. Different ratio of span length to thickness (s/t), from 4 to 7, were compared. **Figure 6-23** shows how changing the span length influence on material behaviour. For the s/t=4 (sample 4), curvilinear increase of the force up to a maximum value around 2200 N was found. Then, force dropped slightly and remained almost steady up to the point where the deflection reached 1 mm. No obvious signs of delamination of the layer were observed. Similar behaviour was represented by sample 5 of the span to thickness ratio equalled to 5. Increasing s/t ratio to 6 of sample 1 shows that, for the first 0.5 mm of deflection force increase almost linearly. Then, a small peak of force occurs, followed by steady a constant value of force at the constant level at 1310 N. This experiment also yielded no interlaminar shear strength. For all three samples, modes of failure were combined plastic deformation and compression.

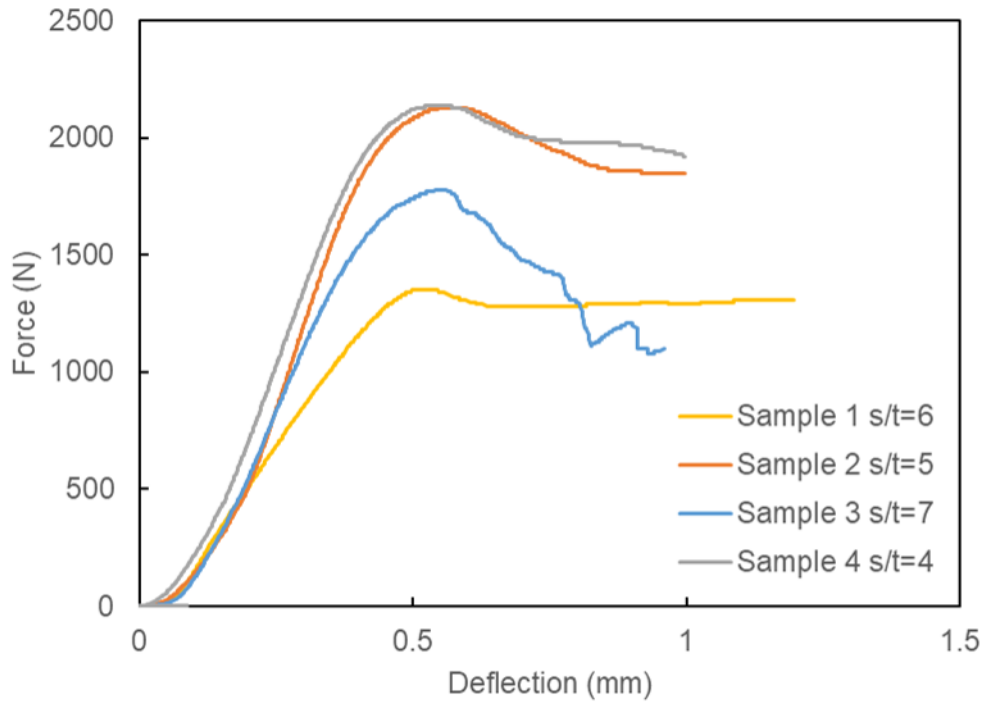


Figure 6-23 *The relationship between force and deflection obtained from short beam test. Influence on the span to thickness (s/t) ratio on the material behaviour.*

Finally, the span length was subsequently increased to 17 mm corresponding to $s/t=7$. During this experiment, the cracking sound accompanied when the sudden drop of force occurred. Visible delamination between the layers was presented as shown in **Figure 6-24a** confirming the acceptable single shear failure mode. Therefore, this span length was used through the remaining experiments.

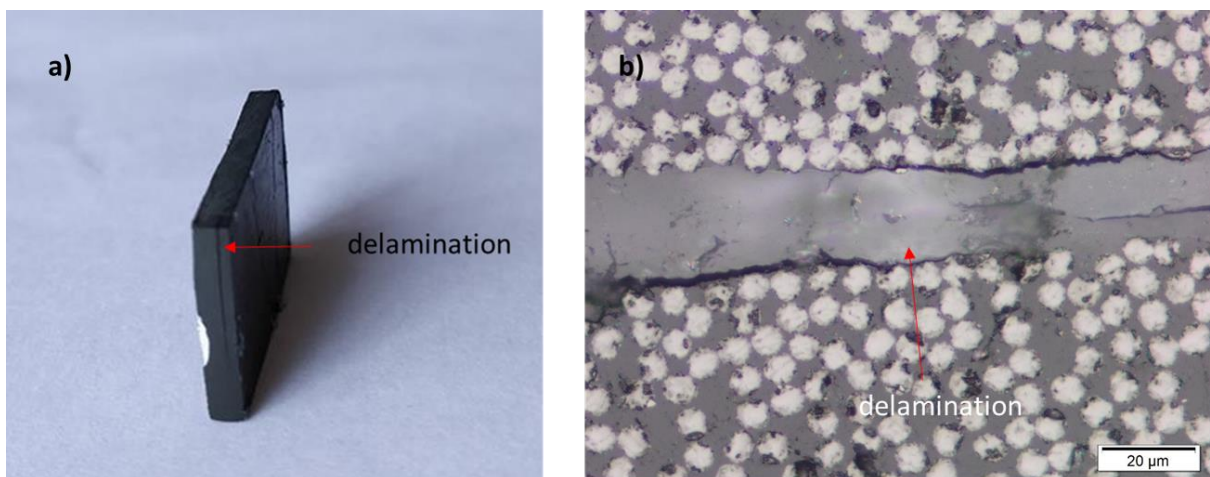


Figure 6-24 (a) *Image of tested SBT specimen (thickness to span ratio=7)* (b) *delamination observed in a cross section of the specimen (magnification 50)*

Figure 6-25 presents the relationship between force and deflection for all samples, where red colour represents the CFRP reinforced with GNPs and black - pure CFRP. All of the specimens failed in acceptable modes such as single or multiple shear. The maximum force for each test was selected to find the value of ILSS. Apparent interlaminar shear strength was calculated according to equation 6-3. The deviations in thickness resulted from the manufacturing technique and are considered in the calculation. The average ILSS for pure CFRP amounted to 35.8 MPa. Surprisingly, the addition of the GNPs caused a small decrease of 0.9 MPa in ILSS corresponding to around 2.5 % of change.

Table 6-7 Apparent interlaminar shear strength results and standard deviations for pure CFRP and CFRP reinforced with GNPs.

| Laminate | UD 0° (Pure CFRP) | UD 0° (CFRP+GNPs) |
|---------------|-------------------|-------------------|
| Span (mm) | 17 | 17 |
| F_{max} (N) | 1710 ±106 | 1836±53 |
| τ (MPa) | 35.8±2.1 | 34.9±1.2 |

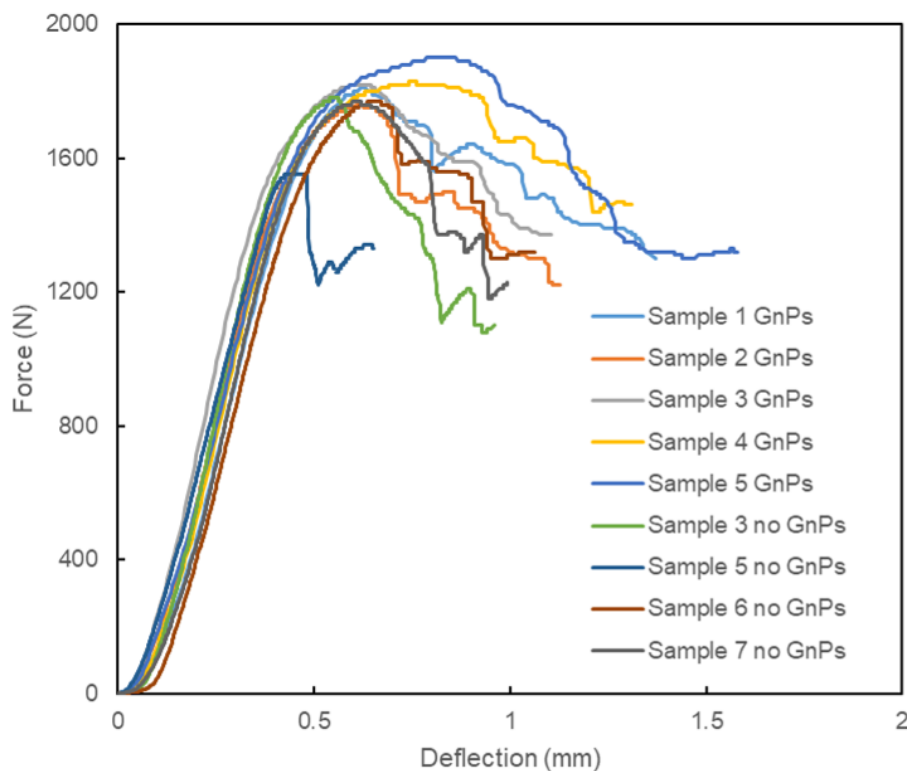


Figure 6-25 The relationship between force and deflection for CFRPs (red colour represents the sample with GNPs, black is pure CFRP)

6.3.3 Discussion

Graphene nanofillers can be coated on carbon fibres interphase by dip coating, electrophoretic deposition or grafting as discussed in Chapter 2.3. Many research works reported the variable extent of improvement of CFRP mechanical properties due to the graphene coating. For example, Chen *et al.* (2016) achieved a 60% increase in ILSS for CFRP dip-coated with 0.5 wt% of SGO. Qin *et al.* (2015) obtained an improvement in the region of 20% in ILSS, and 82% increase in 90° flexural strength for GNPs reinforced CFRP. While Zhang *et al.* (2012) reported 11% improvement in ILSS by adding GO. These methods resulted in a different level of enhancement, which is very much dependent on operating procedure. They are also expensive to scale up. The spraying method is a cost-effective alternative.

The spraying process has some advantages over other coating methods. For example, a dip coating method requires a large amount of nanofillers solution. When the carbon fibre tow is pulled through the nanofillers solution bath, the amount of the deposited GNPs will be affected by the tow feeding speed. After the deposition process, it is difficult to quantify the concentration of residuals nanofillers in the solution bath. This will make difficult if not impossible to prepare the solution of the same GNPs concentration from the “used” solution to achieve a uniform coating. In the case of spraying process, the desired amount of the solution can be calculated, prepared beforehand and used in full. The exact amount of nanofillers in the CFRP can be determined so that the finish will be much easier to repeat.

Spraying on the prepreg surface has shown improvement the interlaminar properties as discussed in section 6.2. In this part, a novel spraying method of GNPs/epoxy/ethanol solution directly on carbon fibre surface was for the first time trialled to make a GNPs reinforced interphase. The nanofillers solution usually consists of nanofillers and solvent. Here epoxy/hardener was purposely added to the spraying solution to assist the bonding of the coating to carbon fibre (Qin *et al.*, 2015). The recommended weight ratio of the hardener as given by supplier was intentionally reduced by 50% (epoxy to resin ratio 100:15) in the spraying solution. The concentration of nanofillers in the published results varies from up to 10 wt% (Zhang *et al.*, 2012). The optimal concentration of the GNPs in the coating was selected as 0.5 wt% in CFRP. When this report was finalised a recently published journal on this work was made available, and GNPs from 0 to 0.5 wt% was used (Wang and Cai, 2018).

To examine the mechanical performance of GNPs reinforced CFRP, three-point bending test and short beam tests were performed. The introduction of GNPs increased some

flexural and interlaminar properties of CFRP samples. The extent of enhancement is smaller than expected. Flexural modulus in 0° GNP sprayed laminate, and flexural strength of 90° GNP sprayed laminate increase a little (1.2%). A small decrease in some properties, i.e. interlaminar shear strength (ILSS) was also observed. Contrarily, other published experimental results of graphene coated CFRP reported significant improvement of the mechanical properties (Wang and Cai, 2018).

One of the possible reasons for the lack of the desired improvement was adhesion of the GNPs coating to fibres surface. The weak adhesion of the GNPs coating to carbon fibre process was observed at the time of samples preparation. During the wet lay-up process, when the resin was applied with brush and roller, some of the weakly bonded nanofillers were taken away from the fibre surface. This was confirmed by the change of resin colour from transparent to black, suggesting that nanofillers transferred from the fibre surface to the matrix as well. This means that the GNPs coating did not bond well to carbon fibres. Many factors can cause the weak adhesion. One of them could be inappropriate curing conditions of the sprayed fabric. These conditions depend not only on the amount of solvent and nanofillers, epoxy and hardener but also on curing time and temperature. The present curing time was 3 hours in 60 degrees. It was taken from literature (Qin *et al.*, 2015), which was designed initially for GNPs/Epon 828/mPDA/NMP solutions. The optimal curing conditions for sprayed fabric at a given composition of the solution needs to be found in order to gain strong bonding with carbon fibre.

Another possible issue of the bad adhesion could be commercial sizing on the ‘as-received’ carbon fibre fabric. This sizing is usually designed to improve the wettability of fibres for resin impregnation, which could have a negative effect on the ability of GNPs solution bonding to the surface. Prior to the coating process, de-sizing carbon fibre was used to remove the commercial sizing which is believed to improve adhesion (Qin *et al.*, 2015). In this wet lay-up, the GNPs coated fabric should be carefully brushed with resin, so that the minimum amount of GNPs are carried away. Other laminate manufacturing process such as resin infusion or prepreg manufacturing could also be considered.

The main challenge of all coating processes is to make nano-reinforced interphase of uniform thickness with a homogenous distribution of nanofillers. Spraying method has a huge potential to be scale-up in industrial level. For the moment, the spraying gun was operated manually. This sample finish is very much dependent on the experience of the operator, which may introduce some non-uniformity of the coating. This can be avoided by the automation of

the spraying process, which will advantageously lead to more controllable process conditions. Also, a continuous mixing process before feeding the solution into the spraying gun could be also beneficial at the industrial scale. The spraying process is limited to certain types of carbon fibre fabric. Under the same spraying process, fabric of lower weight per square metre is easier to achieve an even impregnation of carbon fibre by spraying solution. To achieve a better enhancement, the spraying process could also be applied directly to fibre tow, which later can be made in different types of fabric — this challenge posed for other coating methods as well.

6.4 Summary

The present experimental results have shown that properties of the CFRP like mode I strain energy release increased with an extremely small amount of nanofillers sprayed on the prepreg. This extent of enhancement dependent on the amount and type of nanofillers. It was also found that sprayed nanofillers yielded little improvement in three-point bending flexural modulus in 0 and 90° unidirectional composites. The SEM analysis has shown fracture surface morphologies and the effects of sprayed nanofillers on the crack propagation of CFRP.

A novel spraying process to the GNPs/ethanol/epoxy solution has been successfully applied to the unidirectional carbon fibre fabric. 0.5 wt% reinforced GNPs samples were tested in three-point bending and short beam tests. Various span lengths were compared to obtain interlaminar shear failure between the lamina layers. Possible reasons were identified for unexpected little improvement. Future research was recommended to concentrate on the adhesion between coating and fibres, alternative manufacturing technique such as resin infusion and automation of the spraying process.

7 Prediction of interphase properties via inverse analysis and optimisation

7.1 Introduction

As shown in previous chapters, interphase properties have a significant influence on the mechanical performance of fibre-reinforced polymers. Several test methods have been designed and employed to determine certain properties of the interphase region. Tunnelling electronic Microscopy (TEM) (Wu *et al.*, 2015) was tested to determine the thickness. Nano-indentation test is commonly used to measure the thickness and stiffness of the interphase (Hardiman, Vaughan and McCarthy, 2017). Fibre pull-out (Zhou *et al.*, 2016), and fibre push-out test (Battisti *et al.*, 2014) were used to quantify the interfacial shear strength of fibre with the matrix in the interphase region. Full characterisation of the interphase region is still challenging due to limitations of existing experimental techniques. To overcome the issue encountered in experiments, researchers have used an analytical model to characterise the interphase, i.e. Mori-Tanaka presented in Chapter 4 and 5 or molecular dynamics analysis (Johnston *et al.*, 2017). This prediction of interphase properties is a forward analysis based on each constituent of the interphase, some information of which are difficult to obtain. The inverse procedure is an alternative way that combines interphase parameter identification based on the optimisation algorithms and experimental data. This method was usually performed at one level, i.e. micro or macroscale. For instance, Lu *et al.* (2014) predicted transverse properties of the T300 carbon fibre and stiffness of interphase region simultaneously by optimising three-phase square RVE model using Kriging metamodells and microscale experimental lamina elastic constants.

Material suppliers usually provide macromechanical properties of CFRP laminate, but rarely mention micromechanical properties of single lamina in their data sheets. The interphase's mechanical properties are not directly determining macromechanical properties of the laminate but indirectly via affecting the micromechanical properties of the lamina. The inverse process to predict the interphase from macroscale level requires two-step optimisations involving both macro and microscales. For example, Wang *et al.* (2017) determined interphase properties from vibration test of a cantilever beam sample, where a strain energy method was adopted at the microscale level, and Euler-Bernoulli beam theory was adopted at macroscale level. The relationship between Young's modulus and loss factor of the overall composite and

those of the interphase was established using three-phase strain energy method. Composite properties were determined from the overall frequency response function of a beam and used in the analytical model to determine interphase properties. The analytical work was made possible by assuming isotropic for fibre, matrix, and interphase. However, this is not applicable to carbon fibres, which are strongly transversely isotropic.

This chapter presents a sequential optimisation method to predict the interphase properties inversely, which combines both macro and microscale FEA simulations developed in Chapter 4 and 5. The optimisation process was performed using ANSYS DesignXplorer. Validation of this method was conducted using three-phase RVE model to compare with published results. Various optimisation algorithms like screening, multi-objective and adaptive multi-objective were tested to evaluate their effectiveness and accuracy during the optimisation process.

These two steps in this optimisation procedure were uncoupled but connected via the properties of the lamina. It was performed to determine the properties of the interphase. Three types of composite materials samples including non-coated CFRP epoxy coated CFRP, and GNPs coated CFRP were investigated. Experimental data from three-point bending tests were the objective to satisfy in numerical simulations. During the optimisation process, the macroscale step predicted lamina elastic constants so that numerically calculated flexural modulus of the material matches experimental counterpart. Next, the microscale step determined the interphase properties from predicted lamina elastic constants. For the first time, the nano-reinforced interphase's properties were fully characterised.

7.2 Validation of optimisation

7.2.1 Forward simulations

Although a two-step optimisation was proposed, the optimisation process was validated only at the selected scale. The microscale optimisation was used for the convenience and availability of complete published results. Forward simulations of the 3-phase RVE model were accomplished based on previous work to predict the lamina's properties (Liu *et al.*, 2012). The CFRP sample was carbon fibre reinforced polymer T300/914C. Carbon fibre T300 was treated transversely isotropic, and both epoxy resin 914C and interphase were assumed isotropic. Their properties are shown in **Table 7-1**. The volume fraction of carbon fibre in this model was 60%. According to the fibre diameter and volume fraction, the dimensions of the hexagonal RVE

model were determined as: $a_1 = 1.07\mu\text{m}$, $a_2 = 4.3\mu\text{m}$, $a_3 = 7.44\mu\text{m}$ (refer to equation 3-9). The interphase thickness was set to 100 nm.

Table 7-1 Properties of carbon fibre (T300) epoxy resin (914C) and interphase.

| Carbon Fibre (T300) | | Epoxy Resin 914C | | Interphase | |
|--|------|------------------------------|-----------|------------------------------|-------|
| Longitudinal modulus, E_1^f (GPa) | 230 | Modulus, E^m (GPa) | 4.0 | Modulus, E^i (GPa) | 8.3 |
| Transverse modulus, E_2^f (GPa) | 15 | Poisson's ratio, ν^m | 0.35 | Poisson's ratio, ν^i | 0.176 |
| Longitudinal shear modulus, G_{12}^f (GPa) | 15 | Shear modulus, μ^m (GPa) | 1.48 1 | Shear modulus, μ^i (GPa) | 3.53 |
| Transverse shear modulus, G_{23}^f (GPa) | 7 | | | Thickness, t^i (nm) | 100 |
| Longitudinal Poisson's ratio ν_{12}^f | 0.2 | | | | |
| Transverse Poisson's ratio ν_{23}^f | 0.07 | | | | |
| Diameter (μm) | 7.1 | | | | |

The RVE model was simulated using ANSYS Mechanical APDL 17.2 as discussed in chapter 3.2.2. The script was modified to capture the features of this model including the size of RVE, material properties, and the thickness of the interphase (*Appendix D*). Periodic boundary conditions were applied to the model to determine the unidirectional lamina elastic constants. This step is so-called the forward simulations. The comparison of obtained lamina elastic properties and available literature is provided in **Table 7-2**. It was observed that longitudinal properties such as longitudinal elastic modulus, E_1 , and in-plane Poisson's ratio agreed very well in all three studies. In the case of transverse elastic modulus and out-of-plane Poisson's ratio (ν_{12}), no significant difference was observed for the present model and hexagonal RVE model (Liu *et al.*, 2012). On the other hand, square RVE presented by (Lu *et al.*, 2014). predicted slightly higher E_2 . After a careful examination, the result of the in-plane shear modulus G_{12} predicted by (Liu *et al.*, 2012) was unable to reproduce. It is probable that a typographical mistake occurred in the in-plane shear modulus results. The present work yielded G_{12} results closer to the experimental work (Soden, Hinton and Kaddour, 2004, not included in this table) and another numerical study (Lu *et al.*, 2014). The present findings were in satisfactory agreement with other numerical models.

Table 7-2 Comparison of T300/914C properties predicted by the present model with available published data.

| | E_1 (GPa) | E_2 (GPa) | ν_{12} | ν_{23} | G_{12} (GPa) |
|--------------------------|-------------|-------------|------------|------------|----------------|
| Present RVE model | 140.105 | 9.003 | 0.2506 | 0.3059 | 4.587 |
| Liu <i>et al.</i> (2012) | 139.50 | 8.90 | 0.25 | 0.31 | 8.20 |
| Lu <i>et al.</i> (2014). | 139.40 | 9.90 | 0.248 | 0.246 | 4.9 |

7.2.2 Testing optimisation algorithms at the microscale

Once the forward simulation predicted the elastic constants of the three-phase RVE, these material properties served as output parameters in the optimisation analysis using ANSYS DesignXplorer software. For the above three-phase RVE model, interphase properties are assumed unknown and need to be predicted. Other parameters such as carbon fibre T300, epoxy resin 914C, interphase thickness, and size of the RVE model remained constant. Isotropic interphase properties such as modulus (E^i), and Poisson's ratio (ν^i) became input parameters, which were updated iteratively in the model. Lamina constants from **Table 7-2** corresponded to the output parameters. Thus, material properties such as [$E^i, \nu^i, E_1, E_2, \nu_{12}, \nu_{23}, G_{12}$] were parameterised in the ANSYS software. The upper and lower bounds of interphase parameters were presented in **Table 7-3**. The objective of the optimisation was to find the interphase properties (E^i, ν^i). The algorithm updated the input interphase properties until elastic lamina constants sought defined targets. Definition of the terms using throughout this chapter have been provided in Section 3.3.4.

Table 7-3 Objective and constraints selected in the validation case – ANSYS optimisation process.

| Input parameter | Lower bound | Upper bound | |
|-------------------|-------------|---------------|--------|
| E^i (GPa) | 5 | 10 | |
| ν^i | 0.15 | 0.25 | |
| Output parameters | Constraints | Sought target | |
| E_1 (GPa) | 140.0 | 140.2 | 140.1 |
| E_2 (GPa) | 8.9 | 9.1 | 9.003 |
| ν_{12} | 0.25 | 0.251 | 0.2506 |
| ν_{23} | 0.3055 | 0.306 | 0.3058 |
| G_{12} (GPa) | 4.58 | 4.589 | 4.587 |

The software offers a range of optimisation tools, including various optimisation algorithms. Three main optimisation algorithms namely Screening, Multi-adaptive optimisation algorithms (MOGA) and Adaptive optimisation algorithms (AMO) were tested. The success of the process was assessed by the number of candidate points and the accuracy of the output parameters. Besides, the time of the simulation related to the number of design points to converge was evaluated

Table 7-3 summarised of the optimisation algorithms results including the number of designed points, candidate points and percentage error between predicted interphase properties and input properties in the forward simulation ($E^i=8.3$ GPA, $v^i=0.176$). **Figure 7-1** presents the relationship between input interphase Young’s modulus and a number of iterations. For example in the screening method, the linear relationship between the input parameter against the number of iterations was observed. This technique is generally used for preliminary design to help narrow down the bounds of input parameters. In the case of MOGA, and AMO, the highly nonlinear functions fluctuating from lower to upper bounds in the first 50 iterations were found, which later became more and more steady. This suggests that both algorithms refine the input parameters during the optimisation process.

Table 7-4 Interphase properties predicted by ANSYS goal-driven optimisation.

| Method | Screening | MOGA | | | AMO | | |
|-------------------------|-----------|--------|--------|--------|--------|--------|--------|
| Converged | 100 | 334 | | | 195 | | |
| Candidate points | 1 | 3 | | | 3 | | |
| E^i predicted | 8.33 | 8.32 | 8.316 | 8.32 | 8.28 | 8.27 | 8.28 |
| % error | 0.4 % | 0.24 % | 0.19 % | 0.24 % | -0.24% | -0.36% | -0.24% |
| v^i predicted | 0.176 | 0.175 | 0.176 | 0.176 | 0.175 | 0.174 | 0.174 |
| % error | 0 % | -0.5 % | 0 % | 0% | -0.5 % | -1.1% | -1.1% |

In this study, all three optimisation algorithms converged and provided satisfactory results. Screening algorithm yielded only one candidate point whereas AMO, MOGA three candidate points. The predicted interphase Young’s modulus ranged from 8.27 to 8.33 GPa, whereas Poisson’s ratio varied from 0.174 to 0.176. The percentage error between predicted interphase properties and that input in forward simulations was below 1.1%. AMO algorithm converged twice faster than MOGA. Therefore, the AMO algorithm was used throughout the optimisation process. It was observed that some factors influence the accuracy of the analysis.

Firstly, the number of designed points is related to the range of the input parameter. Also, the more precise the constraints of output parameters, the more accurate the prediction.

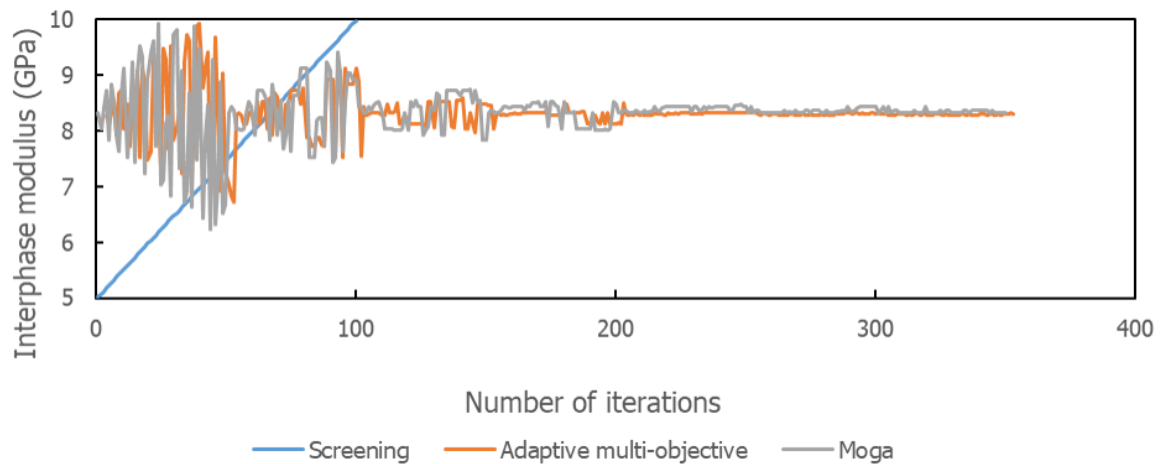


Figure 7-1 Influence of the optimisation algorithm on the behaviour of input parameters. Young's modulus of interphase versus a number of iterations.

7.3 Indirect prediction of the interphase properties

Since the ANSYS DesignXplorer has proven successful in inverse parameter identification, a new optimisation procedure was developed to address the problem of interphase properties. This optimisation model was divided into two-steps based on the macro and microscale.

7.3.1 Optimisation at the macroscale

7.3.1.1 Experimental samples

To solve the optimisation problem, one needs a set of experimental data. Here, results of three-point bending tests were selected (Qin *et al.*, 2015). **Table 7-5** provided the details of sample identifications, dimension and results on flexural modulus, $E_{f_{exp}}$. Three different types of unidirectional laminates (non-coated, epoxy-coated and GNPs coated) were tested in both 0° and 90° fibre orientation resulting in 6 groups of samples. Each laminate sample consisted of 12 laminae. Based on the experimental results and equation **6-2**, displacement on the bottom of the sample middle span (S_{exp} , the same location as S_{ANSYS} in **Figure 7-2**) was calculated and given in **Table 7-5**.

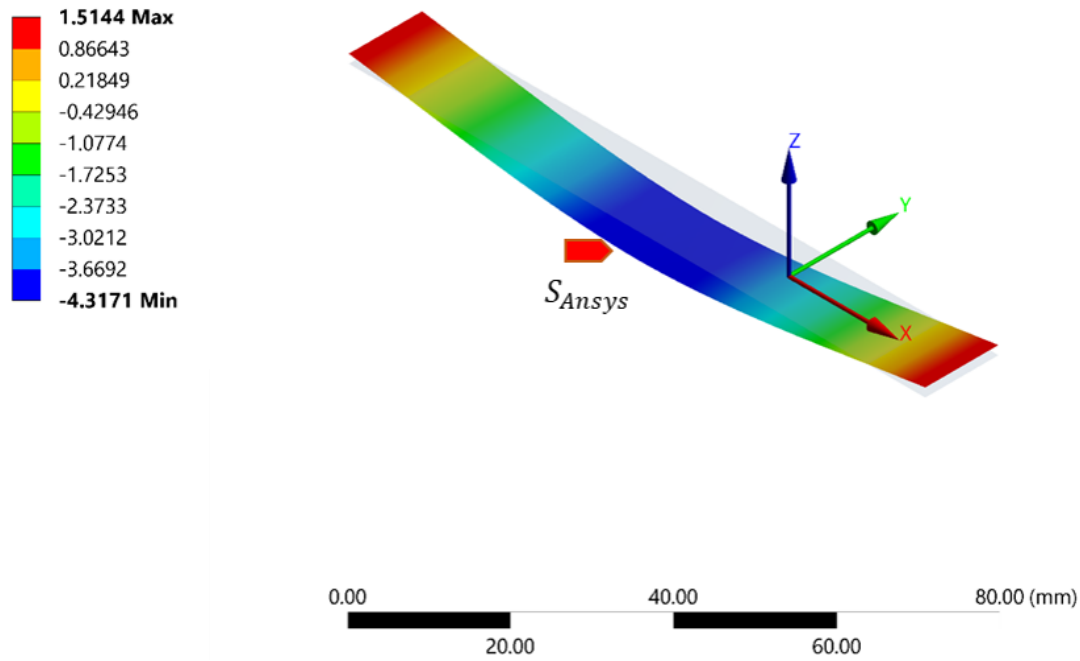


Figure 7-2 Macroscale simulation optimisation. Image use courtesy of Ansys, Inc.

Table 7-5 Samples dimensions and specification used in macroscale simulations.

| Sample ID | Length (mm) | Span (mm) | Width (mm) | Thickness (m) | Force (N) | $E_{f_{exp.}}$ (GPa) | $S_{exp.}$ (mm) |
|------------------|----------------|--------------|---------------|------------------|--------------|-------------------------|--------------------|
| Non-coated 0° | 100 | 80 | 12.7 | 2.3 | 700 | 139 | 4.172 |
| Epoxy-coated 0° | 100 | 80 | 12.7 | 2.3 | 700 | 139 | 4.172 |
| GNNPs-coated 0° | 100 | 80 | 12.7 | 2.3 | 700 | 143 | 4.055 |
| Non-coated 90° | 100 | 80 | 12.7 | 2.3 | 20 | 8.81 | 1.88 |
| Epoxy-coated 90° | 100 | 80 | 12.7 | 2.3 | 20 | 10.8 | 1.53 |
| GNNPs-coated 90° | 100 | 80 | 12.7 | 2.3 | 20 | 11.1 | 1.49 |

The macroscale numerical model was created in ANSYS Workbench based on the same dimensions and lay-up as the experimental CFRP specimen. The orthotropic material model was employed (see section 3.3) so that nine elastic constants were required to describe each lamina - making nine input parameters in this optimisation study. Laminate lay-up was controlled with layered section command. The boundary conditions of the model have been described in Chapter 3.2.3 (Figure 3-9). Applied forces were 700 and 20 N for 0° and 90° unidirectional laminates respectively. The model was simulated to predict the midspan displacement denoted as S_{ANSYS} .

The example of the displacement results of 0° unidirectional laminate in isometric view was presented in **Figure 7-2**. The initial geometry is shown in grey as a comparison. Note that simulations Cartesian coordinate system x-y-z correspond to 1-2-3 in material modelling. The macroscale optimisation process was to update input lamina elastic constants in the way that the numerical deflection (S_{ANSYS}) matched the experimental one ($S_{exp.}$)

7.3.1.2 Parameters sensitivity

As the number of variables increases, the optimisation study may become more and more intractable. Excluding the input parameters with less impact can significantly speed up the optimisation process. Parameters sensitivity studies were conducted to establish the number of lamina elastic constants which have a higher impact on the deflection of the sample. The variation range of elastic constants was estimated from reported experimental measurements (Soden, Hinton and Kaddour, 2004) for this particular type of CFRP (see **Table 7-5**).

The parameter sensitivity results were presented in the form of a bar charts **Figures 7-3** and **7-4**. The x-axis represents the deflection whereas y-axis denotes Spearman correlation coefficient. Note that the closer correlation coefficient to one, the higher the impact of input to output parameters.

Table 7-6 Upper and lower bounds of the parameters sensitivity study – optimisation at macroscale level.

| Lamina Elastic Constants | Symbol | Lower bound | Upper bound |
|--|------------|-------------|-------------|
| Longitudinal modulus (x-direction) | E_1 | 130 GPa | 160 GPa |
| Transverse modulus (y-direction) | E_2 | 8 GPa | 12 GPa |
| Transverse modulus (z-direction) | E_3 | 8 GPa | 12 GPa |
| In-plane Poisson's ratio (x-y direction) | ν_{12} | 0.2 | 0.4 |
| In-plane Poisson's ratio (x-z direction) | ν_{13} | 0.2 | 0.4 |
| Out-of-plane Poisson's ratio (y-z direction) | ν_{23} | 0.3 | 0.5 |
| In-plane shear modulus (x-y direction) | G_{12} | 4 GPa | 7 GPa |
| In-plane shear modulus (x-z direction) | G_{13} | 4 GPa | 7 GPa |
| Out-of-plane shear modulus (y-z direction) | G_{23} | 3 GPa | 4 GPa |

The parameter correlation study of 0° unidirectional laminate (**Figure 7-3**) showed that longitudinal lamina elastic modulus (E_1) had the highest influence on the laminate deflection (sensitivity value is almost one). All remaining parameters had sensitivities values below 0.2; however, in-plane Poisson's ratio (ν_{12}), and in-plane shear modulus (G_{13}) influenced the deflection slightly higher than other elastic constants. Therefore, for the three-point bending simulations of 0° unidirectional laminate, input parameters such as E_1 , ν_{12} and G_{13} were selected.

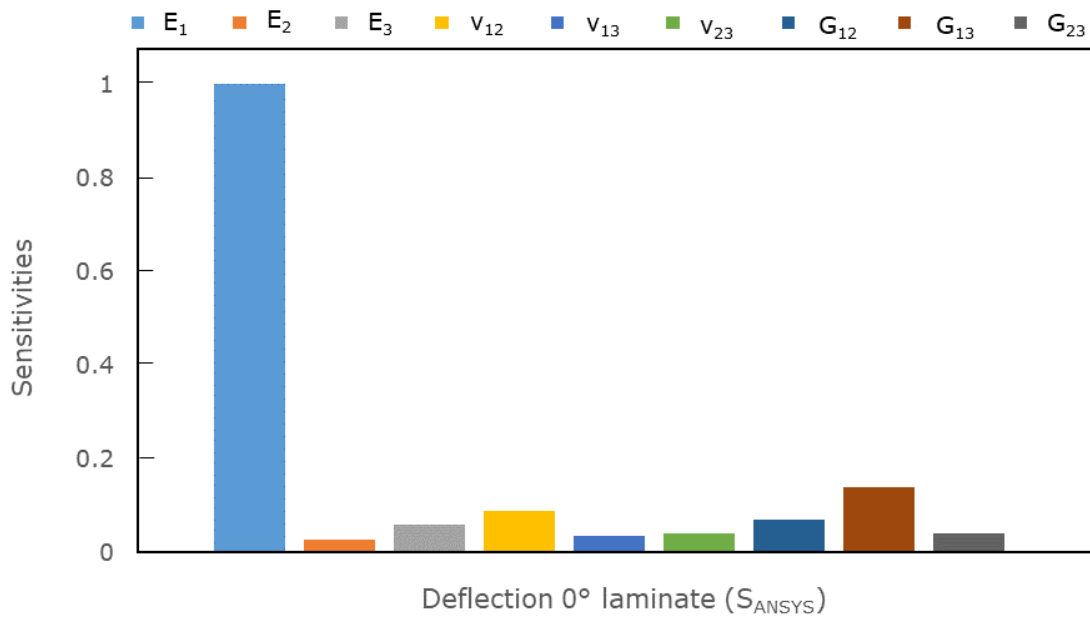


Figure 7-3 Bar chart represents the influence of the input lamina elastic constant on the deflection of 0° unidirectional laminate in three-point bending test simulations.

In the case of 90° fibre orientation, the transverse modulus (E_2) of the lamina affected most the deflection behaviour in three-point bending. While the rest of the lamina parameters had rather low influence. Most sensitive input parameters (E_2 and ν_{23}) were identified. They were optimised in simulations of 90° unidirectional laminate. The relationship between remaining parameters followed transversely isotropic material assumptions, so $G_{12} = G_{13}$, $E_2 = E_3$. The parameter sensitivity study eliminated the number of unnecessary parameters, which, in turn, would improve the efficiency of the optimisation process.

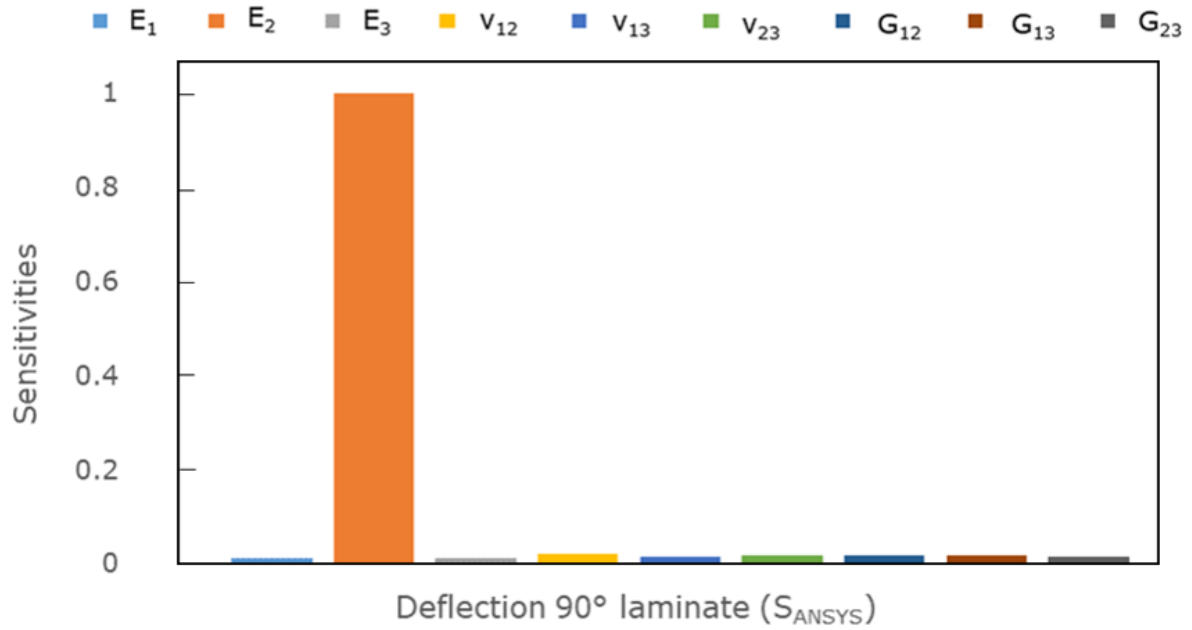


Figure 7-4 Bar chart represents the influence of the input lamina elastic constant on the 90° deflection in three-point bending test simulations.

7.3.1.3 Initial input parameters – elastic lamina constants

Initial input parameters were predicted using the forward simulations through RVE models discussed in Chapter 4.4 and are summarised in **Table 7-7**. The same volume fraction of carbon fibre as the experiment was adopted to calculate the size of RVE. The thickness of the interphase was estimated from SEM images. These lamina properties were input into Engineering Data component in ANSYS Workbench software.

Table 7-7 Initial guess parameters predicted by RVE models.

| Sample | Lay-up | CF AS4 | Epoxy | Inter-phase | E_1 (GPa) | E_2 (GPa) | ν_{12} | ν_{23} | G_{12} (GPa) |
|-------------------|--------|--------|-------|-------------|-------------|-------------|------------|------------|----------------|
| Non-coated CFRP | 0° | 65% | 35% | 0% | 149.7 | 8.95 | 0.24 | 0.48 | 5.08 |
| Epoxy-coated CFRP | 0° | 64% | 35.9% | 1.1% | 144.92 | 8.81 | 0.244 | 0.477 | 4.934 |
| GNPs coated CFRP | 0° | 66% | 32% | 2% | 156.01 | 9.80 | 0.25 | 0.48 | 5.60 |

7.3.1.4 Results

i. Non-coated CFRP

Table 7-8 presents the comparison between input and optimised lamina properties for the non-coated CFRP. Input parameters were predicted by the 2D phase micromechanical model as described in section 4-5. When these parameters were used in the simulation, the deflection of the middle of the samples were 4.05 and 1.9 mm for the 0° and 90° unidirectional laminates respectively. The results of 90 degrees compare favourably with the experimental deflection of 1.88 mm. A small difference of 0.12 mm was observed in the results of 0° unidirectional laminate. The optimisation study was performed in both fibre directions. The optimised lamina elastic constants, such as E_1 , were decreased slightly. The feasibility of optimised lamina elastic constants were checked by performing simulation in both directions. Based on the optimised parameters, recalculated deflection results were in nearly perfect agreement with the experimental data.

Table 7-8 Comparison of input and optimised lamina properties for non-coated CFRP.

| Sample ID | | E_1 (GPa) | E_2 (GPa) | ν_{12} | ν_{23} | G_{12} (GPa) | $S_{Ansys.}$ (mm) | | $S_{exp.}$ (mm) | |
|------------|-----------|----------------|----------------|------------|------------|-------------------|----------------------|-------------|--------------------|-------|
| | | | | | | | 0° | 90° | 0° | 90° |
| Non-coated | Input | 149.7 | 8.95 | 0.24 | 0.48 | 5.08 | 4.050 | 1.90 | 4.172 | 1.880 |
| | Optimised | 145.12 | 8.93 | 0.24 | 0.47 | 5.11 | 4.172 | 1.88 | 4.172 | 1.880 |

ii. epoxy- coated CFRP

In the case of epoxy-coated CFRP, the initial input parameters for the interphase properties in 3-phase RVE model directly adopted the epoxy properties. The three-point bending simulations of initial guess properties yielded the deflection of 4.113 and 1.906 mm for 0 and 90° unidirectional laminates respectively. Small difference of only 0.059 mm was observed for the 0° unidirectional laminate. On the other hand, a much larger discrepancy between numerical and experimental results for 90 ° unidirectional laminate occurred. To eliminate this difference, the numerical model was optimised. Newly obtained lamina transverse modulus differed from initial guess by a significant change of more than 2.0 GPa. Newly optimised set of parameters were implemented into the numerical simulation and no difference between numerical and experimental displacement results was found.

Table 7-9 Comparison of input and optimised lamina properties for epoxy-coated CFRP.

| Sample ID | | E_1 (GPa) | E_2 (GPa) | ν_{12} | ν_{23} | G_{12} (GPa) | $S_{Ansys.}$ (mm) | | $S_{exp.}$ (mm) | |
|----------------|-----------|----------------|----------------|------------|------------|-------------------|----------------------|--------------|--------------------|-------|
| | | | | | | | 0° | 90° | 0° | 90° |
| Epoxy - coated | Input | 147.162 | 8.81 | 0.244 | 0.477 | 4.934 | 4.113 | 1.906 | 4.172 | 1.530 |
| | Optimised | 145.12 | 10.95 | 0.254 | 0.430 | 5.110 | 4.175 | 1.532 | 4.172 | 1.530 |

iii. GNPs coated CFRP

An initial guess of lamina properties assumed the values from the three-phase RVE model (see section 4.4.2). Correspondingly, numerical prediction of mid-span deflections were 3.880 and 1.720 mm for 0 and 90° unidirectional laminates respectively. These deflections were noticeably different from the experiments. Initial input lamina properties underestimated the maximum deflection for the 0° laminate and at the same time overestimated the 90° laminate deflection. After the numerical optimisation, lamina constants E_1 and G_{12} decreased slightly whereas the transverse modulus E_2 increased from 9.80 to 11.28 GPa. Newly obtained lamina properties were tested for the laminate in both directions. The numerical and experimental deflection were almost identical.

Table 7-10 Comparison of input and optimised lamina properties for GNPs-coated CFRP.

| Sample ID | | E_1 (GPa) | E_2 (GPa) | ν_{12} | ν_{23} | G_{12} (GPa) | $S_{Ansys.}$ (mm) | | $S_{exp.}$ (mm) | |
|-------------|-----------|----------------|----------------|------------|------------|-------------------|----------------------|--------------|--------------------|------|
| | | | | | | | 0° | 90° | 0° | 90° |
| GNPs-coated | Input | 156.01 | 9.80 | 0.25 | 0.48 | 5.60 | 3.88 | 1.72 | 4.055 | 1.49 |
| | Optimised | 149.3 | 11.28 | 0.22 | 0.43 | 5.29 | 4.051 | 1.488 | 4.055 | 1.49 |

7.3.2 Optimisation at the microscale

In the second step of the optimisation framework, the three-phase RVE model was used to indirectly determine the interphase properties following similar procedure as in 7.1. Optimisation process was performed for the three materials: non-coated, epoxy coated, and GNPs coated CFRP, which have the same type of fibre and matrix (AS4/Epon 828).

7.3.2.1 Non-coated CFRP

Two-phase RVE model was adopted to represent non-coated CFRP sample, which was composed of 65 % carbon fibre, and 35% epoxy resin and assumes that the interphase did not form. The size of the RVE was calculated as $a_1 = 1.05\mu m$, $a_2 = 4.19\mu m$, $a_3 = 7.25\mu m$ based on the volume fraction and fibre diameter. The fibre transverse isotropic properties were selected as input parameters for this optimisation process. **Figure 7-5** explains how carbon fibre AS4 material properties were parameterised in APDL code.

Epoxy resin properties ($E^m=3.45$ GPa, $\nu^m = 0.34$), fibre size and RVE dimension were prescribed. In ANSYS APDL script, x-y-z coordinate system corresponds to 1-2-3 coordinates throughout this study. Note that carbon fibre behaves transversely isotropic $E_2^f = E_3^f$, $\nu_{12}^f = \nu_{13}^f$ and $G_{12}^f = G_{13}^f$, where 1 is the carbon fibre axial direction.

Upper and lower bounds of fibre parameters were selected based on published carbon fibre properties (Soden, Hinton and Kaddour, 2004; Hexcel, 2016) as shown in **Table 7-10**. The optimised lamina properties from the macroscale study of non-coated CFRP (**Table 7-7**) became so-called 'sought target', i.e. objective of this study. The constraints on those targets were slightly relaxed in **Table 7-10**.

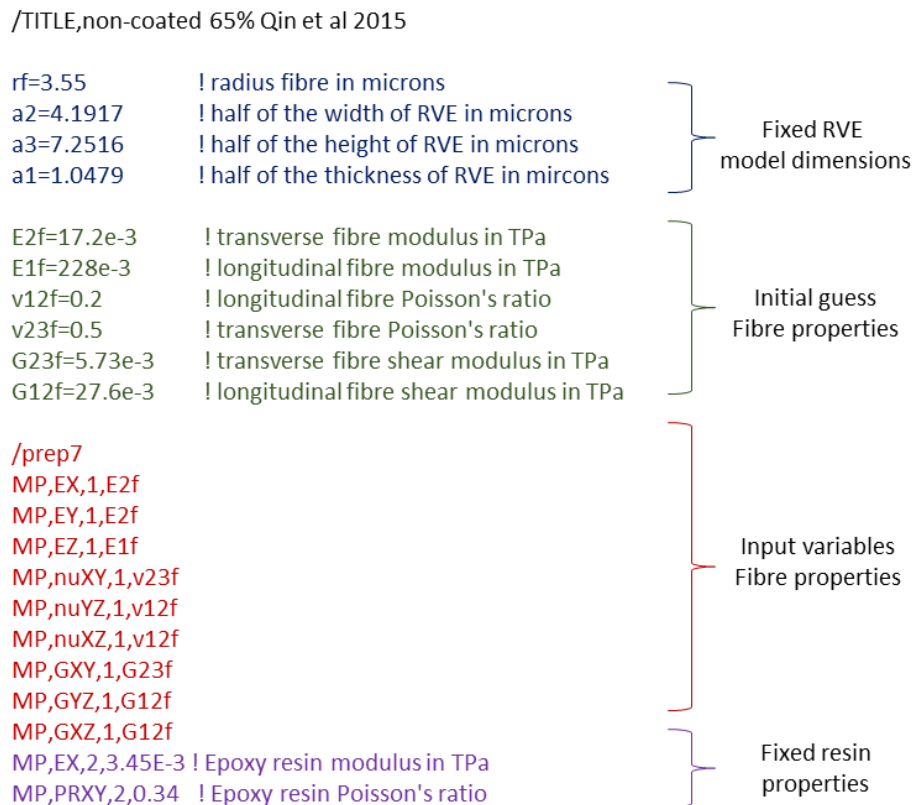


Figure 7-5 Parameterisation of the two-phase RVE model in APDL script.

Table 7-11 Upper and lower bounds of the carbon fibre input parameters.

| Input parameter | Initial guess | Lower bound | Upper bound |
|-----------------------------|---------------|-------------|-------------|
| E_1^f (GPa) | 228 | 220 | 235 |
| $E_2^f = E_3^f$ (GPa) | 17.32 | 15 | 19 |
| $\nu_{12}^f = \nu_{13}^f$ | 0.2 | 0.18 | 0.22 |
| ν_{23}^f | 0.5 | 0.45 | 0.55 |
| $G_{12}^f = G_{13}^f$ (GPa) | 27.6 | 15 | 30 |
| Output parameters | Sought target | Constraints | |
| E_1 (GPa) | 145.12 | 144.5 | 145.5 |
| E_2 (GPa) | 8.93 | 8.9 | 8.98 |
| ν_{12} | 0.24 | 0.235 | 0.45 |
| ν_{23} | 0.47 | 0.47 | 0.48 |
| G_{12} (GPa) | 5.11 | 5.00 | 5.15 |

Table 7-11 presented three candidate points obtained in this optimisation study. The lamina properties based on initial guess parameters were also included. This study was to determine the properties of carbon fibres, so the elastic lamina properties matched the experimental study (**Table 7-7**). CFRP fibre initial input parameters were taken from literature (Ding *et al.*, 2016), and they served as good guess close to optimal values, in particular, on transverse lamina elastic modulus E_2 and lamina Poisson's ratio ν_{12} . Lots of improvement were required for of the parameters of carbon fibre such as E_1 and ν_{23} (**Table 7-12**). The optimised E_1 value is found 220 GPa and lied in the reasonable range of the AS4 properties. Experimental measurement revealed that E_1 can vary from 220 to 235 GPa depending on the testing methods (Isaac and Ori, 2006). Mean average of absolute percentage error between optimised lamina properties and predicted for initial guess and candidate points are given in **Table 7-12**. After optimisation of carbon fibre properties, the average percentage error between numerical and experimental results reduced from 1.192% to 0.406% for candidate point number 3. Newly optimised carbon fibre properties $E_1^f = 220.41$ GPa, $E_2^f = E_3^f = 17.01$ GPa, $\nu_{12}^f = \nu_{13}^f = 0.198$, $\nu_{23}^f = 0.5$, $G_{12}^f = G_{13}^f = 29.04$ GPa and $G_{23}^f = 5.67$ GPa were updated for the following epoxy-coated and GNPs-coated models accordingly. Calculation of transverse fibre shear modulus, G_{23}^f followed equation 2-4.

Table 7-12 Results of the optimisation study on the carbon fibre properties – non-coated CFRP (two-phase RVE model)

| Candidate Point | E_1^f (GPa) | E_2^f (GPa) | ν_{12}^f | ν_{23}^f | G_{12}^f (GPa) | E_1 (GPa) | E_2 (GPa) | ν_{12} | ν_{23} | G_{12} (GPa) |
|---|------------------|------------------|--------------|--------------|---------------------|----------------|----------------|------------|------------|-------------------|
| Initial guess | 228.00 | 17.200 | 0.200 | 0.500 | 27.60 | 149.7 | 8.95 | 0.240 | 0.48 | 5.080 |
| Candidate point 1 | 220.36 | 17.011 | 0.201 | 0.485 | 29.08 | 144.73 | 8.921 | 0.243 | 0.471 | 5.122 |
| Candidate point 2 | 220.73 | 17.011 | 0.198 | 0.500 | 26.62 | 144.97 | 8.917 | 0.241 | 0.476 | 5.045 |
| Candidate point 3 | 220.41 | 17.011 | 0.198 | 0.500 | 29.042 | 144.76 | 8.917 | 0.241 | 0.476 | 5.122 |
| Sought target –lamina properties | | | | | | 145.12 | 8.93 | 0.240 | 0.47 | 5.110 |

Table 7-13 Absolute percentage error results. Difference between calculated lamina properties from new carbon fibre parameters at microscale and lamina properties obtained from the macroscale optimisation study.

| Candidate Point | E_1^f (GPa) | E_2^f (GPa) | ν_{12}^f | ν_{23}^f | G_{12}^f (GPa) | E_1 % error | E_2 % error | ν_{12} % error | ν_{23} % error | G_{12} % error | Mean average percentage error % |
|-------------------|------------------|------------------|--------------|--------------|---------------------|---------------------|---------------------|--------------------------|--------------------------|---------------------|---------------------------------------|
| Initial guess | 228.00 | 17.200 | 0.200 | 0.500 | 27.60 | 3.06 % | 0.23 % | 0.00 % | 2.08% | 0.59 % | 1.192 % |
| Candidate point 1 | 220.36 | 17.011 | 0.201 | 0.485 | 29.08 | 0.27 % | 0.10 % | 1.23 % | 0.21 % | 0.23 % | 0.408 % |
| Candidate point 2 | 220.73 | 17.011 | 0.198 | 0.500 | 26.62 | 0.10 % | 0.15 % | 0.41 % | 1.26 % | 1.27 % | 0.638 % |
| Candidate point 3 | 220.41 | 17.011 | 0.198 | 0.500 | 29.042 | 0.25 % | 0.15 % | 0.41 % | 1.26 % | 0.23 % | 0.406 % |

7.3.2.2 Epoxy-coated CFRP RVE

When epoxy was initially coated on carbon fibres, a distinctive interphase layer formed inside CFRP sample, which required three-phase RVE model in the optimisation. The carbon fibre volume fraction was 64% and corresponded to following RVE dimensions: $a_1 = 1.04\mu m$, $a_2 = 4.16\mu m$, $a_3 = 7.2\mu m$. The interphase layer was assumed isotropic and described by three parameters: elastic modulus (E^i), Poisson's ratio (ν^i) and thickness (t^i). The thickness of the interphase was also treated as the variable, because of its measuring difficulty. The interphase's properties acted as input parameters and initially assumed the properties of epoxy. In the ADPL code, the interphase properties and thickness were updated iteratively in the optimisation study; whereas remaining parameters (RVE size, fibre and epoxy resin properties) were constant see **Figure 7-6**. Note that the rest optimisation study was based on the same fibre AS4 which values have already been predicted in Section 7.2.3.1.

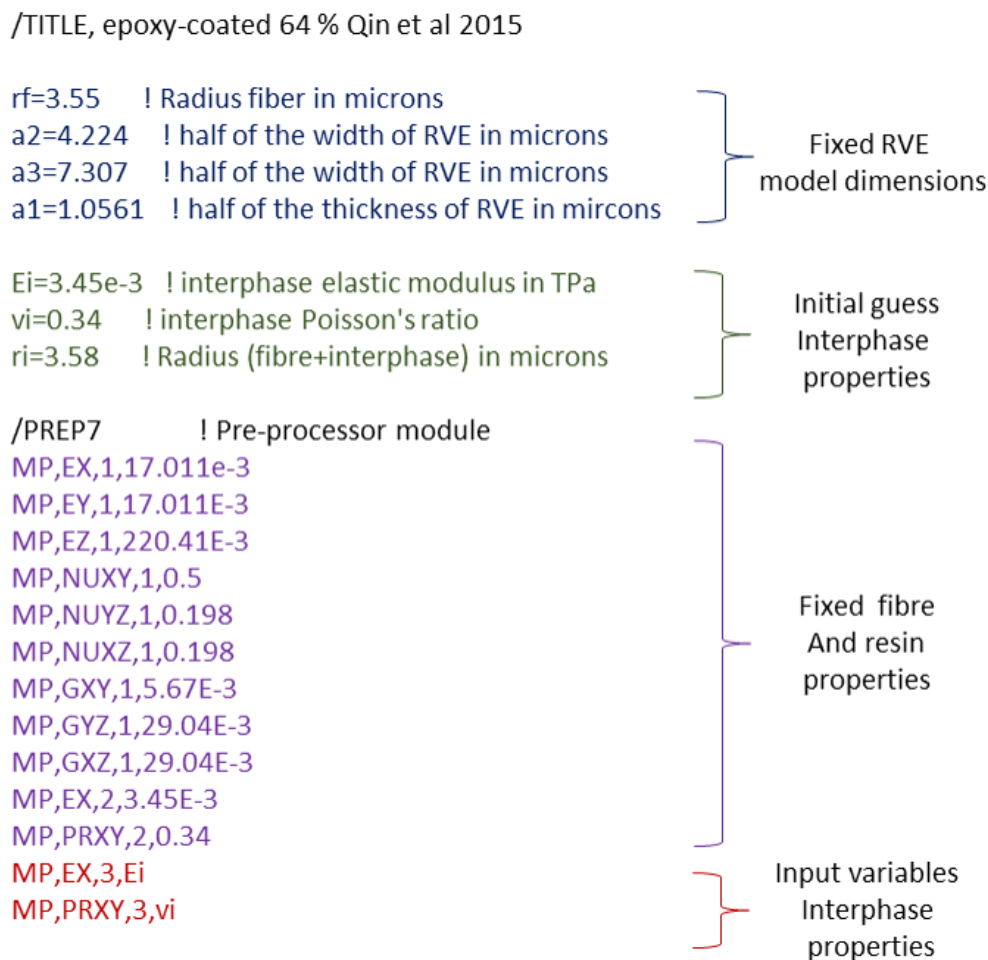


Figure 7-6 Parameterisation of the three-phase RVE model in APDL script.

Upper and lower bounds of the interphase properties were selected based on the experimental measurements and are provided in **Table 7-13**. The interphase modulus was between matrix and fibre properties, whereas the thickness of the interphase varied from 0 to 200 nm. There was no indication of the Poisson's ratio limits in the literature; therefore, a wide range from 0.1 to 0.5 was selected. The sought target parameters were elastic lamina constants predicted in macroscale optimisation study for epoxy-coated CFRP (**Table 7-9**). Constraints were applied to aid fast convergence of the solution.

Table 7-14 Objectives of this optimisation study and upper and lower bounds of interphase properties in epoxy-coated CFRP.

| Input parameter | Initial guess | Lower bound | Upper bound |
|--------------------------|----------------------|--------------------|--------------------|
| E^i (GPa) | 3.45 | 3.45 | 220 |
| ν^i | 0.34 | 0.1 | 0.5 |
| t^i (nm) | 30 | 0 | 200 |
| Output parameters | Sought target | Constraints | |
| E_1 (GPa) | 145.12 | 140 | 160 |
| E_2 (GPa) | 10.95 | 10.5 | 11 |
| ν_{12} | 0.254 | 0.22 | 0.27 |
| ν_{23} | 0.47 | 0.45 | 0.5 |
| G_{12} (GPa) | 5.11 | 5 | 7 |

Parameters sensitivity study was performed to investigate the influence of the interphase properties on the elastic constants of the lamina (**Figure 7-7**). High dependence between interphase modulus and thickness was found for lamina longitudinal modulus E_1 and transverse modulus E_2 and in-plane shear modulus G_{12} . Contrarily, these lamina elastic moduli were completely insensitive to the interphase Poisson's ratio. Interphase Poisson's ratio has the highest impact on in-plane lamina Poisson's ratio. Out-of-plane lamina Poisson's ratio was affected by both interphase moduli and Poisson's ratio.

Results of the optimisation study of three-phase RVE model were presented in **Table 7-14**. Epoxy resin properties were initially assumed for the epoxy coating properties. Their actual values were found by minimizing the difference between predetermined lamina properties at microscale and counterparts of microscale modelling. The ANSYS software returned three possible candidate points, which can meet the required sought targets (**Table 7-**

13). Interphase thickness in the model was found close to 190 nm. The interphase's elastic modulus was found 60.51, 110.42 and 70.42 GPa for 1, 2 and 3 candidate points respectively. This large variation indicates the difficulty of achieving convergence of the optimisation for this case, which was alleviated by introducing some amount of relaxation in the sought target as constraints. Lamina properties were recalculated based on optimised properties of the interphase and compared with given target values. The error of lamina transverse elastic modulus is acceptable whereas the error is more significant for other parameters such as in-plane shear modulus. The percentage error for each parameter and mean average error for the whole optimisation process were also given in **Table 7-15**. Candidate 1 point appears to offer optimal value for the interphase with the lowest mean average error of 4.98 %.

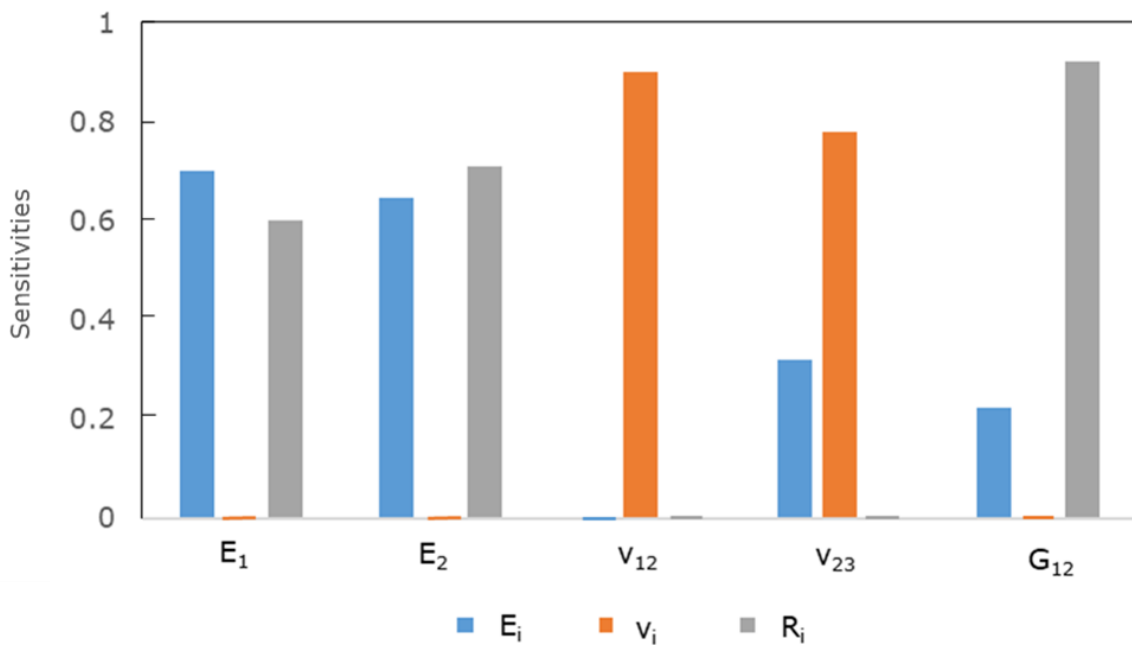


Figure 7-7 Parameters sensitivity study for epoxy-coated CFRP.

Table 7-15 Results of the optimisation study on the carbon fibre properties – epoxy-coated CFRP (three-phase RVE model)

| Candidate Point | E_i (GPa) | ν_i | t_i (nm) | E_1 (GPa) | E_2 (GPa) | ν_{12} | ν_{23} | G_{12} (GPa) |
|--|----------------|---------|---------------|----------------|----------------|------------|------------|-------------------|
| Initial guess | 3.45 | 0.34 | 30 | 142.620 | 8.767 | 0.242 | 0.477 | 4.976 |
| Candidate point 1 | 60.51 | 0.24 | 192 | 146.669 | 10.402 | 0.253 | 0.471 | 6.104 |
| Candidate point 2 | 110.42 | 0.33 | 185 | 150.040 | 10.593 | 0.253 | 0.478 | 6.214 |
| Candidate point 3 | 70.43 | 0.11 | 187 | 147.290 | 10.400 | 0.223 | 0.467 | 6.195 |
| Sought target – Optimised lamina properties | | | | 145.120 | 10.950 | 0.254 | 0.470 | 5.110 |

Table 7-16 Absolute percentage error results. Difference between calculated lamina properties and experimental lamina properties obtained from the macroscale optimisation study.

| Candidate Point | E_i (GPa) | ν_i | t_i (nm) | E_1 % error | E_2 % error | ν_{12} % error | ν_{23} % error | G_{12} % error | Mean average percentage error % |
|--------------------------|----------------|---------|---------------|------------------|------------------|-----------------------|-----------------------|---------------------|--|
| Initial guess | 3.45 | 0.34 | 30 | 1.75 % | 24.90 % | 4.96 % | 1.47 % | 2.69 % | 7.154 % |
| Candidate point 1 | 60.51 | 0.24 | 192 | 1.02 % | 5.27 % | 0.40 % | 0.21 % | 17.63 % | 4.983 % |
| Candidate point 2 | 110.42 | 0.33 | 185 | 3.25 % | 3.37 % | 0.40 % | 1.67 % | 17.77 % | 5.292 % |
| Candidate point 3 | 70.43 | 0.11 | 187 | 1.45 % | 5.29 % | 13.9 % | 0.64 % | 17.55 % | 7.766 % |

7.3.2.3 GNPs-epoxy coated CFRP – RVE model

GNPs epoxy reinforced interphase properties were determined accordingly using the three-phase RVE model. In this model, the carbon fibre volume fraction was 66% and RVE dimensions were: $a_1 = 1.04\mu m$, $a_2 = 4.16\mu m$, $a_3 = 7.2\mu m$. Corresponding to the experimental observation of homogenous distribution of GNPs in the reinforced interphase (Qin *et al.*, 2015), the interphase was assumed isotropic thus characterised by an elastic modulus (E^i), Poisson's ratio (ν^i) and thickness (t^i). They are parameterised in the APDL script in **Figure 7-7**. The size of the RVE, fibre and resin properties were fixed. Interphase modulus, Poisson's ratio and thickness were updated iteratively in the optimisation study.

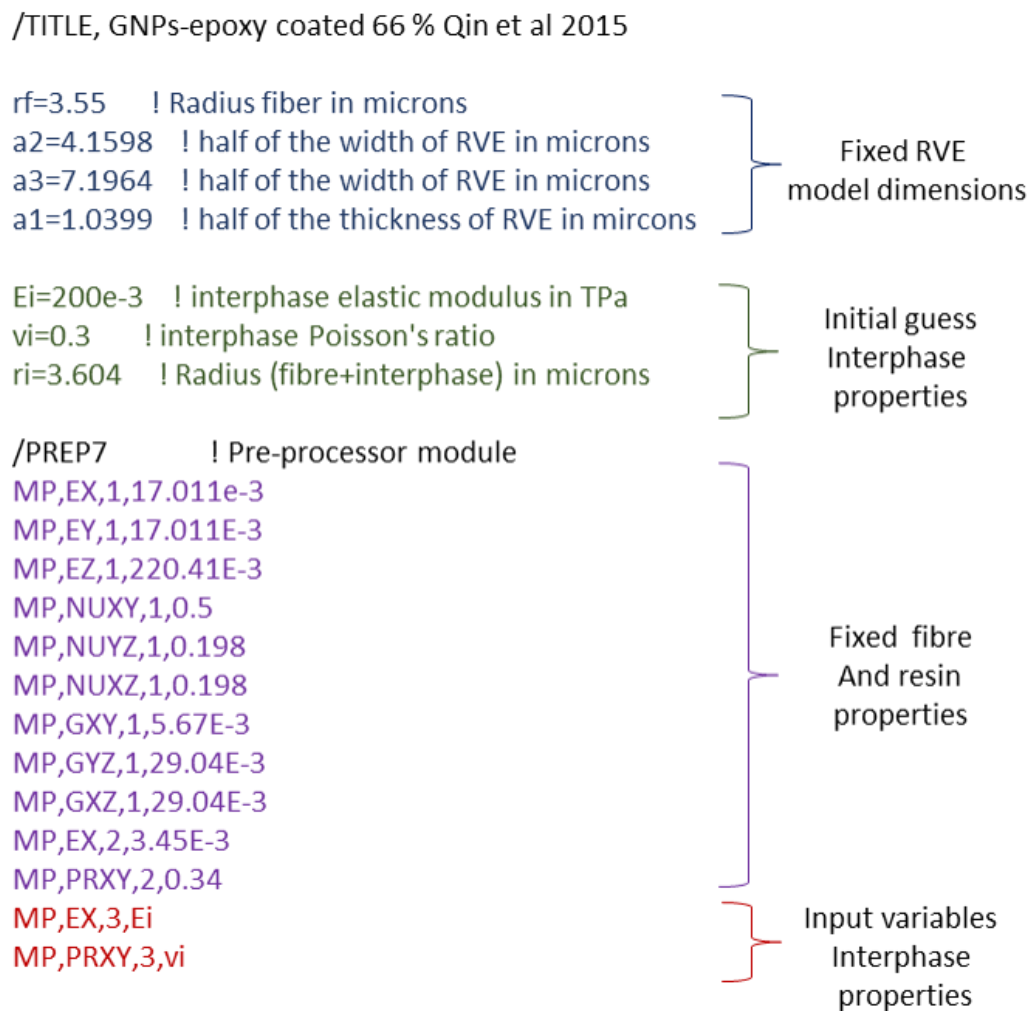


Figure 7-8 Parameterisation of the three-phase RVE model in APDL script.

GNPs reinforced interphase modulus was allowed to vary from 1 to 500 GPa and the Poisson's ratio in the range of 0.1 to 0.5 and thickness from the range of 50 to 200 nm. The lamina properties, which was pre-determined from the microscale optimisation step, acted as

output parameters in the microscale optimisation. A similar relaxation to epoxy-coated case was applied as constraints to facilitate the convergence of this optimisation process (see **Table 7-17**).

Table 7-17 Objectives of this optimisation study and upper and lower bounds of interphase properties – GNP_s coated CFRP

| Input parameter | Initial guess | Lower bound | Upper bound |
|-------------------|---------------|-------------|-------------|
| E^i (GPa) | 200 | 1 | 500 |
| ν^i | 0.3 | 0.1 | 0.5 |
| t^i (nm) | 54 | 0 | 200 |
| Output parameters | Sought target | Constraints | |
| E_1 (GPa) | 149.3 | 140 | 160 |
| E_2 (GPa) | 11.28 | 11.0 | 11.4 |
| ν_{12} | 0.22 | 0.21 | 0.25 |
| ν_{23} | 0.47 | 0.47 | 0.48 |
| G_{12} (GPa) | 5.29 | 5 | 7 |

Tables 7-18 summarised three candidate points for the GNP_s reinforced interphase properties from the microscale optimisation. As the sought target involves multiple objectives, it is impossible to find a unique solution to satisfy all of them. All three candidates showed a consistent thickness value ~ 194.3 nm for this interphase layer. The elastic modulus varies within the range of 129.1 and 132.9 GPa. The Poisson's ratio varies in a larger range from 0.108 to 0.237. The identified candidate did not satisfy each objective to the same extent. Based on identified candidates, output parameters were calculated, and their difference with pre-set targets were compared in **Table 7-19**. The target of transverse elastic modulus was most satisfied with its average difference as low as 0.56%. The longitudinal elastic modulus presents a consistent but finite difference of around 4.4%. The variation of percentage error changes from 2.81% to 6.79% for ν_{12} and is a bit lower for ν_{23} among these three cases. The most significant error percentage was found for the in-plane shear modulus G_{12} , which is as high as 23.05% for the candidate point 1. By comparing the arithmetic average of percentage error for all targets, candidate point 1 was chosen as the determined properties for the GNP_s-reinforced interphase.

Table 7-18 Results of the optimisation study on the carbon fibre properties – GNPs-coated CFRP (three-phase RVE model)

| Candidate Point | E_i (GPa) | ν_i | t_i (nm) | E_1 (GPa) | E_2 (GPa) | ν_{12} | ν_{23} | G_{12} (GPa) |
|--|----------------|---------|---------------|----------------|----------------|------------|------------|-------------------|
| Initial guess | 200 | 0.300 | 54.0 | 150.689 | 9.752 | 0.244 | 0.476 | 5.655 |
| Candidate point 1 | 129.1 | 0.108 | 194.3 | 156.08 | 11.195 | 0.214 | 0.474 | 6.875 |
| Candidate point 2 | 133.2 | 0.203 | 194.39 | 156.3 | 11.217 | 0.231 | 0.477 | 6.861 |
| Candidate point 3 | 132.9 | 0.237 | 194.36 | 156.19 | 11.214 | 0.236 | 0.478 | 6.851 |
| Sought target – Optimised lamina properties | | | | 149.3 | 11.28 | 0.220 | 0.470 | 5.29 |

Table 7-19 Absolute percentage error results for GNPs coated CFR. Difference between calculated lamina properties and experimental lamina properties obtained from the macroscale optimisation study (sought target).

| Candidate Point | E_i (GPa) | ν_i | t_i (nm) | E_1 % error | E_2 % error | ν_{12} % error | ν_{23} % error | G_{12} % error | Mean percentage error % |
|--------------------------|----------------|---------|---------------|------------------|------------------|-----------------------|-----------------------|---------------------|--------------------------------|
| Initial guess | 200 | 0.300 | 54.0 | 0.92 % | 15.66 % | 9.84 % | 1.26 % | 6.45% | 6.826 % |
| Candidate point 1 | 129.1 | 0.108 | 194.3 | 4.34 % | 0.76 % | 2.81 % | 0.84 % | 23.05 % | 6.360 % |
| Candidate point 2 | 133.2 | 0.203 | 194.39 | 4.48 % | 0.56 % | 4.76 % | 1.47 % | 22.89 % | 6.832 % |
| Candidate point 3 | 132.9 | 0.237 | 194.36 | 4.41 % | 0.59 % | 6.78 % | 1.67 % | 22.78 % | 7.246 % |

7.3.3 Discussion

The optimisation exercise was purposely designed to make full use of available experimental data, which nicely demonstrated the important role of the interphase in the development of CFRPs. In the microscale optimisation, simulations were performed for all three laminate samples subjected to the three-point bending test. Among which laminae of a selected laminate sample adopted the same transversely isotropic constitutive model. In unidirectional laminate samples, all laminae assumed the same fibre orientation, either 0° or 90° . Mechanical properties of different lamina were then derived from measurement of corresponding laminate samples. Lamina of GNPs coated laminate presented the highest value for longitudinal (E_1) and transverse (E_2) elastic moduli among all three types of laminate. Significant change was observed in E_2 . When epoxy was used to pre-treat fibre creating a distinctive interphase layer, the lamina was enhanced in E_2 by 2.02 GPa, which is equivalent to a 22.6 % increase. When the GNPs was used to enhance the interphase layer, the resultant lamina transverse property increased up to 11.28 GPa, which is equivalent to a 26.3 % increase of non-coated sample. In the microscale optimisation, the carbon fibre properties were determined firstly from the non-coated samples, which were later used in further optimisation to determine the interphase properties for coated samples. This designed process would rule out possible artefact caused by use of inconsistent carbon fibre properties.

Based on the same carbon fibre properties, the GNPs-coated interphase presented much higher elastic modulus compared with that of epoxy-coated interphase. The increase is 62.47 GPa, which was equivalent to 51 % increase due to the GNPs enhancement. The Poisson's ratio changed from 0.11 to 0.237. However, the change in the interphase layer thickness is small. It increased from 192.0 nm to 194.36 nm. This small change was understandable from the experiment, which used the same setup to introduce the coating to the carbon fibre. This small increase in thickness was attributed to the presence of GNPs nanofillers. Based on the determined properties GNPs reinforced interphase, the Mori-Tanaka method (see Chapter 4.2) was used to evaluate local volume fraction within the interphase. The volume fraction of GNPs in the interphase was found around 20%.

Inverse analysis methods have been used to predict constituents' properties of CFRP. Continuous efforts have been devoted to determining elastic properties of carbon fibres (Rupnowski *et al.*, 2005; Mishra and Chakraborty, 2015; Lim *et al.*, 2016). These studies adopted the two-phase RVE model and assumed known epoxy properties and transversely

isotropic properties of carbon fibres were then determined from given lamina properties. Accordingly, the non-coated sample was used to extract carbon fibre (AS4) properties based on the two-phase RVE model. These properties were within the range of carbon fibre datasheet given by product supplier (Hexcel). E_1 of AS4 carbon fibre was found 220 GPa, which was close to the range of 220 to 235 GPa obtained by a direct test of fibre (Daniel and Ishai 2006).

To consider the distinctive contribution from the interphase more advanced three-phase RVE models have to be used. The forward analysis based on the three-phase model is more complicated than the corresponding optimisation exercise, which is even more challenging. To the best of authors' knowledge, the only reported optimisation work considering the interphase used cohesive zone method and assigned lumped material properties to represent the interphase (Lu *et al.*, 2014). The cohesive zone method was however unable to provide detailed stress distribution information across the interphase layer, which were properly analysed in the three-phase RVE simulation.

In the previous three-phase RVE modelling work, most assumed isotropic constitutive equation for the interphase. In line with the experimental observation of homogeneous distribution of GNPs within the interphase (Qin *et al.*, 2015), this study also assumed interphase isotropic in both epoxy-coated and GNPs-coated CFRPs. This isotropic assumption may be questionable. This was also evidenced by the difficult convergence encountered in the optimisation process. Some relaxation had to be utilised in order to achieve final convergence. Lu *et al.* (2014) reported higher stiffness values for normal than tangential direction. Normal stiffness is comparable to the interphase properties in the carbon fibre transverse direction, whereas tangential one corresponds to the longitudinal direction. In the present analysis, isotropic interphase did not satisfy all targets to the same extent. Longitudinal lamina properties such as E_1 , G_{12} were overestimated. From the relationship between input and output parameter, it can be inferred that the interphase properties in longitudinal fibre direction could be lower than transvers one. These suggested that homogenous distribution of GNPs in the interphase might not be entirely true. GNPs was more likely orientated towards normal direction, which could make modulus in that direction higher.

The comparison of predicted interphase properties with the experimental data was attempted. For epoxy-coated CFRP, the predicted interphase thickness was 192 nm and agreed well with that of 200 nm measured by TEM for similar T300/epoxy CFRP (Wu *et al.*, 2014, 2015). Quantitative characterisation of the interphase region remains a big challenge. It is

commonly accepted that the interphase properties for FRP are somewhere between fibre and matrix (Kim, Sham and Wu, 2001). Interphase modulus is usually measured by nanoindentation, AFM or dynamic mechanical mapping (Gu *et al.*, 2010; Niu, Yang and Wang, 2018). For example, the interphase storage modulus of the CFRP was measured using dynamic nanoscale imaging (Gu *et al.*, 2010). The reported value of 60 GPa was close to the predicted interphase properties for epoxy-coated CFRP in this project. However, these experimental measurement processes are very difficult to conduct due to the surface roughness, size-scale effects and tip blunting (Hardiman, Vaughan and McCarthy, 2017). So far, there are no direct experimental measurements of the GNPs reinforced interphase. More work is needed in this area.

Inverse analysis and optimisation studies are expensive in terms of computational time. The ANSYS software provides different optimisation algorithms to accelerate the computation. From the present study, adaptive multi-objective optimisation algorithm, which combines Kriging metamodeling and genetic algorithm, appears to be most effective. This algorithm required less design point to extract elastic properties. Parameter sensitivity help to identify important input parameters, which will exert a huge influence on output parameters. For example, in the microscale optimisation, the interphase thickness was established important parameter to be included.

7.4 Summary

In conclusion, a two-step inverse analysis framework has been used to determine the interphase properties, which combined both macro and microscale modelling. Efficient optimisation was achieved using Adaptive Multi-Objective algorithm in ANSYS DesignXplorer. Measured flexural moduli of three types of composite materials samples, i.e. non-coated, epoxy-coated and GNPs-coated, were chosen for optimisation. During the optimisation process, the macroscale step optimised lamina elastic constants so that numerically calculated flexural modulus of the material matched experimental counterpart. The consecutive optimisation at microscale step determined the interphase properties from predicted lamina elastic constants. Interphase modulus, Poisson's ratio and thickness for epoxy coated CFRP were determined as $E_i = 60.51 \text{ GPa}$, $\nu_i = 0.24$ and $t_i = 192.0 \text{ nm}$. While the GNPs reinforced properties were found $E_i = 129.1 \text{ GPa}$, $\nu_i = 0.108$ and $t_i = 194.3 \text{ nm}$ respectively. This was for the first time to quantify of the nanofillers reinforced interphase properties indirectly.

8 Conclusions

8.1 Summary of findings and contribution to knowledge

This project aimed to study the effects of the nanofillers on mechanical properties of CFRP by means of numerical and experimental approaches. The multiscale analysis was performed to investigate how and why nanofillers improve mechanical properties of CFRP. Experimental work adopting different methods of introducing nanofillers were compared to examine the effects of orientation and concentration of nanofillers in the interphase. The bridging among nano, micro and macroscale is essential to gain insight in the nanofillers reinforcement. The established modelling framework makes it possible to optimise the interphase properties and to study the behaviour of any new nanofillers-reinforced CFRP. This thesis was mainly composed of three aspects: numerical simulation of CFRP with nanofillers coated on the fibre surface, experimental investigation of the spraying nanofillers to enhance the performance of CFRP and inverse analysis to determine interphase properties. Firstly, a series of multiscale numerical simulations based on the combination of Mori-Tanaka homogenisation, RVE micro modelling, and macroscale simulations were developed to predict the material properties of the CFRP with nano-reinforced interphase. The multiscale framework was further tested for the fuzzy fibre reinforced polymer. Then, CFRP coupons made of carbon fibre prepreg or fabric sprayed with nanofillers solution were prepared and experimentally tested. Finally, a series of optimisation studies were conducted to predict the properties of interphase, which was reinforced by nanofillers. The main finding can be summarised as follows:

Effects of the GNPs reinforced interphase on mechanical properties of CFRP:

1. At the nanoscale, properties of GNPs reinforced interphase were directly predicted from the Mori-Tanaka method. When GNPs were randomly orientated, the resultant interphase properties became isotropic with an elastic modulus $E^I = 200$ GPa at around 40% GNPs volume fraction. While the aligned GNPs reinforced interphase with transversely isotropic material properties' were E_1^I was 280 GPa and E_3^I , was only 8 GPa for the same GNPs volume fraction. The extent of enhancement depends greatly on the GNPs orientation and volume fraction.

2. At the microscale, the three-phase RVE model explicitly took the interphase into account. The lamina properties achieved higher improvement in fibre transverse direction, i.e. 12.3% in transverse elastic modulus was obtained for 60 % of randomly orientated GNPs in the reinforced interphase. Randomly orientated GNPs yielded higher improvement than GNPs aligned along the carbon fibre surface.
3. At the macroscale, three-point bending test was simulated based on predicted lamina properties. The numerical results can reproduce experimental data proving the success of the multiscale modelling framework.

Effects of the CNTs reinforced interphase on elastic constants of fuzzy fibre reinforced polymer:

1. The same multiscale framework was successfully applied to fuzzy fibre reinforced polymer, where CNTs were radially bonded to the fibre. At nanoscale, the properties of CNTs reinforced interphase were predicted with Mori-Tanaka method. The interphase showed transversely isotropic properties with $E_{1'} = 297.29$ GPa and $E_{2'} = 6.99$ GPa (at 42% CNTs volume fraction).
2. At the microscale, the three-phase RVE modelling revealed a significant enhancement in the elastic constants of the CNTs reinforced lamina. For example, for the 20% carbon fibre volume fraction, the CNTs in the interphase contributed to 200% increase in transverse lamina modulus. This was related to the radial orientation of CNTs on carbon fibre.
3. Results obtained from the above multiscale analysis agreed well with the composite cylinder method.

Introduction of nanofillers to CFRP with spraying process:

1. Optical microscopic analysis showed regular packing array of fibre distribution in the prepared samples, which confirm the validity of using hexagonal geometry in RVE modelling.
2. Double cantilever beam, three-point bending and short beam tests were conducted to check improvement of mechanical properties after the introduction of nanofillers (i.e. CNTs, GNPs). SEM images of the tested sample confirmed the nanofillers existence and verified the failure mechanics.
3. Spraying nanofillers-ethanol-PVP solution on carbon fibre prepreg improved moderately mechanical properties. Flexural modulus and strength of 0° laminate

increased by 2 and 4.8 % respectively in comparison to the reference CFRP. The flexural modulus of 90° laminate improved by 1.8%, whereas flexural strength decreased by 5.6%. Strain energy release of GNPs sprayed CFRP increased up to 7%.

4. A novel procedure for applying GNPs coating on the carbon fibre surface was developed. GNPs-epoxy-PVP-ethanol solution was sprayed on the carbon fibre fabric using an airbrush. Some improvement was found in the flexural and interlaminar properties. This process could subsequently replace the dip-coating method.

Optimisation study

1. For the first time, two-step weak couple optimisation method was developed to determine the interphase properties using ANSYS DesignXplorer
2. Different algorithm were tested and the Adaptive Multi-Objective algorithm was found to be most efficient.
3. The interphase modulus, Poisson's ratio and thickness were determined as $E_i = 60.51 \text{ GPa}$, $\nu_i = 0.24$ and $t_i = 192.0 \text{ nm}$ for epoxy coated CFRP. While predicted GNPs reinforced properties were significantly higher and corresponded to $E_i = 129.1 \text{ GPa}$, $\nu_i = 0.108$ and $t_i = 194.3 \text{ nm}$ respectively.

This thesis has contributed to an improved understanding of the effects of nano-reinforced interphase on the CFRP, which leads to some suggestions for optimisation of the coating design. The multiscale model provides a systematic and conclusive study on nanofillers orientation, and volume fraction effects on mechanical properties on fibre-reinforced laminates. Spraying method was developed to introduce GNPs-epoxy coating at the carbon fibre surface. A novel two-step optimisation combining micro and macro scale was established to determine the interphase properties.

8.2 Limitations and future work

There are some limitations in this work. In the Mori-Tanaka method, the GNPs are assumed straight and evenly distributed in the interphase. However, GNPs may have a wrinkle structure due to their two-dimensional features. The agglomeration effects caused by the Van der Waals forces that is negligible when the local volume fraction of GNPs is low. When the GNPs volume fraction reaches a high value, the interaction between GNPs needs to be considered. The local volume fraction of the GNPs has direct effects on the properties of the

laminated CFRP. It would be beneficial to get more details on the GNPs reinforced interphase. Moreover, in the manufacturing processes imperfections are unavoidable. This multiscale approach neglects the production flaws such as voids, fibre misalignment cracks and delamination. In RVE, modelling, perfect bonding was assumed between layers. Future modelling work will incorporate appropriate failure model to study the laminate strength.

In the experiment, the effects of the ethanol solvent on the spraying on the carbon fibre fabric or prepreg should be investigated. In the fracture toughness test, only the mid-plane of the laminate was sprayed with nanofillers. It would be interesting to investigate if spraying more layers the laminate would further increase the extent of fracture toughness properties. More work is needed to refine the process of spraying conditions to the carbon fibre fabric in order to improve the adhesion of the coating to the fibre surface. The quality of the sample manufactured will be improved with an accumulation of more operation experience.

Future work of this optimisation framework will consider non-isotropic properties of the interphase. The microscale and microscale optimisation could be implemented in a strong couple. This optimisation framework could be greatly enhanced by considering failure analysis, which enables to estimate flexural strength.

8.3 Publications from this work

- Pawlik M, Dean A, Lu Y. The numerical investigation of graphene-reinforced interphase effects on the mechanical properties of carbon fibre/epoxy composites. Proc. Int. Conf. Compos. Struct. (ICCS20), 2017, p. 194–5.
- Pawlik M, Lu Y. Prediction of elastic constants of the fuzzy fibre reinforced polymer using computational micromechanics. IOP Conf. Ser. Mater. Sci. Eng. 362 (2018) 012006 doi:10.1088/1757-899X/362/1/012006.
- Pawlik M, Dean A, Lu Y. Micromechanical analysis of elastic constants in fibre reinforced polymer: the effects of graphene nanoplatelets interphase. – Manuscript submitted to Composite Science and Technology under review.

- Pawlik M, Lu Y. Prediction of the interphase properties using combined inverse analysis and optimisation. –in preparation.

- Pawlik M, Le H, Lu Y. Spraying GNPs on prepreg and carbon fibre fabric. Effects of GNPs on mechanical properties of CFRP– in preparation.

References

- Al-Ostaz, A. and Jasiuk, I. (1997) 'The influence of interface and arrangement of inclusions on local stresses in composite materials', *Acta Materialia*, 45(10), pp. 4131–4143. doi: 10.1016/S1359-6454(97)00089-X.
- Almuhammadi, K. *et al.* (2014) 'Analysis of interlaminar fracture toughness and damage mechanisms in composite laminates reinforced with sprayed multi-walled carbon nanotubes', *Materials and Design*. Elsevier Ltd, 53, pp. 921–927. doi: 10.1016/j.matdes.2013.07.081.
- Aluko, O., Gowtham, S. and Odegard, G. M. (2017) 'Multiscale modeling and analysis of graphene nanoplatelet/carbon fiber/epoxy hybrid composite', *Composites Part B: Engineering*. Elsevier Ltd, 131, pp. 82–90. doi: 10.1016/j.compositesb.2017.07.075.
- Andrade-Campos, A., De-Carvalho, R. and Valente, R. A. F. (2012) 'Novel criteria for determination of material model parameters', *International Journal of Mechanical Sciences*. Elsevier, 54(1), pp. 294–305. doi: 10.1016/j.ijmecsci.2011.11.010.
- ANSYS (2018) ANSYS. Available at: www.ansys.com (Accessed: 10 August 2018).
- Ashori, A., Rahmani, H. and Bahrami, R. (2015) 'Preparation and characterization of functionalized graphene oxide/carbon fiber/epoxy nanocomposites', *Polymer Testing*. Elsevier Ltd, 48, pp. 82–88. doi: 10.1016/j.polymertesting.2015.09.010.
- ASTM D 5528-01 (2009) *Standard test method for Mode I Interlaminar Fracture Toughness of Unidirectional Fiber-Reinforced Polymer Matrix Composites*. doi: 10.1520/D5528-01R07E03.2.
- ASTM D2344 (2016) 'Standard Test Method for Short-Beam Strength of Polymer Matrix Composite Materials and Their Laminates', *ASTM International*, 00(Reapproved 2006), pp. 1–8. doi: 10.1520/D2344.
- Atif, R. and Inam, F. (2016b) 'Modeling and simulation of graphene based polymer nanocomposites: advances in the last decade Modeling and Simulation of Graphene Based Polymer Nanocomposites: Advances in the Last Decade', *Graphene*, 05(02), pp. 96–142.
- Barbero, E. J. (2014) *Finite Element Analysis of Composite Materials Using ANSYS*. Second. CRC Press.
- Barbero, E. J., Cosso, F. A. and Campo, F. A. (2013) 'Benchmark solution for degradation of elastic properties due to transverse matrix cracking in laminated composites', *Composite Structures*. Elsevier Ltd, 98, pp. 242–252. doi: 10.1016/j.compstruct.2012.11.009.
- Battisti, A. *et al.* (2014) 'Single fiber push-out characterization of interfacial properties of hierarchical CNT-carbon fiber composites prepared by electrophoretic deposition', *Composites Science and Technology*. Elsevier Ltd, 95, pp. 121–127. doi: 10.1016/j.compscitech.2014.02.017.
- Benveniste, Y. (1987) 'A new approach to the application of Mori-Tanaka's theory in composite materials', *Mechanics of Materials*, 6(2), pp. 147–157. doi: 10.1016/0167-6636(87)90005-6.
- Bhattacharya, M. (2016) 'Polymer nanocomposites-A comparison between carbon nanotubes, graphene, and clay

- as nanofillers', *Materials*, 9(4), pp. 1–35. doi: 10.3390/ma9040262.
- Bhattacharya, S., Kamal, M. and Gupta, R. (2003) *Polymeric Nanocomposites. Theory and Practice*. Munich: Hanser. doi: 10.3139/9783446418523.002.
- Bledzki, A. K. *et al.* (1999) 'Determination of elastic constants of glass / epoxy unidirectional laminates by the vibration testing of plates', 59(1999).
- Boeing 787 (2018) *Boeing: 787 By Design*.
- Bolton, W. and Higgins, R. . (2015) *Materials for engineers and technicians*. Abingdon: Routledge.
- Bruno, L. and Poggialini, A. (2005) 'Elastic Characterization of Anisotropic Materials by Speckle Interferometry', *Experimental Mechanics*, 45, pp. 205–212. doi: 10.1177/0014485105054847.
- BS EN ISO 14125 (1998) *Fibre-reinforced plastic composites — Determination of flexural properties*. doi: 10.1520/E0872-82R13.2.
- BS EN ISO 14130 (1998) *Fibre-reinforced plastic composites Determination of apparent interlaminar shear strength by short-beam method (ISO 14130 : 1997)*.
- Cambridge Nanosystems (2017) *Graphene composites*. Available at: <https://cambridgenanosystems.com/graphene-composites/> (Accessed: 1 August 2018).
- Chatzigeorgiou, G., Seidel, G. D. and Lagoudas, D. C. (2012) 'Effective mechanical properties of “fuzzy fiber” composites', *Composites Part B: Engineering*, 43(6), pp. 2577–2593. doi: 10.1016/j.compositesb.2012.03.001.
- Chen, J. *et al.* (2014) 'Modifying glass fibers with graphene oxide : Towards high-performance polymer composites', *Composites Science and Technology*, 97, pp. 41–45. doi: 10.1016/j.compscitech.2014.03.023.
- Chen, J. *et al.* (2016) 'A Reduced graphene oxide deposited carbon fiber reinforced polymer composites for electromagnetic interference shielding', *Composites Part A*, 82, pp. 141–150. doi: 10.1016/j.compositesa.2015.12.008.
- Chen, L. *et al.* (2014) 'A design of gradient interphase reinforced by silanized graphene oxide and its effect on carbon fiber/epoxy interface', *Materials Chemistry and Physics*. Elsevier B.V, 145(1–2), pp. 186–196. doi: 10.1016/j.matchemphys.2014.02.001.
- Cheng, X. *et al.* (2016) 'Electrical conductivity and interlaminar shear strength enhancement of carbon fiber reinforced polymers through synergetic effect between graphene oxide and polyaniline', *Composites Part A*, 90, pp. 243–249. doi: 10.1016/j.compositesa.2016.07.015.
- Cho, J., Chen, J. Y. and Daniel, I. M. (2007) 'Mechanical enhancement of carbon fiber/epoxy composites by graphite nanoplatelet reinforcement', *Scripta Materialia*, 56, pp. 685–688. doi: 10.1016/j.scriptamat.2006.12.038.
- Cho, J., Luo, J. J. and Daniel, I. M. (2007) 'Mechanical characterization of graphite/epoxy nanocomposites by multi-scale analysis', *Composites Science and Technology*, 67(11–12), pp. 2399–2407. doi: 10.1016/j.compscitech.2007.01.006.

- Christensen, R. . (2005) *Mechanics of composite materials*. New York: Dover Publications.
- Comellas, E. *et al.* (2015) ‘Optimization method for the determination of material parameters in damaged composite structures’, *Composite Structures*, 122, pp. 417–424. doi: 10.1016/j.compstruct.2014.12.014.
- Composite World (2016) *Composite World*. Available at: <http://www.compositesworld.com/news/haydale-huntsman-to-collaborate-on-graphene-reinforced-prepreg> (Accessed: 20 July 2017).
- Cui, W. C., Wisnom, M. R. and Jones, M. (1994) ‘Effect of Specimen Size on Interlaminar Shear-Strength of Unidirectional Carbon Fiber-Epoxy’, *Composites Engineering*, 4(3), pp. 299–307. doi: 10.1016/0961-9526(94)90080-9.
- Cytec Engineered Materials (2012) *Cycom 977-2 Epoxy Resin system*. Available at: https://www.cytec.com/sites/default/files/datasheets/CYCOM_977-2_031912.pdf.
- Dai, G. and Mishnaevsky, L. (2014a) ‘Fatigue of multiscale composites with secondary nanoplatelet reinforcement: 3D computational analysis’, *Composites Science and Technology*, 91, pp. 71–81. doi: 10.1016/j.compscitech.2013.11.024.
- Dai, G. and Mishnaevsky, L. (2014b) ‘Graphene reinforced nanocomposites: 3D simulation of damage and fracture’, *Computational Materials Science*, 95, pp. 684–692. doi: 10.1016/j.commatsci.2014.08.011.
- Dasari, B. L. *et al.* (2017) ‘Graphene and derivatives – Synthesis techniques, properties and their energy applications’, *Energy*, 140, pp. 766–778. doi: 10.1016/j.energy.2017.08.048.
- Davis, D. C. *et al.* (2011) ‘A strategy for improving mechanical properties of a fiber reinforced epoxy composite using functionalized carbon nanotubes’, *Composites Science and Technology*, 71(8), pp. 1089–1097. doi: 10.1016/j.compscitech.2011.03.014.
- Deka, B. K. *et al.* (2016) ‘Interfacial resistive heating and mechanical properties of graphene oxide assisted CuO nanoparticles in woven carbon fiber / polyester composite’, *Composites Part A*, 80, pp. 159–170. doi: 10.1016/j.compositesa.2015.10.023.
- Deng, C. *et al.* (2015) ‘Influence of graphene oxide coatings on carbon fiber by ultrasonically assisted electrophoretic deposition on its composite interfacial property.’, *Surface & Coatings Technology*, 272, pp. 176–181. doi: 10.1016/j.surfcoat.2015.04.008.
- Derakane (2008) *DERAKANE 411-45 Epoxy Vinyl Ester Resin*. Available at: [http://romarvoss.nl/archief/Composites/speciaal/pdf/TDS DERAKANE 411-45 English.pdf](http://romarvoss.nl/archief/Composites/speciaal/pdf/TDS%20DERAKANE%20411-45%20English.pdf).
- Dhand, V. *et al.* (2013) ‘A Comprehensive Review of Graphene Nanocomposites : Research Status and Trends’, *Journal of Nanomaterials*, 2013. doi:10.1155/2013/763953.
- Diba, M. *et al.* (2016) ‘Electrophoretic deposition of graphene-related materials: A review of the fundamentals’, *Progress in Materials Science*, 82, pp. 83–117. doi: 10.1016/j.pmatsci.2016.03.002.
- Ding, A. *et al.* (2016) ‘Prediction of Process-Induced Distortions in L-Shaped Composite Profiles Using Path-Dependent Constitutive Law’, *Applied Composite Materials*, 23(5), pp. 1027–1045. doi: 10.1007/s10443-016-

9501-8.

Dupont (2017) *Technical guide for Kevlar Aramid Fiber*. Available at:
http://www.dupont.com/content/dam/dupont/products-and-services/fabrics-fibers-and-nonwovens/fibers/documents/Kevlar_Technical_Guide.pdf.

Fan, Z., Santare, M. H. and Advani, S. G. (2008) 'Interlaminar shear strength of glass fiber reinforced epoxy composites enhanced with multi-walled carbon nanotubes', *Composites Part A*, 39, pp. 540–554. doi: 10.1016/j.compositesa.2007.11.013.

Frank, I. W. *et al.* (2007) 'Mechanical properties of suspended graphene sheets', *Journal of Vacuum Science & Technology B: Microelectronics and Nanometer Structures*, 25(6), p. 2558. doi: 10.1116/1.2789446.

Gavin, H. P. (2016) 'The Levenberg-Marquardt method for nonlinear least squares curve-fitting problems', pp. 1–17.

Geers, M. G. D., De Borst, R. and Peijs, T. (1999) 'Mixed numerical-experimental identification of non-local characteristics of random-fibre-reinforced composites', *Composites Science and Technology*, 59(10), pp. 1569–1578. doi: 10.1016/S0266-3538(99)00017-2.

Geim, A. K. (2009) 'Graphene: status and prospects.', *Science*, 324.5934, pp. 1530–1534. doi: 10.1126/science.1158877.

Genovese, K. (2004) 'A New Hybrid Technique for In-plane Characterization of Orthotropic Materials', *Experimental Mechanics*, 44(6), pp. 584–592. doi: 10.1177/0014485104048907.

Ghayoor, H., Hoa, S. V. and Marsden, C. C. (2018) 'A micromechanical study of stress concentrations in composites', *Composites Part B: Engineering*, 132, pp. 115–124. doi: 10.1016/j.compositesb.2017.09.009.

Giannopoulos, G. I. and Kallivokas, I. G. (2014) 'Mechanical properties of graphene based nanocomposites incorporating a hybrid interphase', *Finite Elements in Analysis and Design*, 90, pp. 31–40. doi: 10.1016/j.finel.2014.06.008.

Gu, Y. *et al.* (2010) 'Characterization of the interphase in carbon fiber/polymer composites using a nanoscale dynamic mechanical imaging technique', *Carbon*, 48(11), pp. 3229–3235. doi: 10.1016/j.carbon.2010.05.008.

Hadden, C. M. *et al.* (2015) 'Mechanical properties of graphene nanoplatelet/carbon fiber/epoxy hybrid composites: Multiscale modeling and experiments', *Carbon*. Elsevier Ltd, 95, pp. 100–112. doi: 10.1016/j.carbon.2015.08.026.

Hardiman, M., Vaughan, T. J. and McCarthy, C. T. (2017) 'A review of key developments and pertinent issues in nanoindentation testing of fibre reinforced plastic microstructures', *Composite Structures*, 180, pp. 782–798. doi: 10.1016/j.compstruct.2017.08.004.

Hashemi, S., Kinloch, A. J. and Williams, J. G. (1989) 'Corrections needed in double-cantilever beam tests for assessing the interlaminar failure of fibre-composites', *Journal of Materials Science Letters*, 8(2), pp. 125–129. doi: 10.1007/BF00730701.

- Hetron (2015) *Hetron 92 Polyester REsin*. Available at: <http://www.sherfab.com/assets/images/HETRON 92 TDS.pdf>.
- Hexcel (2016) *HexTow® AS4A*. Available at: http://www.hexcel.com/user_area/content_media/raw/AS4A_HexTow_DataSheet.pdf.
- Hummers, W. S. and Offeman, R. E. (1958) 'Preparation of Graphitic Oxide', *Journal of the American Chemical Society*, 80(6), p. 1339. doi: 10.1021/ja01539a017.
- Hung, P. yan *et al.* (2018) 'Surface modification of carbon fibre using graphene-related materials for multifunctional composites', *Composites Part B: Engineering*, 133, pp. 240–257. doi: 10.1016/j.compositesb.2017.09.010.
- Iijima, S. (1991) 'Helical microtubules of graphitic carbon', *Nature*, pp. 56–58. doi: 10.1038/354056a0.
- Isaac, M. D. and Ori, I. (2006) *Engineering mechanics of composite materials*. 2nd editio. New York: Oxford University Press.
- Ji, X.-Y., Cao, Y.-P. and Feng, X.-Q. (2010) 'Micromechanics prediction of the effective elastic moduli of graphene sheet-reinforced polymer nanocomposites', *Modelling and Simulation in Materials Science and Engineering*, 18(4), p. 045005. doi: 10.1088/0965-0393/18/4/045005.
- Jiang, S. *et al.* (2016) 'Composites : Part A Multiscale graphene oxide – carbon fiber reinforcements for advanced polyurethane composites', *Composites Part A*, 87, pp. 1–9. doi: 10.1016/j.compositesa.2016.04.004.
- Jin, S. Y., Young, R. J. and Eichhorn, S. J. (2014) 'Hybrid carbon fibre-carbon nanotube composite interfaces', *Composites Science and Technology*, 95, pp. 114–120. doi: 10.1016/j.compscitech.2014.02.015.
- Johnson, D. W., Dobson, B. P. and Coleman, K. S. (2015) 'A manufacturing perspective on graphene dispersions', *Current Opinion in Colloid and Interface Science*, 20(5–6), pp. 367–382. doi: 10.1016/j.cocis.2015.11.004.
- Johnston, J. P. *et al.* (2017) 'Modeling the molecular structure of the carbon fiber/polymer interphase for multiscale analysis of composites', *Composites Part B: Engineering*, 111, pp. 27–36. doi: 10.1016/j.compositesb.2016.12.008.
- Junhong, C., Zheng, B. and Lu, G. (2015) *Vertically-Oriented Graphene: PECVD Synthesis and Applications*. Springer International Publishing. doi: 10.1007/978-3-319-15302-5.
- Kam, T. Y., Chen, C. M. and Yang, S. H. (2009) 'Material characterization of laminated composite materials using a three-point-bending technique', *Composite Structures*, 88(4), pp. 624–628. doi: 10.1016/j.compstruct.2008.06.015.
- Kamar, N. T. *et al.* (2015) 'Interlaminar reinforcement of glass fiber/epoxy composites with graphene nanoplatelets', *Composites Part A: Applied Science and Manufacturing*, 70, pp. 82–92. doi: 10.1016/j.compositesa.2014.12.010.
- Kandare, E. *et al.* (2015) 'Improving the through-thickness thermal and electrical conductivity of carbon fibre /

epoxy laminates by exploiting synergy between graphene and silver nano-inclusions', *Composites Part A*, 69, pp. 72–82. doi: 10.1016/j.compositesa.2014.10.024.

Karger-Kocsis, J. *et al.* (2017) 'Interphase Engineering with Nanofillers in Fiber-Reinforced Polymer Composites', in Anil N. Netravali K.L. Mittal (ed.) *Interface/Interphase in Polymer Nanocomposites*. Beverly: Wiley & Sons, Scrivener Publishing LLC, pp. 71–102. doi: 10.1002/9781119185093.

Karger-Kocsis, J., Mahmood, H. and Pegoretti, A. (2015) 'Recent advances in fiber/matrix interphase engineering for polymer composites', *Progress in Materials Science*, 73(July), pp. 1–43. doi: 10.1016/j.pmatsci.2015.02.003.

Kari, S. *et al.* (2008) 'Evaluation of influence of interphase material parameters on effective material properties of three phase composites', *Composites Science and Technology*, 68(3–4), pp. 684–691. doi: 10.1016/j.compscitech.2007.09.009.

Kaw, A. K. (2006) *Mechanics of composite materials*. Second Edi. Boca Raton: Taylor & Francis.

Kim, J.-K. and Mai, Y.-W. (1998) *Engineered interfaces in fiber reinforced composites*. First, *Materials Today*. First. Oxford: Elsevier Science LTD. doi: 10.1016/S1369-7021(99)80035-2.

Kim, J., Sham, M. and Wu, J. (2001) 'Nano-scale characterisation of interphase in silane treated glass fibre composite', *Composites Part A*, 32, pp. 607–618. doi: 10.1016/S1359-835X(00)00163-9.

Knoll, J. B. *et al.* (2014) 'The effect of carbon nanoparticles on the fatigue performance of carbon fibre reinforced epoxy', *Composites Part A*, 67, pp. 233–240. doi: 10.1016/j.compositesa.2014.08.022.

Kollar, L. and Springer, G. (2003) *Mechanics of Composites Structures*. Cambridge: Cambridge University Press.

Kostagiannakopoulou, C. *et al.* (2015) 'On the interlaminar fracture toughness of carbon fiber composites enhanced with graphene nano-species', *Composites Science and Technology*, 118, pp. 217–225. doi: 10.1016/j.compscitech.2015.08.017.

Kuila, T. *et al.* (2012) 'Chemical functionalization of graphene and its applications', *Progress in Materials Science*, 57(7), pp. 1061–1105. doi: 10.1016/j.pmatsci.2012.03.002.

Kulkarni, M. *et al.* (2010) 'Elastic response of a carbon nanotube fiber reinforced polymeric composite: A numerical and experimental study', *Composites Part B: Engineering*, 41(5), pp. 414–421. doi: 10.1016/j.compositesb.2009.09.003.

Kumar, P., Chandra, R. and Singh, S. P. (2010) 'Effective elastic constants of fiber-reinforced polymer-matrix composites with the concept of interphase', *Composite Interfaces*, 17(1), pp. 15–35. doi: 10.1163/092764409X12580201111502.

Kundalwal, S. I. and Ray, M. C. (2011) 'Micromechanical analysis of fuzzy fiber reinforced composites', *International Journal of Mechanics and Materials in Design*, 7(2), pp. 149–166. doi: 10.1007/s10999-011-9156-4.

- Kundalwal, S. I. and Ray, M. C. (2012) 'Effective properties of a novel continuous fuzzy-fiber reinforced composite using the method of cells and the finite element method', *European Journal of Mechanics - A/Solids*, 36, pp. 191–203. doi: 10.1016/j.euromechsol.2012.03.006.
- Lecompte, D. *et al.* (2007) 'Mixed numerical-experimental technique for orthotropic parameter identification using biaxial tensile tests on cruciform specimens', *International Journal of Solids and Structures*, 44(5), pp. 1643–1656. doi: 10.1016/j.ijsolstr.2006.06.050.
- Lee, C., Wei, X., Kysar, J. W., *et al.* (2008) 'Measurement of the elastic properties and intrinsic strength of monolayer graphene.', *Science*, 321(5887), pp. 385–388. doi: 10.1126/science.1157996.
- Li, W., Yue, Y. Z., *et al.* (2016) 'Using maleic anhydride functionalized graphene oxide for improving the interfacial properties of carbon fiber/BMI composites', *Express Polymer Letters*, 10(11), pp. 874–882. doi: 10.3144/expresspolymlett.2016.82.
- Li, Y., Guo, L., *et al.* (2016) 'A Novel Multiscale Reinforcement by In-Situ Growing Carbon Nanotubes on Graphene Oxide Grafted Carbon Fibers and Its Reinforced Carbon / Carbon Composites with Improved Tensile Properties', *Journal of Materials Science & Technology*, 32(5), pp. 419–424. doi: 10.1016/j.jmst.2015.12.022.
- Li, Z. *et al.* (2016) 'Effect of the orientation of graphene-based nanoplatelets upon the Young's modulus of nanocomposites', *Composites Science and Technology*, 123, pp. 125–133. doi: 10.1016/j.compscitech.2015.12.005.
- Li, Z. *et al.* (2016) 'Micromechanical modeling and characterization of damage evolution in glass fiber epoxy matrix composites', *Mechanics of Materials*. Elsevier Ltd, 99, pp. 37–52. doi: 10.1016/j.mechmat.2016.05.006.
- Lim, J. H. *et al.* (2016) 'Numerical prediction of fiber mechanical properties considering random microstructures using inverse analysis with quasi-analytical gradients', *Applied Mathematics and Computation*. Elsevier Inc., 273, pp. 201–216. doi: 10.1016/j.amc.2015.09.076.
- Liu, L. *et al.* (2015) 'Interfacial characterization, control and modification of carbon fiber reinforced polymer composites', *Composites Science and Technology*, 121, pp. 56–72. doi: 10.1016/j.compscitech.2015.08.002.
- Liu, W. W. *et al.* (2012) 'Exfoliation and dispersion of graphene in ethanol-water mixtures', *Frontiers of Materials Science*, 6(2), pp. 176–182. doi: 10.1007/s11706-012-0166-4.
- Liu, Y. *et al.* (2012) 'Prediction on macroscopic elastic properties of interphase-contained long-fiber-reinforced composites and multiple nonlinear regression analysis', *Journal of Reinforced Plastics and Composites*, 31(17), pp. 1143–1157. doi: 10.1177/0731684412454461.
- Lu, H. *et al.* (2014) 'Noncovalently functionalized carbon fiber by grafted self-assembled graphene oxide and the synergistic effect on polymeric shape memory nanocomposites', *Composites Part B*, 67, pp. 290–295. doi: 10.1016/j.compositesb.2014.07.022.
- Lu, J. *et al.* (2014) 'Identification of the mechanical properties of the carbon fiber and the interphase region based on computational micromechanics and Kriging metamodel', *Computational Materials Science*, 95, pp. 172–180. doi: 10.1016/j.commatsci.2014.07.034.

- Lu, J. P. (1997) 'Elastic Properties of Carbon Nanotubes and Nanoropes', *Physical Review Letters*, 79, pp. 1297–1300. doi: 10.1103/PhysRevLett.79.1297.
- Luciano, R. (1998) 'Variational methods for the homogenization of periodic heterogeneous media', *Journal Of Mechanics*, 17(4), pp. 599–617.
- Madhukar, M. and Drzal, L. T. (1991) 'Fiber-Matrix Adhesion and Its Effect on Composite Mechanical Properties: II. Longitudinal (0°) and Transverse (90°) Tensile and Flexure Behavior of Graphite/Epoxy Composites', *Journal of Composite Materials*, 25(3), pp. 310–333.
- Mahmood, H. *et al.* (2016) 'Enhancement of interfacial adhesion in glass fiber / epoxy composites by electrophoretic deposition of graphene oxide on glass fibers', *Composites Science and Technology*, 126, pp. 149–157. doi: 10.1016/j.compscitech.2016.02.016.
- Mahmood, H. *et al.* (2018) 'Mechanical properties and strain monitoring of glass-epoxy composites with graphene-coated fibers', *Composites Part A: Applied Science and Manufacturing*, 107, pp. 112–123. doi: 10.1016/j.compositesa.2017.12.023.
- Maligno, A. R., Warrior, N. A. and Long, A. C. (2010) 'Effects of interphase material properties in unidirectional fibre reinforced composites', *Composites Science and Technology*, 70(1), pp. 36–44. doi: 10.1016/j.compscitech.2009.09.003.
- Mannov, E. *et al.* (2013) 'Improvement of compressive strength after impact in fibre reinforced polymer composites by matrix modification with thermally reduced graphene oxide', *Composites Science and Technology*, 87, pp. 36–41. doi: 10.1016/j.compscitech.2013.07.019.
- Mathur, R. B., Chatterjee, S. and Singh, B. P. (2008) 'Growth of carbon nanotubes on carbon fibre substrates to produce hybrid/phenolic composites with improved mechanical properties', *Composites Science and Technology*, 68(7–8), pp. 1608–1615. doi: 10.1016/j.compscitech.2008.02.020.
- Matzenmiller, A. and Gerlach, S. (2005) 'Parameter identification of elastic interphase properties in fiber composites', *Composites Part B: Engineering*, 37(2–3), pp. 117–126. doi: 10.1016/j.compositesb.2005.08.003.
- McNally, T. and Potschke, P. (2011) 'Introduction to polymer-carbon nanotube composites', in *Polymer-Carbon Nanotube Composites- Preparation, Properties, Applications*. Cambridge: Woodhead Publishing Limited.
- Melro, A. R. *et al.* (2013) 'Micromechanical analysis of polymer composites reinforced by unidirectional fibres: Part II-Micromechanical analyses', *International Journal of Solids and Structures*, 50(11–12), pp. 1906–1915. doi: 10.1016/j.ijsolstr.2013.02.007.
- Meng, M. *et al.* (2015) '3D FEA modelling of laminated composites in bending and their failure mechanisms', *Composite Structures*, 119, pp. 693–708. doi: <https://doi.org/10.1016/j.compstruct.2014.09.048>.
- Milewski, J. V. and Rosato, D. V. (1981) *History of Reinforced Plastics*, *Journal of Macromolecular Science: Part A - Chemistry*. doi: 10.1080/00222338108056787.
- Mishnaevsky, L. and Dai, G. (2014) 'Hybrid and hierarchical nanoreinforced polymer composites:

- Computational modelling of structure-properties relationships', *Composite Structures*. Elsevier Ltd, 117(1), pp. 156–168. doi: 10.1016/j.compstruct.2014.06.027.
- Mishra, A. K. and Chakraborty, S. (2015) 'Determination of Material Parameters of FRP Plates With Rotational Flexibility at Boundaries Using Experimental Modal Testing and Model Updating', *Experimental Mechanics*, 55(5), pp. 803–815. doi: 10.1007/s11340-014-9981-0.
- Montazeri, A. and Rafii-Tabar, H. (2011) 'Multiscale modeling of graphene- and nanotube-based reinforced polymer nanocomposites', *Physics Letters, Section A: General, Atomic and Solid State Physics*, 375(45), pp. 4034–4040. doi: 10.1016/j.physleta.2011.08.073.
- Mori, T. and Tanaka, K. (1973) 'Average stress in matrix and average elastic energy of materials with misfitting inclusions.', *Acta Metallurgica*, 21, pp. 571–574.
- Naya, F. *et al.* (2017) 'Computational micromechanics of the transverse and shear behavior of unidirectional fiber reinforced polymers including environmental effects', *Composites Part A: Applied Science and Manufacturing*, 92, pp. 146–157. doi: 10.1016/j.compositesa.2016.06.018.
- Nicholl, R. J. T. *et al.* (2015) 'The effect of intrinsic crumpling on the mechanics of free-standing graphene', *Nature Communications*. Nature Publishing Group, 6, pp. 1–7. doi: 10.1038/ncomms9789.
- Niu, Y. F., Yang, Y. and Wang, X. R. (2018) 'Investigation of the interphase structures and properties of carbon fiber reinforced polymer composites exposed to hydrothermal treatments using peak force quantitative nanomechanics technique', *Polymer Composites*, 39, pp. E791–E796. doi: 10.1002/pc.24245.
- Njuguna, J., Pielichowski, K. and Fan, J. (2012) 'Applications of polymer nanocomposite', in Gao, F. (ed.) *Advance in Polymer Nanocomposites - Types and Applications*. Cambridge: Woodhead Publishing Limited, pp. 472–539.
- Novoselov, K. S. *et al.* (2004) 'Electric Field Effect in Atomically Thin Carbon Films Science', *Science*, 22, pp. 2–6.
- Nye, J. (1985) *Physical Properties of Crystals. Their representation by tensors and matrices*. Oxford: Oxford University Press.
- O'Brien, T. and Martin, R. (1993) 'Robin Testing for Mode I Interlaminar Fracture Toughness for Composite Materials', *Journal of Composites Technology and Research*, 15. doi: <https://doi.org/10.1520/CTR10379J>.
- Pal, G. and Kumar, S. (2016) 'Modeling of carbon nanotubes and carbon nanotube-polymer composites', *Progress in Aerospace Sciences*, 80, pp. 33–58. doi: 10.1016/j.paerosci.2015.12.001.
- Papageorgiou, D. G., Kinloch, I. A. and Young, R. J. (2017) 'Mechanical properties of graphene and graphene-based nanocomposites', *Progress in Materials Science*, 90, pp. 75–127. doi: 10.1016/j.pmatsci.2017.07.004.
- Paper, R. *et al.* (2013) 'Strengthening of a Fibre-Matrix Interface : A Novel Method Using Nanoparticles Regular Paper', *Nanomater. nanotechnol.*, 3, pp. 1–8. doi: 10.5772/56213.
- Pathan, M. V., Tagarielli, V. L. and Patsias, S. (2017) 'Numerical predictions of the anisotropic viscoelastic

- response of uni-directional fibre composites', *Composites Part A: Applied Science and Manufacturing*, 93, pp. 18–32. doi: 10.1016/j.compositesa.2016.10.029.
- Pawlik, M., Dean, A. and Lu, Y. (2017) 'The numerical investigation of graphene-reinforced interphase effects on the mechanical properties of carbon fibre/epoxy composites', in *Proc. International Conference on Composite Structure, (ICCS20)*, pp. 194–195.
- Pontefisso, A. and Mishnaevsky, L. (2016) 'Nanomorphology of graphene and CNT reinforced polymer and its effect on damage: Micromechanical numerical study', *Composites Part B: Engineering*, 96, pp. 338–349. doi: 10.1016/j.compositesb.2016.04.006.
- Popov, V. N. (2004) 'Carbon nanotubes: Properties and application', *Materials Science and Engineering R: Reports*, 43(3), pp. 61–102. doi: 10.1016/j.mser.2003.10.001.
- Pumera, M. (2010) 'Graphene-based nanomaterials and their electrochemistry', *Chemical Society Reviews*, 39(11), pp. 4146–4157. doi: 10.1039/c002690p.
- Qin, W. *et al.* (2015) 'Mechanical and electrical properties of carbon fiber composites with incorporation of graphene nanoplatelets at the fiber – matrix interphase', *Composites Part B*, 69, pp. 335–341. doi: 10.1016/j.compositesb.2014.10.014.
- Rafiee, R. and Ghorbanhosseini, A. (2017a) 'Stochastic multi-scale modeling of randomly grown CNTs on carbon fiber', *Mechanics of Materials*, 106, pp. 1–7. doi: 10.1016/j.mechmat.2017.01.001.
- Ray, M. C. (2010) 'A shear lag model of Piezoelectric composite reinforced with carbon nanotubes-coated Piezoelectric fibers', *International Journal of Mechanics and Materials in Design*, 6(2), pp. 147–155. doi: 10.1007/s10999-010-9118-2.
- Ren, X. *et al.* (2015) 'Computational multiscale modeling and characterization of piezoresistivity in fuzzy fiber reinforced polymer composites', *International Journal of Solids and Structures*, 54, pp. 121–134. doi: 10.1016/j.ijsolstr.2014.10.034.
- Riaño, L. *et al.* (2018) 'Effect of interphase region on the elastic behavior of unidirectional glass-fiber/epoxy composites', *Composite Structures*, 198, pp. 109–116. doi: 10.1016/j.compstruct.2018.05.039.
- Rodríguez-González, J. A. *et al.* (2017) 'Influence of the Hybrid Combination of Multiwalled Carbon Nanotubes and Graphene Oxide on Interlaminar Mechanical Properties of Carbon Fiber/Epoxy Laminates', *Applied Composite Materials*, pp. 1–17. doi: 10.1007/s10443-017-9656-y.
- Romanov, V. *et al.* (2013) 'Statistical analysis of real and simulated fibre arrangements in unidirectional composites', *Composites Science and Technology*, 87, pp. 126–134. doi: 10.1016/j.compscitech.2013.07.030.
- Rucevskis S., R. J. (2002) 'Effective elastic constants of fiber-reinforced polymer-matrix composites with the concept of the interphase.', *Construction Science*, Vol.3, pp. 148–161.
- Rupnowski, P. *et al.* (2005) 'An evaluation of the elastic properties and thermal expansion coefficients of medium and high modulus graphite fibers', *Composites Part A: Applied Science and Manufacturing*, 36(3), pp.

327–338. doi: 10.1016/j.compositesa.2004.07.003.

Sabiston, T. *et al.* (2016) ‘Micromechanics for a long fibre reinforced composite model with a functionally graded interphase’, *Composites Part B: Engineering*, 84, pp. 188–199. doi: 10.1016/j.compositesb.2015.08.070.

Sabuncuoglu, B., Gorbatiikh, L. and Lomov, S. V. (2018) ‘Analysis of stress concentrations in transversely loaded steel-fiber composites with nano-reinforced interphases.’, *International Journal of Solids and Structures*. Elsevier Ltd, 130–131, pp. 248–257. doi: 10.1016/j.ijsolstr.2017.09.031.

Sager, R. J. *et al.* (2009) ‘Effect of carbon nanotubes on the interfacial shear strength of T650 carbon fiber in an epoxy matrix’, *Composites Science and Technology*, 69(7–8), pp. 898–904. doi: 10.1016/j.compscitech.2008.12.021.

Salvetat, J. *et al.* (1999) ‘Elastic and Shear Moduli of Single-Walled Carbon Nanotube Ropes of the tube in colocal’, *Physical Review Letters*, (c), pp. 2–5. doi.org/10.1103/PhysRevLett.82.944.

Seidel, G. D. and Lagoudas, D. C. (2006) ‘Micromechanical analysis of the effective elastic properties of carbon nanotube reinforced composites’, *Mechanics of Materials*, 38(8–10), pp. 884–907. doi: 10.1016/j.mechmat.2005.06.029.

SHD composites (2017) *Graphene Enhanced Epoxy Component Prepreg*. Available at: <http://shdcomposites.com/wp-content/uploads/2017/03/MTC9800-TDS.pdf> (Accessed: 10 May 2018).

Shen, M. *et al.* (2013) ‘Mechanical Properties and Tensile Fatigue of Graphene Nanoplatelets Reinforced Polymer Nanocomposites’, *Journal of Nanomaterials*, 2013, pp. 1-9. doi.org/10.1155/2013/565401.

Shi, D.-L. *et al.* (2004) ‘The Effect of Nanotube Waviness and Agglomeration on the Elastic Property of Carbon Nanotube-Reinforced Composites’, *Journal of Engineering Materials and Technology*, 126(3), p. 250. doi: 10.1115/1.1751182.

Shokrieh, M. M. *et al.* (2014) ‘Stiffness prediction of graphene nanoplatelet/epoxy nanocomposites by a combined molecular dynamics-micromechanics method’, *Computational Materials Science*. Elsevier B.V., 92, pp. 444–450. doi: 10.1016/j.commatsci.2014.06.002.

Shokrieh, M. M. and Rafiee, R. (2010) ‘Stochastic multi-scale modeling of CNT/polymer composites’, *Computational Materials Science*, 50(2), pp. 437–446. doi: 10.1016/j.commatsci.2010.08.036.

Soden, P. D., Hinton, M. J. and Kaddour, A. S. (2004) ‘Lamina properties, lay-up configurations and loading conditions for a range of fibre reinforced composite laminates’, *Failure Criteria in Fibre-Reinforced-Polymer Composites*, 58, pp. 30–51. doi: 10.1016/B978-008044475-8/50003-2.

Spanos, K. N., Georgantinos, S. K. and Anifantis, N. K. (2015) ‘Mechanical properties of graphene nanocomposites : A multiscale finite element prediction’, *Composite Structures*, 132, pp. 536–544. doi: 10.1016/j.compstruct.2015.05.078.

Speciality Materials INC. (2018) *Boron Fiber Properties*. Available at: <http://www.specmaterials.com/boronfiberproperties.htm>.

STREM Graphene Nanoplatelet (no date). Available at: <https://www.strem.com/catalog/family/Graphene/> (Accessed: 2 January 2018).

Strong, A. (2008) *Fundamentals of Composites Manufacturing. Materials, Methods, and Application*. Dearborn: Society of Manufacturing Engineers.

Subramanian, N. *et al.* (2018) 'Interface mechanics of carbon fibers with radially-grown carbon nanotubes', *Carbon*, 134, pp. 123–133. doi: 10.1016/j.carbon.2018.03.090.

Sun, C. T. and Vaidya, R. S. (1996) 'Prediction of composite properties from a representative volume element', *Composites Science and Technology*, 56(2), pp. 171–179. doi: 10.1016/0266-3538(95)00141-7.

Szeliga, D., Gawad, J. and Pietrzyk, M. (2004) 'Parameters Identification of Material Models Based on the Inverse Analysis', *International Journal of Applied Mathematics and Computer Science*, 14(4), pp. 549–556.

Tehrani, M. *et al.* (2014) 'Hybrid composites based on carbon fiber/carbon nanofilament reinforcement', *Materials*, 7(6), pp. 4182–4195. doi: 10.3390/ma7064182.

Terrones, M. (2001) 'Science and technologe of the Twenty-First Century: Synthesis, Properties and Applications of Carbon Nanotubes', *Annual review of materials research*, 33, pp. 419-501.

Tetlow, H. *et al.* (2014) 'Growth of epitaxial graphene: Theory and experiment', *Physics Reports*, 542(3), pp. 195–295. doi: 10.1016/j.physrep.2014.03.003.

Thostenson, E. T. *et al.* (2002) 'Carbon nanotube/carbon fiber hybrid multiscale composites', *Journal of Applied Physics*, 91(9), pp. 6034–6037. doi: 10.1063/1.1466880.

Thostenson, E. T., Ren, Z. and Chou, T.-W. (2001) 'Advances in the science and technology of carbon nanotubes and their composites: a review', *Composites Science and Technology*, 61(13), pp. 1899–1912. doi: 10.1016/S0266-3538(01)00094-X.

Torray (2018) *T800 data sheet*.

Trias, D. *et al.* (2006) 'Random models versus periodic models for fibre reinforced composites', *Computational Materials Science*, 38(2), pp. 316–324. doi: 10.1016/j.commatsci.2006.03.005.

Upadhyaya, P. and Kumar, S. (2015) 'Micromechanics of stress transfer through the interphase in fiber-reinforced composites', *Mechanics of Materials*. Elsevier Ltd, 89, pp. 190–201. doi: 10.1016/j.mechmat.2015.06.012.

Victrex (2014) *Victrex PEEK 90P*.

Wacker, G., Bledzki, a K. and Chateb, A. (1998) 'Effect of interphase on the transverse Young's modulus of glass / epoxy composites.', *Composites Part A: Applied Science and Manufacturing*, 29(5–6), pp. 619–626. doi: DOI: 10.1016/S1359-835X(97)00116-4.

Wang, C. *et al.* (2016) 'Electrophoretic deposition of graphene oxide on continuous carbon fibers for reinforcement of both tensile and interfacial strength', *Composites Science and Technology*, 135, pp. 46–53. doi:

10.1016/j.compscitech.2016.07.009.

Wang, F. and Cai, X. (2018) 'Improvement of mechanical properties and thermal conductivity of carbon fiber laminated composites through depositing graphene nanoplatelets on fibers', *Journal of Materials Science*. Springer US. doi: 10.1007/s10853-018-3097-3.

Wang, J., Crouch, S. L. and Mogilevskaya, S. G. (2006) 'Numerical modeling of the elastic behavior of fiber-reinforced composites with inhomogeneous interphases', *Composites Science and Technology*, 66(1), pp. 1–18. doi: 10.1016/j.compscitech.2005.06.006.

Wang, K. *et al.* (2017) 'Vibration-based identification of interphase properties in long fiber reinforced composites', *Composite Structures*, 174, pp. 244–251. doi: 10.1016/j.compstruct.2017.04.018.

Wang, P. *et al.* (2015) 'Synergetic Effects of Mechanical Properties on Graphene Nanoplatelet and Multiwalled Carbon Nanotube Hybrids Reinforced Epoxy / Carbon Fiber Composites', *Journal of Nanomaterials*, 2015. doi:10.1155/2015/838032.

Wang, W. T. and Kam, T. Y. (2000) 'Material characterization of laminated composite plates via static testing', *Composite Structures*, 50(4), pp. 347–352. doi: 10.1016/S0263-8223(00)00112-4.

Wang, X. *et al.* (2011) 'Effects of interphase properties in unidirectional fiber reinforced composite materials', *Materials and Design*, 32(6), pp. 3486–3492. doi: 10.1016/j.matdes.2011.01.029.

Wichmann, M. H. G. *et al.* (2006) 'Glass-fibre-reinforced composites with enhanced mechanical and electrical properties - Benefits and limitations of a nanoparticle modified matrix', *Engineering Fracture Mechanics*, 73(16), pp. 2346–2359. doi: 10.1016/j.engfracmech.2006.05.015.

Wong, E., Sheehan, P. and Liebert, C. (1997) 'Nanobeam mechanics: elasticity, strength, and toughness of nanorods and nanotubes.', *Science*, 277(5334), pp. 1971–1975.

Wood, C. D. *et al.* (2012) 'Nanoscale structure and local mechanical properties of fiber-reinforced composites containing MWCNT-grafted hybrid glass fibers', *Composites Science and Technology*, 72(14), pp. 1705–1710. doi: 10.1016/j.compscitech.2012.06.008.

Wu, Q. *et al.* (2014) 'Nano-analysis on the structure and chemical composition of the interphase region in carbon fiber composite', *Composites Part A: Applied Science and Manufacturing*, 56, pp. 143–149. doi: 10.1016/j.compositesa.2013.10.003.

Wu, Q. *et al.* (2015) 'Imaging the interphase of carbon fiber composites using transmission electron microscopy: Preparations by focused ion beam, ion beam etching, and ultramicrotomy', *Chinese Journal of Aeronautics*, 28(5), pp. 1529–1538. doi: 10.1016/j.cja.2015.05.005.

Xu, Y. *et al.* (2012) 'Evaluation of the effective elastic properties of long fiber reinforced composites with interphases', *Computational Materials Science*, 61, pp. 34–41. doi: 10.1016/j.commatsci.2012.03.048.

Yang, L. *et al.* (2012) 'Microscopic failure mechanisms of fiber-reinforced polymer composites under transverse tension and compression', *Composites Science and Technology*, 72(15), pp. 1818–1825. doi:

10.1016/j.compscitech.2012.08.001.

Yang, X. *et al.* (2013) ‘Dramatic mechanical and thermal increments of thermoplastic composites by multi-scale synergetic reinforcement : Carbon fiber and graphene nanoplatelet’, *Journal of materials and design*, 44, pp. 74–80. doi: 10.1016/j.matdes.2012.07.051.

Younes, R. *et al.* (2012) ‘Comparative Review Study on Elastic Properties Modeling for Unidirectional Composite Materials’, *Composites and Their Properties*. doi: 10.5772/50362.

Yu, M.-F. *et al.* (2000) ‘Tensile Loading of Ropes of Single Wall Carbon Nanotubes and their Mechanical Properties’, *Physical Review Letters*, 84(24), pp. 5552–5555. doi: 10.1103/PhysRevLett.84.5552.

Zhang, H. *et al.* (2015) ‘Improved fracture toughness and integrated damage sensing capability by spray coated CNTs on carbon fibre prepreg’, *Composites Part A*, 70, pp. 102–110. doi: 10.1016/j.compositesa.2014.11.029.

Zhang, R. L. *et al.* (2016) ‘Directly grafting graphene oxide onto carbon fiber and the effect on the mechanical properties of carbon fiber composites’, *Materials&Design*, 93, pp. 364–369. doi: 10.1016/j.matdes.2016.01.003.

Zhang, S. *et al.* (2016) ‘Graphene oxide reinforced poly(vinyl alcohol) composite fibers via template-oriented crystallization’, *Journal of Polymer Research*, 23(10). doi: 10.1007/s10965-016-1109-z.

Zhang, X. *et al.* (2012) ‘Interfacial microstructure and properties of carbon fiber composites modified with graphene oxide.’, *ACS applied materials & interfaces*, 4(3), pp. 1543–52. doi: 10.1021/am201757v.

Zhao, Z.-G. *et al.* (2005) ‘The growth of multi-walled carbon nanotubes with different morphologies on carbon fibers’, *Carbon*, 43(3), pp. 663–665. doi: 10.1016/j.carbon.2004.10.013.

Zhou, H. W. *et al.* (2016) ‘Carbon fiber/carbon nanotube reinforced hierarchical composites: Effect of CNT distribution on shearing strength’, *Composites Part B: Engineering*, 88, pp. 201–211. doi: 10.1016/j.compositesb.2015.10.035.

APPENDIX A: Multiscale model

I. Nano-interphase properties calculation

| Graphene properties | | | | | | | | | | | | | |
|---|----------|---------------|---------|-----------|----------------------|------|------|------|------|------|----------------------|----------|----------|
| E1 (Gpa) | E3 (Gpa) | v12 | v13 | G12 (Gpa) | | | | | | | | | |
| 1020 | 102000 | 0.4 | 0.004 | 102000 | | | | | | | | | |
| Fibre properties | | | | | | | | | | | | | |
| Ef(Gpa) | vf | diameter (µm) | | | | | | | | | | | |
| 231 | 0.2 | 7.1 | | | | | | | | | | | |
| Matrix properties | | | | | | | | | | | | | |
| Em(Gpa) | vm | | | | | | | | | | | | |
| 2.5 | 0.4 | | | | | | | | | | | | |
| Hill's elastic parameters (r-graphene reinforcement, m-matrix) | | | | | | | | | | | | | |
| kr | lr | nr | mr | pr | cr(volum e fraction) | km | lm | nm | mm | pm | cm (volume fraction) | µm | κm |
| 850 | 6.8 | 102000 | 369 | 102000 | 0.2 | 4.46 | 3.57 | 5.36 | 0.89 | 0.89 | 0.8 | 0.892857 | 4.166667 |
| Aligned graphene nanoplatelet | | | | | | | | | | | | | |
| k | l | m | n | p | | | | | | | | | |
| 173.571 | 3.571 | 74.514 | 6.696 | 1.116 | | | | | | | | | |
| Effective properties - transversly isotropic | | | | | | | | | | | | | |
| E1 (Gpa) | E3(Gpa) | G13(Gpa) | v12 | v13 | | | | | | | | | |
| 207.841 | 6.623 | 1.116 | 0.395 | 0.010 | | | | | | | | | |
| Randomly orientated - overall properties isotropic | | | | | | | | | | | | | |
| Randomly orientated graphene | | | | | | | | | | | | | |
| αr | βr | δr | ηr | κ | μ | | | | | | | | |
| 0.667 | 0.467 | 1137.798 | 409.486 | 84.843 | 46.637 | | | | | | | | |
| Effective properties - isotropic | | | | | | | | | | | | | |
| E (Gpa) | v | | | | | | | | | | | | |
| 118.246 | 0.268 | | | | | | | | | | | | |

Figure A-1 Excel worksheet created to calculate nano-reinforced interphase properties using Hill's parameters

II. RVE script

/TITLE, Full Model of RVE, hexagonal array

```

rf=3.55 ! Radius fiber in microns
a2=4.1598 ! x2 length in microns
a3=7.1964 ! x3 length in microns
a1=1.0399 ! x1 length in microns
Ei=400e-3
vi=0.3
ri=3.604
/PREP7 ! Pre-processor module
MP,EX,1,17.2e-3
MP,EY,1,17.2E-3
MP,EZ,1,224E-3
MP,NUXY,1,0.5
MP,NUYZ,1,0.2
MP,NUXZ,1,0.2
MP,GXY,1,5.73E-3
MP,GYZ,1,27.6E-3
MP,GXZ,1,27.6E-3

```



```

MP,EX,2,3,45E-3
MP,PRXY,2,0,34
MP,EX,3,Ei
MP,PRXY,3,vi

ET,1,SOLID186      ! Choose SOLID186 element type

BLOCK,-A2,A2,-A3,A3,-A1,A1,
CYLIND,RF, ,-A1,A1, 0, 90,
CYLIND,RF, ,-A1,A1, 90,180,
CYLIND,RF, ,-A1,A1,180,270,
CYLIND,RF, ,-A1,A1,270,360,
CYLIND,RF, ,-A1,A1, 0, 90,
CYLIND,RF, ,-A1,A1, 90,180,
CYLIND,RF, ,-A1,A1,180,270,
CYLIND,RF, ,-A1,A1,270,360,
VGEN,1,6,,-A2,-A3,.,.,1
VGEN,1,7,.,. A2,-A3,.,.,1
VGEN,1,8,.,. A2, A3,.,.,1
VGEN,1,9,,-A2, A3,.,.,1
CYLIND,ri, ,-A1,A1, 0, 90,
CYLIND,ri, ,-A1,A1, 90,180,
CYLIND,ri, ,-A1,A1,180,270,
CYLIND,ri, ,-A1,A1,270,360,
CYLIND,ri, ,-A1,A1, 0, 90,
CYLIND,ri, ,-A1,A1, 90,180,
CYLIND,ri, ,-A1,A1,180,270,
CYLIND,ri, ,-A1,A1,270,360,
VGEN,1,14,,-A2,-A3,.,.,1
VGEN,1,15,.,. A2,-A3,.,.,1
VGEN,1,16,.,. A2, A3,.,.,1
VGEN,1,17,,-A2, A3,.,.,1
ALLSEL,ALL
VOVLAP,all      ! Overlap volumes
NUMCMP,all      ! Renumbering all volumes, volume 9 is the matrix
/DEVICE,VECTOR,1
/VIEW,1,1,2,3
/ANG,1
/PNUM,VOLU,1
/PNUM,MAT,1
/REPLOT

VSEL,S,,,1,8
VATT,1
VSEL,S,,,17
VATT,2
VSEL,S,,,9,16
VATT,3
VSEL,ALL
/REPLOT

LSEL,U,LOC,Z,A1  ! meshing control
LSEL,U,LOC,Z,-A1
LESIZE,ALL,,,8  ! number of divisions through the thickness
VSEL,S,,,1,16
ASLV,S
LSLA,S
LESIZE,ALL,,,6  ! number of divisions on the fiber
LSEL,S,LOC,Y,A3
LSEL,A,LOC,Y,-A3
LESIZE,ALL,,,4  ! number of divisions on the matrix
ALLSEL,ALL
LESIZE,ALL,,,8  ! number of divisions on the matrix

VMESH,1,8
VMESH,9,16      ! Mesh area 1 and 2      ! Associate material #2 with volume 3
VSWEEP,17      ! Mesh by sweep procedure area 3
EPLOT
FINISH          ! Exit pre-processor module

*CREATE,ceRVE
! This macro applies CE to a periodic hexaedral RVE
! The RVE must be centred at (0,0,0) and
! a node must exist at (0,0,0)

```

```

a1=arg1
a2=arg2
a3=arg3

! APPLIED STRAINS
eps11=arg4
eps22=arg5
eps33=arg6
!---Note: must enter epsij=1/2*gamma
eps12=arg9/2
eps13=arg8/2
eps23=arg7/2 ! (x-y in model)
!---Note: here recovers the other 1/2*gamma
eps21 = eps12
eps31 = eps13
eps32 = eps23
! PERIODIC BOUNDARY CONDITION EQNS 2-DIR (X-DIR)
! DIR THEORY ANSYS MODEL
! 1 Z
! 2 X
! 3 Y

!-----
! CREATE COMPONENT SET: periodic corners, edges and sides
!-----

! select side +a1 and -a1 -----
nset,s,loc,z,-a1-0.001,-a1+0.001
cm,a1n_nodes,node
nset,s,loc,z,a1-0.001,a1+0.001
cm,a1p_nodes,node

! select side +a2 and -a2 -----
nset,s,loc,x,-a2-0.001,-a2+0.001
cm,a2n_nodes,node
nset,s,loc,x,a2-0.001,a2+0.001
cm,a2p_nodes,node

! select side +a3 and -a3 -----
nset,s,loc,y,-a3-0.001,-a3+0.001
cm,a3n_nodes,node
nset,s,loc,y,a3-0.001,a3+0.001
cm,a3p_nodes,node

! select edges a1 a2 -----
cmset,s,a1n_nodes
cmset,r,a2n_nodes
cm,a1n_a2n_nodes,node
cmset,s,a1p_nodes
cmset,r,a2p_nodes
cm,a1n_a2p_nodes,node
cmset,s,a1p_nodes
cmset,r,a2n_nodes
cm,a1p_a2n_nodes,node
cmset,s,a1p_nodes
cmset,r,a2p_nodes
cm,a1p_a2p_nodes,node

! select edges a1 a3 -----
cmset,s,a1n_nodes
cmset,r,a3n_nodes
cm,a1n_a3n_nodes,node
cmset,s,a1p_nodes
cmset,r,a3p_nodes
cm,a1n_a3p_nodes,node
cmset,s,a1p_nodes
cmset,r,a3n_nodes
cm,a1p_a3n_nodes,node
cmset,s,a1p_nodes
cmset,r,a3p_nodes
cm,a1p_a3p_nodes,node

! select edges a3 a2 -----
cmset,s,a3n_nodes
cmset,r,a2n_nodes

```

```

cm,a3n_a2n_nodes,node
cm,sel,s,a3n_nodes
cm,sel,r,a2p_nodes
cm,a3n_a2p_nodes,node
cm,sel,s,a3p_nodes
cm,sel,r,a2n_nodes
cm,a3p_a2n_nodes,node
cm,sel,s,a3p_nodes
cm,sel,r,a2p_nodes
cm,a3p_a2p_nodes,node

cm,sel,s,a1n_a2n_nodes
cm,sel,a,a1n_a2p_nodes
cm,sel,a,a1p_a2n_nodes
cm,sel,a,a1p_a2p_nodes
cm,sel,a,a1n_a3n_nodes
cm,sel,a,a1n_a3p_nodes
cm,sel,a,a1p_a3n_nodes
cm,sel,a,a1p_a3p_nodes
cm,sel,a,a3n_a2n_nodes
cm,sel,a,a3n_a2p_nodes
cm,sel,a,a3p_a2n_nodes
cm,sel,a,a3p_a2p_nodes
cm,edges_nodes,node

! select corners a1 a2 a3 -----
n,sel,all
a1n_a2n_a3n_comer=node(-a2,-a3,-a1)
a1n_a2p_a3n_comer=node( a2,-a3,-a1)
a1n_a2n_a3p_comer=node(-a2, a3,-a1)
a1n_a2p_a3p_comer=node( a2, a3,-a1)
a1p_a2n_a3n_comer=node(-a2,-a3, a1)
a1p_a2p_a3n_comer=node( a2,-a3, a1)
a1p_a2n_a3p_comer=node(-a2, a3, a1)
a1p_a2p_a3p_comer=node( a2, a3, a1)
n,sel,s,node,,a1n_a2n_a3n_comer
n,sel,a,node,,a1n_a2n_a3p_comer
n,sel,a,node,,a1n_a2p_a3n_comer
n,sel,a,node,,a1n_a2p_a3p_comer
n,sel,a,node,,a1p_a2n_a3n_comer
n,sel,a,node,,a1p_a2n_a3p_comer
n,sel,a,node,,a1p_a2p_a3n_comer
n,sel,a,node,,a1p_a2p_a3p_comer
cm,corners_nodes,node
ALLSEL,ALL

NSEL,S,LOC,x,0
NSEL,R,LOC,Y,0
NSEL,R,LOC,Z,0
D,all,all
ALLSEL,ALL
CEDELE,ALL
ALLSEL,ALL
ceeq=0

! PERIODIC BOUNDARY CONDITION EQNS 2-DIR (X-DIR)
pos_node=
neg_node=
cm,sel,s,a2n_nodes
cm,sel,u,edges_nodes
*get,num_nodes,node,0,count,max
*do,i,1,num_nodes,1
  cm,sel,s,a2n_nodes
  cm,sel,u,edges_nodes
!   neg_node is undefined; use lowest active node number when i=1
  *if,i,ne,1,then
    neg_node=ndnext(neg_node)
  *else
    *get,neg_node,node,0,num,min
  *endif
!   get x,y,z locations of current node in active coord system
  x_=nx(neg_node)
  y_=ny(neg_node)
  z_=nz(neg_node)
  cm,sel,s,a2p_nodes

```

```

! get closest node from component neg_a2
pos_node=node(-x_,y_,z_)
ceeq=ceeq+1
ce,ceeq,(eps22*(a2*2)),neg_node,ux,-1,pos_node,ux,1 ! x->2
ceeq=ceeq+1
ce,ceeq,(eps32*(a2*2)),neg_node,uy,-1,pos_node,uy,1 ! y->3
ceeq=ceeq+1
ce,ceeq,(eps12*(a2*2)),neg_node,uz,-1,pos_node,uz,1 ! z->1
*enddo

! PERIODIC BOUNDARY CONDITION EQNS 3-DIR (Y-DIR)
pos_node=
neg_node=
cmsel,s,a3n_nodes
cmsel,u,edges_nodes
*get,num_nodes,node,0,count,max
*do,i,1,num_nodes,1
  cmsel,s,a3n_nodes
  cmsel,u,edges_nodes
! neg_node is undefined; use lowest active node number when i=1
  *if,i,ne,1,then
    neg_node=ndnext(neg_node)
  *else
    *get,neg_node,node,0,num,min
  *endif
! get x,y,z locations of current node in active coord system
x_=nx(neg_node)
y_=ny(neg_node)
z_=nz(neg_node)
cmsel,s,a3p_nodes
! get closest node from component neg_a2
pos_node=node(x_,-y_,z_)
ceeq=ceeq+1
ce,ceeq,(eps23*(a3*2)),neg_node,ux,-1,pos_node,ux,1 ! x->2
ceeq=ceeq+1
ce,ceeq,(eps33*(a3*2)),neg_node,uy,-1,pos_node,uy,1 ! y->3
ceeq=ceeq+1
ce,ceeq,(eps13*(a3*2)),neg_node,uz,-1,pos_node,uz,1 ! z->1
*enddo

! PERIODIC BOUNDARY CONDITION EQNS 1-DIR (Z-DIR)
pos_node=
neg_node=
cmsel,s,a1n_nodes
cmsel,u,edges_nodes
*get,num_nodes,node,0,count,max
*do,i,1,num_nodes,1
  cmsel,s,a1n_nodes
  cmsel,u,edges_nodes
! neg_node is undefined; use lowest active node number when i=1
  *if,i,ne,1,then
    neg_node=ndnext(neg_node)
  *else
    *get,neg_node,node,0,num,min
  *endif
! get x,y,z locations of current node in active coord system
x_=nx(neg_node)
y_=ny(neg_node)
z_=nz(neg_node)
cmsel,s,a1p_nodes
! get closest node from component neg_a2
pos_node=node(x_,y_,-z_)
ceeq=ceeq+1
ce,ceeq,(eps21*(a1*2)),neg_node,ux,-1,pos_node,ux,1 ! x->2
ceeq=ceeq+1
ce,ceeq,(eps31*(a1*2)),neg_node,uy,-1,pos_node,uy,1 ! y->3
ceeq=ceeq+1
ce,ceeq,(eps11*(a1*2)),neg_node,uz,-1,pos_node,uz,1 ! z->1
*enddo

! PERIODIC BOUNDARY CONDITION EQNS 23-DIR (XY-DIR)
pos_node=
neg_node=
cmsel,s,a3n_a2n_nodes
cmsel,u,corners_nodes

```

```

*get,num_nodes,node,0,count,max
*do,i,1,num_nodes,1
  cmsel,s,a3n_a2n_nodes
  cmsel,u,comers_nodes
!   neg_node is undefined; use lowest active node number when i=1
  *if,i,ne,1,then
    neg_node=ndnext(neg_node)
  *else
    *get,neg_node,node,0,num,min
  *endif
!   get x,y,z locations of current node in active coord system
  x_=nx(neg_node)
  y_=ny(neg_node)
  z_=nz(neg_node)
  cmsel,s,a3p_a2p_nodes
!   get closest node from component neg_a2
  pos_node=node(-x_,y_,z_)
  ceeq=ceeq+1
  ce,ceeq,(eps22*(a2*2))+(eps23*(a3*2)),neg_node,ux,-1,pos_node,ux,1   ! x->2
  ceeq=ceeq+1
  ce,ceeq,(eps32*(a2*2))+(eps33*(a3*2)),neg_node,uy,-1,pos_node,uy,1   ! y->3
  ceeq=ceeq+1
  ce,ceeq,(eps12*(a2*2))+(eps13*(a3*2)),neg_node,uz,-1,pos_node,uz,1   ! z->1
*enddo
!
pos_node=
neg_node=
cmsel,s,a3n_a2p_nodes
cmsel,u,comers_nodes
*get,num_nodes,node,0,count,max
*do,i,1,num_nodes,1
  cmsel,s,a3n_a2p_nodes
  cmsel,u,comers_nodes
!   neg_node is undefined; use lowest active node number when i=1
  *if,i,ne,1,then
    neg_node=ndnext(neg_node)
  *else
    *get,neg_node,node,0,num,min
  *endif
!   get x,y,z locations of current node in active coord system
  x_=nx(neg_node)
  y_=ny(neg_node)
  z_=nz(neg_node)
  cmsel,s,a3p_a2n_nodes
!   get closest node from component neg_a2
  pos_node=node(-x_,y_,z_)
  ceeq=ceeq+1
  ce,ceeq,(-eps22*(a2*2))+(eps23*(a3*2)),neg_node,ux,-1,pos_node,ux,1   ! x->2
  ceeq=ceeq+1
  ce,ceeq,(-eps32*(a2*2))+(eps33*(a3*2)),neg_node,uy,-1,pos_node,uy,1   ! y->3
  ceeq=ceeq+1
  ce,ceeq,(-eps12*(a2*2))+(eps13*(a3*2)),neg_node,uz,-1,pos_node,uz,1   ! z->1
*enddo

! PERIODIC BOUNDARY CONDITION EQNS 31-DIR (YZ-DIR)
pos_node=
neg_node=
cmsel,s,a1n_a3n_nodes
cmsel,u,comers_nodes
*get,num_nodes,node,0,count,max
*do,i,1,num_nodes,1
  cmsel,s,a1n_a3n_nodes
  cmsel,u,comers_nodes
!   neg_node is undefined; use lowest active node number when i=1
  *if,i,ne,1,then
    neg_node=ndnext(neg_node)
  *else
    *get,neg_node,node,0,num,min
  *endif
!   get x,y,z locations of current node in active coord system
  x_=nx(neg_node)
  y_=ny(neg_node)
  z_=nz(neg_node)
  cmsel,s,a1p_a3p_nodes
!   get closest node from component neg_a2

```

```

pos_node=node(x_,-y_-,-z_)
ceeq=ceeq+1
ce,ceeq,(eps21*(a1*2))+(eps23*(a3*2)),neg_node,ux,-1,pos_node,ux,1 ! x->2
ceeq=ceeq+1
ce,ceeq,(eps31*(a1*2))+(eps33*(a3*2)),neg_node,uy,-1,pos_node,uy,1 ! y->3
ceeq=ceeq+1
ce,ceeq,(eps11*(a1*2))+(eps13*(a3*2)),neg_node,uz,-1,pos_node,uz,1 ! z->1
*enddo
!
pos_node=
neg_node=
cmse1,s,a1n_a3p_nodes
cmse1,u,corners_nodes
*get,num_nodes,node,0,count,max
*do,i,1,num_nodes,1
  cmse1,s,a1n_a3p_nodes
  cmse1,u,corners_nodes
! neg_node is undefined; use lowest active node number when i=1
  *if,i,ne,1,then
    neg_node=ndnext(neg_node)
  *else
    *get,neg_node,node,0,num,min
  *endif
! get x,y,z locations of current node in active coord system
x_=nx(neg_node)
y_=ny(neg_node)
z_=nz(neg_node)
cmse1,s,a1p_a3n_nodes
! get closest node from component neg_a2
pos_node=node(x_,-y_-,-z_)
ceeq=ceeq+1
ce,ceeq,(eps21*(a1*2))-(eps23*(a3*2)),neg_node,ux,-1,pos_node,ux,1 ! x->2
ceeq=ceeq+1
ce,ceeq,(eps31*(a1*2))-(eps33*(a3*2)),neg_node,uy,-1,pos_node,uy,1 ! y->3
ceeq=ceeq+1
ce,ceeq,(eps11*(a1*2))-(eps13*(a3*2)),neg_node,uz,-1,pos_node,uz,1 ! z->1
*enddo

! PERIODIC BOUNDARY CONDITION EQNS 12-DIR (YZ-DIR)
pos_node=
neg_node=
cmse1,s,a1n_a2n_nodes
cmse1,u,corners_nodes
*get,num_nodes,node,0,count,max
*do,i,1,num_nodes,1
  cmse1,s,a1n_a2n_nodes
  cmse1,u,corners_nodes
! neg_node is undefined; use lowest active node number when i=1
  *if,i,ne,1,then
    neg_node=ndnext(neg_node)
  *else
    *get,neg_node,node,0,num,min
  *endif
! get x,y,z locations of current node in active coord system
x_=nx(neg_node)
y_=ny(neg_node)
z_=nz(neg_node)
cmse1,s,a1p_a2p_nodes
! get closest node from component neg_a2
pos_node=node(-x_,-y_-,-z_)
ceeq=ceeq+1
ce,ceeq,(eps21*(a1*2))+(eps22*(a2*2)),neg_node,ux,-1,pos_node,ux,1 ! x->2
ceeq=ceeq+1
ce,ceeq,(eps31*(a1*2))+(eps32*(a2*2)),neg_node,uy,-1,pos_node,uy,1 ! y->3
ceeq=ceeq+1
ce,ceeq,(eps11*(a1*2))+(eps12*(a2*2)),neg_node,uz,-1,pos_node,uz,1 ! z->1
*enddo
!
pos_node=
neg_node=
cmse1,s,a1n_a2p_nodes
cmse1,u,corners_nodes
*get,num_nodes,node,0,count,max
*do,i,1,num_nodes,1
  cmse1,s,a1n_a2p_nodes

```

```

cmsgel,u,comers_nodes
! neg_node is undefined; use lowest active node number when i=1
*if,i,ne,1,then
  neg_node=ndnext(neg_node)
*else
  *get,neg_node,node,0,num,min
*endif
! get x,y,z locations of current node in active coord system
x_=nx(neg_node)
y_=ny(neg_node)
z_=nz(neg_node)
cmsgel,s,a1p_a2n_nodes
! get closest node from component neg_a2
pos_node=node(-x_,y_,-z_)
ceeq=ceeq+1
ce,ceeq,(eps21*(a1*2))-(eps22*(a2*2)),neg_node,ux,-1,pos_node,ux,1 ! x->2
ceeq=ceeq+1
ce,ceeq,(eps31*(a1*2))-(eps32*(a2*2)),neg_node,uy,-1,pos_node,uy,1 ! y->3
ceeq=ceeq+1
ce,ceeq,(eps11*(a1*2))-(eps12*(a2*2)),neg_node,uz,-1,pos_node,uz,1 ! z->1
*enddo

! PERIODIC BOUNDARY CONDITION Corners
nsgel,s,node,,a1n_a2n_a3n_corner
*get,neg_node,node,0,num,min
! get x,y,z locations of current node in active coord system
x_=nx(neg_node)
y_=ny(neg_node)
z_=nz(neg_node)
nsgel,a,node,,a1p_a2p_a3p_corner
pos_node=node(-x_,y_,-z_)
ceeq=ceeq+1
ce,ceeq,(eps21*(a1*2))+(eps22*(a2*2))+(eps23*(a3*2)),neg_node,ux,-1,pos_node,ux,1 ! x->2
ceeq=ceeq+1
ce,ceeq,(eps31*(a1*2))+(eps32*(a2*2))+(eps33*(a3*2)),neg_node,uy,-1,pos_node,uy,1 ! y->3
ceeq=ceeq+1
ce,ceeq,(eps11*(a1*2))+(eps12*(a2*2))+(eps13*(a3*2)),neg_node,uz,-1,pos_node,uz,1 ! z->1

nsgel,s,node,,a1n_a2n_a3p_corner
*get,neg_node,node,0,num,min
! get x,y,z locations of current node in active coord system
x_=nx(neg_node)
y_=ny(neg_node)
z_=nz(neg_node)
nsgel,a,node,,a1p_a2p_a3n_corner
pos_node=node(-x_,y_,-z_)
ceeq=ceeq+1
ce,ceeq,(eps21*(a1*2))+(eps22*(a2*2))-(eps23*(a3*2)),neg_node,ux,-1,pos_node,ux,1 ! x->2
ceeq=ceeq+1
ce,ceeq,(eps31*(a1*2))+(eps32*(a2*2))-(eps33*(a3*2)),neg_node,uy,-1,pos_node,uy,1 ! y->3
ceeq=ceeq+1
ce,ceeq,(eps11*(a1*2))+(eps12*(a2*2))-(eps13*(a3*2)),neg_node,uz,-1,pos_node,uz,1 ! z->1

nsgel,s,node,,a1n_a2p_a3n_corner
*get,neg_node,node,0,num,min
! get x,y,z locations of current node in active coord system
x_=nx(neg_node)
y_=ny(neg_node)
z_=nz(neg_node)
nsgel,a,node,,a1p_a2n_a3p_corner
pos_node=node(-x_,y_,-z_)
ceeq=ceeq+1
ce,ceeq,(eps21*(a1*2))-(eps22*(a2*2))+(eps23*(a3*2)),neg_node,ux,-1,pos_node,ux,1 ! x->2
ceeq=ceeq+1
ce,ceeq,(eps31*(a1*2))-(eps32*(a2*2))+(eps33*(a3*2)),neg_node,uy,-1,pos_node,uy,1 ! y->3
ceeq=ceeq+1
ce,ceeq,(eps11*(a1*2))-(eps12*(a2*2))+(eps13*(a3*2)),neg_node,uz,-1,pos_node,uz,1 ! z->1

nsgel,s,node,,a1n_a2p_a3p_corner
*get,neg_node,node,0,num,min
! get x,y,z locations of current node in active coord system
x_=nx(neg_node)
y_=ny(neg_node)
z_=nz(neg_node)
nsgel,a,node,,a1p_a2n_a3n_corner

```

```

pos_node=node(-x_,-y_,-z_)
ceeq=ceeq+1
ce,ceeq,(eps21*(a1*2))-(eps22*(a2*2))-(eps23*(a3*2)),neg_node,ux,-1,pos_node,ux,1 ! x->2
ceeq=ceeq+1
ce,ceeq,(eps31*(a1*2))-(eps32*(a2*2))-(eps33*(a3*2)),neg_node,uy,-1,pos_node,uy,1 ! y->3
ceeq=ceeq+1
ce,ceeq,(eps11*(a1*2))-(eps12*(a2*2))-(eps13*(a3*2)),neg_node,uz,-1,pos_node,uz,1 ! z->1

ALLSEL,ALL
*END

/SOLU ! Solution module
! ceRVE arguments:
! a1,a2,a3,eps1,eps2,eps3,eps4,eps5,eps6

*use,ceRVE,a1,a2,a3,1.,0,0,0,0,0
SOLVE ! Solve analysis
*use,ceRVE,a1,a2,a3,0,1.,0,0,0,0
SOLVE ! Solve analysis
*use,ceRVE,a1,a2,a3,0,0,1.,0,0,0
SOLVE ! Solve analysis
*use,ceRVE,a1,a2,a3,0,0,0,1.,0,0
SOLVE ! Solve analysis
*use,ceRVE,a1,a2,a3,0,0,0,0,1.,0
SOLVE ! Solve analysis
*use,ceRVE,a1,a2,a3,0,0,0,0,0,1.
SOLVE ! Solve analysis
FINISH ! Exit solution module

*create,srecover!,mac ! Create macro to calculate average stress
/nopr
ETABLE, ,VOLU, ! Get element volume
ETABLE, ,S,X ! Get element stress
ETABLE, ,S,Y
ETABLE, ,S,Z
ETABLE, ,S,XY
ETABLE, ,S,XZ
ETABLE, ,S,YZ
SMULT,SXV,VOLU,SX,1,1, ! Stress by element volume
SMULT,SYV,VOLU,SY,1,1,
SMULT,SZV,VOLU,SZ,1,1,
SMULT,SXYV,VOLU,SXY,1,1,
SMULT,SXZV,VOLU,SXZ,1,1,
SMULT,SYZV,VOLU,SYZ,1,1,
SSUM
*get,totvol,ssum,,item,volu ! Integer stress along total volume
*get,totsx ,ssum,,item,sxv
*get,totsy ,ssum,,item,syv
*get,totsz ,ssum,,item,svz
*get,totsxy ,ssum,,item,sxyv
*get,totsxz ,ssum,,item,sxzv
*get,totsyz ,ssum,,item,syzv

Sxx0 = totsx/totvol ! Compute average RVE stress
Syy0 = totsy/totvol
Szz0 = totsz/totvol
Sxy0 = totsxy/totvol
Sxz0 = totsxz/totvol
Syz0 = totsyz/totvol
/gopr
*end !srecover

/POST1 ! Post-processor module
/DEVICE,VECTOR,0
/PNUM,MAT,0
PLESOL,S,Z,1

SET,1 ! First column coefficients
*use,srecover
C11 = Szz0
C21 = Sxx0
C31 = Syy0

SET,2 ! Second column coefficients
*use,srecover

```



```

C12 = Szz0
C22 = Sxx0
C32 = Syy0

SET,3      ! Third column coefficients
*use,srecover
C13 = Szz0
C23 = Sxx0
C33 = Syy0

EL=C11-2*C12*C12/(C22+C23)
nuL=C12/(C22+C23)
ET=(C11*(C22+C23)-2*C12*C12)*(C22-C23)/(C11*C22-C12*C12)
nuT=(C11*C23-C12*C12)/(C11*C22-C12*C12)
GT=(C22-C23)/2 ! or GT=ET/2/(1+nuT)

SET,4      ! Fith column coefficients
*use,srecover
C44 = Sxy0

SET,5      ! Fith column coefficients
*use,srecover
C55 = Syz0

SET,6      ! Sixth column coefficients
*use,srecover
C66 = Sxz0

```

III. Classical Lamination Theory (CLT)

This section of *Appendix A* presents preliminary results and comparison between CLT and FEA analysis computed by ANSYS Mechanical. Laminate consisting of five glass/epoxy plies with stacking sequence [0, 45, 0,-45, 0] was analysed (as shown in Figure A1). The material properties were taken from literature (see Table A-1)

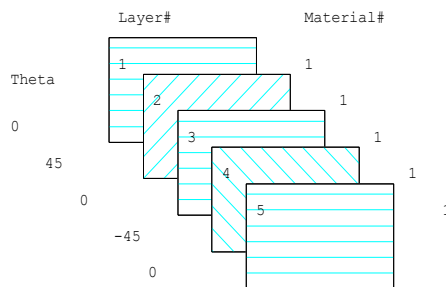


Figure A-2 Laminate stacking sequence.

| Property | Symbol | Units | Glass / epoxy |
|------------------------------|------------|-------|---------------|
| Fibre volume fraction | V_f | | 0.45 |
| Longitudinal elastic modulus | E_1 | GPa | 38.6 |
| Transverse elastic modulus | E_2 | GPa | 8.27 |
| Major Poisson's ratio | ν_{12} | | 0.26 |
| Shear modulus | G_{12} | GPa | 4.14 |

Table A-1 Engineering constants of glass/epoxy (Kaw and Group 2006 p.106).

The model was created in x-y-z coordinate system using shell 181 as an element type (Figure A3). Layered section command was applied with each lamina of thickness 0.005 m. Mesh was generated by element edge length 0.25 (m). Model was constraint by node at the centre of laminate where all degrees of freedom were set to zero. Loading of 1000 N/m were applied on each edge in both x and y direction (Figure A3).

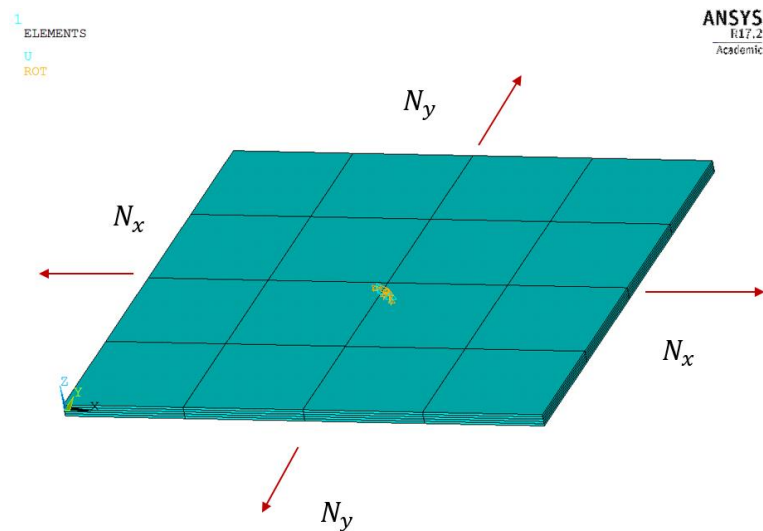


Figure A3 Ansys APDL – boundary conditions.

Comparison between CLT and ANSYS.

Table A2-A6 presents the comparison between stresses at the top and bottom surface of each ply predicted by CLT and ANSYS. Results obtained by CLT agreed very closely with Ansys results. The percentage error is less than 1% in all results and is a consequent of rounding practice. This prediction illustrate the mechanical behaviour of the specimen under biaxial

load, but can be easily adapt to simulate different loading conditions, for example: bending test, uniaxial tensile test or compression test, by changing boundary conditions in the software and resultant forces and moments in CLT.

| Stresses | By CLT | | By Ansys | | % Error | |
|------------------|-------------|----------------|-------------|----------------|---------|-------|
| | Top Surface | Bottom Surface | Top Surface | Bottom Surface | | |
| σ_x (Pa) | 42762.0 | 42741.8 | 42695.1 | 42765.1 | 0.669 | 0.005 |
| σ_y (Pa) | 29613.2 | 29596.3 | 29559.1 | 29559.1 | 0.541 | 0.372 |
| τ_{xy} (Pa) | -16651.0 | -7000.8 | -16605.1 | -6963.1 | 0.600 | 0.377 |

Table A2 Results – layer 1 (0°)

| Stresses | By CLT | | By Ansys | | % Error | |
|------------------|-------------|----------------|-------------|----------------|---------|-------|
| | Top Surface | Bottom Surface | Top Surface | Bottom Surface | | |
| σ_x (Pa) | 31626.1 | 40270.6 | 31643.9 | 40270.9 | 0.178 | 0.003 |
| σ_y (Pa) | 51355.7 | 59987.9 | 51347.8 | 59974.8 | 0.079 | 0.131 |
| τ_{xy} (Pa) | 14042.8 | 26191.6 | 14103.3 | 26211.6 | 0.605 | 0.200 |

Table A3 Results – layer 2 (45°)

| Stresses | By CLT | | By Ansys | | % Error | |
|------------------|-------------|----------------|-------------|----------------|---------|-------|
| | Top Surface | Bottom Surface | Top Surface | Bottom Surface | | |
| σ_x (Pa) | 42721.7 | 42701.6 | 42695.1 | 42695.1 | 0.266 | 0.065 |
| σ_y (Pa) | 29579.4 | 29562.5 | 29559.1 | 29559.1 | 0.203 | 0.034 |
| τ_{xy} (Pa) | -2336.5 | 2327.8 | -2335.0 | 2321.0 | 0.155 | 0.068 |

Table A4 Results – layer 3 (0°)

| Stresses | By CLT | | By Ansys | | % Error | |
|------------------|-------------|----------------|-------------|----------------|---------|-------|
| | Top Surface | Bottom Surface | Top Surface | Bottom Surface | | |
| σ_x (Pa) | 40262.9 | 31570.6 | 40270.9 | 31643.9 | 0.080 | 0.733 |
| σ_y (Pa) | 59967.7 | 51263.0 | 59974.8 | 51347.8 | 0.071 | 0.848 |
| τ_{xy} (Pa) | -26196.4 | -14011.9 | -26211.6 | -14103.3 | 0.152 | 0.914 |

Table A5 Results – layer 4 (-45°)

| Stresses | By CLT | | By Ansys | | % Error | |
|------------------|-------------|----------------|-------------|----------------|---------|-------|
| | Top Surface | Bottom Surface | Top Surface | Bottom Surface | | |
| σ_x (Pa) | 42681.4 | 42661.3 | 42695.1 | 42695.1 | 0.137 | 0.338 |
| σ_y (Pa) | 29545.6 | 29528.7 | 29559.1 | 29559.1 | 0.135 | 0.304 |
| τ_{xy} (Pa) | 6992.1 | 11656.4 | 6963.1 | 11605.1 | 0.291 | 0.513 |

Table A6 Results – layer 5 (0°)

APPENDIX B: Experimental results

I. Polishing samples

| | Surface | Abrasive | Pressure | Speed - Direction | Time |
|------------------------|---------|----------|----------|--------------------|--------------|
| Primary Grinding Stage | Paper | P320gSiC | 25 N | 150 rev/min - Comp | Until planar |

| | Surface | Abrasive | Pressure | Speed - Direction | Time |
|---------------------------|---------------|-------------------|----------|--------------------|-----------|
| Additional Grinding Stage | Piano cloth H | 9 μm (WB) Diamond | 25 N | 150 rev/min - Comp | 5 minutes |

| | Surface | Abrasive | Pressure | Speed - Direction | Time |
|-----------------|-------------|--------------------|----------|-------------------|-----------|
| Polishing Stage | Multi cloth | 0.06 μm (WB) Silco | 15 N | 80 rev/min - Comp | 2 minutes |

II. Three point bending test results - prepreg

| CNT and GNP sprayed CFRP | | | | | | | | | | | | |
|--------------------------|--------------|---------------|------------------|--------------------|-------------------------------|------------------------|-------------------------|----------------------------|---------------|---|-------------------|---|
| Number of sample | Width b (mm) | Length l (mm) | Thickness h (mm) | Span length L (mm) | Loading member radius R1 (mm) | Support radius R2 (mm) | Room temperature T (°C) | Crosshead speed V (mm/min) | Slope (ΔF/Δs) | $E_f = \frac{L^3}{4bh^3} \frac{\Delta F}{\Delta s}$ Flexural modulus | maximum force (N) | $\sigma_f = \frac{3FL}{2bh^2}$ Flexural strength |
| 1 | 14.99 | 100 | 1.97266667 | 80 | 5 (±0.2) | 5 (±0.2) | 20 | 1 | 97.602 | 108569.024 | 803.9 | 1653.76665 |
| 2 | 15.01 | 100 | 2.00166667 | 80 | 5 (±0.2) | 5 (±0.2) | 20 | 1 | 104.32 | 110922.994 | 753.85 | 1504.187513 |
| 3 | 15.01 | 100 | 2.00033333 | 80 | 5 (±0.2) | 5 (±0.2) | 20 | 1 | 102.31 | 108979.249 | 797.2 | 1592.453152 |
| 4 | 15.02 | 100 | 1.95633333 | 80 | 5 (±0.2) | 5 (±0.2) | 20 | 1 | 103.44 | 117733.481 | 793 | 1655.384144 |
| 5 | 15.02 | 100 | 1.99466667 | 80 | 5 (±0.2) | 5 (±0.2) | 20 | 1 | 112.26 | 120546.355 | 773 | 1552.208821 |
| 6 | 15.03 | 100 | 1.97966667 | 80 | 5 (±0.2) | 5 (±0.2) | 20 | 1 | 109.03 | 119679.782 | 832 | 1694.967794 |
| | | | | | | | | | Mean modulus | 114405.15 | Mean strength | 1591.60056 |
| Reference CFRP | | | | | | | | | | | | |
| Number of sample | Width b (mm) | Length l (mm) | Thickness h (mm) | Span length L (mm) | Loading member radius R1 (mm) | Support radius R2 (mm) | Room temperature T (°C) | Crosshead speed V (mm/min) | Slope (ΔF/Δs) | $E_f = \frac{L^3}{4bh^3} \frac{\Delta F}{\Delta s}$ Flexural modulus | maximum force (N) | $\sigma_f = \frac{3FL}{2bh^2}$ Flexural strength |
| 1 | 15.02 | 100 | 1.92 | 80 | 5 (±0.2) | 5 (±0.2) | 20 | 1 | 89.501 | 107785.57 | 682.63 | 1479.757734 |
| 2 | 15.02 | 100 | 2.03033333 | 80 | 5 (±0.2) | 5 (±0.2) | 20 | 1 | 104.84 | 106772.99 | 861.28 | 1669.619 |
| 3 | 15.04 | 100 | 1.972 | 80 | 5 (±0.2) | 5 (±0.2) | 20 | 1 | 96.677 | 107315.10 | 762.5 | 1564.788697 |
| 4 | 15.03 | 100 | 2.09333333 | 80 | 5 (±0.2) | 5 (±0.2) | 20 | 1 | 111.59 | 117144.07 | 628 | 1241.875134 |
| 5 | 15.02 | 100 | 2.05066667 | 80 | 5 (±0.2) | 5 (±0.2) | 20 | 1 | 118.26 | 116867.22 | 834.57 | 1585.564591 |
| 6 | 15.03 | 100 | 1.87033333 | 80 | 5 (±0.2) | 5 (±0.2) | 20 | 1 | 85.342 | 111060.71 | 682 | 1556.224705 |
| | | | | | | | | | Mean modulus | 111157.61 | Mean strength | 1516.304977 |

3 POINT BENDING






24/07/2018

BS EN ISO 14125:1998

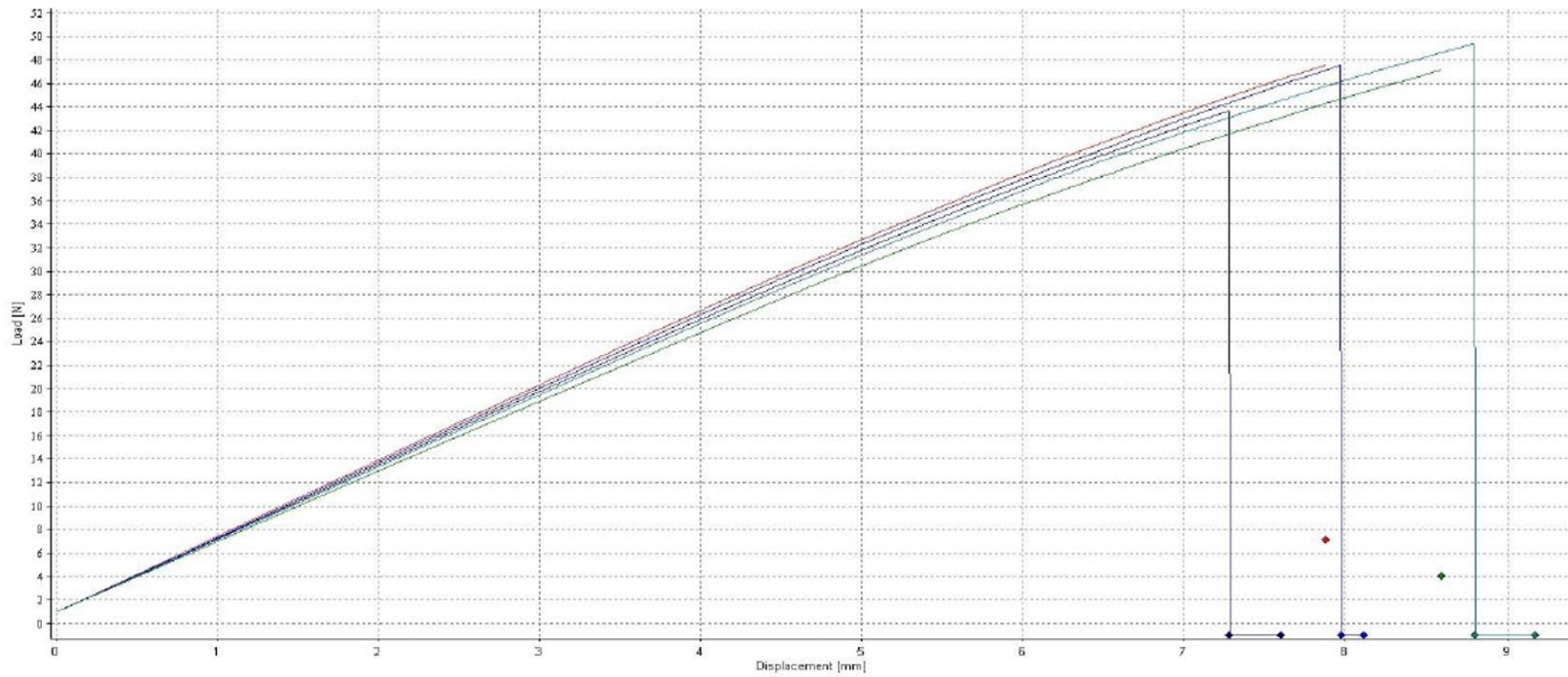
Class IV material (carbon fibres reinforced systems)

Load Cell: 2 kN
Test speed: 2 mm/min

Support radius: 2 mm
Loading radius: 5 mm

| Sample | Thickness (mm) | Width (mm) | Span (mm) | Max Load (N) | σ_f (MPa) | Ef (GPa) | Observations, failure mode |
|--|----------------|------------|-----------|--------------|------------------|----------|----------------------------|
| MTC801-UD-i-90° | | | | | | | |
| 1  MTC801-UD-i-90°_01 | 1.88 | 15.03 | 80.00 | 48 | 107.3 | | |
| 15 Plies Sprayed with GNP&s & CNTs | | | | | | | |
| 2  MTC801-UD-i-90°_02 | 1.85 | 14.99 | 80.00 | 44 | 102.1 | | |
| 3  MTC801-UD-i-90°_03 | 1.85 | 15.01 | 80.00 | 49 | 115.6 | | |
| 4  MTC801-UD-i-90°_04 | 1.86 | 15.03 | 80.00 | 48 | 109.6 | | |
| 5  MTC801-UD-i-90°_05 | 1.82 | 14.99 | 80.00 | 47 | 114.6 | | |

Average: 1.85 15.01 80.00 47 109.8 #DIV/0!
 Standard deviation: 80.00 #DIV/0!
 Coefficient of variation: 4% #DIV/0!



3 POINT BENDING






24/07/2018

BS EN ISO 14125:1998

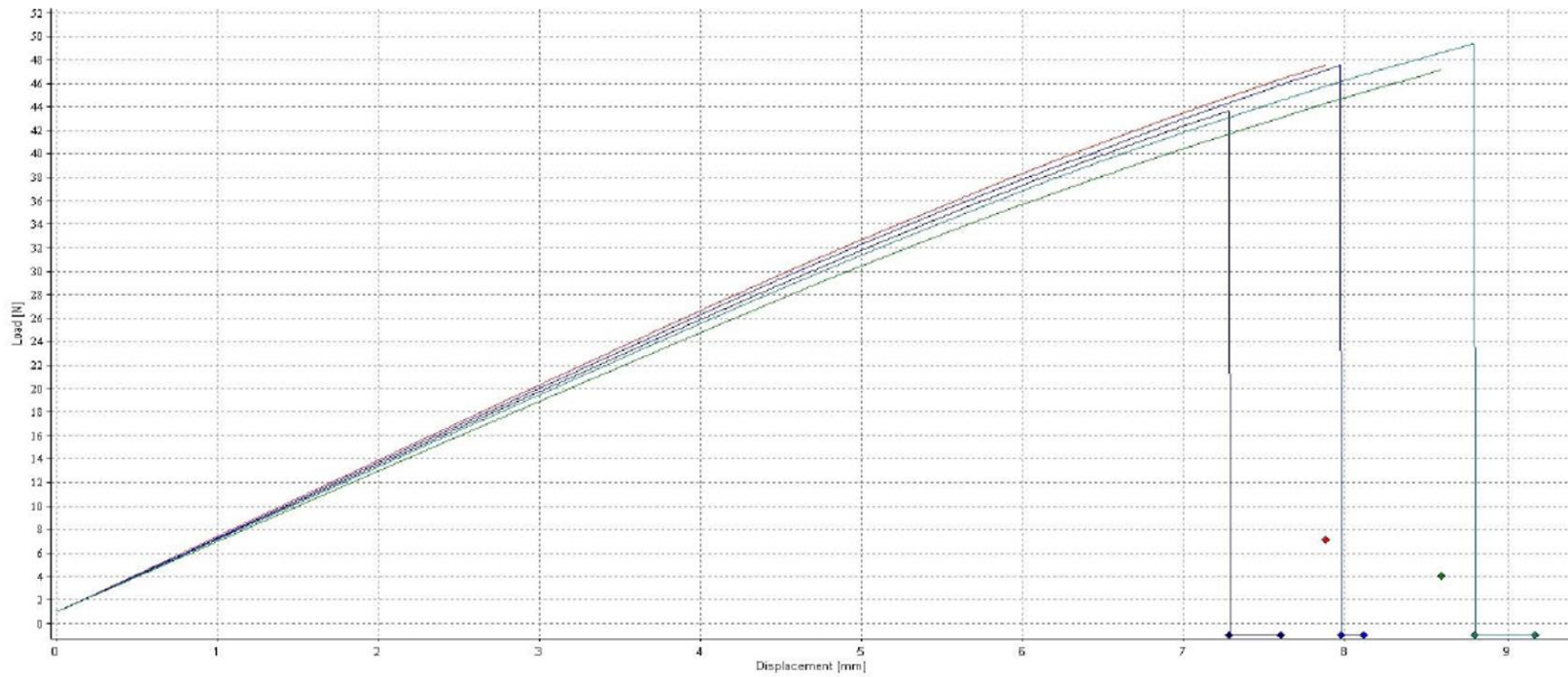
Class IV material (carbon fibres reinforced systems)

Load Cell: 2 kN
Test speed: 2 mm/min

Support radius: 2 mm
Loading radius: 5 mm

| Sample | Thickness (mm) | Width (mm) | Span (mm) | Max Load (N) | σ_f (MPa) | Ef (GPa) | Observations, failure mode |
|--|----------------|------------|-----------|--------------|------------------|----------|----------------------------|
| MTC801-UD-i-90° | | | | | | | |
| 1  MTC801-UD-i-90°_01 | 1.88 | 15.03 | 80.00 | 48 | 107.3 | | |
| 15 Plies Sprayed with GNP&s & CNTs | | | | | | | |
| 2  MTC801-UD-i-90°_02 | 1.85 | 14.99 | 80.00 | 44 | 102.1 | | |
| 3  MTC801-UD-i-90°_03 | 1.85 | 15.01 | 80.00 | 49 | 115.6 | | |
| 4  MTC801-UD-i-90°_04 | 1.86 | 15.03 | 80.00 | 48 | 109.6 | | |
| 5  MTC801-UD-i-90°_05 | 1.82 | 14.99 | 80.00 | 47 | 114.6 | | |

Average: 1.85 15.01 80.00 47 109.8 #DIV/0!
 Standard deviation: 80.00 4.9 #DIV/0!
 Coefficient of variation: 4% #DIV/0!



INTERLAMINAR SHEAR STRENGTH

24/07/2018

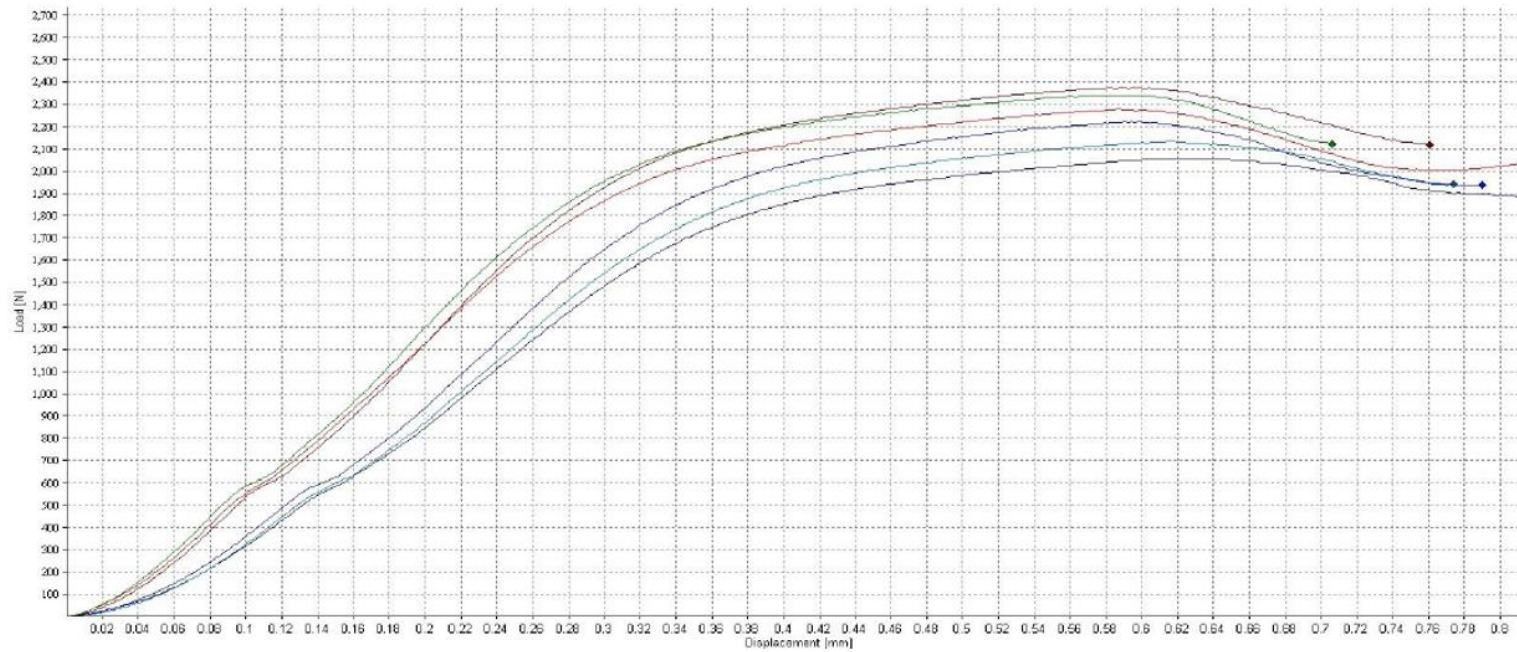
BS EN ISO 14130:1998

Load Cell: 50 kN
 Test speed: 1 mm/min
 Support radius: 2 mm
 Loading radius: 5 mm

| Sample | Thickness (mm) | Width (mm) | Span (mm) | Max Load (N) | ILSS (MPa) | Observations, failure mode |
|---------------------------------|----------------|------------|-----------|--------------|------------|--------------------------------------|
| MTC801-UD-i-0° | | | | | | |
| 1 <i>////</i> MTC801-UD-i-0°_01 | 1.90 | 10.02 | 9.58 | 2277 | 89.7 | Unacceptable Failure - Plastic Shear |
| 2 <i>////</i> MTC801-UD-i-0°_02 | 1.75 | 10.00 | 9.58 | 2057 | 88.2 | Unacceptable Failure - Plastic Shear |
| 3 <i>////</i> MTC801-UD-i-0°_03 | 1.80 | 10.01 | 9.58 | 2132 | 88.5 | Unacceptable Failure - Plastic Shear |
| 4 <i>////</i> MTC801-UD-i-0°_04 | 1.86 | 10.03 | 9.58 | 2220 | 89.3 | Unacceptable Failure - Plastic Shear |
| 5 <i>////</i> MTC801-UD-i-0°_05 | 1.94 | 10.01 | 9.58 | 2342 | 90.5 | Unacceptable Failure - Plastic Shear |
| 6 <i>////</i> MTC801-UD-i-0°_06 | 1.97 | 10.01 | 9.58 | 2374 | 90.3 | Unacceptable Failure - Plastic Shear |

15 Plies Sprayed with GNP & CNTs

Average: 1.87 10.01 9.58 2234 89.4
 Standard deviation: 0.9
 Coefficient of variation: 1%



INTERLAMINAR SHEAR STRENGTH

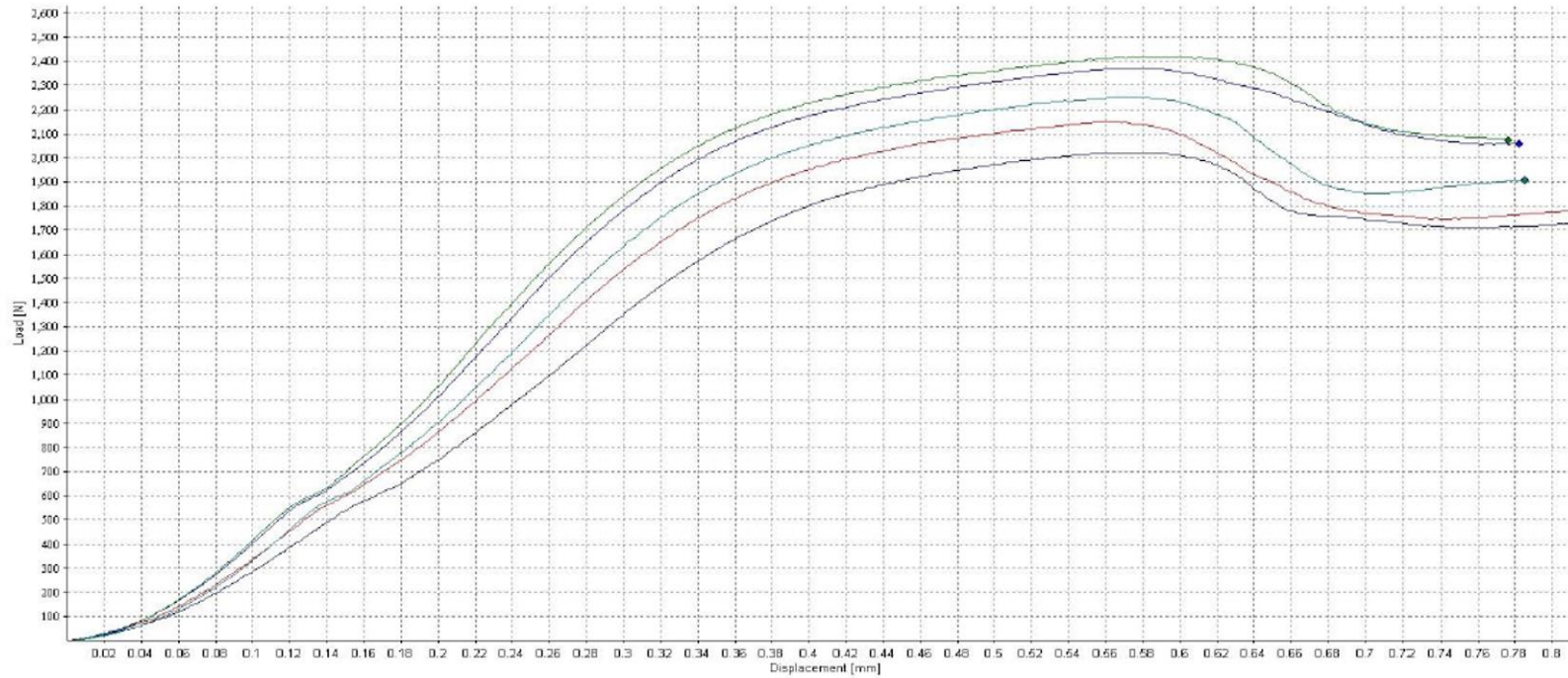
BS EN ISO 14130:1998

24/07/2018

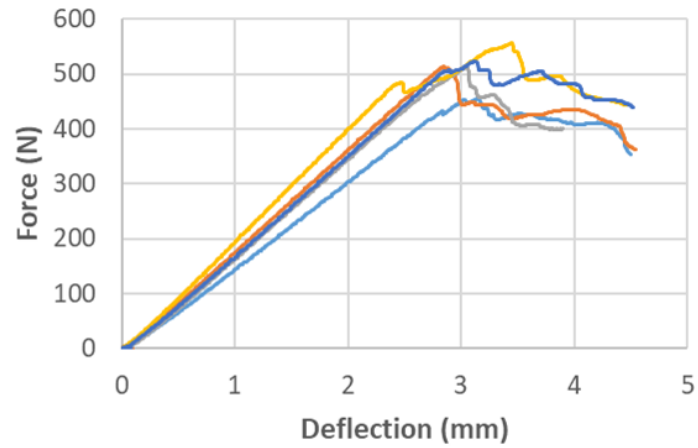
Load Cell: 50 kN Support radius: 2 mm
 Test speed: 1 mm/min Loading radius: 5 mm

| Sample | Thickness (mm) | Width (mm) | Span (mm) | Max Load (N) | ILSS (MPa) | Observations, failure mode |
|----------------------------------|----------------|------------|-----------|--------------|------------|--------------------------------------|
| MTC801-UD-ii-0° | | | | | | |
| 1 <i>////</i> MTC801-UD-ii-0°_01 | 1.82 | 10.01 | 9.58 | 2147 | 88.4 | Unacceptable Failure - Plastic Shear |
| Pure CFRP | | | | | | |
| 2 <i>////</i> MTC801-UD-ii-0°_02 | 1.72 | 10.02 | 9.58 | 2021 | 87.9 | Unacceptable Failure - Plastic Shear |
| 3 <i>////</i> MTC801-UD-ii-0°_03 | 1.89 | 10.02 | 9.58 | 2254 | 89.5 | Unacceptable Failure - Plastic Shear |
| 4 <i>////</i> MTC801-UD-ii-0°_04 | 1.98 | 10.00 | 9.58 | 2370 | 90.0 | Unacceptable Failure - Plastic Shear |
| 5 <i>////</i> MTC801-UD-ii-0°_05 | 1.99 | 10.07 | 9.58 | 2419 | 90.4 | Unacceptable Failure - Plastic Shear |

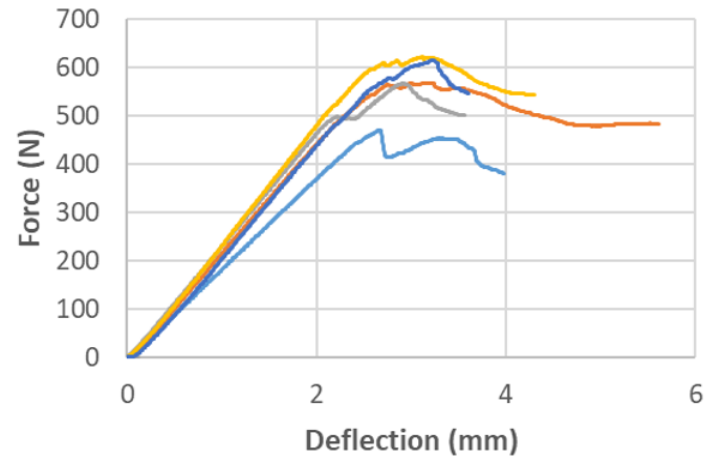
Average: 1.88 10.02 9.58 2242 89.2
 Standard deviation: 0.9
 Coefficient of variation: 1%



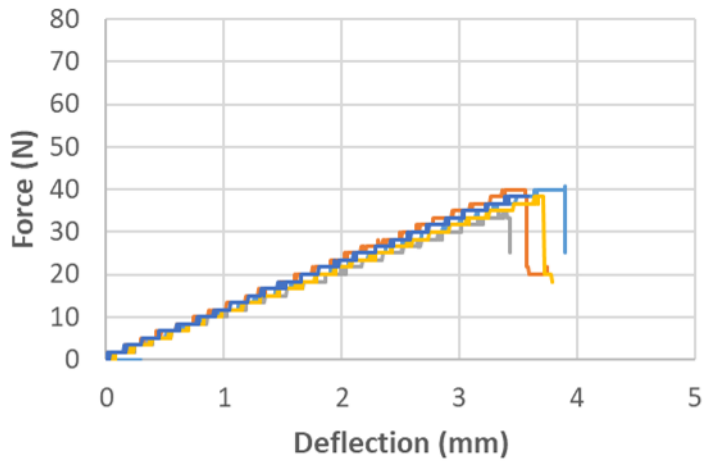
III. Three point bending test results – wet lay- up



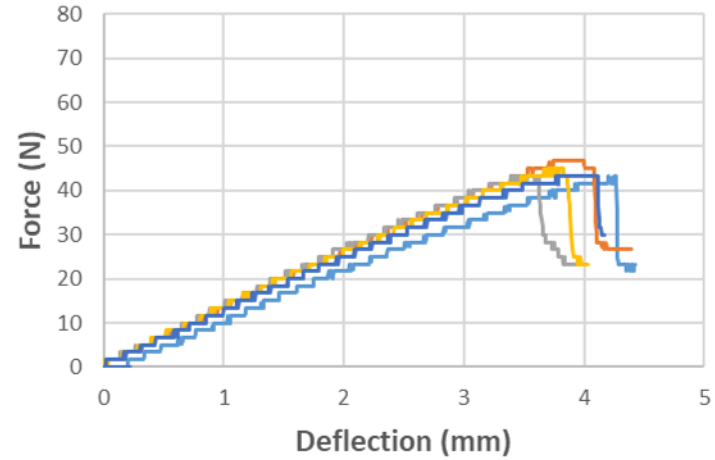
- Sample 1
- Sample 2
- Sample 3
- Sample 4
- Sample 5



- Sample 11
- Sample 12
- Sample 13
- Sample 14
- Sample 15

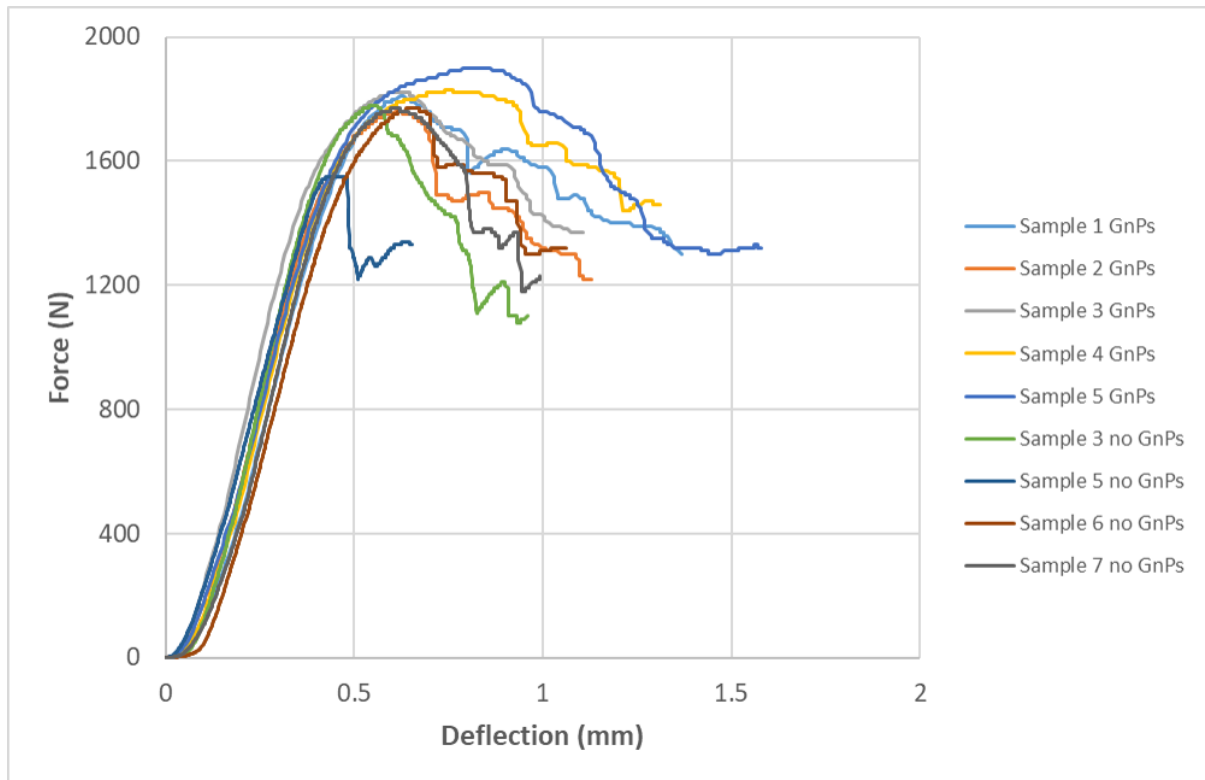


- Sample 6
- Sample 7
- Sample 8
- Sample 9
- Sample 10

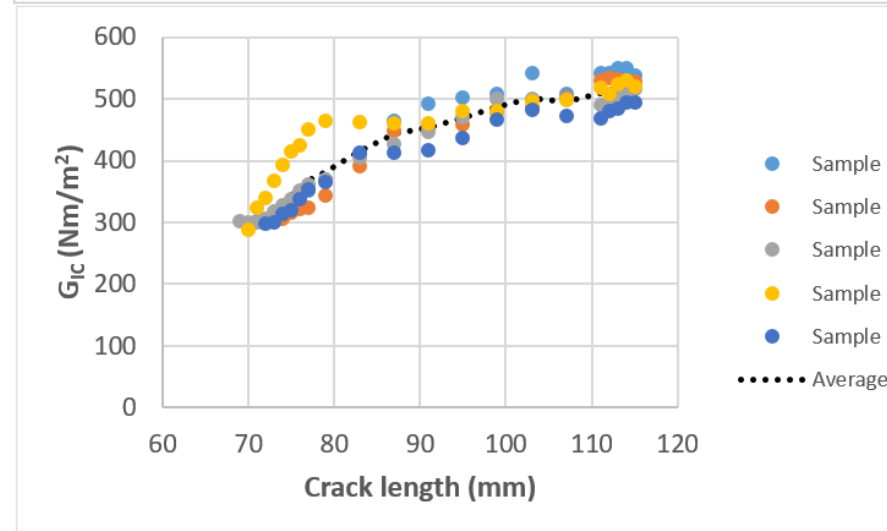
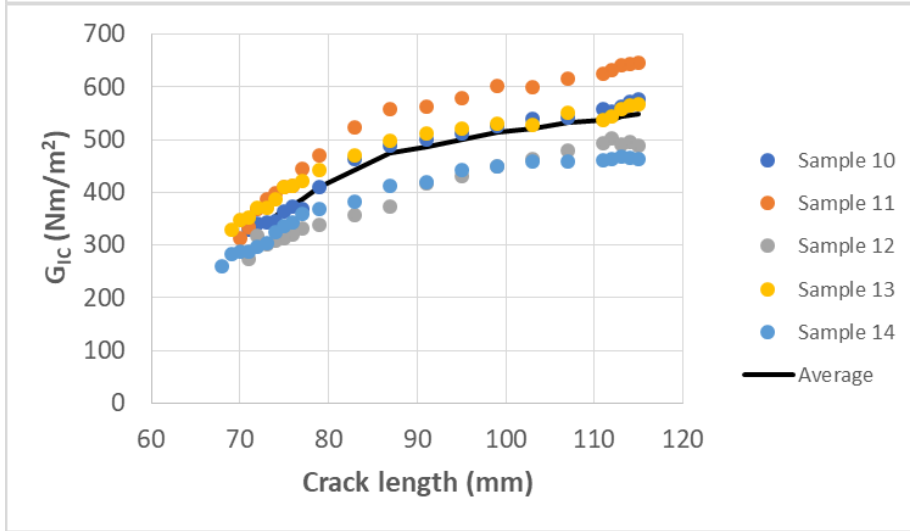
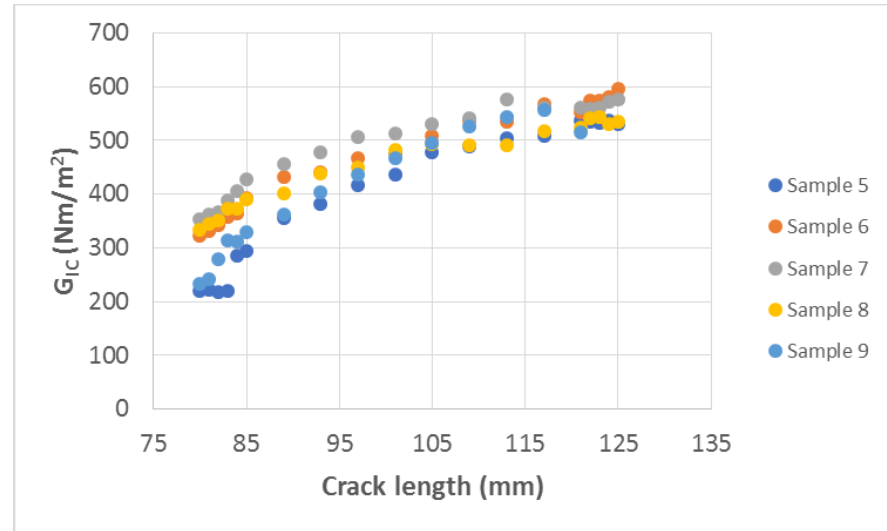
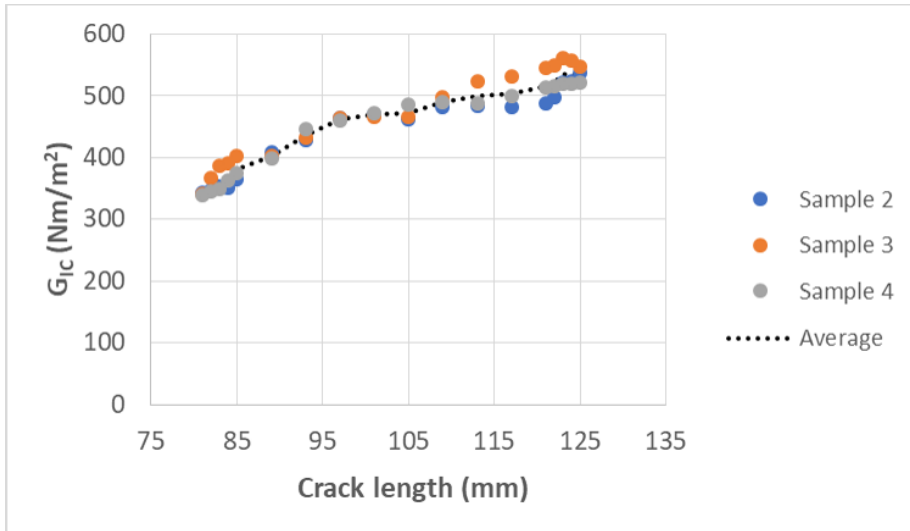


- Sample 16
- Sample 17
- Sample 18
- Sample 19
- Sample 20

IV. Short beam test results



V. Fracture toughness



APPENDIX C: Fuzzy fibre reinforced polymer

/TITLE fuzzy fibre hexagonal rve

rf=2.5
a2=4.76
a3=8.234
a1=1.19

/prep7
MP,EX,1,14.5e-3
MP,EY,1,14.5e-3
MP,EZ,1,241E-3
MP,nuXY,1,0.51
MP,nuYZ,1,0.27
MP,nuXZ,1,0.27
MP,GXY,1,4.8E-3
MP,GYZ,1,22.8e-3
MP,GXZ,1,22.8E-3
MP,EX,2,3E-3
MP,PRXY,2,0.3
MP,EX,3,7.01e-3
MP,EY,3,7.01E-3
MP,EZ,3,298.64E-3
MP,nuXY,3,0.29
MP,nuYZ,3,0.1
MP,nuXZ,3,0.1
MP,GXY,3,2.52E-3
MP,GYZ,3,2.81E-3
MP,GXZ,3,2.81E-3

ET,1,SOLID186
KEYOPT,1,3,1

BLOCK,-A2,A2,-A3,A3,-A1,A1,
CYLIND,RF,,-A1,A1,0,90,
CYLIND,RF,,-A1,A1,90,180,
CYLIND,RF,,-A1,A1,180,270,
CYLIND,RF,,-A1,A1,270,360,
CYLIND,RF,,-A1,A1,0,90,
CYLIND,RF,,-A1,A1,90,180,
CYLIND,RF,,-A1,A1,180,270,
CYLIND,RF,,-A1,A1,270,360,
VGEN,1,6,,,-A2,-A3,,1
VGEN,1,7,, A2,-A3,,1
VGEN,1,8,, A2, A3,,1
VGEN,1,9,,-A2, A3,,1
CYLIND,4.5,,-A1,A1,0,90,
CYLIND,4.5,,-A1,A1,90,180,
CYLIND,4.5,,-A1,A1,180,270,
CYLIND,4.5,,-A1,A1,270,360,
CYLIND,4.5,,-A1,A1,0,90,
CYLIND,4.5,,-A1,A1,90,180,
CYLIND,4.5,,-A1,A1,180,270,
CYLIND,4.5,,-A1,A1,270,360,
VGEN,1,14,,-A2,-A3,,1
VGEN,1,15,, A2,-A3,,1
VGEN,1,16,, A2, A3,,1
VGEN,1,17,,-A2, A3,,1
ALLSEL,ALL
VOVLAP,all ! Overlap volumes
NUMCMP,all ! Renumbering all volumes, volume 9 is the matrix
/DEVICE,VECTOR,1
/VIEW,1,1,2,3
/ANG,1
/PNUM,VOLU,1
/PNUM,MAT,1
/REPLOT

```

VSEL,S,,,1,8
VATT,1
VSEL,S,,,17
VATT,2
VSEL,S,,,9,16
VATT,3
VSEL,ALL
/REPLOT

VEORIENT,13,LINE,50
VEORIENT,12,LINE,46
VEORIENT,10,LINE,38
VEORIENT,11,LINE,42
VEORIENT,15,LINE,106
VEORIENT,16,LINE,109
VEORIENT,14,LINE,102
VEORIENT,9,LINE,33
/REPLOT

LSEL,U,LOC,Z,A1 ! meshing control
LSEL,U,LOC,Z,-A1
LESIZE,ALL,,,6 ! number of divisions through the thickness
VSEL,S,,,1,8
ASLV,S
LSLA,S
LESIZE,ALL,,,6 ! number of divisions on the fiber
LSEL,S,LINE,,32,33
LESIZE,ALL,,,12 ! number of divisions on the interphase
LSEL,S,LINE,,38,39
LESIZE,ALL,,,12
LSEL,S,LINE,,42,43
LESIZE,ALL,,,12
LSEL,S,LINE,,46,47
LESIZE,ALL,,,12
LSEL,S,LINE,,50,51
LESIZE,ALL,,,12
LSEL,S,LINE,,102,103
LESIZE,ALL,,,12
LSEL,S,LINE,,106,109
LESIZE,ALL,,,12
LSEL,S,LINE,,92,98
LESIZE,ALL,,,4
LSEL,S,LINE,,84,91
LESIZE,ALL,,,4
LSEL,S,LINE,,80,83
LESIZE,ALL,,,4
LSEL,S,LINE,,99,101
LESIZE,ALL,,,4
LSEL,S,LINE,,104,105
LESIZE,ALL,,,4
LSEL,S,LOC,Y,A3
LSEL,A,LOC,Y,-A3
LESIZE,ALL,,,8 ! number of divisions on the matrix
ALLSEL,ALL
LESIZE,ALL,,,16 ! number of divisions on the matrix

VMESH,1,8
VMESH,9,16 ! Mesh area 1 and 2 ! Associate material #2 with volume 3
VSWEEP,17 ! Mesh by sweep procedure area 3
EPLOT
FINISH ! Exit pre-processor module

*CREATE,ceRVE
! This macro applies CE to a periodic hexaedral RVE
! The RVE must be centred at (0,0,0) and
! a node must exist at (0,0,0)

a1=arg1
a2=arg2
a3=arg3

! APPLIED STRAINS
eps11=arg4
eps22=arg5
eps33=arg6

```

```

!---Note: must enter epsij=1/2*gamma
eps12=arg9/2
eps13=arg8/2
eps23=arg7/2 ! (x-y in model)
!---Note: here recovers the other 1/2*gamma
eps21 = eps12
eps31 = eps13
eps32 = eps23
! PERIODIC BOUNDARY CONDITION EQNS 2-DIR (X-DIR)
! DIR THEORY ANSYS MODEL
! 1 Z
! 2 X
! 3 Y

!-----
! CREATE COMPONENT SET: periodic corners, edges and sides
!-----

! select side +a1 and -a1 -----
nset,s,loc,z,-a1-0.001,-a1+0.001
cm,a1n_nodes,node
nset,s,loc,z,a1-0.001,a1+0.001
cm,a1p_nodes,node

! select side +a2 and -a2 -----
nset,s,loc,x,-a2-0.001,-a2+0.001
cm,a2n_nodes,node
nset,s,loc,x,a2-0.001,a2+0.001
cm,a2p_nodes,node

! select side +a3 and -a3 -----
nset,s,loc,y,-a3-0.001,-a3+0.001
cm,a3n_nodes,node
nset,s,loc,y,a3-0.001,a3+0.001
cm,a3p_nodes,node

! select edges a1 a2 -----
cmsel,s,a1n_nodes
cmsel,r,a2n_nodes
cm,a1n_a2n_nodes,node
cmsel,s,a1n_nodes
cmsel,r,a2p_nodes
cm,a1n_a2p_nodes,node
cmsel,s,a1p_nodes
cmsel,r,a2n_nodes
cm,a1p_a2n_nodes,node
cmsel,s,a1p_nodes
cmsel,r,a2p_nodes
cm,a1p_a2p_nodes,node

! select edges a1 a3 -----
cmsel,s,a1n_nodes
cmsel,r,a3n_nodes
cm,a1n_a3n_nodes,node
cmsel,s,a1n_nodes
cmsel,r,a3p_nodes
cm,a1n_a3p_nodes,node
cmsel,s,a1p_nodes
cmsel,r,a3n_nodes
cm,a1p_a3n_nodes,node
cmsel,s,a1p_nodes
cmsel,r,a3p_nodes
cm,a1p_a3p_nodes,node

! select edges a3 a2 -----
cmsel,s,a3n_nodes
cmsel,r,a2n_nodes
cm,a3n_a2n_nodes,node
cmsel,s,a3n_nodes
cmsel,r,a2p_nodes
cm,a3n_a2p_nodes,node
cmsel,s,a3p_nodes
cmsel,r,a2n_nodes
cm,a3p_a2n_nodes,node
cmsel,s,a3p_nodes

```

```

cm,sel,r,a2p_nodes
cm,a3p_a2p_nodes,node

```

```

cm,sel,s,a1n_a2n_nodes
cm,sel,a,a1n_a2p_nodes
cm,sel,a,a1p_a2n_nodes
cm,sel,a,a1p_a2p_nodes
cm,sel,a,a1n_a3n_nodes
cm,sel,a,a1n_a3p_nodes
cm,sel,a,a1p_a3n_nodes
cm,sel,a,a1p_a3p_nodes
cm,sel,a,a3n_a2n_nodes
cm,sel,a,a3n_a2p_nodes
cm,sel,a,a3p_a2n_nodes
cm,sel,a,a3p_a2p_nodes
cm,edges_nodes,node

```

```

! select corners a1 a2 a3 -----

```

```

n,sel,all
a1n_a2n_a3n_corner=node(-a2,-a3,-a1)
a1n_a2p_a3n_corner=node( a2,-a3,-a1)
a1n_a2n_a3p_corner=node(-a2, a3,-a1)
a1n_a2p_a3p_corner=node( a2, a3,-a1)
a1p_a2n_a3n_corner=node(-a2,-a3, a1)
a1p_a2p_a3n_corner=node( a2,-a3, a1)
a1p_a2n_a3p_corner=node(-a2, a3, a1)
a1p_a2p_a3p_corner=node( a2, a3, a1)
n,sel,s,node,,a1n_a2n_a3n_corner
n,sel,a,node,,a1n_a2n_a3p_corner
n,sel,a,node,,a1n_a2p_a3n_corner
n,sel,a,node,,a1n_a2p_a3p_corner
n,sel,a,node,,a1p_a2n_a3n_corner
n,sel,a,node,,a1p_a2n_a3p_corner
n,sel,a,node,,a1p_a2p_a3n_corner
n,sel,a,node,,a1p_a2p_a3p_corner
cm,corners_nodes,node
ALLSEL,ALL

```

```

NSEL,S,LOC,x,0
NSEL,R,LOC,Y,0
NSEL,R,LOC,Z,0
D,all,all
ALLSEL,ALL
CEDELE,ALL
ALLSEL,ALL
ceeq=0

```

```

! PERIODIC BOUNDARY CONDITION EQNS 2-DIR (X-DIR)

```

```

pos_node=
neg_node=
cm,sel,s,a2n_nodes
cm,sel,u,edges_nodes
*get,num_nodes,node,0,count,max
*do,i,1,num_nodes,1
  cm,sel,s,a2n_nodes
  cm,sel,u,edges_nodes
!   neg_node is undefined; use lowest active node number when i=1
  *if,i,ne,1,then
    neg_node=ndnext(neg_node)
  *else
    *get,neg_node,node,0,num,min
  *endif
!   get x,y,z locations of current node in active coord system
  x_=nx(neg_node)
  y_=ny(neg_node)
  z_=nz(neg_node)
  cm,sel,s,a2p_nodes
!   get closest node from component neg_a2
  pos_node=node(-x_,y_,z_)
  ceeq=ceeq+1
  ce,ceeq,(eps22*(a2*2)),neg_node,ux,-1,pos_node,ux,1 ! x->2
  ceeq=ceeq+1
  ce,ceeq,(eps32*(a2*2)),neg_node,uy,-1,pos_node,uy,1 ! y->3
  ceeq=ceeq+1
  ce,ceeq,(eps12*(a2*2)),neg_node,uz,-1,pos_node,uz,1 ! z->1

```

```

*enddo

! PERIODIC BOUNDARY CONDITION EQNS 3-DIR (Y-DIR)
pos_node=
neg_node=
cmsel,s,a3n_nodes
cmsel,u,edges_nodes
*get,num_nodes,node,0,count,max
*do,i,1,num_nodes,1
  cmsel,s,a3n_nodes
  cmsel,u,edges_nodes
!   neg_node is undefined; use lowest active node number when i=1
  *if,i,ne,1,then
    neg_node=ndnext(neg_node)
  *else
    *get,neg_node,node,0,num,min
  *endif
!   get x,y,z locations of current node in active coord system
  x_=nx(neg_node)
  y_=ny(neg_node)
  z_=nz(neg_node)
  cmsel,s,a3p_nodes
!   get closest node from component neg_a2
  pos_node=node(x_,y_,z_)
  ceeq=ceeq+1
  ce,ceeq,(eps23*(a3*2)),neg_node,ux,-1,pos_node,ux,1 ! x->2
  ceeq=ceeq+1
  ce,ceeq,(eps33*(a3*2)),neg_node,uy,-1,pos_node,uy,1 ! y->3
  ceeq=ceeq+1
  ce,ceeq,(eps13*(a3*2)),neg_node,uz,-1,pos_node,uz,1 ! z->1
*enddo

! PERIODIC BOUNDARY CONDITION EQNS 1-DIR (Z-DIR)
pos_node=
neg_node=
cmsel,s,a1n_nodes
cmsel,u,edges_nodes
*get,num_nodes,node,0,count,max
*do,i,1,num_nodes,1
  cmsel,s,a1n_nodes
  cmsel,u,edges_nodes
!   neg_node is undefined; use lowest active node number when i=1
  *if,i,ne,1,then
    neg_node=ndnext(neg_node)
  *else
    *get,neg_node,node,0,num,min
  *endif
!   get x,y,z locations of current node in active coord system
  x_=nx(neg_node)
  y_=ny(neg_node)
  z_=nz(neg_node)
  cmsel,s,a1p_nodes
!   get closest node from component neg_a2
  pos_node=node(x_,y_,z_)
  ceeq=ceeq+1
  ce,ceeq,(eps21*(a1*2)),neg_node,ux,-1,pos_node,ux,1 ! x->2
  ceeq=ceeq+1
  ce,ceeq,(eps31*(a1*2)),neg_node,uy,-1,pos_node,uy,1 ! y->3
  ceeq=ceeq+1
  ce,ceeq,(eps11*(a1*2)),neg_node,uz,-1,pos_node,uz,1 ! z->1
*enddo

! PERIODIC BOUNDARY CONDITION EQNS 23-DIR (XY-DIR)
pos_node=
neg_node=
cmsel,s,a3n_a2n_nodes
cmsel,u,corners_nodes
*get,num_nodes,node,0,count,max
*do,i,1,num_nodes,1
  cmsel,s,a3n_a2n_nodes
  cmsel,u,corners_nodes
!   neg_node is undefined; use lowest active node number when i=1
  *if,i,ne,1,then
    neg_node=ndnext(neg_node)
  *else

```



```

    *get,neg_node,node,0,num,min
*endif
!   get x,y,z locations of current node in active coord system
x_=nx(neg_node)
y_=ny(neg_node)
z_=nz(neg_node)
cmsel,s,a3p_a2p_nodes
!   get closest node from component neg_a2
pos_node=node(-x_,-y_,-z_)
ceeq=ceeq+1
ce,ceeq,(eps22*(a2*2))+(eps23*(a3*2)),neg_node,ux,-1,pos_node,ux,1   ! x->2
ceeq=ceeq+1
ce,ceeq,(eps32*(a2*2))+(eps33*(a3*2)),neg_node,uy,-1,pos_node,uy,1   ! y->3
ceeq=ceeq+1
ce,ceeq,(eps12*(a2*2))+(eps13*(a3*2)),neg_node,uz,-1,pos_node,uz,1   ! z->1
*enddo
!
pos_node=
neg_node=
cmsel,s,a3n_a2p_nodes
cmsel,u,comers_nodes
*get,num_nodes,node,0,count,max
*do,i,1,num_nodes,1
    cmsel,s,a3n_a2p_nodes
    cmsel,u,comers_nodes
!   neg_node is undefined; use lowest active node number when i=1
    *if,i,ne,1,then
        neg_node=ndnext(neg_node)
    *else
        *get,neg_node,node,0,num,min
    *endif
!   get x,y,z locations of current node in active coord system
x_=nx(neg_node)
y_=ny(neg_node)
z_=nz(neg_node)
cmsel,s,a3p_a2n_nodes
!   get closest node from component neg_a2
pos_node=node(-x_,-y_,-z_)
ceeq=ceeq+1
ce,ceeq,(-eps22*(a2*2))+(eps23*(a3*2)),neg_node,ux,-1,pos_node,ux,1   ! x->2
ceeq=ceeq+1
ce,ceeq,(-eps32*(a2*2))+(eps33*(a3*2)),neg_node,uy,-1,pos_node,uy,1   ! y->3
ceeq=ceeq+1
ce,ceeq,(-eps12*(a2*2))+(eps13*(a3*2)),neg_node,uz,-1,pos_node,uz,1   ! z->1
*enddo

! PERIODIC BOUNDARY CONDITION EQNS 31-DIR (YZ-DIR)
pos_node=
neg_node=
cmsel,s,a1n_a3n_nodes
cmsel,u,comers_nodes
*get,num_nodes,node,0,count,max
*do,i,1,num_nodes,1
    cmsel,s,a1n_a3n_nodes
    cmsel,u,comers_nodes
!   neg_node is undefined; use lowest active node number when i=1
    *if,i,ne,1,then
        neg_node=ndnext(neg_node)
    *else
        *get,neg_node,node,0,num,min
    *endif
!   get x,y,z locations of current node in active coord system
x_=nx(neg_node)
y_=ny(neg_node)
z_=nz(neg_node)
cmsel,s,a1p_a3p_nodes
!   get closest node from component neg_a2
pos_node=node(x_,-y_,-z_)
ceeq=ceeq+1
ce,ceeq,(eps21*(a1*2))+(eps23*(a3*2)),neg_node,ux,-1,pos_node,ux,1   ! x->2
ceeq=ceeq+1
ce,ceeq,(eps31*(a1*2))+(eps33*(a3*2)),neg_node,uy,-1,pos_node,uy,1   ! y->3
ceeq=ceeq+1
ce,ceeq,(eps11*(a1*2))+(eps13*(a3*2)),neg_node,uz,-1,pos_node,uz,1   ! z->1
*enddo

```

```

!
pos_node=
neg_node=
cmsel,s,a1n_a3p_nodes
cmsel,u,comers_nodes
*get,num_nodes,node,0,count,max
*do,i,1,num_nodes,1
  cmsel,s,a1n_a3p_nodes
  cmsel,u,comers_nodes
!   neg_node is undefined; use lowest active node number when i=1
  *if,i,ne,1,then
    neg_node=ndnext(neg_node)
  *else
    *get,neg_node,node,0,num,min
  *endif
!   get x,y,z locations of current node in active coord system
  x_=nx(neg_node)
  y_=ny(neg_node)
  z_=nz(neg_node)
  cmsel,s,a1p_a3n_nodes
!   get closest node from component neg_a2
  pos_node=node(x_-y_-z_)
  ceeq=ceeq+1
  ce,ceeq,(eps21*(a1*2))-(eps23*(a3*2)),neg_node,ux,-1,pos_node,ux,1   ! x->2
  ceeq=ceeq+1
  ce,ceeq,(eps31*(a1*2))-(eps33*(a3*2)),neg_node,uy,-1,pos_node,uy,1   ! y->3
  ceeq=ceeq+1
  ce,ceeq,(eps11*(a1*2))-(eps13*(a3*2)),neg_node,uz,-1,pos_node,uz,1   ! z->1
*enddo

! PERIODIC BOUNDARY CONDITION EQNS 12-DIR (YZ-DIR)
pos_node=
neg_node=
cmsel,s,a1n_a2n_nodes
cmsel,u,comers_nodes
*get,num_nodes,node,0,count,max
*do,i,1,num_nodes,1
  cmsel,s,a1n_a2n_nodes
  cmsel,u,comers_nodes
!   neg_node is undefined; use lowest active node number when i=1
  *if,i,ne,1,then
    neg_node=ndnext(neg_node)
  *else
    *get,neg_node,node,0,num,min
  *endif
!   get x,y,z locations of current node in active coord system
  x_=nx(neg_node)
  y_=ny(neg_node)
  z_=nz(neg_node)
  cmsel,s,a1p_a2p_nodes
!   get closest node from component neg_a2
  pos_node=node(-x_-y_-z_)
  ceeq=ceeq+1
  ce,ceeq,(eps21*(a1*2))+(eps22*(a2*2)),neg_node,ux,-1,pos_node,ux,1   ! x->2
  ceeq=ceeq+1
  ce,ceeq,(eps31*(a1*2))+(eps32*(a2*2)),neg_node,uy,-1,pos_node,uy,1   ! y->3
  ceeq=ceeq+1
  ce,ceeq,(eps11*(a1*2))+(eps12*(a2*2)),neg_node,uz,-1,pos_node,uz,1   ! z->1
*enddo
!
pos_node=
neg_node=
cmsel,s,a1n_a2p_nodes
cmsel,u,comers_nodes
*get,num_nodes,node,0,count,max
*do,i,1,num_nodes,1
  cmsel,s,a1n_a2p_nodes
  cmsel,u,comers_nodes
!   neg_node is undefined; use lowest active node number when i=1
  *if,i,ne,1,then
    neg_node=ndnext(neg_node)
  *else
    *get,neg_node,node,0,num,min
  *endif
!   get x,y,z locations of current node in active coord system

```

```

x_=nx(neg_node)
y_=ny(neg_node)
z_=nz(neg_node)
cmsel,s,alp_a2n_nodes
! get closest node from component neg_a2
pos_node=node(-x_,y_,z_)
ceeq=ceeq+1
ce,ceeq,(eps21*(a1*2))-(eps22*(a2*2)),neg_node,ux,-1,pos_node,ux,1 ! x->2
ceeq=ceeq+1
ce,ceeq,(eps31*(a1*2))-(eps32*(a2*2)),neg_node,uy,-1,pos_node,uy,1 ! y->3
ceeq=ceeq+1
ce,ceeq,(eps11*(a1*2))-(eps12*(a2*2)),neg_node,uz,-1,pos_node,uz,1 ! z->1
*enddo

! PERIODIC BOUNDARY CONDITION Corners
nset,s,node,,aln_a2n_a3n_corner
*get,neg_node,node,0,num,min
! get x,y,z locations of current node in active coord system
x_=nx(neg_node)
y_=ny(neg_node)
z_=nz(neg_node)
nset,a,node,,alp_a2p_a3p_corner
pos_node=node(-x_,y_,z_)
ceeq=ceeq+1
ce,ceeq,(eps21*(a1*2))+(eps22*(a2*2))+(eps23*(a3*2)),neg_node,ux,-1,pos_node,ux,1 ! x->2
ceeq=ceeq+1
ce,ceeq,(eps31*(a1*2))+(eps32*(a2*2))+(eps33*(a3*2)),neg_node,uy,-1,pos_node,uy,1 ! y->3
ceeq=ceeq+1
ce,ceeq,(eps11*(a1*2))+(eps12*(a2*2))+(eps13*(a3*2)),neg_node,uz,-1,pos_node,uz,1 ! z->1

nset,s,node,,aln_a2n_a3p_corner
*get,neg_node,node,0,num,min
! get x,y,z locations of current node in active coord system
x_=nx(neg_node)
y_=ny(neg_node)
z_=nz(neg_node)
nset,a,node,,alp_a2p_a3n_corner
pos_node=node(-x_,y_,z_)
ceeq=ceeq+1
ce,ceeq,(eps21*(a1*2))+(eps22*(a2*2))-(eps23*(a3*2)),neg_node,ux,-1,pos_node,ux,1 ! x->2
ceeq=ceeq+1
ce,ceeq,(eps31*(a1*2))+(eps32*(a2*2))-(eps33*(a3*2)),neg_node,uy,-1,pos_node,uy,1 ! y->3
ceeq=ceeq+1
ce,ceeq,(eps11*(a1*2))+(eps12*(a2*2))-(eps13*(a3*2)),neg_node,uz,-1,pos_node,uz,1 ! z->1

nset,s,node,,aln_a2p_a3n_corner
*get,neg_node,node,0,num,min
! get x,y,z locations of current node in active coord system
x_=nx(neg_node)
y_=ny(neg_node)
z_=nz(neg_node)
nset,a,node,,alp_a2n_a3p_corner
pos_node=node(-x_,y_,z_)
ceeq=ceeq+1
ce,ceeq,(eps21*(a1*2))-(eps22*(a2*2))+(eps23*(a3*2)),neg_node,ux,-1,pos_node,ux,1 ! x->2
ceeq=ceeq+1
ce,ceeq,(eps31*(a1*2))-(eps32*(a2*2))+(eps33*(a3*2)),neg_node,uy,-1,pos_node,uy,1 ! y->3
ceeq=ceeq+1
ce,ceeq,(eps11*(a1*2))-(eps12*(a2*2))+(eps13*(a3*2)),neg_node,uz,-1,pos_node,uz,1 ! z->1

nset,s,node,,aln_a2p_a3p_corner
*get,neg_node,node,0,num,min
! get x,y,z locations of current node in active coord system
x_=nx(neg_node)
y_=ny(neg_node)
z_=nz(neg_node)
nset,a,node,,alp_a2n_a3n_corner
pos_node=node(-x_,y_,z_)
ceeq=ceeq+1
ce,ceeq,(eps21*(a1*2))-(eps22*(a2*2))-(eps23*(a3*2)),neg_node,ux,-1,pos_node,ux,1 ! x->2
ceeq=ceeq+1
ce,ceeq,(eps31*(a1*2))-(eps32*(a2*2))-(eps33*(a3*2)),neg_node,uy,-1,pos_node,uy,1 ! y->3
ceeq=ceeq+1
ce,ceeq,(eps11*(a1*2))-(eps12*(a2*2))-(eps13*(a3*2)),neg_node,uz,-1,pos_node,uz,1 ! z->1

```

```

ALLSEL,ALL
*END

/SOLU          ! Solution module
! ceRve arguments:
! a1,a2,a3,eps1,eps2,eps3,eps4,eps5,eps6

*use,ceRVE,a1,a2,a3,1.,0,0,0,0,0
SOLVE         ! Solve analysis
*use,ceRVE,a1,a2,a3,0,1.,0,0,0,0
SOLVE         ! Solve analysis
*use,ceRVE,a1,a2,a3,0,0,1.,0,0,0,0
SOLVE         ! Solve analysis
*use,ceRVE,a1,a2,a3,0,0,0,1.,0,0,0,0
SOLVE         ! Solve analysis
*use,ceRVE,a1,a2,a3,0,0,0,0,1.,0
SOLVE         ! Solve analysis
*use,ceRVE,a1,a2,a3,0,0,0,0,0,1.
SOLVE         ! Solve analysis
FINISH        ! Exit solution module

*create,srecover !,mac ! Create macro to calculate average stress
/nopr
ETABLE, ,VOLUME,          ! Get element volume
ETABLE, ,SX              ! Get element stress
ETABLE, ,SY
ETABLE, ,SZ
ETABLE, ,SXY
ETABLE, ,SXZ
ETABLE, ,SYZ
SMULT,SXV,VOLUME,SX,1,1.  ! Stress by element volume
SMULT,SYV,VOLUME,SY,1,1.
SMULT,SZV,VOLUME,SZ,1,1.
SMULT,SXYV,VOLUME,SXY,1,1.
SMULT,SXZV,VOLUME,SXZ,1,1.
SMULT,SYZV,VOLUME,SYZ,1,1.
SSUM
*get,totvol,ssum,,item,volu ! Integer stress along total volume
*get,totsx ,ssum,,item,sxv
*get,totsy ,ssum,,item,syv
*get,totsz ,ssum,,item,szv
*get,totsxy ,ssum,,item,sxyv
*get,totsxz ,ssum,,item,sxzv
*get,totsyz ,ssum,,item,syzv

Sxx0 = totsx/totvol  ! Compute average RVE stress
Syy0 = totsy/totvol
Szz0 = totsz/totvol
Sxy0 = totsxy/totvol
Sxz0 = totsxz/totvol
Syz0 = totsyz/totvol
/gopr
*end !srecover

/POST1        ! Post-processor module
/DEVICE,VECTOR,0
/PNUM,MAT,0
PLESOL,S,Z,1

SET,1         ! First column coefficients
*use,srecover
C11 = Szz0
C21 = Sxx0
C31 = Syy0

SET,2         ! Second column coefficients
*use,srecover
C12 = Szz0
C22 = Sxx0
C32 = Syy0

SET,3         ! Third column coefficients
*use,srecover
C13 = Szz0
C23 = Sxx0

```

C33 = Syy0

$EL = C11 - 2 * C12 * C12 / (C22 + C23)$

$nuL = C12 / (C22 + C23)$

$ET = (C11 * (C22 + C23) - 2 * C12 * C12) * (C22 - C23) / (C11 * C22 - C12 * C12)$

$nuT = (C11 * C23 - C12 * C12) / (C11 * C22 - C12 * C12)$

$GT = (C22 - C23) / 2$! or $GT = ET / 2 / (1 + nuT)$

SET,4 ! Fith column coefficients

*use,srecover

C44 = Sxy0

SET,5 ! Fith column coefficients

*use,srecover

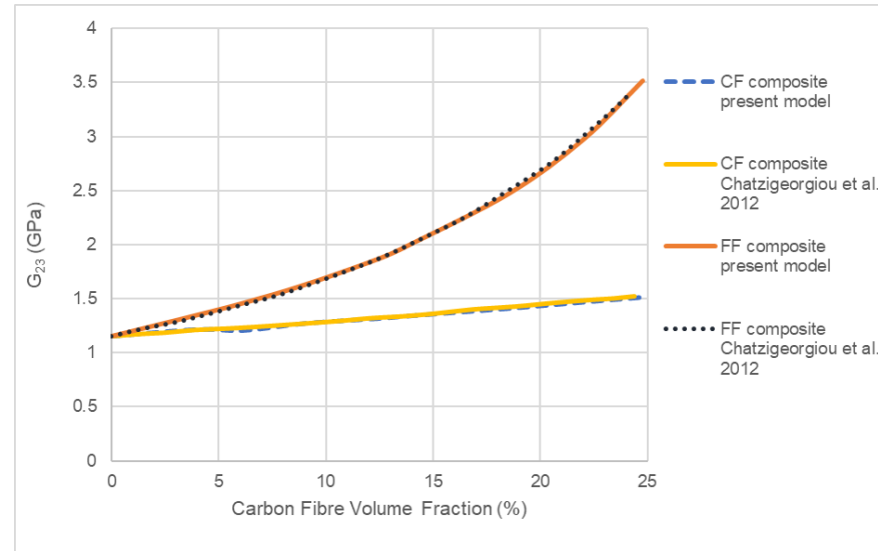
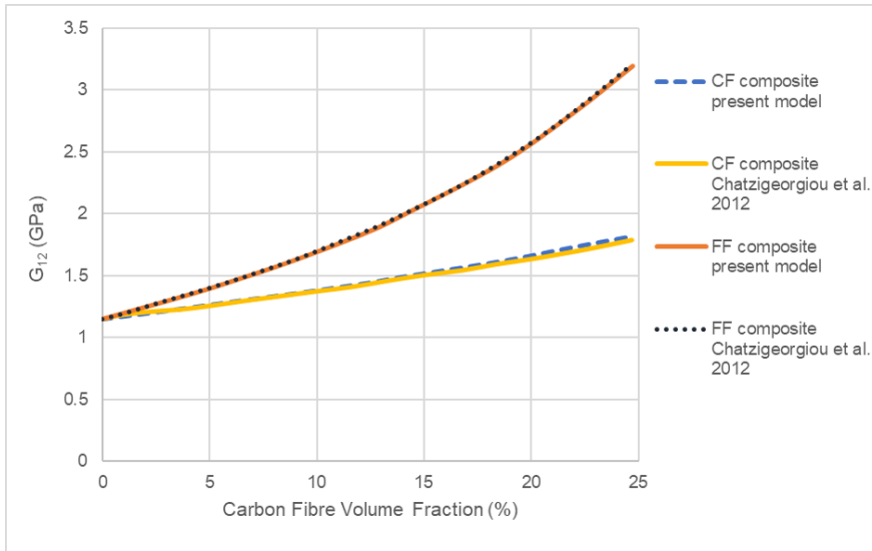
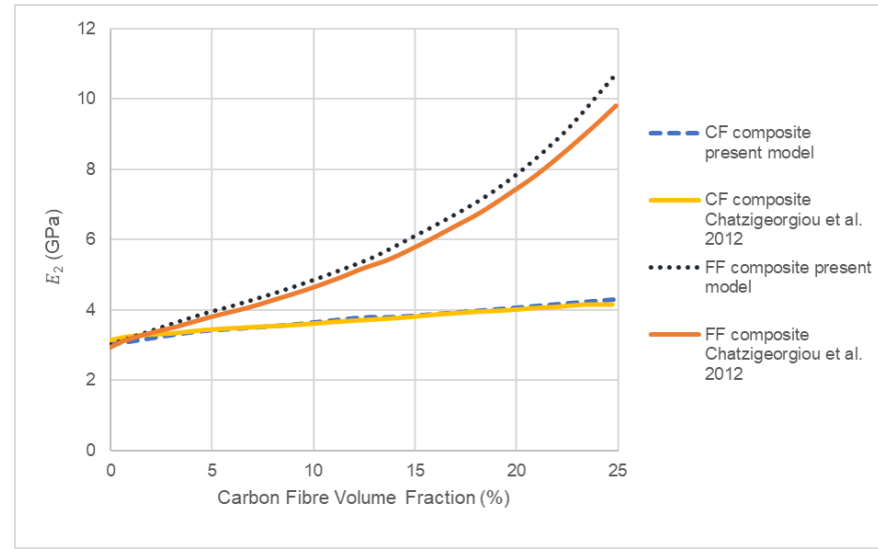
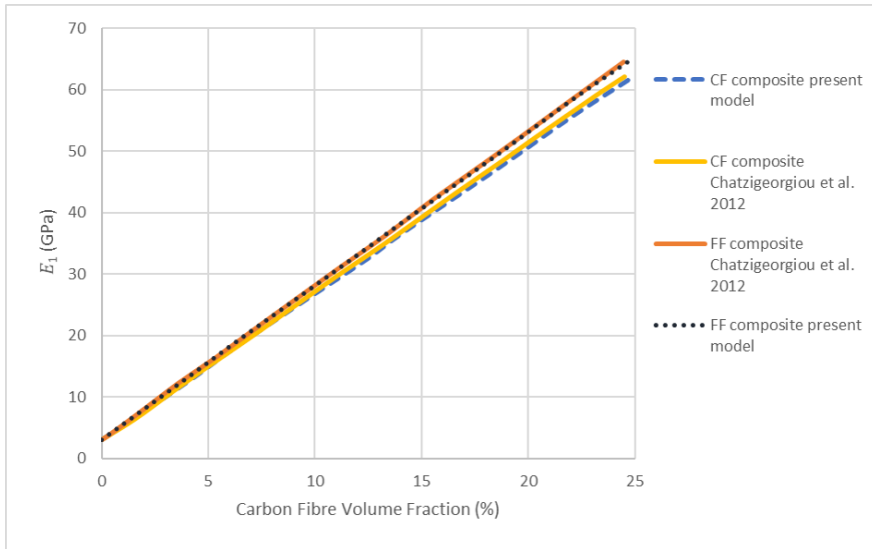
C55 = Syz0

SET,6 ! Sixth column coefficients

*use,srecover

C66 = Sxz0

FINISH ! Exit post-processor module



APPENDIX D: Optimisation

/TITLE,ONE-EIGHT Symmetric Model of RVE hexagonal array

```
RF=3.5
a2=4.3
a3=7.44
a1=1.07
Ei=8.3e-3
vi=0.176
ri=3.6
/prep7
MP,EX,1,15e-3
MP,EY,1,15e-3
MP,EZ,1,230e-3
MP,nuXY,1,0.07
MP,nuYZ,1,0.2
MP,nuXZ,1,0.2
MP,GXY,1,7E-3
MP,GYZ,1,15e-3
MP,GXZ,1,15E-3
MP,EX,2,4e-3
MP,PRXY,2,0.35
MP,EX,3,Ei
MP,PRXY,3,vi
```

```
ET,1,SOLID186 ! Choose SOLID186 element type
```

```
BLOCK,-A2,A2,-A3,A3,-A1,A1,
CYLIND,RF,,-A1,A1, 0, 90,
CYLIND,RF,,-A1,A1, 90,180,
CYLIND,RF,,-A1,A1,180,270,
CYLIND,RF,,-A1,A1,270,360,
CYLIND,RF,,-A1,A1, 0, 90,
CYLIND,RF,,-A1,A1, 90,180,
CYLIND,RF,,-A1,A1,180,270,
CYLIND,RF,,-A1,A1,270,360,
VGEN,1,6,,,-A2,-A3,,,,,1
VGEN,1,7,,, A2,-A3,,,,,1
VGEN,1,8,,, A2, A3,,,,,1
VGEN,1,9,,,-A2, A3,,,,,1
CYLIND,ri,,-A1,A1, 0, 90,
CYLIND,ri,,-A1,A1, 90,180,
CYLIND,ri,,-A1,A1,180,270,
CYLIND,ri,,-A1,A1,270,360,
CYLIND,ri,,-A1,A1, 0, 90,
CYLIND,ri,,-A1,A1, 90,180,
CYLIND,ri,,-A1,A1,180,270,
CYLIND,ri,,-A1,A1,270,360,
VGEN,1,14,,,-A2,-A3,,,,,1
VGEN,1,15,,, A2,-A3,,,,,1
VGEN,1,16,,, A2, A3,,,,,1
VGEN,1,17,,,-A2, A3,,,,,1
ALLSEL,ALL
VOVLAP,all ! Overlap volumes
NUMCMP,all ! Renumbering all volumes, volume 9 is the matrix
/DEVICE,VECTOR,1
/VIEW,1,1,2,3
/ANG,1
/PNUM,VOLU,1
/PNUM,MAT,1
/REPLOT
```

```

VSEL,S,,,1,8
VATT,1
VSEL,S,,,17
VATT,2
VSEL,S,,,9,16
VATT,3
VSEL,ALL
/REPLOT

LSEL,U,LOC,Z,A1 ! meshing control
LSEL,U,LOC,Z,-A1
LESIZE,ALL,,,10 ! number of divisions through the thickness
VSEL,S,,,1,16
ASLV,S
LSLA,S
LESIZE,ALL,,,6 ! number of divisions on the fiber
LSEL,S,LOC,Y,A3
LSEL,A,LOC,Y,-A3
LESIZE,ALL,,,6 ! number of divisions on the matrix
ALLSEL,ALL
LESIZE,ALL,,,16 ! number of divisions on the matrix

VMESH,1,8
VMESH,9,16 ! Mesh area 1 and 2 ! Associate material #2 with volume 3
VSWEEP,17 ! Mesh by sweep procedure area 3
EPLOT
FINISH ! Exit pre-processor module

*CREATE,ceRVE
! This macro applies CE to a periodic hexaedral RVE
! The RVE must be centred at (0,0,0) and
! a node must exist at (0,0,0)

a1=arg1
a2=arg2
a3=arg3

! APPLIED STRAINS
eps11=arg4
eps22=arg5
eps33=arg6
!--Note: must enter epsij=1/2*gamma
eps12=arg9/2
eps13=arg8/2
eps23=arg7/2 ! (x-y in model)
!--Note: here recovers the other 1/2*gamma
eps21 = eps12
eps31 = eps13
eps32 = eps23
! PERIODIC BOUNDARY CONDITION EQNS 2-DIR (X-DIR)
! DIR THEORY ANSYS MODEL
! 1 Z
! 2 X
! 3 Y

!-----
! CREATE COMPONENT SET: periodic corners, edges and sides
!-----

! select side +a1 and -a1 -----
nsel,s,loc,z,-a1-0.001,-a1+0.001
cm,a1n_nodes,node
nsel,s,loc,z,a1-0.001,a1+0.001
cm,a1p_nodes,node

```



```

! select side +a2 and -a2 -----
nset,s,loc,x,-a2-0.001,-a2+0.001
cm,a2n_nodes,node
nset,s,loc,x,a2-0.001,a2+0.001
cm,a2p_nodes,node

! select side +a3 and -a3 -----
nset,s,loc,y,-a3-0.001,-a3+0.001
cm,a3n_nodes,node
nset,s,loc,y,a3-0.001,a3+0.001
cm,a3p_nodes,node

! select edges a1 a2 -----
cmset,s,a1n_nodes
cmset,r,a2n_nodes
cm,a1n_a2n_nodes,node
cmset,s,a1n_nodes
cmset,r,a2p_nodes
cm,a1n_a2p_nodes,node
cmset,s,a1p_nodes
cmset,r,a2n_nodes
cm,a1p_a2n_nodes,node
cmset,s,a1p_nodes
cmset,r,a2p_nodes
cm,a1p_a2p_nodes,node

! select edges a1 a3 -----
cmset,s,a1n_nodes
cmset,r,a3n_nodes
cm,a1n_a3n_nodes,node
cmset,s,a1n_nodes
cmset,r,a3p_nodes
cm,a1n_a3p_nodes,node
cmset,s,a1p_nodes
cmset,r,a3n_nodes
cm,a1p_a3n_nodes,node
cmset,s,a1p_nodes
cmset,r,a3p_nodes
cm,a1p_a3p_nodes,node

! select edges a3 a2 -----
cmset,s,a3n_nodes
cmset,r,a2n_nodes
cm,a3n_a2n_nodes,node
cmset,s,a3n_nodes
cmset,r,a2p_nodes
cm,a3n_a2p_nodes,node
cmset,s,a3p_nodes
cmset,r,a2n_nodes
cm,a3p_a2n_nodes,node
cmset,s,a3p_nodes
cmset,r,a2p_nodes
cm,a3p_a2p_nodes,node

cmset,s,a1n_a2n_nodes
cmset,a,a1n_a2p_nodes
cmset,a,a1p_a2n_nodes
cmset,a,a1p_a2p_nodes
cmset,a,a1n_a3n_nodes
cmset,a,a1n_a3p_nodes
cmset,a,a1p_a3n_nodes
cmset,a,a1p_a3p_nodes
cmset,a,a3n_a2n_nodes
cmset,a,a3n_a2p_nodes
cmset,a,a3p_a2n_nodes
cmset,a,a3p_a2p_nodes

```

cm,edges_nodes,node

! select corners a1 a2 a3 -----

```
nsel,all
a1n_a2n_a3n_corner=node(-a2,-a3,-a1)
a1n_a2p_a3n_corner=node( a2,-a3,-a1)
a1n_a2n_a3p_corner=node(-a2, a3,-a1)
a1n_a2p_a3p_corner=node( a2, a3,-a1)
a1p_a2n_a3n_corner=node(-a2,-a3, a1)
a1p_a2p_a3n_corner=node( a2,-a3, a1)
a1p_a2n_a3p_corner=node(-a2, a3, a1)
a1p_a2p_a3p_corner=node( a2, a3, a1)
nsel,s,node,,a1n_a2n_a3n_corner
nsel,a,node,,a1n_a2n_a3p_corner
nsel,a,node,,a1n_a2p_a3n_corner
nsel,a,node,,a1n_a2p_a3p_corner
nsel,a,node,,a1p_a2n_a3n_corner
nsel,a,node,,a1p_a2n_a3p_corner
nsel,a,node,,a1p_a2p_a3n_corner
nsel,a,node,,a1p_a2p_a3p_corner
cm,corners_nodes,node
ALLSEL,ALL
```

```
NSEL,S,LOC,x,0
NSEL,R,LOC,Y,0
NSEL,R,LOC,Z,0
D,all,all
ALLSEL,ALL
CEDELE,ALL
ALLSEL,ALL
ceeq=0
```

! PERIODIC BOUNDARY CONDITION EQNS 2-DIR (X-DIR)

```
pos_node=
neg_node=
cmsel,s,a2n_nodes
cmsel,u,edges_nodes
*get,num_nodes,node,0,count,max
*do,i,1,num_nodes,1
  cmsel,s,a2n_nodes
  cmsel,u,edges_nodes
! neg_node is undefined; use lowest active node number when i=1
  *if,i,ne,1,then
    neg_node=ndnext(neg_node)
  *else
    *get,neg_node,node,0,num,min
  *endif
! get x,y,z locations of current node in active coord system
  x_=nx(neg_node)
  y_=ny(neg_node)
  z_=nz(neg_node)
  cmsel,s,a2p_nodes
! get closest node from component neg_a2
  pos_node=node(-x_,y_,z_)
  ceeq=ceeq+1
  ce,ceeq,(eps22*(a2*2)),neg_node,ux,-1,pos_node,ux,1 ! x->2
  ceeq=ceeq+1
  ce,ceeq,(eps32*(a2*2)),neg_node,uy,-1,pos_node,uy,1 ! y->3
  ceeq=ceeq+1
  ce,ceeq,(eps12*(a2*2)),neg_node,uz,-1,pos_node,uz,1 ! z->1
*enddo
```

! PERIODIC BOUNDARY CONDITION EQNS 3-DIR (Y-DIR)

```
pos_node=
neg_node=
cmsel,s,a3n_nodes
```

```

cmset,u,edges_nodes
*get,num_nodes,node,0,count,max
*do,i,1,num_nodes,1
  cmset,s,a3n_nodes
  cmset,u,edges_nodes
! neg_node is undefined; use lowest active node number when i=1
  *if,i,ne,1,then
    neg_node=ndnext(neg_node)
  *else
    *get,neg_node,node,0,num,min
  *endif
! get x,y,z locations of current node in active coord system
x_=nx(neg_node)
y_=ny(neg_node)
z_=nz(neg_node)
cmset,s,a3p_nodes
! get closest node from component neg_a2
pos_node=node(x_,y_,z_)
ceeq=ceeq+1
ce,ceeq,(eps23*(a3*2)),neg_node,ux,-1,pos_node,ux,1 ! x->2
ceeq=ceeq+1
ce,ceeq,(eps33*(a3*2)),neg_node,uy,-1,pos_node,uy,1 ! y->3
ceeq=ceeq+1
ce,ceeq,(eps13*(a3*2)),neg_node,uz,-1,pos_node,uz,1 ! z->1
*enddo

! PERIODIC BOUNDARY CONDITION EQNS 1-DIR (Z-DIR)
pos_node=
neg_node=
cmset,s,a1n_nodes
cmset,u,edges_nodes
*get,num_nodes,node,0,count,max
*do,i,1,num_nodes,1
  cmset,s,a1n_nodes
  cmset,u,edges_nodes
! neg_node is undefined; use lowest active node number when i=1
  *if,i,ne,1,then
    neg_node=ndnext(neg_node)
  *else
    *get,neg_node,node,0,num,min
  *endif
! get x,y,z locations of current node in active coord system
x_=nx(neg_node)
y_=ny(neg_node)
z_=nz(neg_node)
cmset,s,a1p_nodes
! get closest node from component neg_a2
pos_node=node(x_,y_,z_)
ceeq=ceeq+1
ce,ceeq,(eps21*(a1*2)),neg_node,ux,-1,pos_node,ux,1 ! x->2
ceeq=ceeq+1
ce,ceeq,(eps31*(a1*2)),neg_node,uy,-1,pos_node,uy,1 ! y->3
ceeq=ceeq+1
ce,ceeq,(eps11*(a1*2)),neg_node,uz,-1,pos_node,uz,1 ! z->1
*enddo

! PERIODIC BOUNDARY CONDITION EQNS 23-DIR (XY-DIR)
pos_node=
neg_node=
cmset,s,a3n_a2n_nodes
cmset,u,corners_nodes
*get,num_nodes,node,0,count,max
*do,i,1,num_nodes,1
  cmset,s,a3n_a2n_nodes
  cmset,u,corners_nodes
! neg_node is undefined; use lowest active node number when i=1

```

```

*if,i,ne,1,then
  neg_node=ndnext(neg_node)
*else
  *get,neg_node,node,0,num,min
*endif
! get x,y,z locations of current node in active coord system
x_=nx(neg_node)
y_=ny(neg_node)
z_=nz(neg_node)
cmsel,s,a3p_a2p_nodes
! get closest node from component neg_a2
pos_node=node(-x_,-y_,z_)
ceeq=ceeq+1
ce,ceeq,(eps22*(a2*2))+(eps23*(a3*2)),neg_node,ux,-1,pos_node,ux,1 ! x->2
ceeq=ceeq+1
ce,ceeq,(eps32*(a2*2))+(eps33*(a3*2)),neg_node,uy,-1,pos_node,uy,1 ! y->3
ceeq=ceeq+1
ce,ceeq,(eps12*(a2*2))+(eps13*(a3*2)),neg_node,uz,-1,pos_node,uz,1 ! z->1
*enddo
!
pos_node=
neg_node=
cmsel,s,a3n_a2p_nodes
cmsel,u,corners_nodes
*get,num_nodes,node,0,count,max
*do,i,1,num_nodes,1
  cmsel,s,a3n_a2p_nodes
  cmsel,u,corners_nodes
! neg_node is undefined; use lowest active node number when i=1
  *if,i,ne,1,then
    neg_node=ndnext(neg_node)
  *else
    *get,neg_node,node,0,num,min
  *endif
  ! get x,y,z locations of current node in active coord system
  x_=nx(neg_node)
  y_=ny(neg_node)
  z_=nz(neg_node)
  cmsel,s,a3p_a2n_nodes
! get closest node from component neg_a2
  pos_node=node(-x_,-y_,z_)
  ceeq=ceeq+1
  ce,ceeq,(-eps22*(a2*2))+(eps23*(a3*2)),neg_node,ux,-1,pos_node,ux,1 ! x->2
  ceeq=ceeq+1
  ce,ceeq,(-eps32*(a2*2))+(eps33*(a3*2)),neg_node,uy,-1,pos_node,uy,1 ! y->3
  ceeq=ceeq+1
  ce,ceeq,(-eps12*(a2*2))+(eps13*(a3*2)),neg_node,uz,-1,pos_node,uz,1 ! z->1
*enddo

! PERIODIC BOUNDARY CONDITION EQNS 31-DIR (YZ-DIR)
pos_node=
neg_node=
cmsel,s,a1n_a3n_nodes
cmsel,u,corners_nodes
*get,num_nodes,node,0,count,max
*do,i,1,num_nodes,1
  cmsel,s,a1n_a3n_nodes
  cmsel,u,corners_nodes
! neg_node is undefined; use lowest active node number when i=1
  *if,i,ne,1,then
    neg_node=ndnext(neg_node)
  *else
    *get,neg_node,node,0,num,min
  *endif
  ! get x,y,z locations of current node in active coord system
  x_=nx(neg_node)

```

```

y_ =ny(neg_node)
z_ =nz(neg_node)
cmsel,s,a1p_a3p_nodes
! get closest node from component neg_a2
pos_node=node(x_,-y_,-z_)
ceeq=ceeq+1
ce,ceeq,(eps21*(a1*2))+(eps23*(a3*2)),neg_node,ux,-1,pos_node,ux,1 ! x->2
ceeq=ceeq+1
ce,ceeq,(eps31*(a1*2))+(eps33*(a3*2)),neg_node,uy,-1,pos_node,uy,1 ! y->3
ceeq=ceeq+1
ce,ceeq,(eps11*(a1*2))+(eps13*(a3*2)),neg_node,uz,-1,pos_node,uz,1 ! z->1
*enddo
!
pos_node=
neg_node=
cmsel,s,a1n_a3p_nodes
cmsel,u,corners_nodes
*get,num_nodes,node,0,count,max
*do,i,1,num_nodes,1
cmsel,s,a1n_a3p_nodes
cmsel,u,corners_nodes
! neg_node is undefined; use lowest active node number when i=1
*if,i,ne,1,then
neg_node=ndnext(neg_node)
*else
*get,neg_node,node,0,num,min
*endif
! get x,y,z locations of current node in active coord system
x_ =nx(neg_node)
y_ =ny(neg_node)
z_ =nz(neg_node)
cmsel,s,a1p_a3n_nodes
! get closest node from component neg_a2
pos_node=node(x_,-y_,-z_)
ceeq=ceeq+1
ce,ceeq,(eps21*(a1*2))-(eps23*(a3*2)),neg_node,ux,-1,pos_node,ux,1 ! x->2
ceeq=ceeq+1
ce,ceeq,(eps31*(a1*2))-(eps33*(a3*2)),neg_node,uy,-1,pos_node,uy,1 ! y->3
ceeq=ceeq+1
ce,ceeq,(eps11*(a1*2))-(eps13*(a3*2)),neg_node,uz,-1,pos_node,uz,1 ! z->1
*enddo

! PERIODIC BOUNDARY CONDITION EQNS 12-DIR (YZ-DIR)
pos_node=
neg_node=
cmsel,s,a1n_a2n_nodes
cmsel,u,corners_nodes
*get,num_nodes,node,0,count,max
*do,i,1,num_nodes,1
cmsel,s,a1n_a2n_nodes
cmsel,u,corners_nodes
! neg_node is undefined; use lowest active node number when i=1
*if,i,ne,1,then
neg_node=ndnext(neg_node)
*else
*get,neg_node,node,0,num,min
*endif
! get x,y,z locations of current node in active coord system
x_ =nx(neg_node)
y_ =ny(neg_node)
z_ =nz(neg_node)
cmsel,s,a1p_a2p_nodes
! get closest node from component neg_a2
pos_node=node(-x_,-y_,-z_)
ceeq=ceeq+1
ce,ceeq,(eps21*(a1*2))+(eps22*(a2*2)),neg_node,ux,-1,pos_node,ux,1 ! x->2

```

```

    ceeq=ceeq+1
    ce,ceeq,(eps31*(a1*2))+(eps32*(a2*2)),neg_node,uy,-1,pos_node,uy,1 ! y->3
    ceeq=ceeq+1
    ce,ceeq,(eps11*(a1*2))+(eps12*(a2*2)),neg_node,uz,-1,pos_node,uz,1 ! z->1
*enddo
!
pos_node=
neg_node=
cmsel,s,a1n_a2p_nodes
cmsel,u,corners_nodes
*get,num_nodes,node,0,count,max
*do,i,1,num_nodes,1
    cmsel,s,a1n_a2p_nodes
    cmsel,u,corners_nodes
!   neg_node is undefined; use lowest active node number when i=1
    *if,i,ne,1,then
        neg_node=ndnext(neg_node)
    *else
        *get,neg_node,node,0,num,min
    *endif
!   get x,y,z locations of current node in active coord system
    x_=nx(neg_node)
    y_=ny(neg_node)
    z_=nz(neg_node)
    cmsel,s,a1p_a2n_nodes
!   get closest node from component neg_a2
    pos_node=node(-x_,y_,-z_)
    ceeq=ceeq+1
    ce,ceeq,(eps21*(a1*2))-(eps22*(a2*2)),neg_node,ux,-1,pos_node,ux,1 ! x->2
    ceeq=ceeq+1
    ce,ceeq,(eps31*(a1*2))-(eps32*(a2*2)),neg_node,uy,-1,pos_node,uy,1 ! y->3
    ceeq=ceeq+1
    ce,ceeq,(eps11*(a1*2))-(eps12*(a2*2)),neg_node,uz,-1,pos_node,uz,1 ! z->1
*enddo

! PERIODIC BOUNDARY CONDITION Corners
nset,s,node,,a1n_a2n_a3n_corner
*get,neg_node,node,0,num,min
!   get x,y,z locations of current node in active coord system
    x_=nx(neg_node)
    y_=ny(neg_node)
    z_=nz(neg_node)
nset,a,node,,a1p_a2p_a3p_corner
pos_node=node(-x_,y_,-z_)
ceeq=ceeq+1
ce,ceeq,(eps21*(a1*2))+(eps22*(a2*2))+(eps23*(a3*2)),neg_node,ux,-1,pos_node,ux,1 ! x->2
ceeq=ceeq+1
ce,ceeq,(eps31*(a1*2))+(eps32*(a2*2))+(eps33*(a3*2)),neg_node,uy,-1,pos_node,uy,1 ! y->3
ceeq=ceeq+1
ce,ceeq,(eps11*(a1*2))+(eps12*(a2*2))+(eps13*(a3*2)),neg_node,uz,-1,pos_node,uz,1 ! z->1

nset,s,node,,a1n_a2n_a3p_corner
*get,neg_node,node,0,num,min
!   get x,y,z locations of current node in active coord system
    x_=nx(neg_node)
    y_=ny(neg_node)
    z_=nz(neg_node)
nset,a,node,,a1p_a2p_a3n_corner
pos_node=node(-x_,y_,-z_)
ceeq=ceeq+1
ce,ceeq,(eps21*(a1*2))+(eps22*(a2*2))-(eps23*(a3*2)),neg_node,ux,-1,pos_node,ux,1 ! x->2
ceeq=ceeq+1
ce,ceeq,(eps31*(a1*2))+(eps32*(a2*2))-(eps33*(a3*2)),neg_node,uy,-1,pos_node,uy,1 ! y->3
ceeq=ceeq+1
ce,ceeq,(eps11*(a1*2))+(eps12*(a2*2))-(eps13*(a3*2)),neg_node,uz,-1,pos_node,uz,1 ! z->1

```

```

nset,s,node,,a1n_a2p_a3n_corner
*get,neg_node,node,0,num,min
! get x,y,z locations of current node in active coord system
x_=nx(neg_node)
y_=ny(neg_node)
z_=nz(neg_node)
nset,a,node,,a1p_a2n_a3p_corner
pos_node=node(-x_,-y_,-z_)
ceeq=ceeq+1
ce,ceeq,(eps21*(a1*2))- (eps22*(a2*2))+ (eps23*(a3*2)),neg_node,ux,-1,pos_node,ux,1 ! x->2
ceeq=ceeq+1
ce,ceeq,(eps31*(a1*2))- (eps32*(a2*2))+ (eps33*(a3*2)),neg_node,uy,-1,pos_node,uy,1 ! y->3
ceeq=ceeq+1
ce,ceeq,(eps11*(a1*2))- (eps12*(a2*2))+ (eps13*(a3*2)),neg_node,uz,-1,pos_node,uz,1 ! z->1

nset,s,node,,a1n_a2p_a3p_corner
*get,neg_node,node,0,num,min
! get x,y,z locations of current node in active coord system
x_=nx(neg_node)
y_=ny(neg_node)
z_=nz(neg_node)
nset,a,node,,a1p_a2n_a3n_corner
pos_node=node(-x_,-y_,-z_)
ceeq=ceeq+1
ce,ceeq,(eps21*(a1*2))- (eps22*(a2*2))- (eps23*(a3*2)),neg_node,ux,-1,pos_node,ux,1 ! x->2
ceeq=ceeq+1
ce,ceeq,(eps31*(a1*2))- (eps32*(a2*2))- (eps33*(a3*2)),neg_node,uy,-1,pos_node,uy,1 ! y->3
ceeq=ceeq+1
ce,ceeq,(eps11*(a1*2))- (eps12*(a2*2))- (eps13*(a3*2)),neg_node,uz,-1,pos_node,uz,1 ! z->1

ALLSEL,ALL
*END

/SOLU ! Solution module
! ceRve arguments:
! a1,a2,a3,eps1,eps2,eps3,eps4,eps5,eps6

*use,ceRVE,a1,a2,a3,1.,0,0,0,0
SOLVE ! Solve analysis
*use,ceRVE,a1,a2,a3,0,1.,0,0,0,0
SOLVE ! Solve analysis
*use,ceRVE,a1,a2,a3,0,0,1.,0,0,0
SOLVE ! Solve analysis
*use,ceRVE,a1,a2,a3,0,0,0,1.,0,0
SOLVE ! Solve analysis
*use,ceRVE,a1,a2,a3,0,0,0,0,1.,0
SOLVE ! Solve analysis
*use,ceRVE,a1,a2,a3,0,0,0,0,0,1.
SOLVE ! Solve analysis
FINISH ! Exit solution module

*create,srecover!,mac ! Create macro to calculate average stress
/nopr
ETABLE,,VOLU, ! Get element volume
ETABLE,,SX, ! Get element stress
ETABLE,,SY
ETABLE,,SZ
ETABLE,,SXY
ETABLE,,SXZ
ETABLE,,SYZ
SMULT,SXV,VOLU,SX,1,1, ! Stress by element volume
SMULT,SYV,VOLU,SY,1,1,
SMULT,SZV,VOLU,SZ,1,1,
SMULT,SXYV,VOLU,SXY,1,1,
SMULT,SXZV,VOLU,SXZ,1,1,
SMULT,SYZV,VOLU,SYZ,1,1,

```

```

SSUM
*get,totvol,ssum,,item,volu ! Integer stress along total volume
*get,totsx ,ssum,,item,sxv
*get,totsy ,ssum,,item,syv
*get,totsz ,ssum,,item,szv
*get,totsxy ,ssum,,item,sxyv
*get,totsxz ,ssum,,item,sxzv
*get,totsyz ,ssum,,item,syzv

Sxx0 = totsx/totvol ! Compute average RVE stress
Syy0 = totsy/totvol
Szz0 = totsz/totvol
Sxy0 = totsxy/totvol
Sxz0 = totsxz/totvol
Syz0 = totsyz/totvol
/gopr
*end !srecover

/POST1 ! Post-processor module
/DEVICE,VECTOR,0
/PNUM,MAT,0
PLESOL,S,Z,1

SET,1 ! First column coefficients
*use,srecover
C11 = Szz0
C21 = Sxx0
C31 = Syy0

SET,2 ! Second column coefficients
*use,srecover
C12 = Szz0
C22 = Sxx0
C32 = Syy0

SET,3 ! Third column coefficients
*use,srecover
C13 = Szz0
C23 = Sxx0
C33 = Syy0

EL=C11-2*C12*(C22+C23)
nuL=C12/(C22+C23)
ET=(C11*(C22+C23)-2*C12*C12)*(C22-C23)/(C11*C22-C12*C12)
nuT=(C11*C23-C12*C12)/(C11*C22-C12*C12)
GT=(C22-C23)/2 ! or GT=ET/2/(1+nuT)

SET,4 ! Fith column coefficients
*use,srecover
C44 = Sxy0

SET,5 ! Fith column coefficients
*use,srecover
C55 = Syz0

SET,6 ! Sixth column coefficients
*use,srecover
C66 = Sxz0

```